



Visualisation of nanoparticle-cell interactions by correlative microscopy

Dissertation

Zur Erlangung des akademischen Grades

Doktor der Naturwissenschaften

Am Fachbereich Biologie

der Johannes Gutenberg-Universität Mainz

vorgelegt von

Shen Han, M.Sc.

geboren am 20.09.1990 in Shenzhen, China

Mainz, Juli 2021

The presented thesis was carried out from December 2016 until July 2021 in the department of Physical Chemistry of Polymers at the Max Planck Institute for Polymer Research in Mainz (Germany).

1. Gutachter:

2. Gutachter:

Tag der mündlichen Prüfung:

“New directions in science are launched by new tools much more often than by new concepts. The effect of a concept-driven revolution is to explain old things in new ways. The effect of a tool-driven revolution is to discover new things that have to be explained.”

— *Freeman Dyson*

Eigenständigkeitserklärung

I hereby declare that I wrote the dissertation submitted without any unauthorised external assistance and used only sources acknowledged in the work. All textual passages, which are appropriated verbatim or paraphrased from published and unpublished texts, as well as all information obtained from oral sources are duly indicated and listed in accordance with bibliographical rules. In carrying out this research, I complied with the rules of standard scientific practice as formulated in the statutes of the Johannes Gutenberg University Mainz to ensure standard scientific practice.

Mainz, July 2021

Abstract

Nanoparticles (NPs) have been a part of our daily life and have emerged to be ideal drug carriers mainly due to their small size and controllable functionalisation for potential cell targeting. Since the 1990s, NPs have been used for clinical purposes, and they have been continuously showing their immense capacity in drug delivery such as the recent RNA vaccine. On one hand, engineered NPs provide a relatively stable carrier system for fragile but active agents like proteins and RNAs. On the other hand, NPs inevitably interact with components in biological milieu and the interaction is define and affect the efficacy of these NPs. Therefore, it is very crucial to understand and to visualise the interactions between the engineered NPs and cells in order to facilitate the smarter design of more effective nanomedicine. The aim of this thesis is to extract useful information from the intracellular journey of NPs by the leverage of various microscopic techniques.

With the elemental mapping by energy-dispersive X-ray (EDX) spectroscopy in transmission electron microscopy (TEM), inorganic silica nanocapsules (SiNCs) were clearly identified from the organic cellular environment. It was demonstrated that different stages of SiNCs in HeLa cells including the initiate uptake and the distribution in late endosomes were pinpointed. The possible degradation of SiNCs was further confirmed by EDX elements mapping. It was proven that SiNCs were degradable in HeLa cells and could be a potential candidate for drug carrier despite their inorganic composition.

In order to achieve an equally efficient identification of organic NPs in cells, light microscopy (LM) and electron microscopy (EM) were combined to image carbon-based fluorescent nanodiamonds (fNDs) with inherent fluorescence. The exploitation of in-dish and on-section correlative light and electron microcopy (CLEM) proposed general strategies to balance the preservation of fluorescence and cellular structures after EM preparations. Further applications of several imaging techniques in TEM revealed even single fND upon uptake and in a mitochondrion. By employing these precise imaging techniques to visualise fNDs in cells, single particle events like subcellular targeting in mitochondria or endosomal escape are able to be captured.

The application of core-shell NCs for medical purposes have gained so much attention especially the NCs made from biocompatible materials such as proteins. In order to achieve the precise localisation of such NCs, on-section CLEM was performed to identify bovine serum albumin

(BSA) NCs, marked with nanoplatelets (NPLs) in cells. With the help of the fluorescence from NPLs, the distribution of intracellular NCs were tracked at different time points. It was shown that the internalised BSA NCs followed the endolysosomal pathway and ended up in endolysosomes and late endosomes for degradation. This work shows how to trace the intracellular fate of protein NCs with the help of particles exhibiting inherent fluorescence.

The ultimate goal to visualise intracellular polymeric NPs by on-section CLEM is to resolve the fluorescence from organic dyes which are used for the labelling. In order to achieve this goal, an optimised on-section CLEM workflow was developed for organic dye-labelled NPs and NCs. It was demonstrated that organic dyes BODIPY and Cy5 were preserved within polystyrene NPs (PS NPs) and hydroxyethyl starch (HES) NCs after EM preparation with osmium tetroxide (OsO₄) and EPON resin embedding. This work presented for the first time how CLEM could be applied to localise intracellular polymeric NPs which are labelled with organic dyes.

The most troublesome problem when developing polymeric NPs for medical applications is the formation of the protein corona. It represents the protein coat which adsorbs onto the NPs once they are introduced into biological fluid and will eventually alter the biological behaviour of NPs. We took advantages of the optimised on-section CLEM to further explore the intracellular fate of protein corona. By performing volume CLEM with array tomography (AT) using a Cy5 labelled protein corona and BODIPY labelled PS NPs, the unique endosomal distribution of protein corona and NPs was illustrated within a 3-dimensional model. It was shown that the protein corona was gradually separated from the NPs. This happens during the maturation from early endosomes to late endosomes and multivesicular bodies (MVBs).

Zusammenfassung

Nanopartikel (NPs) sind ein Teil unseres täglichen Lebens und haben sich als ideale Wirkstoffträger erwiesen, vor allem aufgrund ihrer geringen Größe und der kontrollierbaren Funktionalisierung für ein mögliches Zell-Targeting. Seit den 1990er Jahren werden NPs für klinische Zwecke eingesetzt, und sie haben kontinuierlich ihre immensen Fähigkeiten bei der Entwicklung von Medikamenten gezeigt, wie z. B. der jüngste RNA-Impfstoff. Auf der einen Seite bieten NPs ein relativ stabiles Trägersystem für fragile, aber aktive Wirkstoffe wie Proteine und RNAs. Auf der anderen Seite interagieren NPs unweigerlich mit Komponenten im biologischen Milieu, und diese Interaktion ist definiert und beeinflusst die Wirksamkeit dieser NPs. Daher ist es von entscheidender Bedeutung, die Wechselwirkungen zwischen den künstlich hergestellten NPs und Zellen zu verstehen und zu visualisieren, um ein intelligentes Design von Nanotherapeutika zu ermöglichen. Das Ziel der vorliegenden Arbeit ist es, nützliche Informationen aus der intrazellulären Reise der NPs durch den Einsatz verschiedener mikroskopischer Techniken zu extrahieren.

Mit dem chemischen Mapping mittels energiedispersiver Röntgenspektroskopie (EDX) in der Transmissionselektronenmikroskopie (TEM) wurden anorganische Siliziumdioxid-Nanokapseln (SiNCs) in zellulärer Umgebung eindeutig identifiziert. Es konnte gezeigt werden, dass verschiedene Stadien der SiNCs in HeLa-Zellen einschließlich der initiierten Aufnahme und der Verteilung in späten Endosomen lokalisiert werden konnten. Der Abbau von SiNCs wurde durch EDX-Mapping weiter bestätigt. Es wurde nachgewiesen, dass SiNCs in HeLa-Zellen abbaubar sind und trotz ihrer anorganischen Zusammensetzung ein potenzieller Kandidat für einen Medikamententräger sein könnten.

Um eine ebenso effiziente Identifizierung von organischen NPs in Zellen zu erreichen, wurden Lichtmikroskopie (LM) und Elektronenmikroskopie (EM) kombiniert, um Kohlenstoff-basierte fluoreszierende Nanodiamanten (fNDs) mit inhärenter Fluoreszenz abzubilden. Mit der In-Dish- und On-Section-CLEM Methode haben wir eine allgemeine Strategien entwickelt, um die Fluoreszenz in zellulären Strukturen nach EM-Präparationen zu konservieren. Weitere Anwendungen verschiedener Bildgebungstechniken im TEM zeigten sogar den Aufnahmeprozess eines einzelnen fND und ebenso fNDs in einem Mitochondrium. Durch den Einsatz dieser präzisen

Bildgebungstechniken zur Visualisierung von fNDs in Zellen können einzelne Partikelereignisse wie subzelluläres Targeting in Mitochondrien oder endosomales Entweichen erfasst werden.

Die Anwendung von Core-Shell-NCs für medizinische Zwecke hat ein großes Potential, und hier insbesondere die NCs aus biokompatiblen Materialien wie Proteinen. Um eine präzise Lokalisierung solcher NCs zu erreichen, wurde die On-Section-CLEM Methode durchgeführt, um die mit Nanoplättchen (NPLs) markierten NCs aus Rinderserumalbumin (BSA) intrazellulär zu identifizieren. Mit Hilfe der Fluoreszenz von NPLs wurde die Verteilung der intrazellulären NCs zu verschiedenen Zeitpunkten verfolgt. Es zeigte sich, dass die internalisierten BSA-NCs dem endolysosomalen Weg folgten und zum Abbau in Endolysosomen und späten Endosomen landeten. Diese Arbeit zeigt, wie das intrazelluläre Schicksal von Protein-NCs mit Hilfe von fluoreszenten Partikeln verfolgt werden kann.

Das ultimative Ziel, um intrazelluläre polymere NPs mittels On-Section-CLEM sichtbar zu machen, ist die Konservierung der Fluoreszenz von organischen Farbstoffen, die für die Markierung der NPs verwendet werden. Um dieses Ziel zu erreichen, wurde ein optimierter on-section CLEM-Workflow für NPs und NCs entwickelt, welche mit einem organischen Farbstoff markiert sind. Wir konnten erreichen, dass die organischen Farbstoffe BODIPY und Cy5 innerhalb von Polystyrol-NPs (PS NPs) und Hydroxyethylstärke (HES) NCs nach der EM-Präparation mit Osmiumtetroxid (OsO_4) und EPON-Harzeinbettung erhalten bleiben. In dieser Arbeit wurde zum ersten Mal gezeigt, wie CLEM zur Lokalisierung intrazellulärer polymerer NPs, die mit organischen Farbstoffen markiert sind, eingesetzt werden kann.

Das schwierigste Problem bei der Entwicklung polymerer NPs als Wirkstoffträgersystem in der nanomedizinischen Anwendung ist die Bildung einer Proteinkorona. Diese ist eine Proteinhülle, die sich an die NPs anlagert, sobald diese in einer biologischen Flüssigkeit eingebracht werden. Die Proteinkorona kann das biologische Verhalten der NPs verändern. Wir nutzten die Vorteile der optimierten On-Section-CLEM Methode, um das intrazelluläre Schicksal der Proteinkorona weiter zu untersuchen. Mittels Volumen-CLEM mit Array-Tomographie (AT) an einer mit Cy5-markierten Proteinkorona und BODIPY-markierten PS NPs konnte die endosomale Verteilung der Proteinkorona und der NPs 3-dimensional dargestellt werden. Es konnte gezeigt werden, dass die Proteinkorona allmählich von den NPs getrennt wird. Dies geschieht bei der Reifung der frühen Endosomen zu späten Endosomen und multivesikulären Körpern (MVBs).

Contents

Abstract	I
Zusammenfassung	III
1. State of the art.....	1
1.1 Applications of NPs for nanomedicine.....	1
1.2 Visualisation of NPs in cells.....	5
1.2.1 Visualisation of polymer-based NPs in cells.....	5
1.2.2 Application of NPs in correlative light and electron microscopy (CLEM)	10
1.3 Application of CLEM in biology	12
2. Results and discussions—application of correlative microscopy methods to study cellular uptake, distribution and degradation of nanoparticles.....	17
2.1 Correlating TEM and energy-dispersive X-ray spectroscopy (EDX) to localise intracellular silica nanocapsules.....	23
2.2 High-contrast imaging of nanodiamonds in cells by energy filtered and correlative light-electron microscopy: toward a quantitative nanoparticle-cell analysis	34
2.3. Visualising the destiny of protein nanocarriers along the endolysosomal pathway – different compartments are involved in processing protein nanocarriers.....	57
2.4. Correlative microscopy to visualise polymeric nanoparticles in cells.....	78
2.5 In-cell separation of the protein corona from nanoparticles and snapshots of how it evolves intracellularly	93
3. Experimental methods	113
3.1 General protocols for the preparation of cells for EM and CLEM.....	113
3.1.1 Cell culture for adherent cells	113
3.1.2 Cellular uptake experiments and high pressure freezing (HPF)	113
3.1.3 Freeze substitution and embedding in resin.....	114
3.1.4 Ultramicrotomy and imaging.....	114

3.1.5 Confocal laser scanning microscopy (cLSM).....	115
3.1.6 Transmission electron microscopy (TEM) and Scanning electron microscopy (SEM).....	115
3.1.7 Electron energy loss spectroscopy (EELS).....	116
3.2 Correlating TEM and EDX to localise intracellular SiO ₂ NCs.....	117
3.2.1 Energy-dispersive X-ray spectroscopy (EDX)	117
3.3 CLEM for intracellular NDs.....	117
3.3.1 Material.....	117
3.3.2 Preparation of in-dish CLEM specimens for cLSM and TEM	118
3.3.3 Preparation of in-resin CLEM specimens for cLSM and TEM	118
3.3.4 Image alignment and analysis.....	119
3.3.6 Image registration for CLEM in icy eC-CLEM.....	120
3.3.5 Transmission electron microscopy (TEM)	120
3.4 CLEM for intracellular polymeric NPs	121
3.4.1 Cell culture and co-incubation with NPs	121
3.4.2 Sample preparation for correlative light and electron microscopy (CLEM)	121
3.4.3 For CLEM by TEM inspection.....	122
3.4.4 For CLEM by SEM inspection.....	122
3.5 CLEM for intracellular protein corona.....	122
3.5.1 Synthesis of carboxy-functionalised PS NPs.....	123
3.5.2 RAW264.7 cell culture.....	123
3.5.3 Sample preparation for CLEM	124
3.5.4 Serial sectioning and CLEM imaging.....	124
3.5.5 Fluorescence colocalisation measurement.....	125
4. Summary and outlook.....	126
Literatures.....	132
Publication list.....	146
Curriculum Vitae	147

1. State of the art

1.1 Applications of NPs for nanomedicine

In modern medicine, much consideration is given to the availability and selectivity of a drug to the destination, and the bio-compatibility of the carrier material used. NPs gain attention for being suitable drug delivery carriers due to their small size in dimension and relatively easy surface functionalisation.^[1] This facilitates easier cellular/tissue penetration which, with the help of surface functionalisation, makes directed targeting possible.^[1] There are different types of NPs that are used in biomedical research and applications, which are practical in use because of their individual convenience.^[1, 2] Inorganic NPs like gold particles and quantum dots are easy to be modified via straightforward chemical reactions and are easy to produce at large scales.^[2, 3] Polymeric NPs and lipid-based NPs are much more biocompatible while also being biodegradable, and water-soluble compared to inorganic NPs.^[1, 4] The versatile formulation procedures provide them with core-shell structures to encapsulate vulnerable active agents like mRNA and small peptides or imaging agents.^[5-8] The core-shell structure not only protects the therapeutic/imaging payload from the enzymatic environment but also provides the surface for possible modifications such as cross-linking antibodies for targeting^[9, 10] and PEGylation to increase stability and decrease immunogenicity (Figure 1.1.1).^[11, 12]

As the most commonly FDA-approved nanomedicine in the category,^[13, 14] lipid-based NPs (LNPs) offer relatively simple formulation and controllable (physicochemical) properties for the dynamic biological environment.^[15, 16] The most recent mRNA vaccine against SARS-CoV-2 corona virus uses LNPs as the delivery system.^[17, 18] The structure of a LNP represents a typical core-shell assembly, which consists of a neutral phospholipid, cholesterol, a polyethylene-glycol (PEG)-lipid, and an ionisable cationic lipid.^[17] The anionic mRNA interacts directly with a cationic lipid during particle formation, and the PEGylated lipid is responsible for the stabilisation and reduction of aggregation during transportation. Although the uptake mechanism of LNPs is still not entirely understood, it is suggested that the cationic lipid within the compositions of LNPs enhances the membrane fusion.^[19, 20]

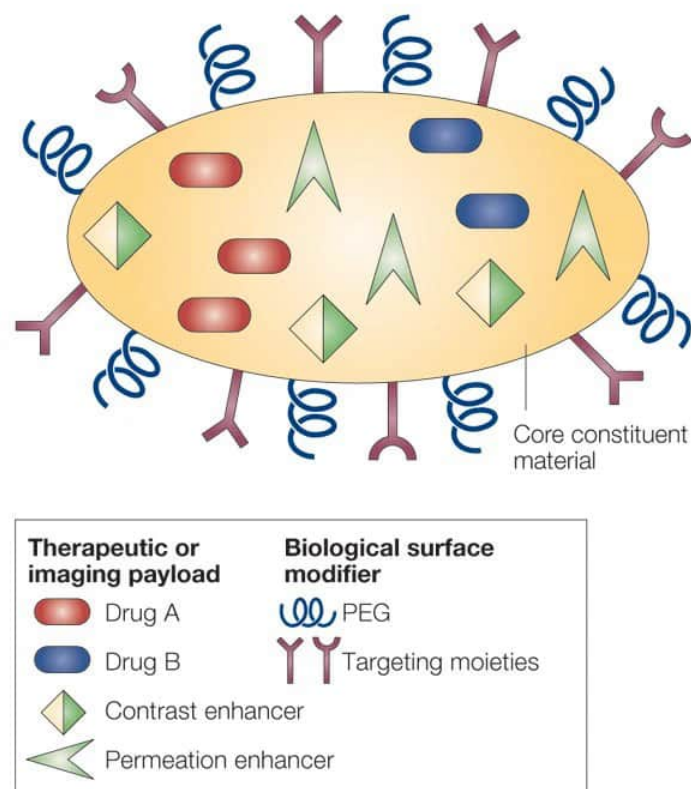


Figure 1.1.1 Demonstration of an engineered nanocarrier with different components or therapeutic/imaging purposes. Reproduced with permission from ref [12], Copyrights © 2005 Nature Publishing Group.

Polymeric NPs are also promising drug carriers with the capacity to deliver various kinds of payloads such as proteins or macromolecules with different molecular weights,^[21-23] and genetic materials like siRNA.^[24] With the modulation of their compositional and responsive properties, precise controlled release of certain active components can be achieved.^[25] Although there are still limited numbers of polymer-based NPs which have been approved by the FDA for clinical purposes, many ongoing clinical trials focus on polymer NPs.^[14] As one of the largest groups of polymer NPs, nanocapsules (NCs) show tremendous potential for being multifunctional drug delivery systems. Baier et al. used hydroxyethyl starch (HES), which is a proven drug to treat several blood circulation diseases, to synthesise nanocapsules (NCs) for drug delivery.^[26] In the study, HES capsules were conjugated with folic acid as a model targeting agent due to its high affinity with folate receptor (FR α) overexpressing cell lines. Non-functionalised and folic acid conjugated HES NCs were co-incubated with FR α expressing HeLa cells and FR α non-expressing

A549 cells. A very low cellular uptake was observed with non-functionalised NCs in HeLa cells by flow cytometry, while both NCs showed inhibited cellular uptake in A549 cells. The results of this study gave a good example of the versatility of synthesis material of NCs and demonstrated that modulating the surface functionalisation of NCs greatly assisted the desired targeting to specific cell lines.

Besides the precise targeting effect, the other important criteria for biocompatible polymer-based nanomedicine is the possibility of intracellular degradation. The searching of biodegradable materials ranges widely from inorganic [27, 28] to organic [29, 30] substances. A proper shell material for NCs is able to sequester the core active agents from the extracellular environment and at the same time permits the convection of the agents intracellularly. The realisation of intracellular payload release relies strongly on the biodegradability of the polymer materials. Silica-based NCs emerged as a nice carrier system by showing biodegradability within hours.[28, 31] Chen et al. found out that the mesoporous silica NPs exhibited a multistage rapid degradation in simulated body fluid, and the strongest degradation happened at the first stage after incubation at 2 h.[31] Jiang et al. used sol-gel derived PEGylated silica NCs to suppress inflammatory responses in murine liver cells.[28] In the study, the degradation of silica NCs in endolysosome was observed in HeLa cells at 2 h by TEM and further confirmed by energy-dispersive X-ray (EDX) spectroscopy. Other than the possible biodegradability of silica NCs, Hirsch et al. demonstrated a tunable gold-coated silica NCs system to locally eradicate tumours in mice by selective near-infrared light radiation.[32] This study additionally indicates that silica-based NCs are suitable for location-specific therapy by external activation.

Recently, protein-based NCs have drawn massive attention for being even more suitable nanocarriers to execute efficient intracellular payload release. Because proteins can be lysed by the corresponding protease within a cellular environment, the release of payload from NCs can be then achieved. Piradashvili et al. synthesised protein NCs with bovine serum albumin (BSA) and ovalbumin (OVA) individually and were subjected to human monocyte-derived dendritic cells (moDCs).[33] The protein NCs showed no cytotoxicity to cells in confocal laser scanning microscope (cLSM) with a concentration up to 100 µg/mL for 24 h. Degradability of the NCs was confirmed in vitro with proteolytic reactions and further in moDCs by observing the release of the fluorescently labelled protein in cLSM. This study introduces the concept that protein NCs are

promising for further therapeutic applications such as a vaccine or antigen delivery, and they are degradable by innate proteolytic lysing in cells.

Frey et al. further exploited the concept of protein NCs by introducing bio-orthogonal reactions with triazolinediones (TADs) and 2,4-toluene diisocyanate (TDI) as crosslinkers into a more controllable and efficient synthesis procedure.^[34] In the study, BSA, human serum albumin (HSA) and OVA were used to make NCs respectively. Differences in cellular uptake in HeLa Cells were observed with NCs synthesised with different crosslinkers in serum free environment. TAD crosslinked NCs showed more interactions with cells than TDI crosslinked NCs in general. This phenomenon was explained by the hydrophobicity/hydrophilicity of the crosslinkers which could sequentially affect the surface properties of protein NCs. The protein corona compositions of NCs with different crosslinkers showed significant differences which might eventually lead to the divided cellular behaviours of the NCs. This study discusses the possibility of optimising the synthesis of protein NCs to achieve wider applications beyond their existing merits.

Despite the mentioned accomplishments in producing a perfect drug delivery system with NPs, there are still many challenges such as in vivo stability and circulation time. These challenges inevitably influence the effective biodistribution of the NPs and eventually hamper the desired purposes. Numerous measures have been made to enhance the stability of NPs such as introducing cholesterol and PEGylated lipids in lipid-based NPs ^[17, 35] or involving surface PEG chains ^[36] or different crosslinking methods.^[37] However, exposure to PEG inevitably induces anti-PEG antibodies which will facilitate the clearance of PEGylated NPs by the immune system.^[38, 39] Therefore, a balance between physiological stability and circulation time of NPs is essential for successful and precise drug delivery. Furthermore, because of the heterogeneity among diseases and patients, the microenvironment of different diseases in individual patients react differently to the same NPs.^[40] Hence, designing personalised NPs therapy could be the ultimate solution.

1.2 Visualisation of NPs in cells

The most reliable way to understand the efficacy and cytotoxicity of nanomedicine is by studying the cellular internalisations and interactions. In order to clearly elucidate how NPs interact with mammalian cells, characterisation of these particular events are often necessary. Generally, characterisation methods such as flow cytometry, SDS-PAGE, and LC-MS are essential for the indirect characterisation of such events. However, the most direct details of these interactions are only provided by advanced imaging techniques.^[41] Generally, light microscopes (LM) are used to determine the internalisation of fluorescently labelled NPs in cells. But due to the diffraction limit of light for illumination, the lateral resolution of traditional LM is limited to around 200 nm.^[42] Although with the most upscale super-resolution techniques, resolution can be greatly improved to achieve single-particle imaging, the localisation of individual particles within the subcellular milieu is still a demanding and challenging process.^[43] EM compensates for the weakness of LM by providing unmatched resolution and fine ultrastructures of subcellular environment. Accelerated by the well-developed sample preparation, EM continues to grow importance in the field of biological study.^[44] The resolution of EM enables the visualisation of single NPs in cells and the investigation of particle-cell interactions. Therefore, EM has become an irreplaceable imaging method to visualise intracellular inorganic/polymeric NPs.^[45, 46] Despite the small amounts of literature focusing on harnessing EM to visualise intracellular polymer NPs, this section will discuss the leverage of EM as a powerful imaging method for this purpose.

1.2.1 Visualisation of polymer-based NPs in cells

Visualisations of intracellular polymeric NPs in EM poses more challenges than inorganic NPs because the latter usually possess electron-dense core which can be conveniently identified within EM. Whereas, intracellular polymeric NPs provide low contrast in EM since their elemental constitutions are mostly the same as the cellular environment. The heavy metal staining during the EM preparation equally labels both NPs and the cell which sometimes creates difficulty to differentiate both components. However, due to the exposure to OsO₄ and uranyl acetate (UA) during the staining process, the functional groups on the surface of polymeric NPs are sometimes stained more pronouncedly than the cellular structures because the existing density of these

functional groups are sometimes higher on the surface of NPs than on the cellular components like proteins and nucleic acids.^[45]

As one of the most widely employed polymers, polystyrene (PS) appears in most packaging of commercial products like food, cosmetics and pharmaceuticals.^[47] Recently, increasing concerns about PS have raised because of the pollution with nano-plastics,^[48, 49] more extensive investigations are needed to understand the cellular impact of the polymer. Besides the potential pollution, polystyrene NPs are frequently used as a model system to study the cellular interactions and physiochemical properties of polymer NPs for potential therapeutical purposes.^[50, 51]

Firdessa et al. conducted cellular uptake experiments of commercial unmodified PS NPs with primary bone marrow-derived macrophages (BMDM).^[52] Macrophages were incubated with the same concentration of PS NPs with a diameter of 100 nm at different time intervals of 30 min, 6 h and 12 h. The authors determined from the fluorescence intensity of the internalised PS NPs that the cellular internalisation followed a time-dependent manner. Most of PS NPs appeared in the cells after 12 h. The internalisation of PS NPs was confirmed by transmission electron microscopy (TEM). Interesting, the authors also observed different endocytosis pathways and early endosomes containing PS NPs in TEM after 30 min (Figure 1.2.1.1). The EM preparation of the samples was performed via chemical fixation with glutaraldehyde at 4 °C and further heavily stained with 50 % OsO₄ and 0.5 % UA followed by gradient dehydration in ethanol. Although the identification of endocytotic vesicles and PS NPs were only dependent on the morphology, the observations still provided initial impressions of how PS NPs were internalised and distributed in the cellular environment by EM.

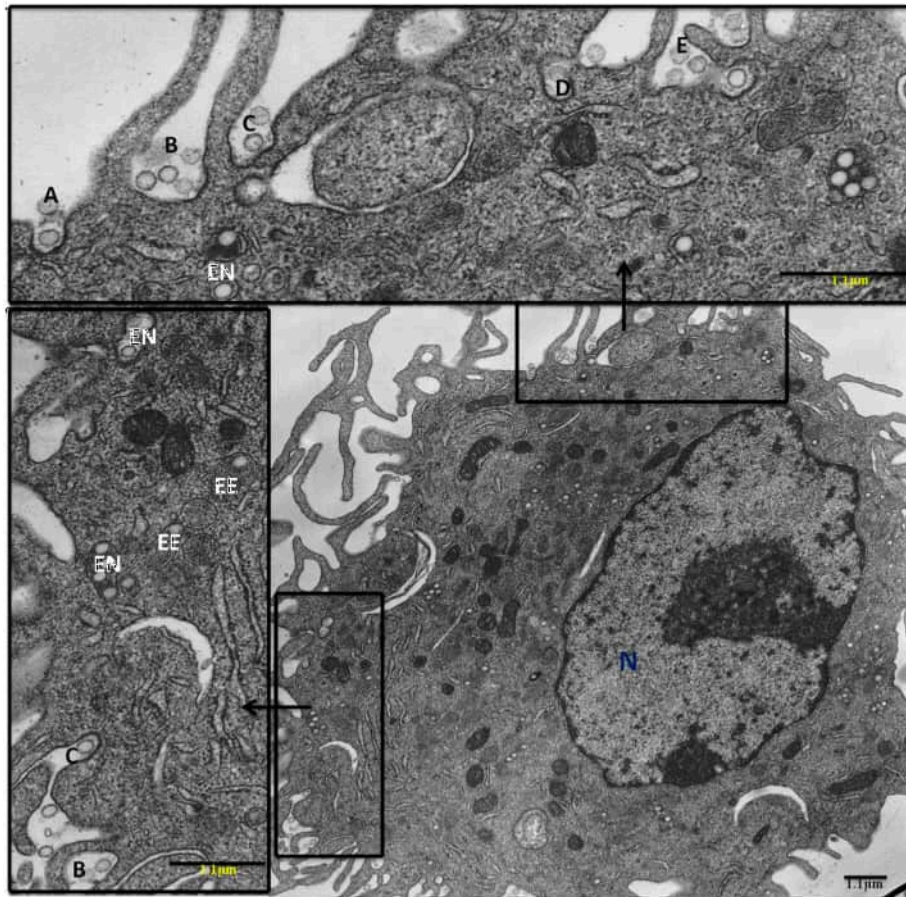


Figure 1.2.1.1 Multiple endocytic pathways used simultaneously by BMDM to take up 100 nm polystyrene NPs after 30min of exposure. Clathrin-mediated endocytosis (A), phagocytosis (B), clathrin- and caveolae-independent endocytotic pathways (C), caveolae-mediated endocytosis (D), and macropinocytosis (E) are indicated. Intracellular vesicles containing the endocytosed NPs (EN), localization of the NPs in early endosomes (EE) and the nucleus (N) are also shown. Labelled structures (A-E) are the zoomed out portions of the depicted cell for clarity. Reproduced with permission from ref [52], Copyrights © 2014 Elsevier GmbH.

Musyanovych et al. performed cellular experiments with PS NPs and poly(L-lactic acid) (PLLA) nanoparticles with different surface charges in HeLa cells.^[53] The authors showed that cationic PS NPs and PLLA NPs were taken up by cells more efficiently than anionic particles. Whereas the presence of a cationic surfactant on both NPs altered the cellular structures, the anionic PS NPs were more densely filled within endosomes than PLLA NPs. It is worth mentioning that the authors used ruthenium tetroxide (RuO₄) instead of OsO₄ as a staining agent and fixative after the cryofixation for better contrast in cells in EM. Because the aromatic groups within the NPs reacted more intensively with RuO₄ to create better contrast by introducing a higher electron density.

Lerch et al. produced a nanoparticle pH sensor system by coupling a pH sensitive dual wavelength dye carboxy seminaphthorhodafluor-1 (SNARF-1) to amino functionalised PS NPs to monitor the changing pH environment in different endosomes along the endolysosomal pathway.^[54] The authors investigated the distribution and localisation of the NPs by their evolving fluorescence within endosomes with different acidified conditions. They found out that PS NPs followed the endo/lysosome pathway after being internalised and ended up in late endosomes after 3 h. The EM results further confirmed the internalisation events and the distribution of NPs in early endosomes after 1 h and in late endosomes/lysosomes/multivesicular bodies (MVBs) after 3 h (Figure 1.2.1.2). The number of NPs also increased in the endosomes in the later stages compared to the early endosomes. This study presents hints and strategies for monitoring NPs in cells by integrating synthetic and imaging techniques.

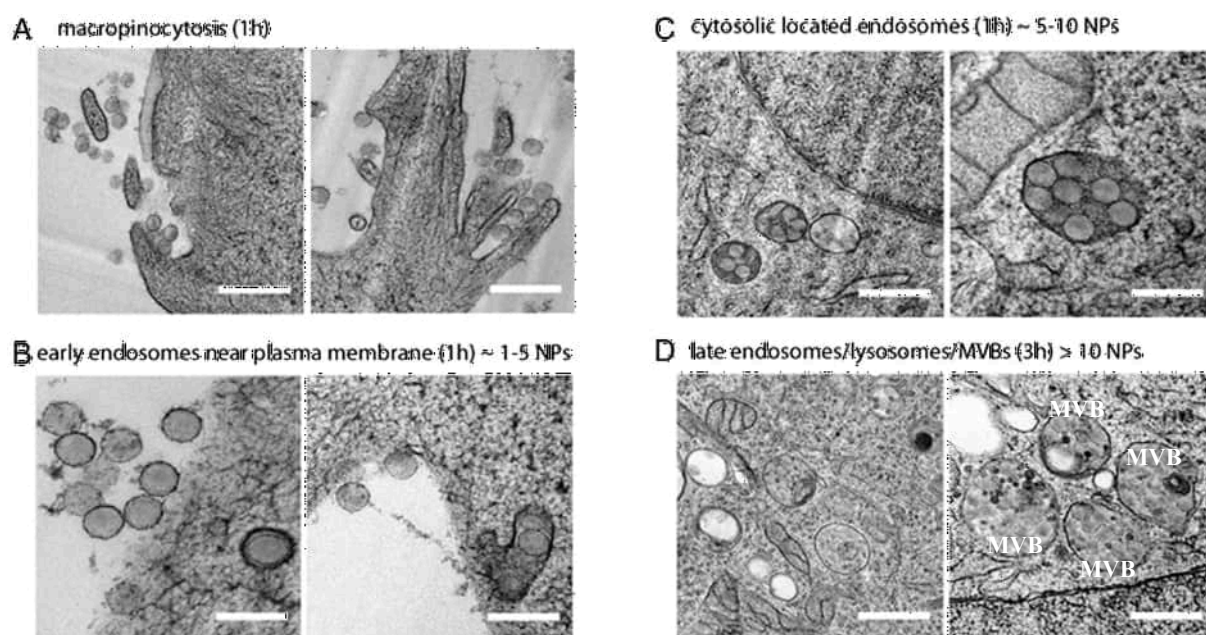


Figure 1.2.1.2 Transmission electron microscopy (TEM) images of SNARF-1-NP uptake in HeLa cells. HeLa cells were loaded with SNARF-1-NPs (0.3 g/L) and prepared for TEM imaging after 1 h and 3 h incubation time. MVBs: multivesicular bodies. Scale bars: 300 nm. Reproduced with permission from ref [54], Copyrights © 2015 Elsevier Inc.

There are even fewer studies focusing on utilising EM techniques to visualise core-shell polymeric NCs in cells since the thinness of the polymer shell fortifies the difficulties for both sample preparation and imaging. Yan et al. introduced a class of polymeric NCs with a protein core and co-incubated them to HeLa cells.^[55] The NCs were synthesised by polymerising the monomers which were covalently bound onto the proteins of choice with degradable and non-degradable crosslinkers. In this study, the authors applied a chemical fixation and TEM approach to visualise the intracellular polymeric horseradish peroxidase (HRP) NCs (Figure 1.2.1.3). In order to better identify the NCs in cells, gold quantum dots were encapsulated into the NCs to give higher contrast in EM. Although the magnification and resolution of EM figure did not present adequate information on either the integrity of the NCs or the cellular structures, this study provides valuable opinions on efficiently localising core-shell polymeric NCs in cells.

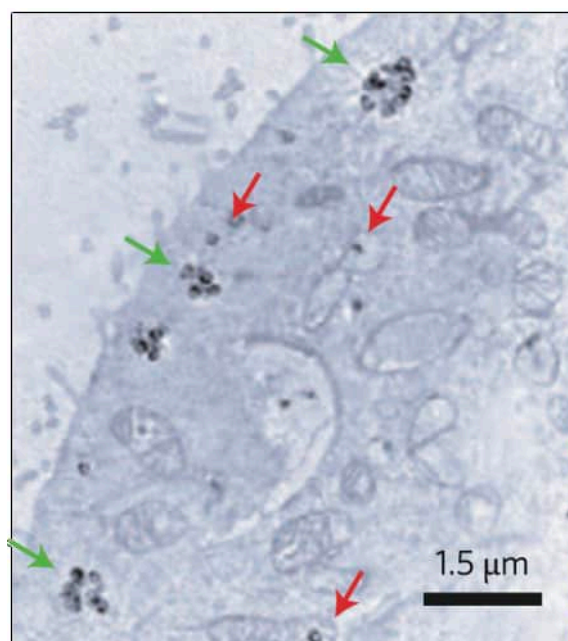


Figure 1.2.1.3 TEM image of a HeLa cell after incubation with gold quantum-dot-labelled HRP nanocapsules. Red arrows show dispersion of single nanocapsules in the cell cytosol; green arrows show clusters of nanocapsules. Reproduced with permission from ref [55], Copyrights © 2009 Nature Publishing Group.

1.2.2 Application of NPs in correlative light and electron microscopy (CLEM)

Correlative light and electron microscopy (CLEM) is a powerful imaging technique that combines the strength from both LM and EM. The most significant merit of this technique is embodied in the capacity of localising molecules/particles in high resolution EM micrographs with fluorescence.^[56] However, the application of CLEM with intracellular polymeric NPs has not yet been established. This paragraph will discuss the use of gold particles and quantum dots (QDs) as fluorescent markers for CLEM study.

Gold nanoparticles (AuNPs) are one of the most commonly used synthesised NPs in biological imaging. Due to its tunable size, relatively high electron density and easy surface modification,^[57] antibody-conjugated AuNPs can be used to localise macromolecules in cells as immunolabelling markers in EM.^[57-60] At the same time, fluorophores can be easily introduced onto AuNPs to produce fluorescence in LM,^[61, 62] enabling CLEM investigation for possible cellular events. Böse et al. described a CLEM study of polymer-coated AuNPs (around 8 nm) with fluorescence label Atto 647N in A549 cells. In the study, a concentration of 0.02 µg/mL of coated-AuNPs was introduced to the cell and then the whole cell was sequentially examined in cLSM and TEM after dehydration by a critical point dryer.^[63] Although the correlation accuracy of single particles signal between two microscopes is above average, the detachment of fluorophores from AuNPs occurs and the correlation efficiency is highly restricted by the thickness of the sample. In order to overcome the disadvantages, thinner sections of the samples need to be prepared and a more stable conjugation between fluorophores and the particles is needed.

Robinson et al. compared traditional colloid gold particles (CG) and fluoronanogold (FNG) as immunolabels.^[61] FNGs represents uniform gold clusters with a diameter of 1.4 nm, and they are routinely conjugated with antibody fragments and fluorophores, making them much more stable than the antibody labelled CG particles. The authors also revealed that FNGs perform higher penetration efficiency on ultrathin cryosection and pre-embedding cell samples mainly due to the smaller size. A CLEM study on the microtubules in lymphocytes and the granules of human neutrophils using fluorophores conjugated FNGs as the reporting system. Both experiments yield precise correlations between fluorescence signals and EM morphology on ultrathin cryosections. Suggesting that the potential of using antibody-conjugated gold clusters as CLEM probes.

Quantum dots (QDs) are semiconductive nanocrystals and possess intrinsic fluorescence of different wavelength depending on their sizes and shapes,^[64-66] making them suitable for many biological studies in LM. Moreover, the relatively high atomic number enables them to be identified in EM.^[67] Dukes et al. reported using epidermal growth factor (EGF) to conjugate QDs and sequentially co-incubated with COS7 fibroblast cells for 5 min in order to target EGF receptor on the cell membrane. In the study, CLEM was done with fluorescence microscopy and scanning transmission electron microscopy (STEM) in a microfluidic system. The authors described a spatial resolution of 3 nm and suggested that it is adequate to identify QDs for further CLEM study.^[68] However, the possibility of exploiting multicolour labelling with QDs and most importantly the localisation of intracellular protein was not discussed in the article. Giepmans et al. took the advantage of the QDs for multicolour labelling of intracellular proteins. A total of six different streptavidin-conjugated QDs with different emission wavelength were used to label α -tubulin in RFL6 fibroblasts and the QDs were internalised by the cells before fixation and staining. All of the six QDs emit bright fluorescence signal in LM after EM cryofixation and staining process without OsO₄. Although the difference in sizes among QDs is not significant in EM, the characteristic fluorescence of each kind of QD compensates for this shortcoming. The authors also further described the feasibility to apply two QDs (QD565 QD655) to mouse cerebellum in order to accomplish multi-colour labelling in tissue for CLEM study.^[69]

As discussed above, AuNPs and QDs are versatile probes for CLEM study. Yet, the cytotoxicity of these two nanomaterials has to be taken into account when applied to cells. Since the relatively small size of these NPs offers satisfactory penetration ability in both cells and tissues, the higher dosage of materials is likely to facilitate the accuracy of labelling.^[63] Both AuNPs ^[70] and QDs ^[71, 72] exhibit cytotoxicity and induce cellular stress due to size, surface charging, and material properties,^[57] so balancing the dosage and labelling efficiency would still be a challenge when applying these NPs with cells.

1.3 Application of CLEM in biology

As briefly discussed above, CLEM is a versatile and powerful imaging technique used to precisely localise small molecules in cells. This technique offers simultaneous read-outs of the same sample from two or multiple imaging modalities which ultimately provides more reliable and unbiased results. The application of CLEM is designated for use in biology to uncover the localisation of molecules like proteins or specific cellular structures like microtubules. These molecules and structures are extremely difficult or sometimes impossible to identify with traditional EM. However, by labelling the objects of interest with fluorescence it is possible to track those structures with LM. Hence, combining LM and EM conveniently brings together high resolution and precise localisation. The concept of CLEM was firstly introduced in the 70s,^[73] and the technique is further accelerated by the developments of various sample preparations such as using low cross linked resin for embedding and applications such as cryo-CLEM and volume CLEM.^[74]

Zila and Margiotta et al. took advantages of CLEM and electron tomography to capture how human immunodeficiency viruses subtype-1 (HIV-1) infect human T-lymphoblast cells (SupT1-R5).^[75] In order to capture the viral structure during the nuclear import, the authors infected the cleavage and polyadenylation specificity factor 6 (CPSF6) knockout T-cells with viral capsid (CA) mutated virus because CPSF6 is known for binding with CA for the release of viral transcription complexes into the nucleus. Preventing the binding of CPSF6 and CA results in accumulating more viral particles at the site of nuclear pores. They performed in-resin CLEM with cryofixation and embedding in low-crosslinked Lowicryl HM20 resin. The core of HIV-1 virus was labelled with IN.mScarlet (red) and cellular membrane and endosomes were labelled with mCLING (pink). Hence the IN.mScarlet positive viruses which were independent to the mCLING signal were the viral cores after cellular fusion. With the help of CLEM and tomography, the viral capsid was precisely located at nuclear pores and was found penetrating into the central channel of the nuclear pore (Figure 1.3.1). Additionally, the authors also discovered that the capsid was disrupted during the entry into the nuclear pores and their structures were altered in the nucleoplasm compared to the ones in the cytoplasm.

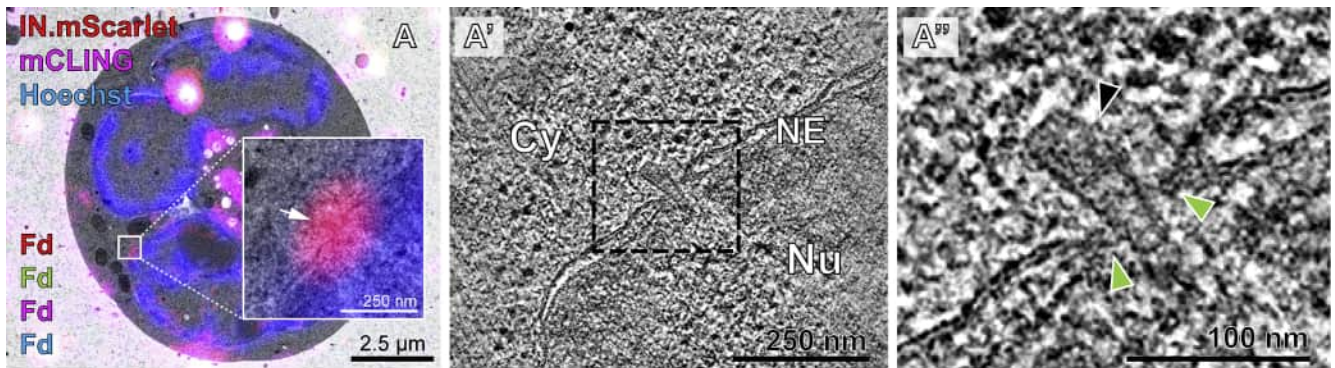


Figure 1.3.1 Intact HIV-1 viral capsids penetrate into the central channel of the nuclear pore. A. Overlay of a fluorescence image with the correlated electron micrograph. The enlarged region displays the position of the IN.mScarlet signal (red) at the nuclear envelope (white arrow). A'. Slice through a tomographic reconstruction at the correlated position. A''. Enlarged region in A' highlighting an apparently intact capsid (black arrowhead) deep inside the central channel of the NPC (green arrowheads), exposing its narrow end toward the nucleoplasm. Cy: cytosol; Nu,: nucleus; NE: nuclear envelope. Reproduced with permission from ref [75], Copyrights © 2021 Elsevier Inc.

Fermie et al. conducted volume-CLEM with focused ion beam scanning electron microscopy (FIB-SEM) on HeLa cells to actively track early and late endosomes in the endosomal pathways.^[74, 76] The HeLa cells were genetically modified to express LAMP-1-GFP which are majorly presented in late endosomes and lysosomes. The authors also included Dextran-Alexa568 as a fluorescent marker to label early, late endosomes and lysosomes. In the study, the endosome identification of early and later stage was not only dependent on the fluorescence but also the morphology in FIB-SEM. The CLEM workflow started with live-cell fluorescence imaging, and the samples underwent chemical fixation and resin embedding for subsequent FIB-SEM imaging. With the help of fluorescence markers, endosomes were efficiently located within the cellular environment and the subcellular structures of other organelles such as endoplasmic reticulum (ER) and mitochondria (MT) were also clearly revealed. Despite the impaired resolution in SEM, this study suggests a straightforward routine for studying general biological questions such as membrane tracking and organelles positioning.

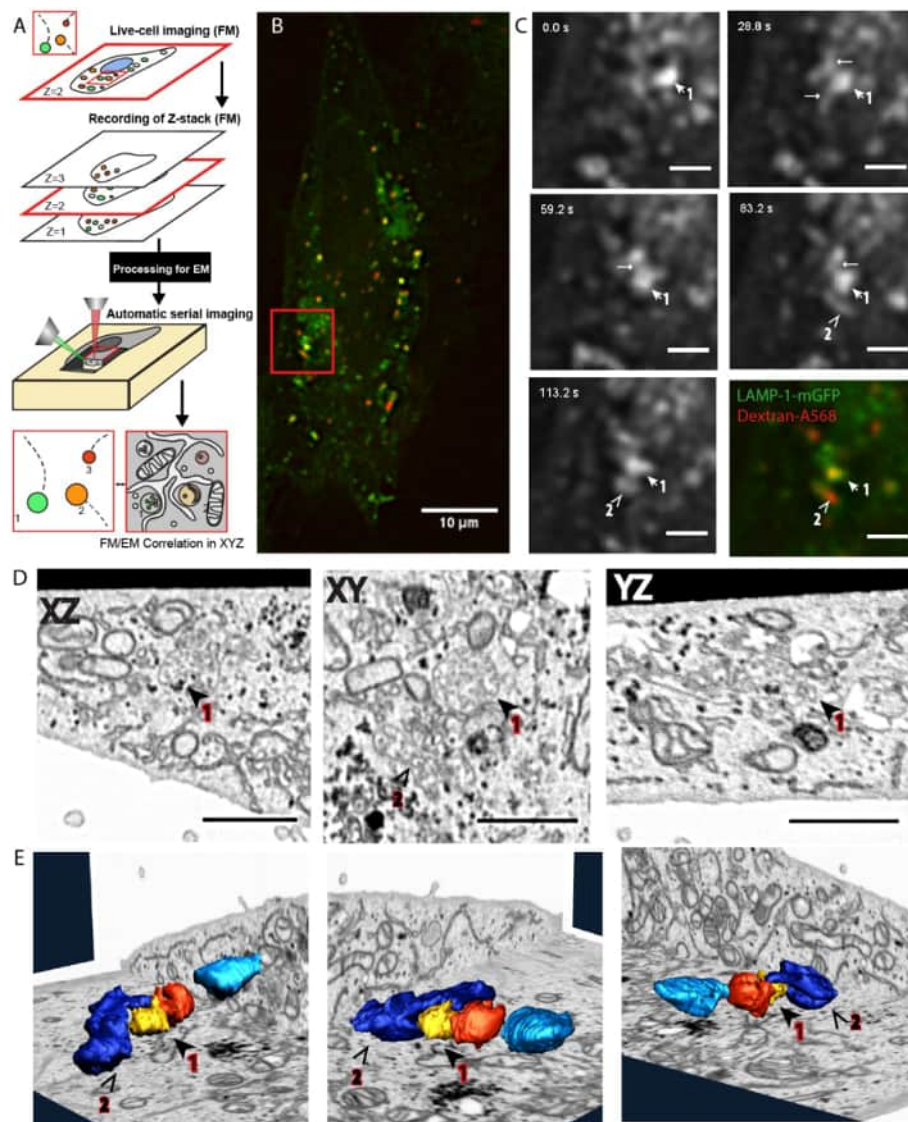


Figure 1.3.2 Volume-CLEM providing a direct link between live cell dynamics and 3D ultrastructure on the single organelle level. A. Schematic representation of the complete live-cell fluorescence to volume-EM workflow. B. As an example, a fluorescence image of a LAMP-1-GFP transfected cell, incubated with Dextran-Alexa568 as an endocytic marker. C. The cell was imaged live for several minutes, followed by in situ fixation. Stills show the LAMP-1-GFP spots (spot 1, 2) during 142 s of imaging. After fixation the cell is stained, embedded in resin, and imaged in FIB-SEM. D. Shows the slices on all three viewing axes (XZ/XY/YZ) of the reconstructed FIB-SEM dataset containing the live-cell region of interest (ROI) (B, C red square). Both spots 1 and 2 are classified as late endosomes based on their high number of intraluminal vesicles. E. FIB-SEM segmentation and 3D reconstructions of spots 1 and 2; the organelles imaged in live-cell fluorescence microscopy (1,2) were segmented and correlated with reference LM data. Reproduced with permission from ref [74]. Copyrights © 2018 IOP Publishing Ltd.

Besides the traditional CLEM with light and electron microscopy, Scotuzzi, Kuipers and Wensveen et al. performed a proof-of-principle ‘colourEM’ method with the help of EDX analysis to colour the greyscale EM images by different element constitutions.^[77] The authors suggested with immunolabelling of Au nanoparticles and QDs onto the molecule/site of interest, EDX were able to precisely map the elements of Au and Cadmium (Cd) from the cellular contents. They successfully performed this imaging method in labelling DNA, insulin and zymogen granules with 10 nm immunogold and QD655 in pancreatic rat islet. The tissue samples were chemically fixed followed by serial dehydration steps and finally embedded in EPON resin. The immunolabelling was conducted after the resin embedding on 100 nm sections. This straightforward imaging approach opens up possibilities to quantitative analysis endogenous and exogenous elements in cells which will potentially benefit the field of nanomedicine.

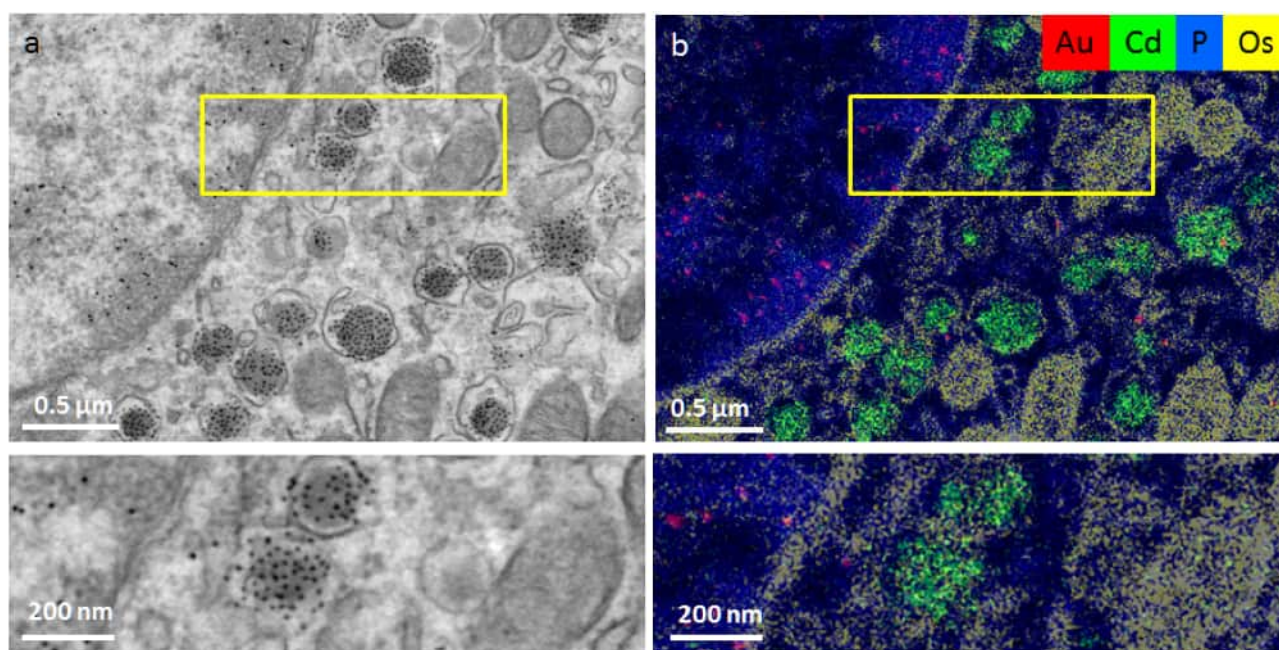


Figure 1.3.3 'ColourEM' using elemental analysis by EDX. ColourEM: label-free (P), stain (Os) and labelling DNA (Au) and insulin (Cd) is compatible. a. Part of an islet immuno-labelled for structures in DNA (10 nm gold) and insulin (QD). b. Overlay image of Au (red), Cd (green), Os (yellow) and P (blue) allows identification of guanine quadruplexes (G4) structures (gold labels) and insulin (Cd). Reproduced with permission from ref [74]. Copyrights © 2018 IOP Publishing Ltd.

2. Results and discussions—application of correlative microscopy methods to study cellular uptake, distribution and degradation of nanoparticles

NPs have opened up a new dimension for pharmaceutical applications, bioimaging, and sensing. Owing to their ultra-small size and controllable synthesis, many delicate applications such as cellular targeting and controlled release can be realised.^[1] On the other hand, these powerful feature also hampers the possibilities to visually characterise these NPs, especially in a cellular environment and thus to determine their biological impact. However, the intracellular behaviour of NPs determines their biocompatibility, efficacy and finally their potential to become a promising candidate for a drug delivery system. Hence, in order to directly characterise any NPs-cell interactions on a nanometer scale, microscopy techniques are inevitable. But since the NPs have to be visualised and unequivocally identified in a biological environment as e.g. a cell, adequate new strategies had to be developed. Due to the structural overload in a cell, any NP inside might be camouflaged by the surrounding cell components and the identification based on the NP morphology alone can become impossible. Accordingly, here I will present methods I developed to overcome this problem of unequivocal identification of NPs, especially of polymeric NPs.

Depending on the NP system that is going to be visualised, different strategies can be applied to adapt for different materials and different circumstances. There are two main fundamentally different approaches for the visualisation of intracellular NPs: using two different microscopy methods and correlate the obtained data or exhaust all possible analytical methods of just one microscope. For the latter, mainly TEM with its capability of energy-dispersive X-ray spectroscopy (EDX) and energy filtered TEM (EFTEM) and electron energy loss spectroscopy (EELS) is used. Combining two basically different microscopy techniques with subsequent correlation of both data is the domain of correlative light and electron microscopy (CLEM). Here, the very different potentials of both techniques are combined and yield a synergetic gain. However, any of the mentioned techniques and even more can be combined to extract the desired data, as will be demonstrated in this Chapter.

Section 2 focuses on the microscopic applications that are aimed to study interactions between NPs and a cell. At the same time, different visualisation techniques such as EDX, CLEM and EFTEM were applied onto biological samples so that inorganic and organic NPs can be unequivocally identified. As will become clear from the following paragraphs, the different analytical methods have to be combined to adapt for the specific NP system that is going to be visualised.

Section 2.1 describes the application of EDX to identify intracellular silica nanocapsules (SiO_2 NCs). EDX is a powerful method to identify different elements in the specimen depending on the unique characteristic x-ray emission spectrum of each element. In combination with the very precise, focused electron beam in an electron microscope, EDX yields local information on the chemical composition down to a sub-nanometer resolution. And by using this technique, silicon can be easily distinguished from the carbon-based cellular environment. Moreover, in this NP system the SiO_2 NCs were also containing iron oxide nanoparticles (Fe_3O_4 NPs) for an even easier initial localisation of the NPs in the cells and to follow any release processes. In all, this chapter suggests a useful way by applying EDX to identify intracellular NCs which were not synthesised by abundant element in cells. By correlating EDX and TEM, high resolution subcellular environment can be retained and intracellular distribution of SiO_2 NCs can be efficiently identified.

The situation is different, when the NPs to be identified do not have heteroatoms, as in the case of polymeric NPs or even nanodiamonds. To realise a precise localisation of carbon-based NPs, I developed two different CLEM routines as demonstrated in **Chapter 2.2** with fluorescent nanodiamonds (fNDs). The fNDs we used are fully carbon-based NPs with diameters around 35 nm. They are inherently fluorescent and possess nice crystalline structures under high resolution TEM. In-dish and on-section CLEM were performed with fNDs in HeLa cells and the fluorescence of fNDs was successfully retained after different EM preparations. These two methods are fundamentally different, and the development challenge was to create the most versatile platform possible for CLEM. The main problem for the application of fluorescent dyes is the straining process during the preparation for EM. Many fluorescent dyes do not survive this process due to the use of highly oxidative staining agents like OsO_4 . The protocol for the in-dish CLEM preparation circumvents this problem by separating the fluorescence imaging from the EM preparation step and thus being the most versatile CLEM protocol without any restrictions to the used fluorophores. However, this versatility comes for the price of spacial resolution and structure preservation in the

EM specimen. On the other side, the on-section method developed for this project receives its advantages from an optimal EM preparation, e.g. by high pressure freezing and freeze substitution. Here, the fluorescent dye has to survive all the harsh preparation steps in order to yield data with the best EM structure preservation in combination with the fluorescence based localisation of the regions of interest. Here, the two CLEM imaging methods were performed on the very same specimen (ultramicrotome thin section used for cLSM and EM) and hence will yield the best structural data.

To explore the capabilities of the in-dish and on-section protocols, the fNDs served as an ideal candidate. It turned out, that the intrinsic fluorescence of the NDs, which is based on a colour centre caused by an atomic displacement [78] is not affected by the preparation for the EM imaging. Hence, I could use both, the in-dish and especially the on-section method. In the ultramicrotome thin sections used for TEM, the fNDs were still fluorescent and hence the very same specimen was used for cLSM and for TEM imaging. With the help of the fluorescence data, regions of interests (ROIs) were identified and subsequently investigated in the TEM. Moreover, electron tomography (ET) gave a 3-dimensional insight of the surrounding of the fNDs within the cell. And finally individual fNDs were identified by EFTEM, because these isolated fNDs have a too low signal in the cLSM.

Section 2.3 shows the further development of the on-section method presented in the previous section. The system under investigation here are bovine serum albumin nanocapsules (BSA NCs) which are labelled with CdSe based nanoplatelets (NPLs). These NPs are taken up by RAW264.7 macrophages and their fate was examined by CLEM methods. BSA NCs possess good biocompatibility and are a very promising candidate for a protein-based drug delivery system. However, these NPs show poor contrast in cells in EM imaging and hence their identification in the EM is difficult. In order to precisely localise the NCs, polymer-coated NPLs were used to label the NCs by their inherent fluorescence. The fluorescence of NPLs is retained even after the harsh EM preparation and was used to subsequently track the intracellular BSA NCs at different time points. BSA NCs were found in different endosomes as ripening time developed. CLEM images confirmed that intracellular BSA NCs followed endolysosomal pathway and eventually ending up in endolysosomes for degradation. This section further exploits NPs with inherent fluorescence and used them to localise carbon-based NCs.

Section 2.4 optimised the on-section CLEM method to apply on organic dye labelled polymer NPs and NCs. Despite the assumption about organic dyes losing fluorescence after EM preparation with OsO₄ and EPON resin embedding, we performed on-section CLEM with both OsO₄ staining (0.1 %) and EPON embedding in order to preserve the best cellular structures. By acquiring the fluorescence images of 100 nm EPON sections on ITO-coated coverslips and sequentially imaging the same sections in SEM, BODIPY-labelled polystyrene NPs (PS NPs) and Cy5-labelled hydroxyethyl starch NCs (HES NCs) were successfully localised in high resolution EM images with fluorescence. The optimised CLEM routine in this section extends the application on localising intracellular NPs/NCs with organic dyes, and faithfully identified NPs/NCs in cells for the first time.

Finally, **Section 2.5** demonstrates how far the CLEM method can be pushed and what basic findings can be made. Here, CLEM is used to study the intracellular fate of the protein corona. Carboxyl-functionalised PS NPs were used as a model particle to study the intracellular fate of the protein corona. The protein corona is the result of the adsorption of proteins to any surface, that comes into contact with a biological fluid like e.g. blood.^[79] Accordingly, any colloid particle that comes into contact with a protein containing fluid will adsorb proteins; the so-called protein corona is formed. Here, murine serum was covalently bounded with Cy5 dye which is a far-red fluorescent label for proteins and the labelled serum was used to generate a protein corona on BODIPY-labelled PS NPs. After making sure that the compositions of Cy5-labelled and unlabelled protein corona were not significantly different, cellular uptake of protein corona labelled PS NPs were performed with RAW264.7 macrophages. On-section CLEM was carried out after 24 h of internalisation in order to study the intracellular distribution of protein corona and PS NPs. In order to further understand the intracellular fate of protein corona in the volume of cells, array tomography was performed with 15 physical sections to demonstrate the 3-dimensional distribution of protein corona and NPs. According to our CLEM results and reconstruction model, protein coronae were found gradually separated from NPs along with the endosomal maturation and eventually ending up in morphologically different endosomes. This section fully exploits CLEM techniques and array tomography to initially shine light on the ultimate question about intracellular fate of protein corona.

To summarise, **Chapter 2** explores and correlates different imaging techniques to visualise intracellular NPs, from using EDX in TEM to identify inorganic NCs in cells in **Section 2.1**, to exploiting CLEM to visualise carbon-based fNDs with inherent fluorescent or identify organic BSA NCs with fluorescent NPLs in **Section 2.2** and **Section 2.3**, and eventually further optimised CLEM to visualise organic dye labelled polymer NPs and study the intracellular fate of protein corona in **Section 2.4** and **Section 2.5**.

2.1 Correlating TEM and energy-dispersive X-ray spectroscopy (EDX) to localise intracellular silica nanocapsules

This section is based on publication *Part. Part. Syst. Charact.* 2020, 37, 1900484 and *Nanoscale*, 2020, 12, 2626-2637. Reproduced with permission from Ref [80] and [28], Copyrights © John Wiley & Sons, Inc. 2020 and © The Royal Society of Chemistry 2020.

This section explores the application of SiNCs as drug carrier and correlates EDX with TEM to specifically localise Fe₃O₄ NPs encapsulated SiNCs intracellularly. By precise element mapping in carbon-based cellular environment, elements like Si and Fe can be pinpointed easily within the cells. This section serves as an initiate attempt for correlative microscopy imaging to visualise intracellular NPs.

Contributions:

I performed most of the cellular experiments with nanoparticles uptake for EM preparation, including cellular culture, ultramicrotomy sectioning, TEM imaging, and image analysis and interpretation. Shuai Jiang synthesised the particles. Domenik Prozeller performed the colloidal stability study. Jorge Pereira performed some cell experiments. Johanna Simon performed the protein corona study. Sebastian Wirsching performed the biological study of the dexamethasone effect. Michael Fichter, Ingo Lieberwirth, Svenja Morsbach, Volker Mailänder, Stephan Gehring, Daniel Crespy, and Katharina Landfester supervised and corrected the manuscript.

Abstract

Core-shell nanocapsules are receiving increasing interest for drug delivery applications. Silica nanocapsules have been the focus of intensive studies due to their biocompatibility, versatile silica chemistry, and tunable porosity. However, a versatile one-step preparation of silica nanocapsules with well-defined core-shell structure, tunable size, flexible interior loading, and tailored shell composition, permeability, and surface functionalisation for site-specific drug release and therapeutic tracking remains a challenge. Herein, we develop an interfacially confined sol-gel process in miniemulsion for the one-step versatile preparation of functional silica nanocapsules. Uniform nanocapsules with diameters from 60 to 400 nm are obtained and a large variety of hydrophobic liquids are encapsulated in the core. When solvents with low boiling point are loaded, subsequent solvent evaporation converts the initially hydrophobic cavity into an aqueous environment. Stimuli-responsive permeability of nanocapsules is programmed by introducing disulfide or tetrasulfide bonds in the shell. Fluorescence labelling of the silica shell and magnetic loading in the internal cavity enable therapeutic tracking of nanocapsules by fluorescence and electron microscopies. Thus, silica nanocapsules represent a promising theranostic nanoplatform for targeted drug delivery applications.

Introduction

Multifunctional nanocarriers integrating the properties of bioimaging, targeting, and stimuli-responsive release of guest molecules allow a spatiotemporal controlled delivery and tracking of therapeutics, which is the prime prerequisite for *in vivo* nanocarrier-mediated drug delivery.^[81-84] Driven by the rapid progress in their synthetic control, mesoporous silica nanomaterials have attracted increasing attention due to their large specific surface area, tunable pore volume and structure, and facile surface modification, thus showing a wide application prospect for drug delivery and biomedicine.^[85-93] Compared with mesoporous silica nanoparticles with a solid core, core-shell silica nanocapsules (SiO₂ NCs) have the advantages that their interior cavity offers a large loading capacity for guest molecules and the shell can be designed to display a tunable permeability for specific cargo release.^[94] In spite of recent progress in nanocapsules design, a versatile approach for the preparation of functional SiO₂ NCs for biomedical applications with control at morphological and molecular levels, e.g. the core-shell structure, tunable size, interior contents, and the shell composition, permeability, and surface functionalisation, is still needed.

Hard-templating approaches are often used for preparing SiO₂ NCs as they typically result in well-defined size and shape.^[95] For example, redox-triggered biodegradable NCs with disulfide-bridged silsesquioxane frameworks were synthesised by using poly(acrylic acid) nanoaggregates^[96] and silica nanoparticles^[97] as templates, which were subsequently removed. The payloads were post-loaded in the hollow capsules by adsorption. This strategy often results in low loading efficiency and initial burst release especially for water-soluble molecules.^[94, 98, 99] Alternatively the payloads can be pre-dissolved or adsorbed in the template material. Nonetheless, this approach takes several steps and the loading efficiency of guest molecules relies highly on their adsorption to the template nanoparticles.^[94]

Emulsion-based approaches have been widely studied for the encapsulation of payloads in nanocapsules. Guest molecules or particles are first dissolved or dispersed in template liquid droplets, followed by the formation of a surrounding silica shell. A range of materials with different sizes and polarities such as enzymes,^[100, 101] corrosion inhibitors,^[102, 103] self-healing agents,^[104] agrochemicals,^[105, 106] therapeutic agents,^[107, 108] imaging probes,^[109, 110] and organic dyes^[107, 111] were encapsulated in SiO₂ NCs by using water-in-oil or oil-in-water emulsions.^[94] Cationic surfactants such as cetyltrimethylammonium bromide and chloride were often used as templating agents for confining silica formation at droplets interface.^[102-104] Wibowo et al. developed a biomimetic templating technique by designing a dual functional peptide by modularising a surface-active sequence capable of stabilising oil droplets in water with another sequence for catalysing biosilicification at oil-water interfaces.^[106] This biomineralising peptide enabled the formation of SiO₂ NCs at near-neutral pH value and ambient temperature. However, the large scale production of complex peptides is a limiting factor.^[112, 113] Jakhmola et al. synthesised SiO₂ NCs via a biosilicification process induced by poly(l-lysine) immobilised on the surface of emulsion droplets.^[114] This synthetic process requires several steps. Firstly, a central oil core was stabilised by a lecithin surfactant, followed by the adsorption of positively charged poly(l-lysine) on the droplets. Afterwards, negatively charged silica species were attached onto nanodroplets and formed a silica shell. Erni et al. synthesised microcapsules with dense walls composed entirely of a biopolymer scaffold interpenetrated with amorphous silica.^[115] A weakly acidic hydrogel shell was first formed around oil droplets, which then served as a scaffold to induce protein-directed mineralization of silica. The precipitation process, occurring in the hydrogel scaffold, consumed water to form silica, yielding dense shells with a very low permeability for volatile organic compounds. However, the

diameter of capsules was hundreds of micrometers, which is out of the applicability range for in vivo drug delivery via intravenous administration ($\gg 5 \mu\text{m}$).^[116] Although these synthetic approaches were successful, effective and versatile synthetic approaches that are independent of customised templating agents and avoid multiple steps are still needed to prepare well-defined SiO_2 NCs for biomedical applications.

In this study, we developed a one-step approach for versatile preparation of functional SiO_2 NCs for biomedical applications. The SiO_2 NCs were synthesised via a confined sol-gel process at the nanodroplet-water interface of oil-in-water miniemulsions. By this approach, a versatile synthesis of SiO_2 NCs with morphological and molecular control was achieved, including a defined core-shell structure, tunable size, flexible interior loading, and tailored shell composition, permeability, and surface functionalisation. These features allow site-specific drug release and enable therapeutic tracking of labelled SiO_2 NCs by fluorescence and electron microscopic techniques.

Results and discussions

Visualisation of intracellular SiO_2 NCs relies strongly on the fluorescence microscopy.^[117, 118] In order to reveal a detailed cellular distribution of NCs, a higher resolution imaging technique should be applied. Transmission electron microscopy (TEM) provides higher resolution imaging for investigating cellular uptake and intracellular trafficking of nanocarriers. However, core-shell nanocapsules have a size and morphology that are similar to cellular organelles. Therefore, both types of compartments are difficult to distinguish. To overcome this issue, we loaded SiO_2 NCs with iron oxide nanoparticles (Fe_3O_4 NPs), which provided a higher contrast and also allowed the localisation of NCs by monitoring elemental distribution of silicon and iron. As shown in the TEM micrographs in Figure 2.1.1, various amounts of iron oxide can be encapsulated in NCs. By encapsulating Fe_3O_4 NPs as contrast agent, SiO_2 NCs can be initially located extracellularly (Figure 2.1.2 a) and intracellularly (Figure 2.1.2 b-d). Combined with elemental mapping of silicon and iron obtained by electron energy loss spectroscopy (EELS, Figure 2.1.3 c) and energy dispersive X-ray spectroscopy (EDS, Figure 2.1.3 d), cellular uptake of nanocapsules and their localisation in intracellular environment were successfully confirmed (Figure 2.1.3 e). Since application of EDX to identify elements is broadly used in material science, localisation of non-abundant elements in cells by using EDX is beneficial in EM-prepared plastic embedded samples. Superparamagnetism of Fe_3O_4 NPs was preserved after the encapsulation, with a saturated magnetisation of 10.0 emu/g

nanocapsules (Figure 2.1.1 d). Therefore, the magnetic NCs are also potentially useful for magnetic resonance imaging and magnetic-guided targeted delivery.

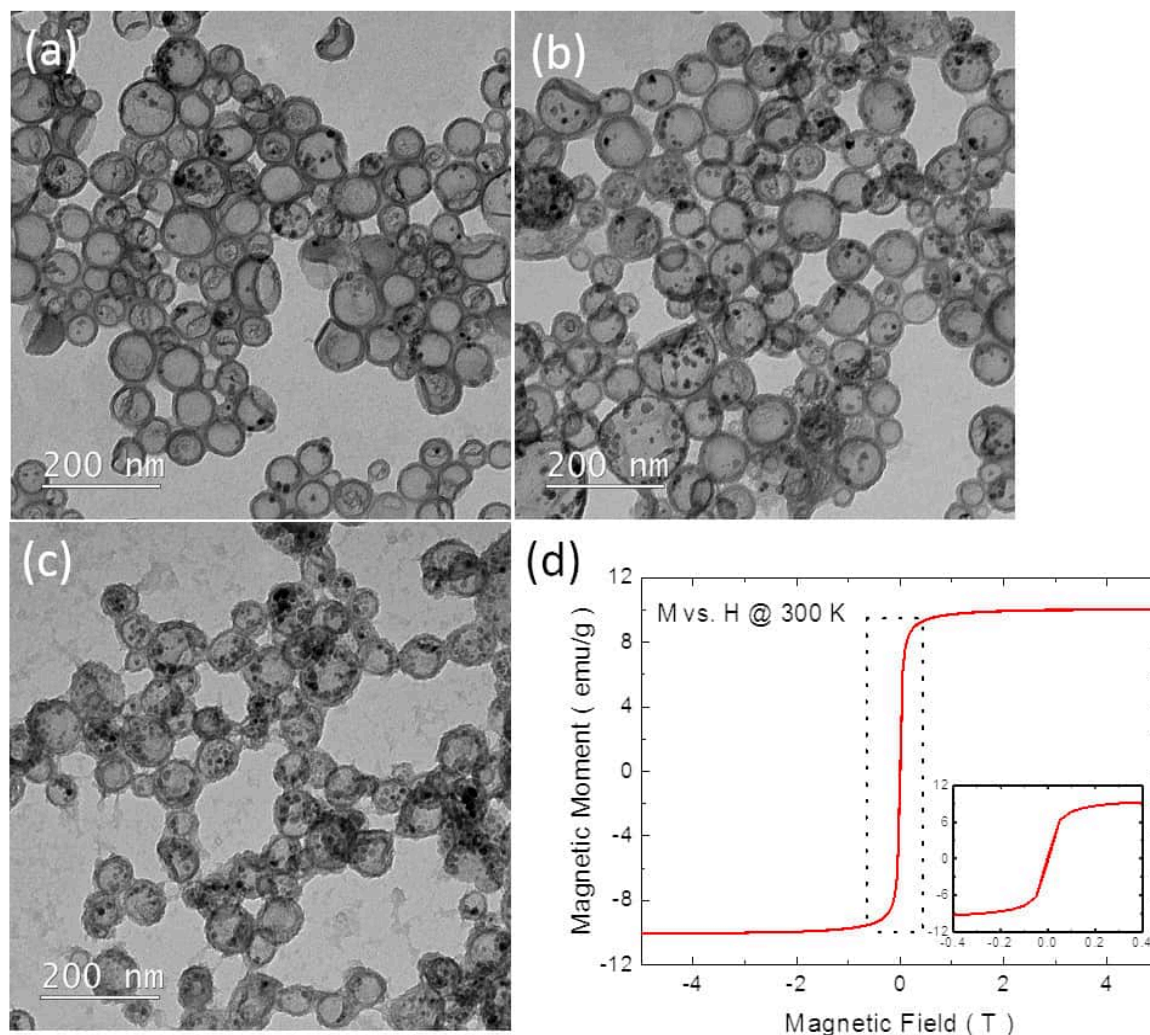


Figure 2.1.1 Characterisation of SiO_2 NCs loaded with various amounts of iron oxide nanoparticles. TEM micrographs of NCs with iron oxide:silica = **a.** 1:6.2 (sample SJP29-2), **b.** 1:2.8 (sample SJP29-3), and **c.** 1:1.7 (sample SJP29-4). **d.** VSM magnetisation curve of NCs with iron oxide:silica = 1:2.8. magnetisation measurement was performed by Shuai Jiang.

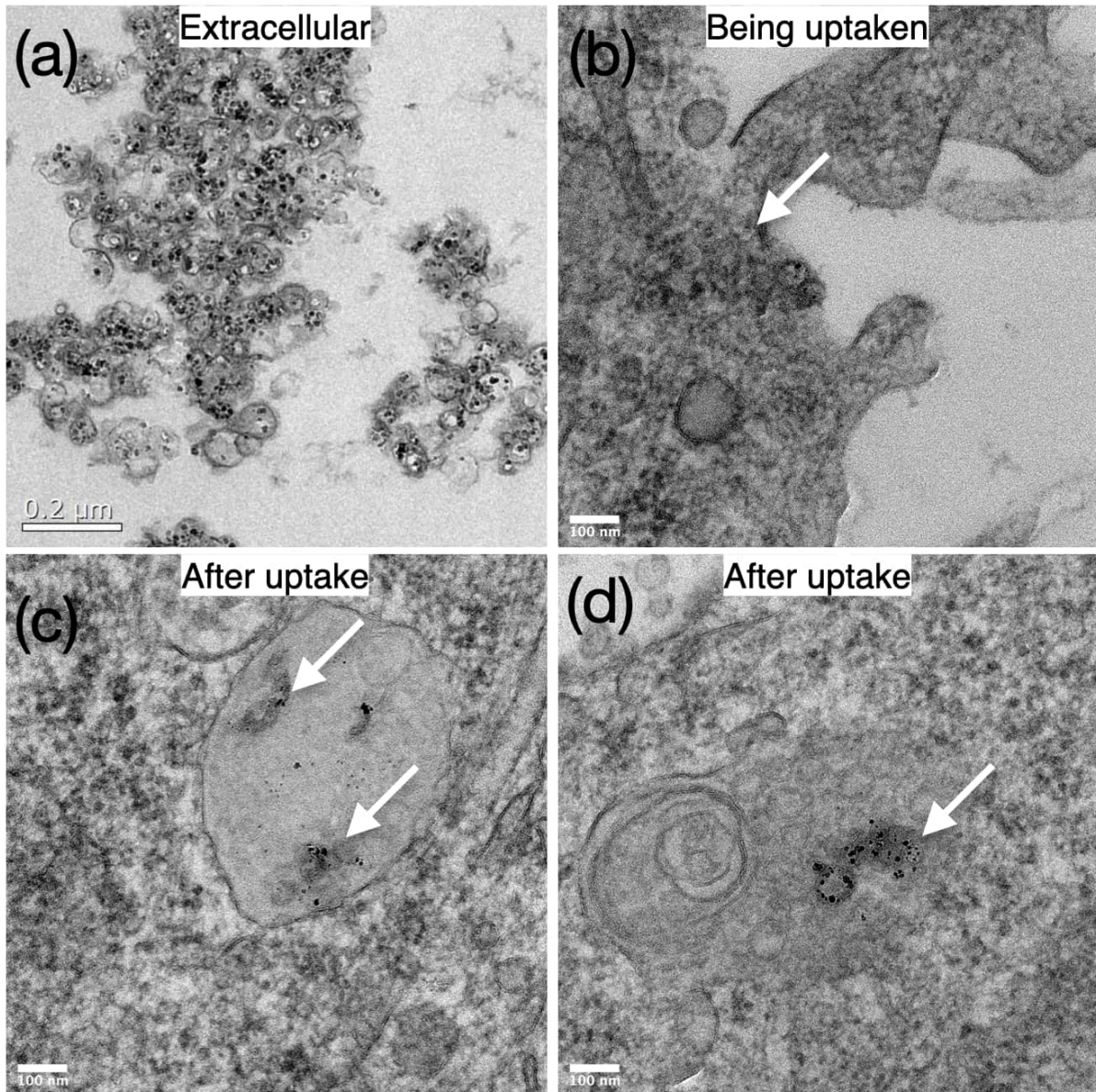


Figure 2.1.2 TEM micrographs showing extracellular and intracellular SiO₂ NCs. **a.** extracellular SiO₂ NCs. **b.** SiO₂ NCs under uptake process. **c** and **d** SiO₂ NCs after uptake in the cells.

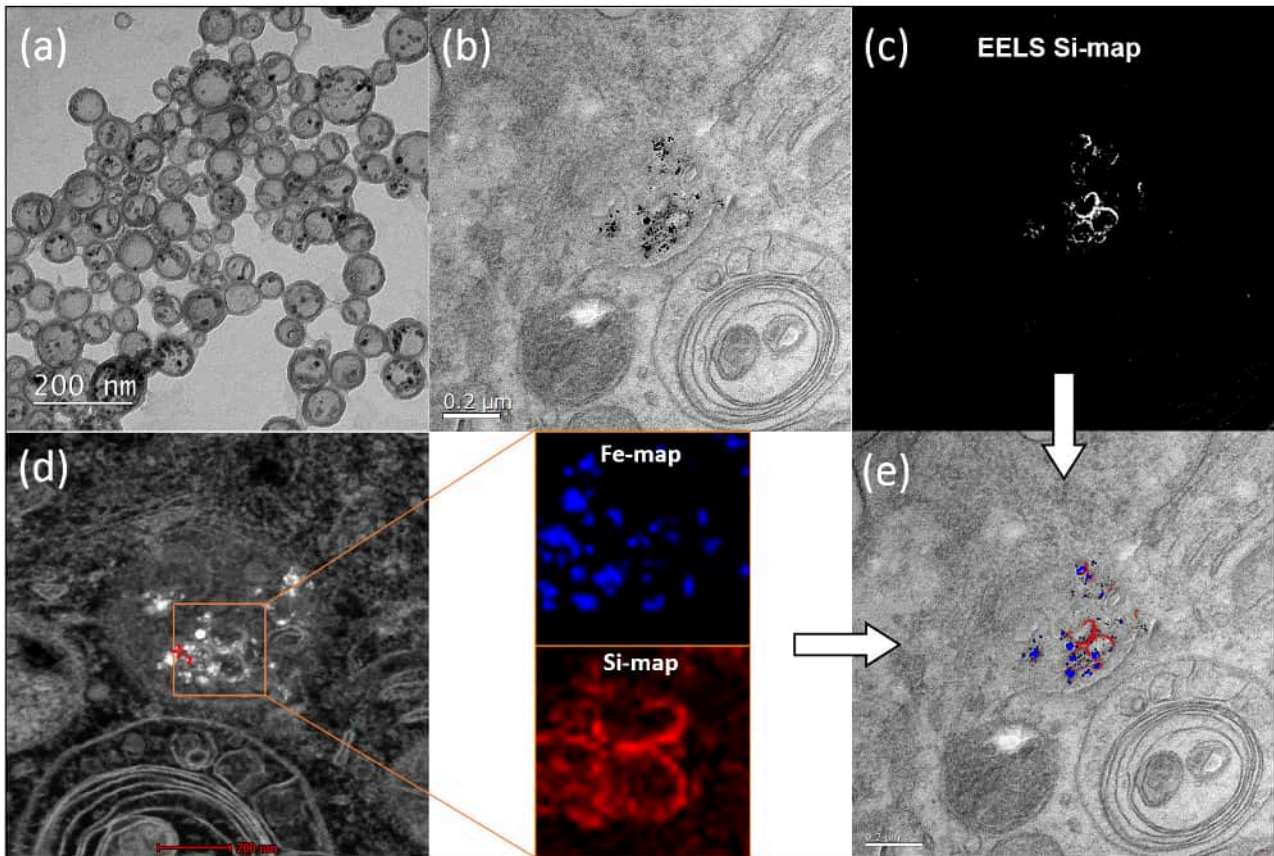


Figure 2.1.3 Intracellular localisation of SiO₂ NCs labelled with Fe₃O₄ NPs in HeLa cells by TEM and elemental mapping. TEM micrographs of **a.** SiO₂ NCs containing Fe₃O₄ NPs, **b.** NCs in cells, **c.** elemental mapping of silicon obtained by EELS, **d.** elemental mapping of silicon and iron obtained by EDX, **(e)** colocalisation of NCs based on TEM, EELS, and EDX data.

Understanding cellular uptake, intra-, and intercellular trafficking mechanisms of nanocarriers is critical for designing efficient and safe nanomedicines.^[119] We studied the cellular uptake behaviour and intracellular trafficking of the SiO₂ NCs by TEM in different time points. As mentioned before, morphological identification of pure SiO₂ NCs is difficult in cells. Hence, encapsulation of Fe₃O₄ NPs was done to give better contrast and localisation of the NCs. As shown in Figure 2.1.1, the Fe₃O₄ NPs with diameter of ~8 nm were encapsulated in the inner core of NCs. To prove the efficient loading of Fe₃O₄ NPs in NCs, the gradient centrifugation technique was applied. No free Fe₃O₄ NPs were separated from the SiO₂ NCs present in the upper phase, indicating a high encapsulation efficiency of the NPs. By encapsulating Fe₃O₄ NPs as contrast agent, SiO₂ NCs were clearly distinguished from cellular organelles (Figure 2.1.4 b-e). Combined with elemental mapping of silicon and iron obtained by electron energy loss spectroscopy (EELS) and energy dispersive X-ray spectroscopy (EDX), cellular uptake of the SiO₂ NCs and their localisation in intracellular environment were successfully identified (Figure 2.1.4 g). Intracellular trafficking of the NCs was studied at different incubation times (Figure 2.1.4 c-f). Iron oxide labelled NCs were found in multivesicular bodies after 2 h incubation (Figure 2.1.4 d). After incubating the cells with magnetic NCs for 10 h and 24 h, some free Fe₃O₄ NPs, without surrounding silica shell, were observed (Figure 2.1.4 e-f). This observation indicates a plausible intracellular degradation of the ultrathin silica shell (~5 nm), which is consistent with previous findings from other groups. Chen et al. found that the degradation of surfactant-extracted MCM-41-type mesoporous silica nanoparticles exhibited a very fast initial degradation within 2 h in simulated body fluid.^[31] The incomplete -Si-O- tetrahedral network in the nanoparticles, containing plenty of Si-R and Si-OH groups, facilitated their easy degradation. Bein et al. found that small particle size (50-70 nm) with a low condensation degree and a highly mesoporous texture (pore size~3-4 nm), and high surface area accelerated the degradation reactions.^[120] In our case, the SiO₂ NCs showed also a low condensation degree, as shown by the Q2 signal of 1 %, Q3 signal of 43 %, and Q4 signal of 56 % determined by ²⁹Si MAS NMR spectroscopy. The combination of the presence of free Si-R and Si-OH groups with the thin shell and a pore size of ~3-6 nm is therefore likely to facilitate the intracellular degradation of the SiO₂ NCs.

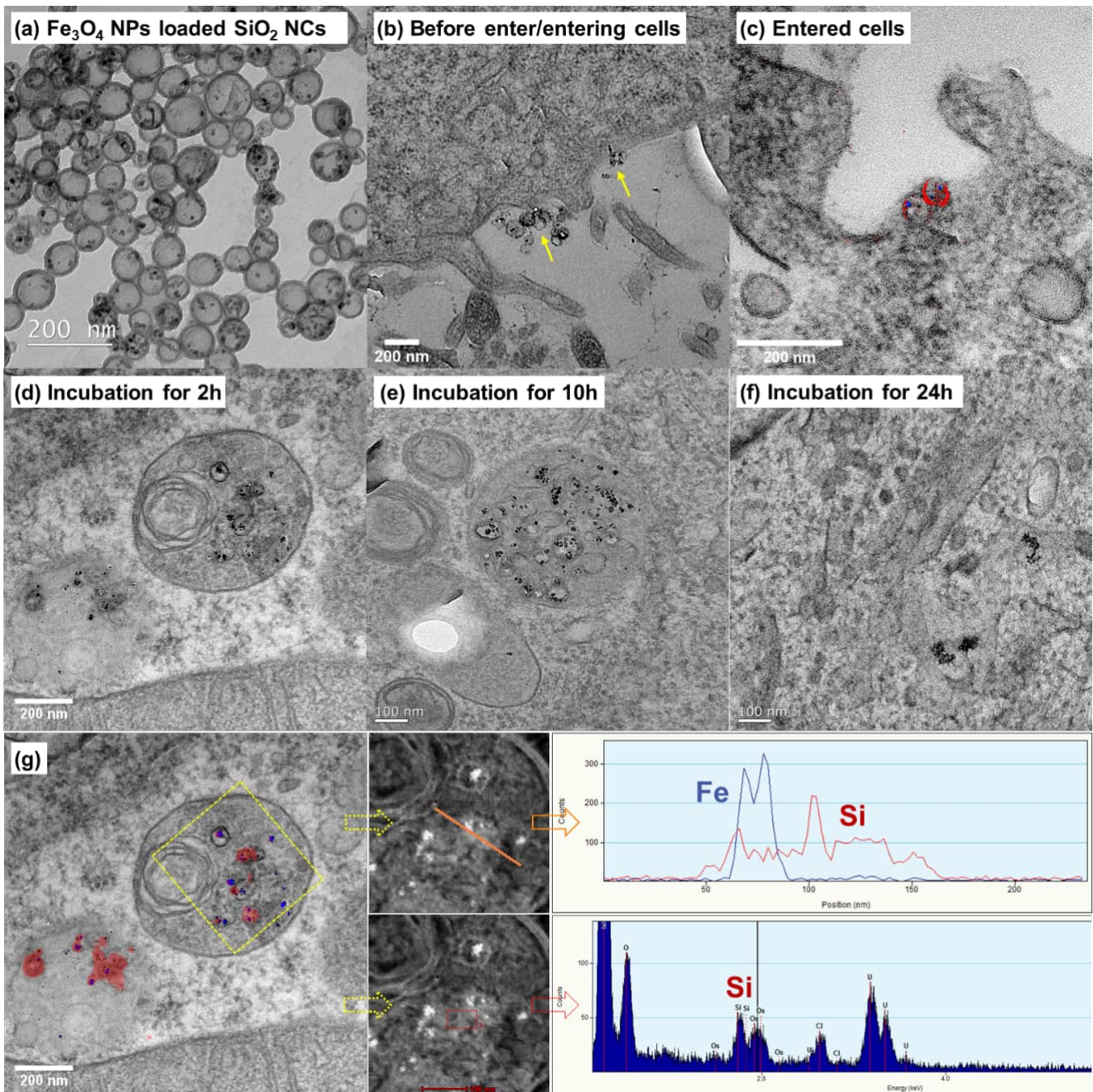


Figure 2.1.4 Cellular uptake and localisation of iron oxide labelled SiO_2 NCs in HeLa cells based on TEM and elemental mapping techniques. TEM micrographs of **a.** Fe_3O_4 NPs labelled SiO_2 NCs. **b.** NCs that are entering cell membrane shown by yellow arrows. **c.** NCs internalised in cell. **d-f.** Localisation of NCs in intracellular environments after incubation for 2, 10, and 24 h. **g.** Blue colour represents signal of iron and red colour represents signal of silicon.

Conclusions

We demonstrated here a versatile one-step synthesis of SiO₂ NCs for biomedical applications. This approach is based on a sol-gel process confined at the interface of oil-in-water miniemulsion droplets. Fluorescent and magnetic labelling enables monitoring of cellular uptake and intracellular trafficking of the NCs by fluorescence microscopy and TEM combined with elemental mapping. With the help of correlating EDX and TEM, intracellular SiO₂ NCs can be successfully located and tracked in different time points. At the same time, element mapping is also proven to be very beneficial to precisely identify NPs/NCs which are not carbon-based. This efficient visualisation method enables us to further facilitate the study of functional SiO₂ NCs for drug delivery applications.

2.2 High-contrast imaging of nanodiamonds in cells by energy filtered and correlative light-electron microscopy: toward a quantitative nanoparticle-cell analysis

This section is based on publication *Nano Lett.* 2019, 19, 3, 2178–2185. Reproduced with permission from Ref [121]. Copyright © 2019 American Chemical Society.

This section is moving from EDX to leveraging light and electron microscopy for correlative microscopy imaging. We used a special NPs with inherent fluorescence called fNDs to initially try the correlative light and electron microscopy method in resin embedded cells.

Contributions:

I performed the cell experiments with the nanoparticles and the correlative light and electron microscopy experiments and further images processing, interpretations and evaluations. Marco Raabe prepared the coated fluorescent nanodiamonds and performed DLS, zeta-potential characterisation, and fluorescence spectroscopy. Both, Marco Raabe and me, wrote the manuscript. Lorna Hodgson and Paul Verkade designed and supervised of the CLEM experiments. Judith Mantell supervised to perform transmission electron microscopy tomography. Ingo Lieberwirth performed energy filtered electron microscopy and HAADF STEM. Theo Lasser corrected the manuscript and gave scientific suggestions. Ingo Lieberwirth, Katharina Landfester, Tanja Weil supervised and corrected the manuscript.

Abstract

Fluorescent nanodiamonds (fNDs) represent an emerging class of nanomaterials offering great opportunities for ultra-high resolution imaging, sensing and drug delivery applications. Their biocompatibility, exceptional chemical and consistent photostability renders them particularly attractive for correlative light-electron microscopy (CLEM) studies providing unique insights into nanoparticle-cell interactions. Herein, we demonstrate a stringent procedure to image and quantify fNDs with a high contrast down to the single particle level in cells. Individual fNDs were directly visualised by energy-filtered transmission electron microscopy i.e. inside newly forming, early endosomal vesicles during their cellular uptake processes as well as inside cellular organelles such as a mitochondrion. Furthermore, we demonstrate the unequivocal identification, localisation and quantification of individual fNDs in larger fND clusters inside intracellular vesicles. Our studies are of great relevance to obtain quantitative information on nanoparticle trafficking and their various interactions with cells, membranes and organelles, which will be crucial to design improved sensors, imaging probes and nanotherapeutics based on quantitative data.

Introduction

During the past decades, nanoparticles have transformed biomedicine as traceable drug carriers and sensitive probes for therapy and diagnostics.^[122] They have provided important insights into diseases and serve as valuable platform for imaging and therapy of e.g. cancer cells and tissue in (pre)clinical studies.^[123] To further advance nanomedicine approaches and to avoid risks of nanoparticle-induced toxicity, deeper understanding of nanoparticle-cell interactions,^[26, 124] during their cellular uptake processes,^[125, 126] intracellular release and trafficking^[127] is crucial. Light microscopy (LM) and transmission electron microscopy (TEM) have been applied to visualise nanoparticle-cell interactions. However, classical LM is limited by the wavelength of light and does not provide resolution beyond the diffraction limit (~200 nm).^[42] Super-resolution techniques such as stimulated emission depletion (STED), stochastic optical reconstruction microscopy (STORM), photo-activated localisation microscopy (PALM), or super-resolution optical fluctuation imaging (SOFI) enabled resolutions down to the nanometer scale^[128, 129] but these optical imaging techniques require very photostable fluorescent markers. Super-resolution microscopy techniques like STED provide spatial resolution of 40 nm in HeLa cells, which is still about 100 times lower compared to the resolution of TEM (below 1 nm) and surrounding structures could not be imaged.^[69, 130] In

contrast, electron microscopy provides morphological visualisation at unmatched resolution without the need to apply specific marker molecules. Recently, correlative light-electron microscopy (CLEM) has emerged as the method of choice to gain unique insights into exo- and endogenous cellular structures and to precisely localise endogenous proteins^[69, 131, 132] or nanoparticles with high resolution providing important information on e.g. transporter trafficking^[133] and membrane uptake.^[134, 135] Quantum dots (QDs) and gold nanoparticles have been applied as imaging probes for CLEM but they are limited by their weak fluorescence,¹⁸ blinking problems of QDs^[136] and their inherent cytotoxicity, raising various concerns for long-term in vitro and in vivo studies.^[137, 138]

Fluorescent nanodiamonds (fNDs) have emerged as promising and biocompatible^[139] imaging probes in LM, and they have been used for traceable drug delivery as well as nanoscale-sensing applications.^[139] These carbon-based nanoparticles with nitrogen vacancy (NV-) defect colour centres^[140-143] provide stable fluorescence without blinking, which represents an ideal prerequisite for single-particle tracking^[140, 144] and super-resolution studies^[78] in cells. In addition, the unique magneto-optical properties of NV- centres in diamond allow sensing of local magnetic fields,^[145] temperature,^[146-148] electric potentials,^[149] and pH value^[146] with high sensitivity in living cells.

We have established a straightforward imaging approach using high-precision CLEM and dark-field energy filtered transmission electron microscopy (EFTEM) to localise fNDs in cells down to the single particle level. Until now, single fND tracking remained challenging^[150-152] and only information of their approximate location and tracking paths was resolved. In previous work, image quality of NDs in CLEM studies was limited due to the weak contrast of the all-carbon composition of the diamond lattice, which has a similar chemical composition as the resin matrix used in EM preventing imaging of individual fNDs^[153, 154] due to their low contrast within cells.^[154-156] Attempts to increase contrast and detectability in EM and/or LM focused on labelling of the fNDs by gold nanoparticles^[153] or by coating with a silica shell.^[154]

Herein, dark field contrast enhancement provided high image quality with greatly enhanced contrast suitable for resolving unlabelled single fNDs during their cellular uptake process and within cellular organelles for the first time. In a first demonstration experiment, the number of fNDs inside an endosomal vesicle was quantified. We envision that the technique developed herein will provide quantitative understanding of the various interactions of nanoparticles with cells and ultimately pave the way to a rational design of nanoscale markers, sensors and reliable and reproducible nanotherapeutics.

Results and discussions

After synthesis, fNDs strongly aggregate in aqueous buffer due to their high number of negatively charged surface groups. Therefore, uncoated fNDs could not be used as single particle probes for cellular studies, and fND surface coating is essential to stabilise them in cellular environments. Herein, fNDs with 35 nm mean-diameter have been used whose surface was oxidised under harsh conditions in oxidising acids (Figure 2.2.1 d) and their dispersibility was enhanced in MilliQ water at low concentrations (0.1 mg/mL) by ultrasonification. We have developed previously a copolymer derived from the blood plasma protein human serum albumin (dcHSA-PEG(2000)18), termed dcHSA-PEG, containing multiple positively charged primary amino groups and grafted poly(ethylene oxide) side chains (Figure 2.2.1 c; the synthesis of this polymer was reported before^[157, 158]) that readily adsorbed to the surface of fNDs. Coated fND were purified by centrifugation (18,000 g) and separated from the unbound biopolymer. After coating with dcHSA-PEG, the surface charges changed from a negative to a positive value (Figure 2.2.1 d) and their hydrodynamic radius R_h increased from 44.5 nm to 61.7 nm (dynamic light scattering, DLS, Figure 2.2.2-2.2.3). This relatively large increase of about 17 nm was also due to the loss of small fNDs during purification by ultracentrifugation. For the *in vitro* studies, narrowly dispersed fNDs of high colloidal stability in Dulbecco's Phosphate-Buffered Saline (DPBS) were required. A monomodal distribution of coated fNDs was detected in the dynamic light scattering (DLS) recorded at different angles indicating no fND aggregate formation (Figure 2.2.2-2.2.3). Subsequently, the fNDs dissolved in DPBS were visualised by TEM revealing well-dispersed single nanoparticles distributed over the TEM grid (Figure 2.2.1 b), whereas uncoated fNDs appeared mostly aggregated in DPBS on the TEM grid (Figure 2.2.1 a). The negatively charged nitrogen vacancy (NV-) centres in fNDs emit light at a wavelength of 680 nm after excitation with a 561 nm laser. Their emission

intensity depends on the number, size and shape of the fNDs. Herein, about 15 NV- on average were present statistically distributed within the fNDs and their optical properties were not affected by the biopolymer coating (Figure 2.2.1 e). These coated fNDs were then used to study their cellular uptake and trafficking by confocal laser scanning microscopy (CLSM) and TEM in HeLa cells.

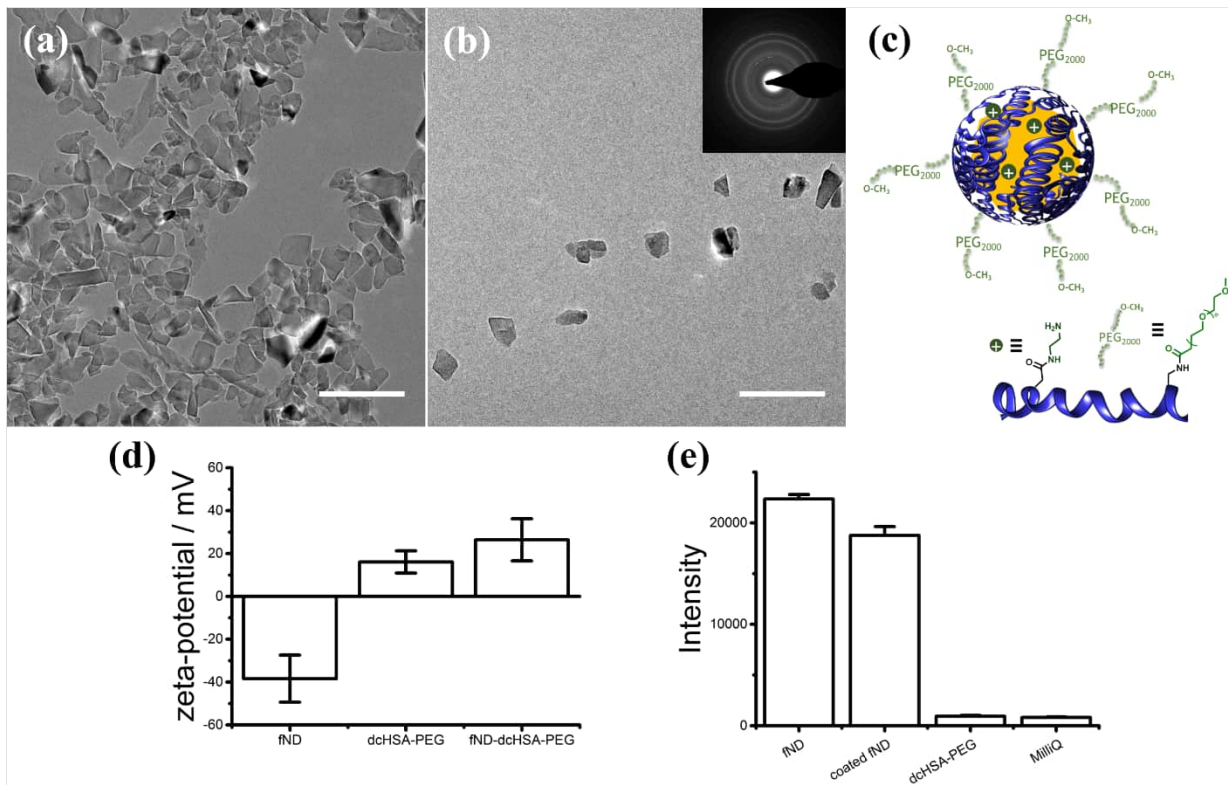


Figure 2.2.1 Characterisation of fND. **a.** Transmission electron microscopy (TEM) images of uncoated fND aggregates diluted in PBS. **b.** Coated single fNDs diluted in PBS; fresnel diffraction pattern of ND. **c.** Scheme of protein coated fNDs. **d.** Zeta-potential values. **e.** Fluorescence intensity of uncoated fNDs, coated fNDs (both 0.5 mg/mL), dcHSA-PEG (2 mg/mL) and MilliQ water. DLS, zeta-potential and fluorescence intensity of fNDs were performed by Dr. Marco Raabe. Scale bars: 200 nm.

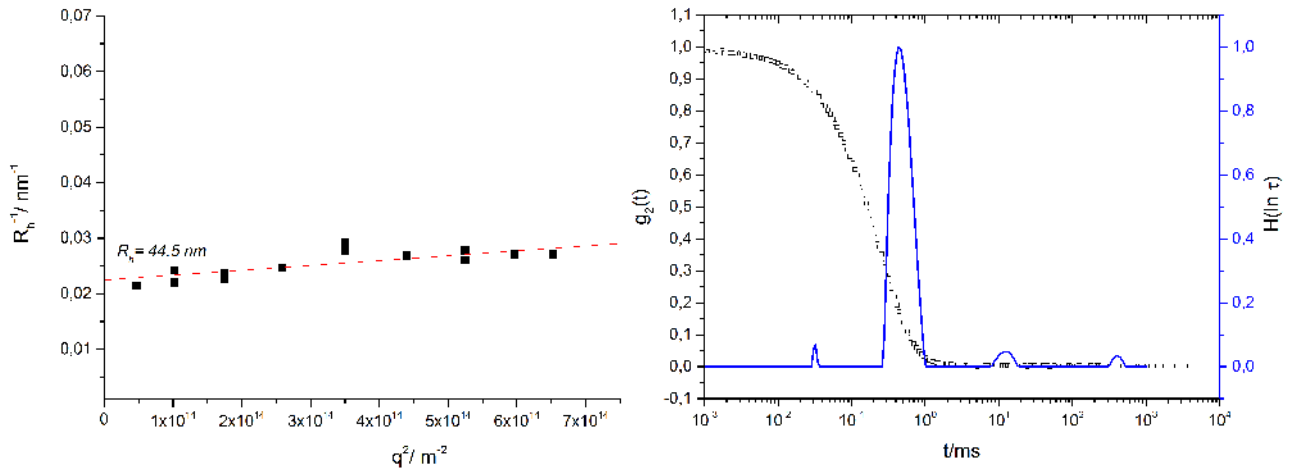


Figure 2.2.2 DLS of uncoated fNDs. Left DLS measurements from 30° to 150° . Right Autocorrelation curve (black dotted line) and time based function (blue) at 90° . DLS was performed by Dr. Marco Raabe.

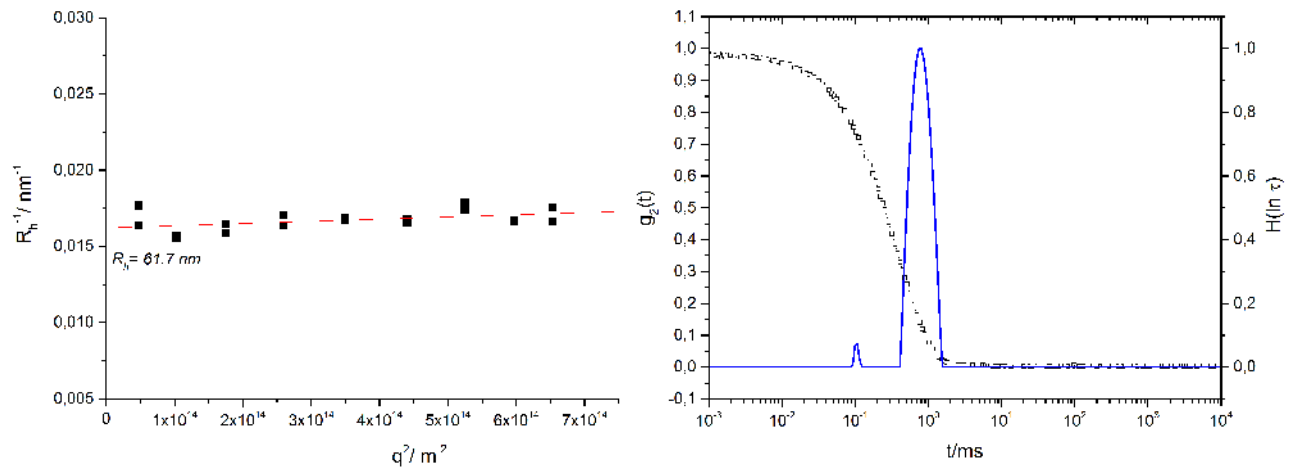


Figure 2.2.3 DLS of fNDs coated with dcHSA-PEG. Left DLS measurements from 30° to 150° . Right Autocorrelation curve (black dotted line) and time based function (blue) at 90° . DLS was performed by Dr. Marco Raabe.

First, the coated fNDs were vitrified and embedded prior to LM and EM acquisition providing images from the same cellular location (“in-resin CLEM”). Then, fNDs were examined by LM followed by EM acquisition (“in-dish CLEM”). The correlative imaging method provided localisation of fNDs in fluorescence microscopy and high-resolution EM micrographs from the same cellular ROI. Due to their stable emission intensity, fNDs could be identified in CLSM as well as in EM despite their all-carbon composition. Figure 2.2.4 a-b reveals LM and EM images from the in-resin CLEM imaging of the same section, where fND fluorescence was retained after the harsh resin and polymerisation treatment. The cellular structures appeared well preserved even after staining with low amounts (0.1 %) of UA. Noteworthy, our imaging procedure did not rely on OsO₄ as contrast enhancer. Compared to previously reported epoxy resins for embedding,^[154] the Lowicryl matrix applied herein allowed efficient nucleus staining with Hoechst dye (blue) on the section facilitating the selection of the cells of interest in LM. Figure 2.2.4 c shows fNDs clusters of different sizes, whose emission was precisely colocalised with CLEM with high contrast.

The structural information (in-resin CLEM) was obtained within one thin cell slice. In addition, we performed in-dish CLEM aiming for 3D tomography. Since z-stack images of the sample were recorded with CLSM first (Figure 2.2.4 d), spatial information of the sample as well as the fluorescence signals of the fNDs were obtained before the EM preparation. Cellular structures such as mitochondria remained well preserved, and they could be imaged with high resolution and contrast. Pronounced vesicle membranes around the fNDs clusters were detected (Figure 2.2.5). Background fluorescence was largely suppressed for an improved colocalisation and the CLSM and EM images appeared only slightly shifted (white arrows, Figure 2.2.4 f), which was mainly due to small changes in the position or shape changes of the living cells before fixation.

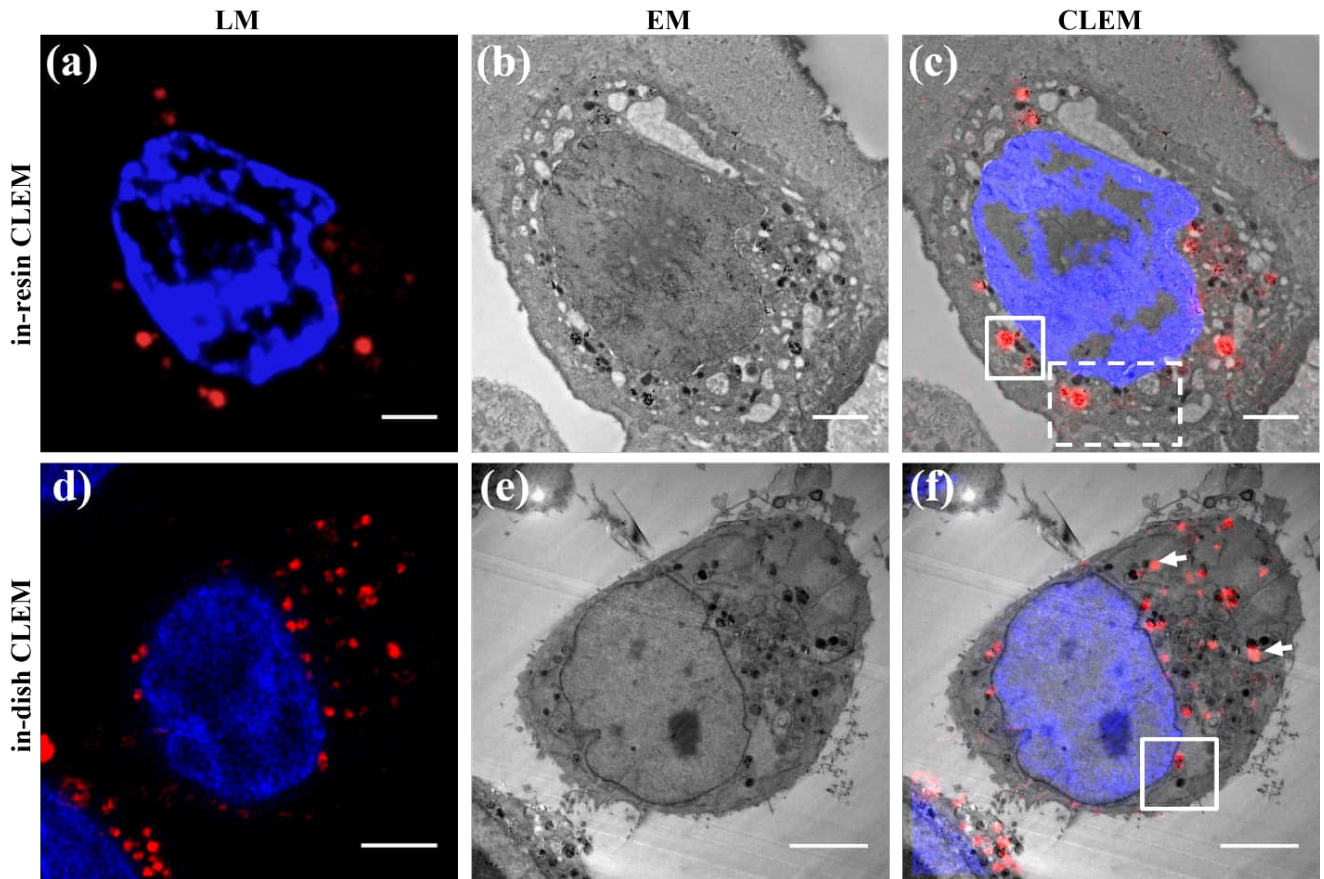


Figure 2.2.4 Correlative light-electron microscopy (CLEM) of fNDs in HeLa cells showing the results of the in-resin (top) and in-dish (bottom) preparation. **a.** Confocal laser scanning microscopy (CLSM) of fNDs (red) and nucleus (blue, Hoechst) on ultrathin section (120 nm nominal thickness). **b.** Transmission electron microscopy (TEM) of the same section as in **a.** **c.** Overlay of **a** and **b.** **d.** A selected image (of LM stack) with fNDs (red) and nucleus (blue, Hoechst) of a paraformaldehyde (PFA) fixed HeLa cell. **e.** Corresponding epoxy resin section of the same cell as shown in **d** and the resulting CLEM overlay **f.** Scale bars: **a-c** 2 μm , **d-f** 5 μm . The white boxes denoted in **c** refer to the areas displayed in Figure 2.2.10, and the box denoted in **f** refers to the area shown in Figure 2.2.7.

Table 1. Comparison of different methods to image single intracellular fNDs including a qualitative assessment on their performance.

Technique	Specificity for fND clusters	Specificity for single NDs	Resolution	Fluorescence (FL)
CLEM	High specificity depending on the fND emission	Low specificity	High resolution (EM grade)	FL information from both fNDs and labelled organelles
EFTEM	High specificity depending on the fND unique energy absorption	High specificity depending on the unique energy adsorption of fNDs	High resolution (EM grade)	No FL information
HAADF STEM	Medium specificity depending on the fND orientation	Medium specificity depending on the fND orientation	High resolution (EM grade)	No FL information
TEM (overfocus)	Medium specificity depending on the fND Fresnel contrast fringes	Medium specificity depending on the fND Fresnel contrast fringes	High resolution (EM grade)	No FL information

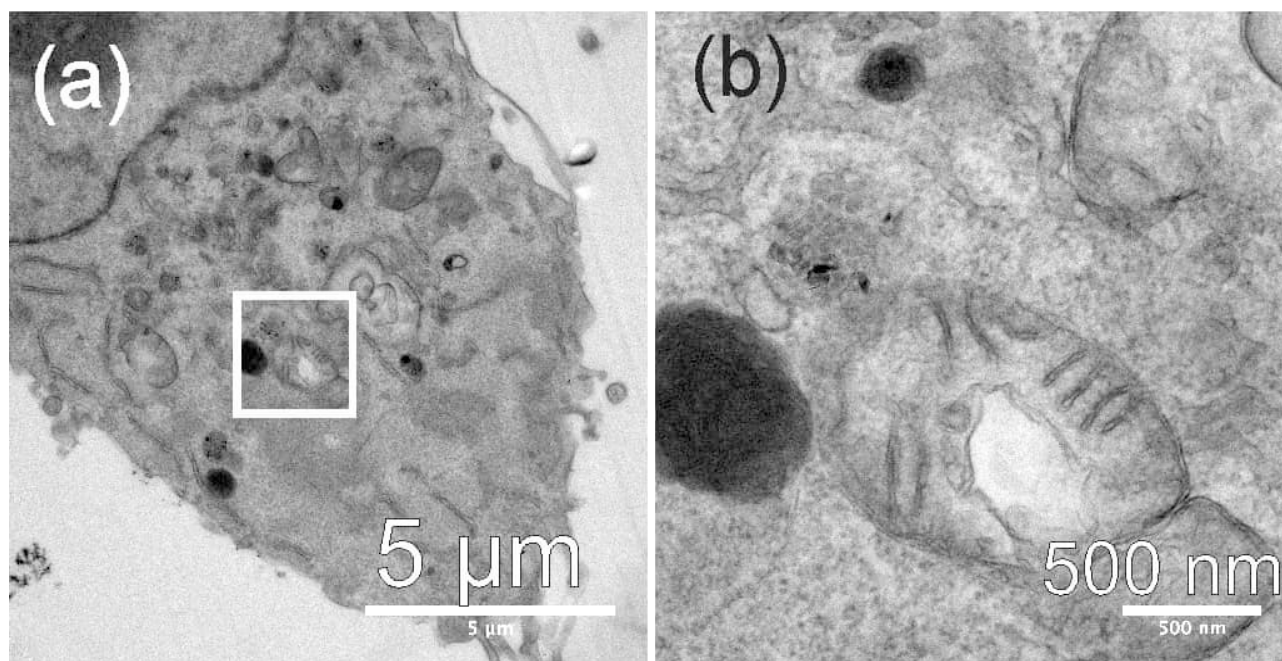


Figure 2.2.5 TEM bright field (BF) micrographs showing the preservation quality of the in-dish preparation method.

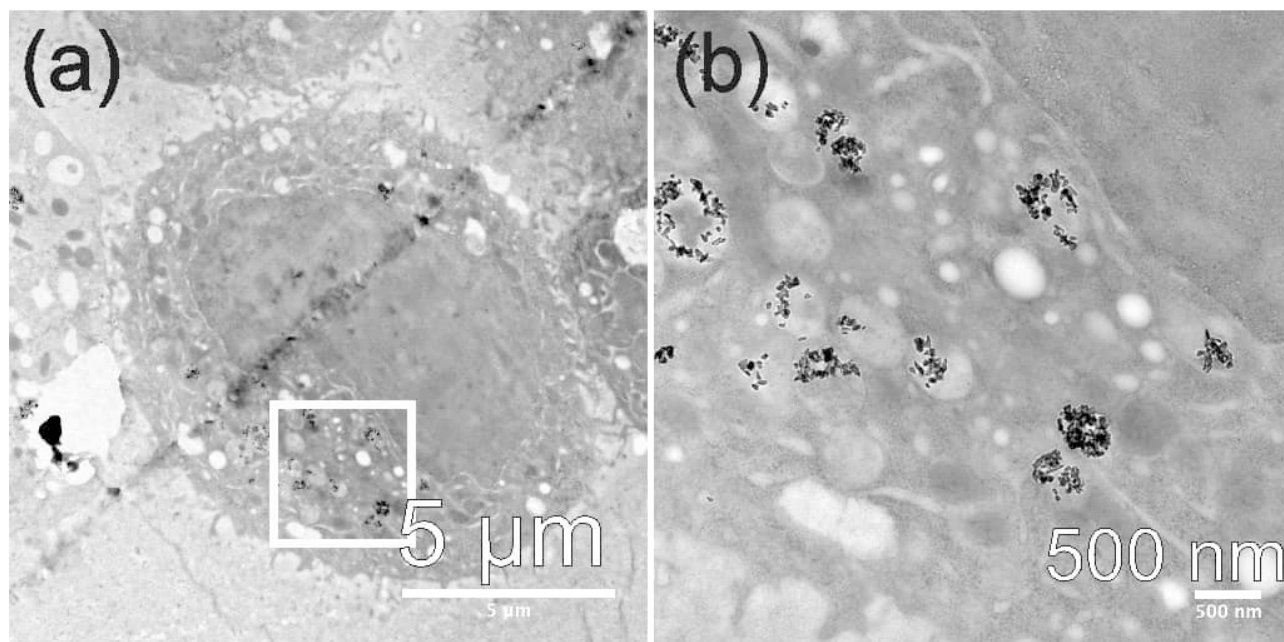


Figure 2.2.6 TEM BF micrographs showing the preservation quality of the in-resin preparation. Compared to the in-dish method, the contrast of the cellular structures is lower, presumably due to the missing OsO_4 staining and lower UA concentration. However, post staining of the sections should be possible.

The coated fNDs showed pronounced cellular uptake due to attractive electrostatic interactions with the negatively charged cellular membrane as reported previously.^[157] They were mainly localised in spherical clusters inside intracellular vesicles such as endosomes, lysosomes or autophagosomes (Figure 2.2.4). EM provided the required nanoscale resolution required to precisely quantify fNDs inside these intracellular vesicles and to image their endosomal escape. Figure 2.2.7 is an enlargement of the area indicated in Figure 2.2.4 f and clearly reveals a vesicle in close proximity to the cell nucleus (blue staining) and a mitochondrion located below. In total, three clusters of fNDs were found inside the vesicle: Two at the top and a third smaller cluster at the bottom right close to the membrane of the vesicle. Tomography of this vesicle was performed to study the vesicle integrity. Figure 2.2.7 b shows a cross section matching the LM overlay of Figure 2.2.7 a. Despite the high resolution, some parts (black arrows) of the membrane appeared disrupted, especially at positions where the upper left and lower right fNDs clusters were localised. This effect appeared even more pronounced when analysing the entire tomogram. Obviously, fNDs induced disruption of the vesicular membrane, which likely allowed their escape from vesicles as suggested also by previous studies with labelled nanoparticles.^[153, 159] Segmentation of the vesicle together with fNDs

is shown in Figure 2.2.7 c and as a result of the high resolution TEM tomography; even single fNDs in the cluster were identified. In Figure 2.2.7 c, a total number of 101 fNDs (in red) and the outer membrane of the endosome were segmented (in green) now allowing a quantification of the fNDs per cluster. The fND clusters in the endosomal vesicles were divided into three subvolumes: 1) The cluster located close to the vesicle membrane at the upper left part contained 27 fNDs in total (reconstructed in red); 2) the cluster located in the mid of the endosome was formed by 61 fNDs, whereas 3) the clusters located at the bottom right consisted of 13 fNDs. In addition, five small vesicles were identified and segmented (in light green) within the endosome.

TEM micrographs did not provide sufficient contrast for the detection of single fNDs within the embedding resin as both materials mainly consist of carbon-based structures. In addition, their detection by LM was limited by low fND concentrations within the thin sections (in-resin CLEM) as well as the varying fluorescence quantum yields among individual NDs, which resulted in fNDs occasionally not emitting and therefore remaining invisible. Although previous CLEM studies demonstrated an improvement for the visualisation of intracellular NDs with STED,^[154] the discrimination of individual ND in larger clusters still remains challenging, if not impossible. In order to compare and optimise fND imaging at the nanoscale, we evaluated additional EM imaging methods summarised in Table 1 highlighting the specificity and resolution of the different techniques for detecting fNDs in clusters as well as single fNDs.

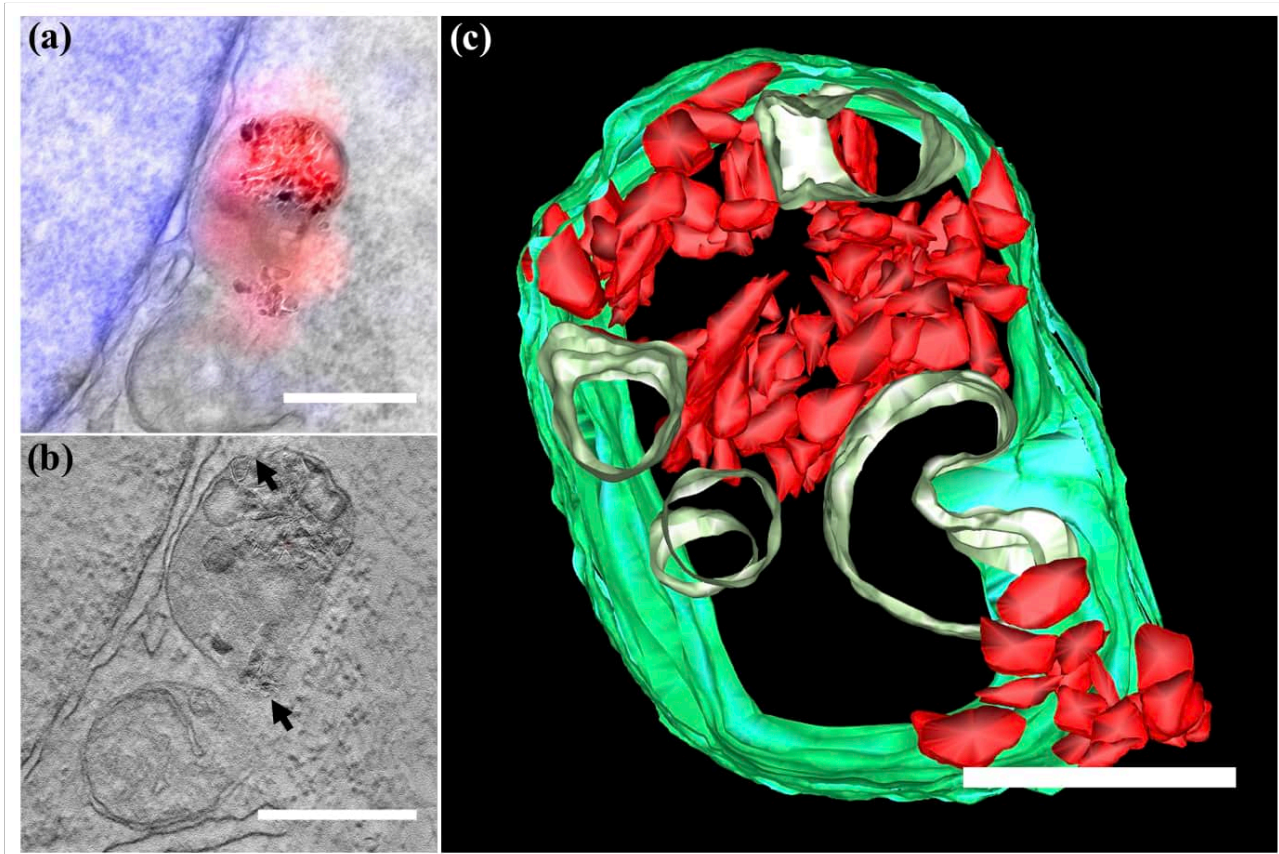


Figure 2.2.7 a. CLEM micrograph constructed from the overlay of LM and TEM micrograph showing the area denoted by the box in Figure 2.2.4 f. The localisation of the fNDs by LM is shown in red, whereas the nucleus appears in blue. **b.** Tomogram section of the same region; black arrows indicate the disappearance of the vesicle membrane. **c.** 3D model of fNDs clusters inside the endosomal vesicle; fNDs appear in red and the cellular membrane is shown in green; five vesicles are given in light green. Scale bars: **a** and **b**: 500 nm, **c**: 250 nm.

HAADF STEM Darkfield imaging (DF) using a high angular annular dark field detector with scanning TEM (HAADF STEM, Figures 2.2.8, 2.2.9) could in principle visualise single fNDs. However, diffraction-based identification techniques like HAADF STEM and conventional DF imaging rely on the correct orientation of the crystal with regard to the incident electron beam and therefore, only few individual nanodiamond crystals were detected, as demonstrated in Figure 2.2.9.

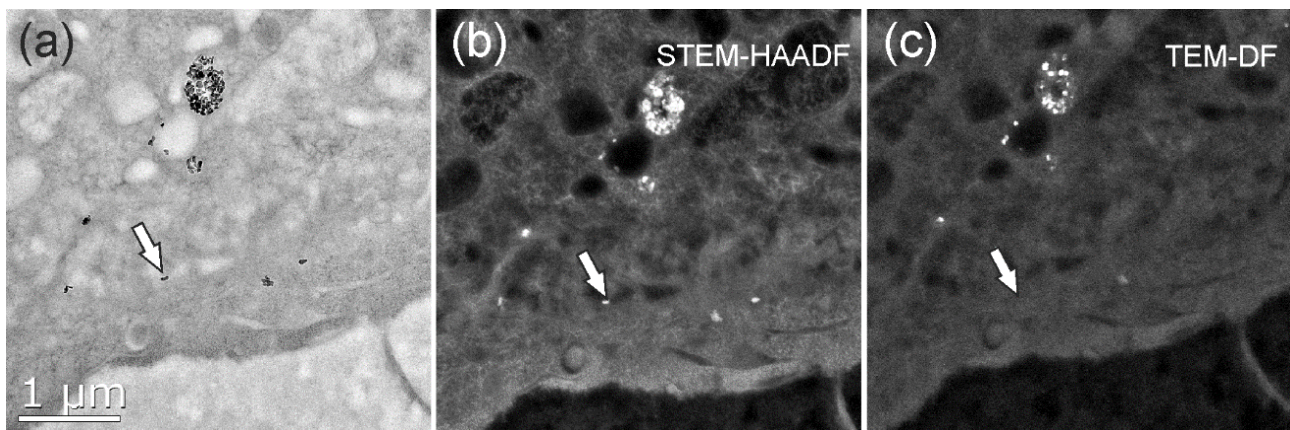


Figure 2.2.8 TEM and STEM micrographs showing the same area. In the bright field micrograph **a** the NDs are clearly visible by their dark contrast and in the STEM micrograph **b** the NDs appear bright because their diffraction contributes to the HAADF signal. All the NDs in the bright field micrograph are also visible in the STEM micrograph. When using the conventional TEM dark field **c** mode, some of the NDs are not visible, as exemplarily marked by the arrow.

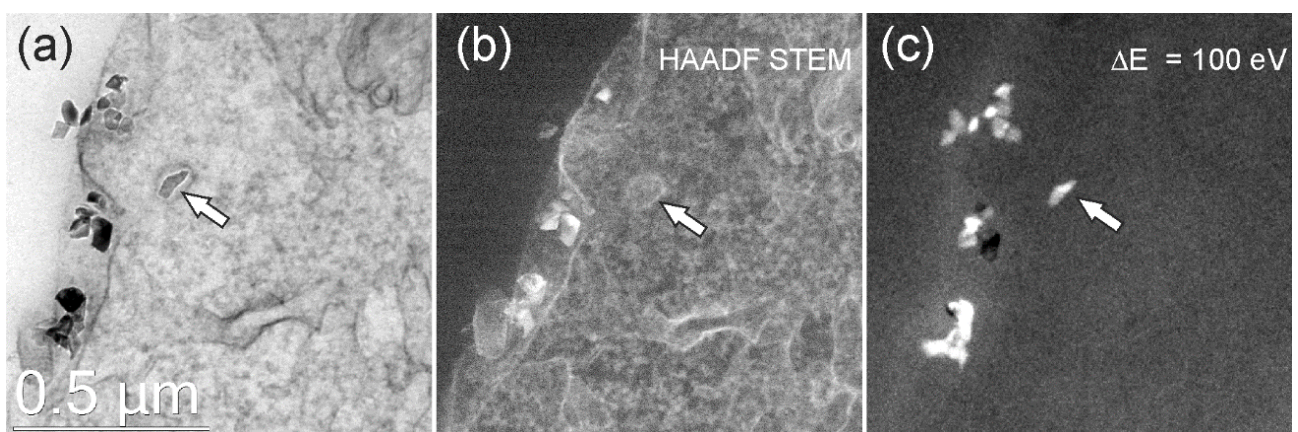


Figure 2.2.9 **a.** TEM-BF **b.** STEM-HAADF **c.** EFTEM micrographs of the same area. The ND marked with an arrow is visible in the BF and the EFTEM micrograph, but it does not appear in the HAADF-STEM mode.

EFTEM allows the identification and localisation of individual fNDs in the in-resin and in-dish preparations as this technique depends on the electron density but not on the orientations of the fNDs. EFTEM has been applied previously to image gold particles and QDs in HEp-2 cells for correlative microscopy studies,^[160] but it has not yet been used to identify intracellular fNDs. Figure 2.2.10 shows the corresponding CLEM micrographs, TEM bright field micrographs and EFTEM micrographs of fNDs in HeLa cells. Two fNDs clusters (Figures 2.2.10 a-b) were detected in the TEM micrograph, which was confirmed by the fluorescence signal in the LM image. The EFTEM micrograph in Figure 2.2.10 c reveals the presence of two single fNDs (arrows), which were barely visible in the bright field micrographs and could not be detected by fluorescence imaging. After inverting Figure 2.2.10 b, we calculated the line value (red dotted line) crossing two single fNDs (Figure 2.2.10 b-c). A Gaussian fit was used to calculate the signal to noise ratio in the EFTEM image (Figure 2.2.10 c), which was significantly improved (4.0 and 3.3) compared to the signal to noise ratio (2.3 and 1.5) of the TEM bright field image. In addition, we estimated the resolution using the line profile crossing two fNDs (Figure 2.2.10 h). The distance between the two peaks was 30 nm as calculated by a Gaussian function and the Gaussian fitting result highly matched the line value ($R^2 = 0.974$). The detection limit of fluorescence imaging becomes apparent in Figure 2.2.10 d-e. The cluster in the left corner of Figure 2.2.10 d consists of three fNDs, whose fluorescence signal could still be resolved (the slight mismatch was due to the time gap of the in-dish preparation), whereas EFTEM (Figure 2.2.10 f) clearly shows the presence of three individual fNDs. The remarkable contrast of fNDs in EFTEM imaging was attributed to the higher density of NDs compared to the surrounding resin. The mean free path λ (the average distance an electron propagates through the specimen before being scattered) was lower in diamond compared to the surrounding material and hence, the inelastic scattering intensity was increased, which was experimentally confirmed by the electron energy loss (EEL) spectra in Figure 2.2.10 g. Accordingly, fNDs appeared with bright contrast when imaged with an energy loss ΔE ranging from 50 eV up to 190 eV (Figure 2.2.11). This assumption was further corroborated by the observation, that fNDs could be detected easily in bright field imaging at large overfocus (Figure 2.2.12).

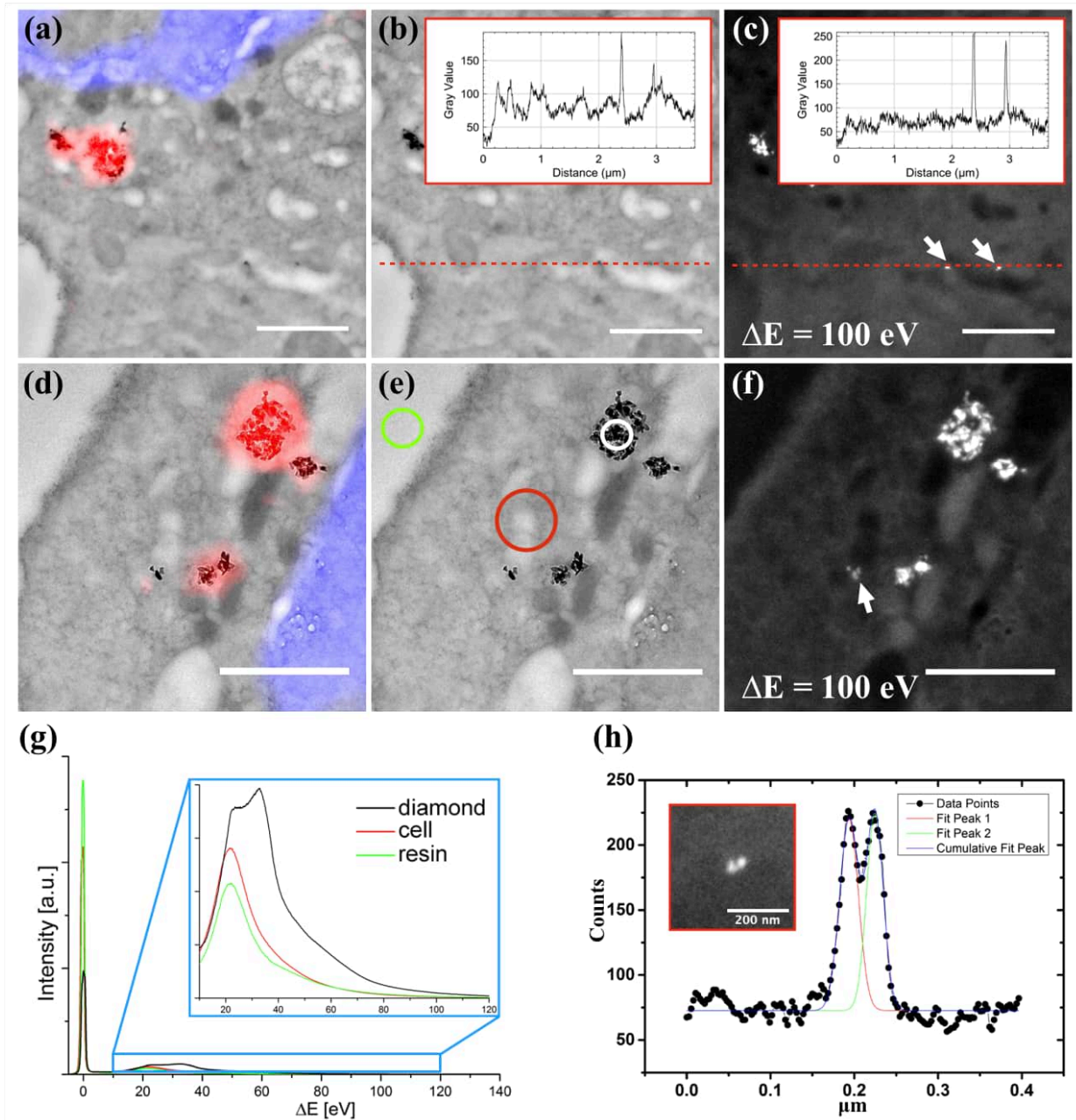


Figure 2.2.10 Single fND and fND clusters imaged by energy filtered transmission electron microscopy (EFTEM). **a** and **d**: CLEM overlay, **b** and **e** the corresponding TEM bright-field micrograph. **c** and **f**: EFTEM micrograph acquired at an energy loss of 100 eV with 10 eV slit width. The white arrows indicate the detection of individual fNDs. The insets in **b** and **c** represent line profile values of respective selected line (red dots line). **g**. EEL spectra of embedded fNDs (black), the embedded cell (red) and a resin-only area (green), corresponding to the positions indicated in **e** (the inset of **g** shows a zoom into the energy loss range from 10 to 120 eV). The spectra were acquired by focusing the electron beam on the respective area. **h**. The line profile value of the inset (EFTEM micrograph of two closely located fNDs), Gaussian function fit of the data. **a** to **c** show the magnification of the region marked by the dashed box in Figure 2.2.4 c); **d** to **f** display a magnification of the area marked by the solid box in Figure 2.2.4 c). Scale bar: 1 μm

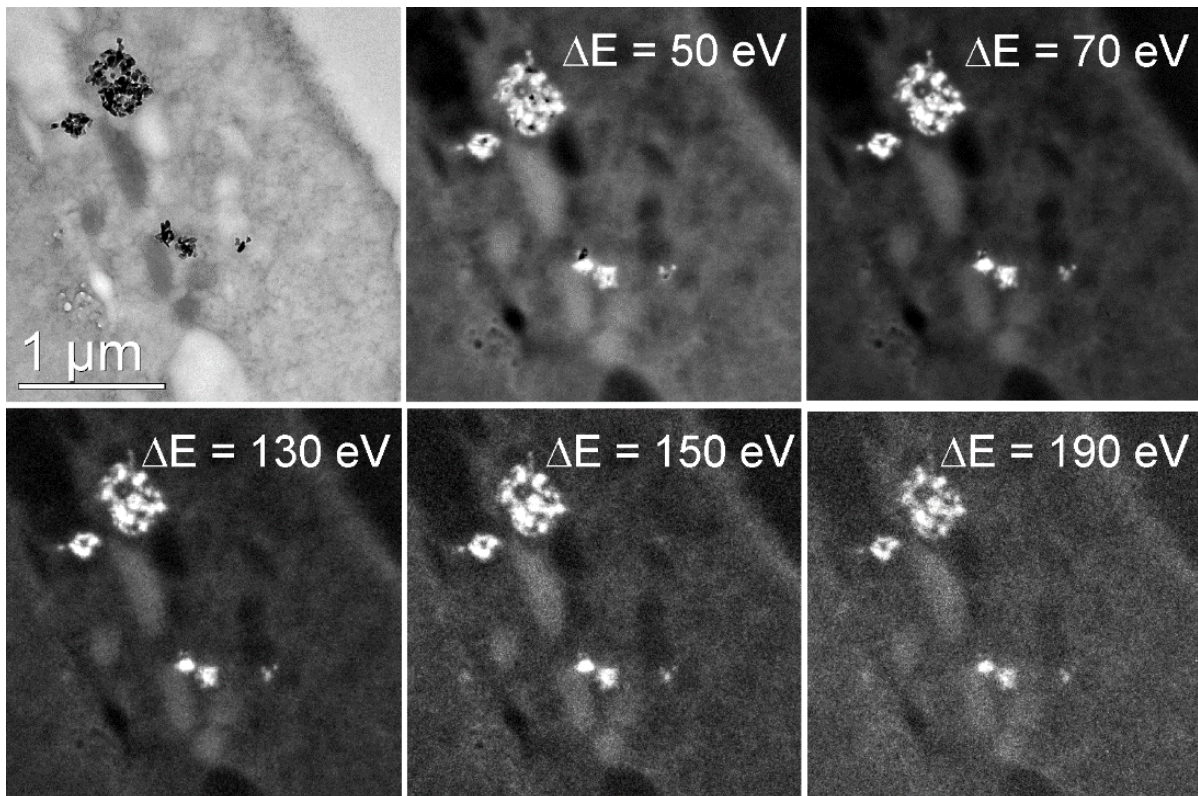


Figure 2.2.11 Energy filtered TEM micrographs: The sample area is imaged with increasing energy loss from bright field (0 eV, upper left) to 190 eV (lower right). The slit width of the spectrometer was adjusted to 10 eV. In the bright field micrograph the ND are clearly visible by their dark contrast.

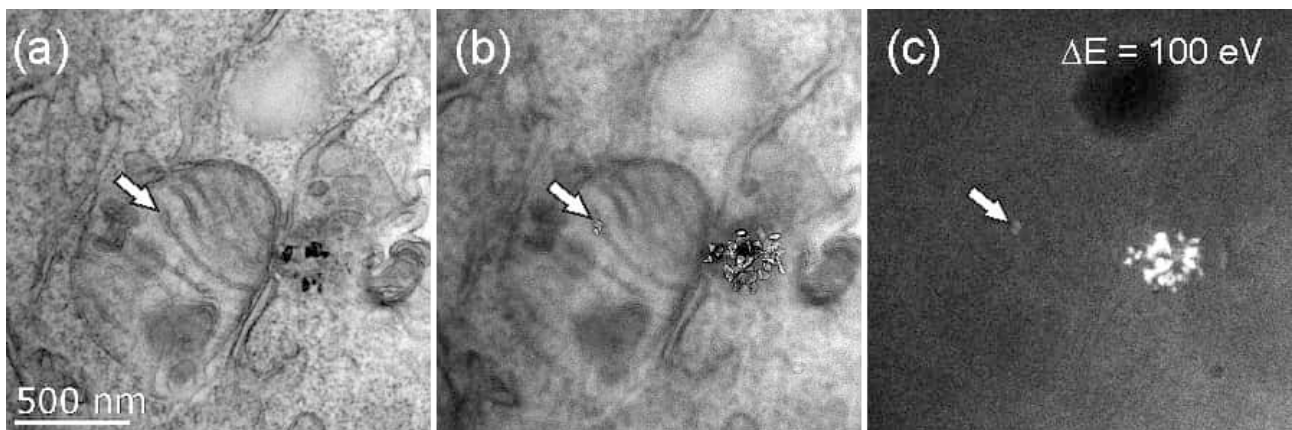


Figure 2.2.12 TEM and EFTEM micrographs of the same sample area demonstrating the ease and power of overfocus identification of phase objects like NDs in a resin matrix. a. The TEM BF micrograph does not reveal the presence of a ND at the position marked with an arrow. Over focused TEM micrograph b clearly shows the ND which can be seen in the EFTEM micrograph c as well.

TEM (overfocus) The bright Fresnel contrast fringes, which were formed around the individual fNDs in TEM bright field imaging, indicated that the fNDs were phase objects attributed to their higher electron density, which also offers potential for detecting individual fNDs without the need for EFTEM or CLEM. The Fresnel fringes in the TEM micrograph appeared due to the discontinuous potential change at the edge of the fND. In overfocus conditions, this yielded a bright fringe around the object in the TEM micrograph.^[161] However, also other phase objects presented in the specimen could be misinterpreted as fND by this method.

Our results clearly indicate that the EFTEM approach represents the method of choice for detecting single fNDs with high contrast and great spatial resolution within cells. EFTEM even allowed an autonomous TEM screening of the entire sample and subsequent qualitative data analysis was accomplished conveniently, which offers the great potential to accelerate the precise identification and quantification of intracellular fNDs.

Figure 2.2.13 a reveals a TEM image of fNDs close to the extracellular matrix of the cellular membrane. The presence of the single fND was clearly confirmed by EFTEM (Figure 2.2.13 b), which was not detectable by CLEM and standard TEM. It seemed that several fNDs formed clusters close to the extracellular matrix, and a single fND was located already inside the cell, presumably inside an early endosomal vesicle. Electron tomography was performed on this site, and Figure 2.2.13 c shows a virtual slice of the tomogram. Obviously, the formation of the early endosome was still in process, and the membrane of the endosome appeared still connected to the membrane of the cell. In order to gain deeper insights into this process, the tomogram of this site was segmented yielding a 3D model (Figure 2.2.13 d), in which four fNDs were localised close to the cellular membrane (in green), and a single fND appeared inside the newly formed endosomal vesicle, highlighted in red. This 3D tomography captured for the first time the process of cellular uptake of a single fND as well as the presence of a membrane tunnel connecting the endosome with the cellular membrane.

Inside the cell, we screened for single fNDs that were taken up into organelles, which is of great interest for sensing,^[139] drug delivery^[162] as well as understanding nanoparticle-related toxicity.^[139] Single fNDs localised in cellular organelles are particularly challenging to detect. Figure 2.2.13 e shows the TEM image of a cluster of fNDs in direct proximity to a mitochondrion. The fND cluster with dimensions of around 200 nm in diameter was detected in the upper right corner in close

vicinity to the mitochondrion, which was probably too bulky to enter the cell organelle. EFTEM clearly showed the presence of individual fNDs inside this mitochondrion (Figure 2.2.13 f). The virtual section from the tomogram (Figure 2.2.13 g) reveals two fNDs inside the mitochondrion and the segmentation (Figure 2.2.13 h) of the tomogram clearly supported that the fNDs were located close to the inner membrane. Interestingly, there was no membrane formed around the fNDs suggesting that during their uptake process into the mitochondrion, the endosomal membrane surrounding the two fNDs most likely coalesced with the mitochondrial membrane. One could speculate that the two fNDs might originate from the larger fND cluster located close to the mitochondrion. However, additional studies are necessary to unravel the intracellular transport processes of nanoparticles into mitochondria.

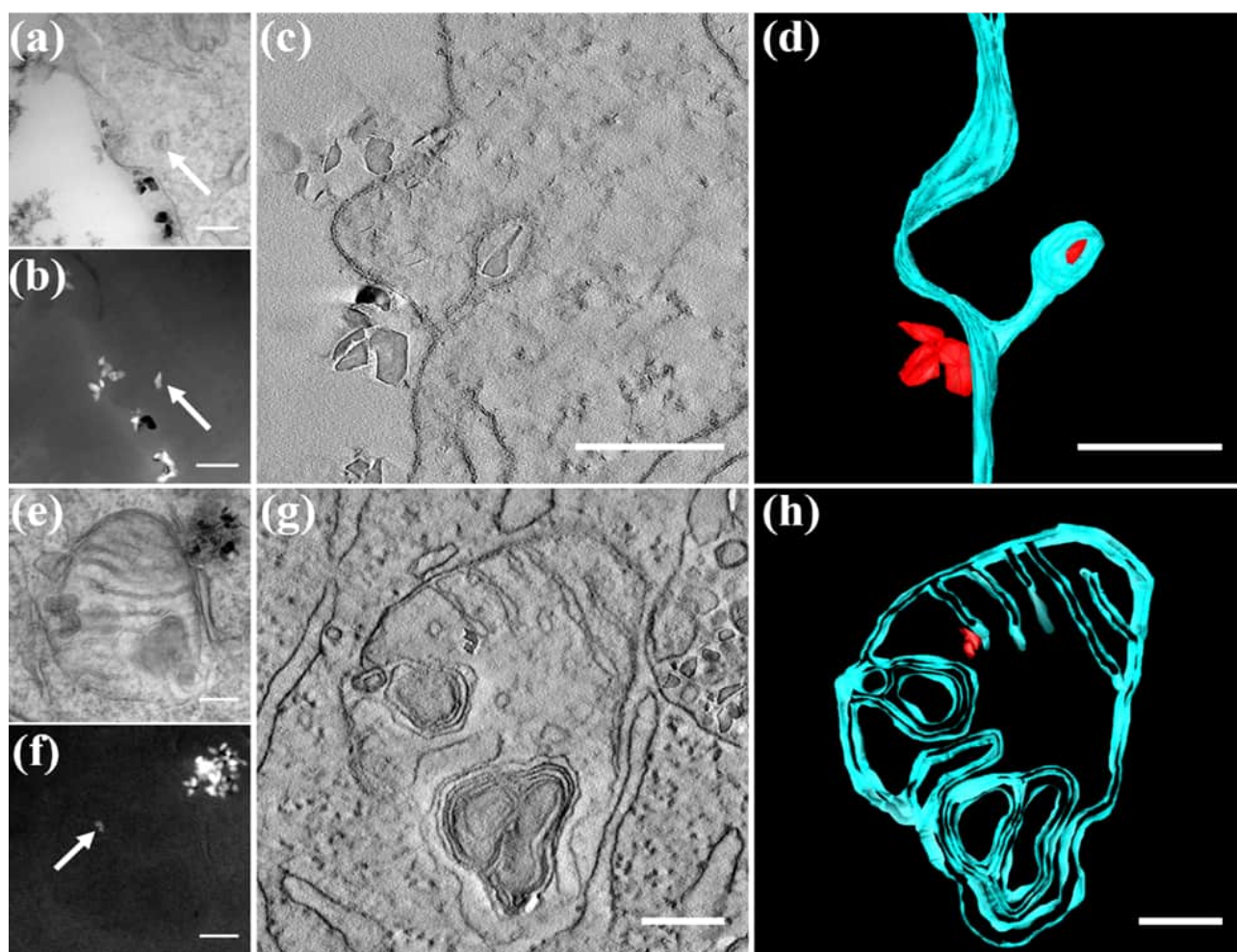


Figure 2.2.13 Interactions of single fNDs with cellular substructures. a and b show bright-field TEM and dark-field EFTEM of single fND uptake; e and f depict bright-field TEM and dark-field EFTEM of fNDs inside a mitochondrion. c and g reveal the virtual slices from the tomogram, whereas d and h give the segmentation of the tomograms of single fND uptake and localisation inside a mitochondrion, respectively. Scale bars: 200 nm.

Imaging of NDs in the TEM in general. Imaging of NDs and especially individual NDs in TEM can be facilitated by using different imaging methods, depending on the configuration of the respective instrument. The main problem when imaging NDs in a resin matrix, as commonly prepared for TEM ultrastructural examination of biological samples, is their low contrast with regard to the surrounding resin. However, there are some physical features of NDs that promote their discrimination from the resin matrix. The density of a diamond is with 3.5 g/cm^3 much higher than that of the surrounding resin and, as every diamond, NDs are crystalline. Imaging crystalline areas is one of the strengths of the TEM. By simply selecting the position of the objective aperture, it is possible to select electrons, that have left the sample under a certain angle, e.g. due to diffraction. This method is called dark field mode and can be easily achieved in any TEM. The strongest diffraction spot of diamond is the (111) with a d-spacing of 2.058 \AA . This corresponds to a diffraction angle of $2\Theta = 12.2 \text{ mrad}$ for 200 keV electrons. When the objective aperture of the TEM is adjusted in a way that electrons leaving the sample under this angle can pass (but the transmitted beam is blocked), the crystalline areas appear with bright contrast. But because the aperture allows only a small azimuth area of the diffraction ring to pass, only those crystals with the correct orientation become visible (arrow in Figure 2.2.8 c).

In order to overcome this azimuthal restriction, annular detection methods like conical dark field or HAADF-STEM can be used. Due to the annular geometry of the HAADF detector all directions of the diffraction ring are detected and the crystal areas appear with bright contrast (Figure 2.2.8 b). But even using the whole (111) diffraction ring does not guarantee that every ND crystal becomes visible, because this depends on the crystalline orientation; if the Bragg-condition is not fulfilled due to an odd orientation of the crystal there is no signal in the dark field micrograph. This is exemplarily demonstrated in Figure 2.2.9, where the ND marked by the arrow is clearly seen in the TEM BF Figure 2.2.9 a and in the EFTEM micrograph Figure 2.2.9 c, but not in the HAADF-STEM Figure 2.2.9 b.

Another alternative to image NDs in a resin matrix is to use EFTEM imaging. Here, the identification does not rely on the correct orientation of the crystal but rather on the difference in electron density between the ND and the surrounding matrix. NDs are a pure carbon material and the surrounding matrix of polymerised resin is a carbon rich material as well. Accordingly, element specific discrimination by EFTEM is eliminated. But the mean free electron path λ depends on the

local electron density and then finally on the density of the respective material. In a simplified explanation the probability for inelastic scattering depends on the local electron density and with that on the material density. This is shown in the electron energy loss (EEL) spectra Figure 2.2.10 g. The intensity in the areas of the nanodiamonds is greater in the entire spectral range measured from 50 to 200 eV than where resin or cellular material is present in the sample. Therefore, the nanodiamonds appear brighter in the EFTEM micrographs. Figure 2.2.11 shows an EFTEM series acquired at different energy losses using an energy selecting slit width of 10 eV. The NDs are clearly visible up to 190 eV energy loss. We did not checked higher loss values because this would unnecessarily increase the exposure time without yielding more information. Accordingly, EFTM imaging is the appropriate way to identify and image NDs in an embedded cell samples. Even single fNDs can be detected this way, which is not possible by fluorescence imaging at all.

However, if you have neither an energy filter nor a scanning unit at the TEM, there is another, very easy way to locate the embedded NDs. Hereby one can simplify the tedious search for the NDs considerably. Like other objects, NDs are phase objects that change the phase of the electron waves as they exit the sample.

If the TEM is now heavily overfocused, this will cause the resulting Fresnel fringes of the NDs to show bright contrast on the resulting image, as shown in Figure 2.2.12 b. Although these images are useless for further processing, they clearly show the position of the NDs. For comparison, Figure 2.2.12 c shows the corresponding EFTEM image, on which individual NDs can be recognised as well (marked by the arrow).

Images alignment and analysis. The alignment of the in-resin acquired data was straightforward, because both, electron and light microscopical imaging originate from the very same specimen. However, for the in-dish preparation, there is a certain time span between the LM imaging and the final fixation for EM preparation and subsequent imaging. This time span already leads to systematic mismatch in the alignment. In addition, the preparation of the ultrathin sections might lead to problems with the CLEM alignment. The sections suffer a certain compression during sectioning, which can be easily compensated by a simple affine transformation (stretching of the EM micrographs parallel to the cutting direction). However, we did not observe noticeable compression of the sections and within the accuracy of the LM images we did not need to compensate for this. On the other hand, the normal of the sections and the optical axis of the LM

might not coincide. With other words, there is a certain angle between the cutting direction and the imaging direction of the LM. For this case, there is a certain tolerance of the preparation method due to the rather large confocal optical section thickness compared to ultramicrotomy sections. A confocal microscope can reach thicknesses down to 500 nm. The effect of a misaligned cutting angle would result in the disappearance of (correlative) objects, especially at the image periphery. Accordingly, we put much effort in aligning the block phase of the resin block as parallel as possible to the diamond knife and we did not encounter any problems with a misalignment of the cutting angle with regard to the imaging plane of the LM.

Conclusions

In summary, we have demonstrated a stringent procedure to image and quantify coated fNDs as clusters as well as down to the single particle level inside cells. A bioinspired protein coating was used to stabilise the fNDs inside cells, which has similarities to the natural protein corona, formed when nanoparticles are subjected to blood serum providing high colloidal stability and biocompatibility. fNDs were detected at different stages during their cellular uptake and intracellular trafficking highlighting that many cellular barriers have to be crossed inside cells. fND clusters appeared outside the cellular membrane as well as in endosomal vesicles as detected by CLEM with a high contrast by colocalisation of LM and EM signals. EM images of fND clusters were obtained with the highest resolution reported yet, which even allowed quantification of individual fNDs in the larger fND clusters inside intracellular vesicles. Moreover, individual fNDs were detected for the first time by EFTEM. In this way, the cellular uptake process of a single fND inside a newly forming, early endosomal vesicle was imaged, and the presence of single fNDs inside a mitochondrion was demonstrated. The localisation and quantification of fNDs inside mitochondria is of particular interest since drug delivery into these organelles represents an emerging strategy in cancer cell treatment.^[162] Conventional LM studies could not unambiguously differentiate whether nanoparticles were taken up into mitochondria or if they only colocalised with their outer membranes. Applying dark-field EFTEM, we were able to resolve the presence of individual fNDs inside the mitochondrion, whereas a larger fND cluster remained outside this organelle in close vicinity to its outer membrane.

We believe that our approach offers the great potential to resolve fNDs within clusters as well as single fNDs and to allow the quantification of their exact number and image their locations within the various cellular compartments. In this way, one could gain fundamental insights into intracellular transport processes of fNDs and how these pathways are interconnected, which provides great opportunities to ultimately correlate bioactivities and potential toxic effects of nanomaterials based on quantitative data. We believe that such studies will be of great relevance to obtain reliable and reproducible information of nanotherapeutics that ultimately facilitate rational design of efficient and safe drug transporter and imaging probes.

2.3. Visualising the destiny of protein nanocarriers along the endolysosomal pathway – different compartments are involved in processing protein nanocarriers

This section is based on a submitted manuscript.

This section took advantage of the on-section CLEM from the last section to precisely visualise NPLs encapsulated BSA NCs in the cells. This section serves as an application of on-section CLEM to visualise protein NCs in cells.

Contributions:

I performed CLEM and electron microscopy imaging as well as image interpretations and manuscript writing regarding the imaging and discussion parts. Marie-Luise Frey synthesised the bovine serum albumin nanocapsules (BSA NCs) and performed the encapsulation of nanoplatelets (NPLs) as well as characterisation and fluorescence intensity measurements and manuscript writing. Henry Halim synthesised the NPLs. Anke Kaltbeitzel performed the cLSM measurement. Andreas Riedinger, Katharina Landfester and Ingo Lieberwirth supervised and wrote the manuscript.

Abstract

We analyse the intracellular fate of protein based nanocarriers (NCs) along their endolysosomal pathway by means of correlative light and electron microscopy (CLEM) methods. To unambiguously identify the NCs and their degradation remnants in the cellular environment, they are labelled with fluorescent, inorganic nanoplatelets (NPLs). This allows tracking the NCs on their intracellular pathway by means of electron microscopy imaging. From the present data, we can identify different cell compartments in which the NCs are processed. Finally, three different terminal routes for the intracellular destiny of the NCs are presented. Our findings are important to reveal the degradation process of protein nanocapsules and contribute to the understanding of the therapeutic success of an encapsulated drug.

Introduction

The use of nanocarriers for drug delivery is becoming increasingly popular in medical research.^[12, 163] Besides liposomes and nanoparticles, which already find applications in clinics, also core-shell structures like nanocapsules (NCs) are appropriate candidates for the use as drug delivery platform.^[14, 164-166] Especially NCs made from proteins have many advantages, such as their biodegradability, high loading capacity with a combination of hydrophilic drugs and low toxicity.^[33, 34] Due to their size, nanocarriers can permeate cells easily and therefore it is of great importance to elucidate how the uptake and the further fate of the nanocarrier in the cell occur.^[167]

Nanocarriers are usually processed along the endolysosomal pathway.^[168] However, polymeric nanocarriers, such as protein NCs, are hard to track within this pathway since they cannot be clearly identified: they require either fluorescent markers to be observed by light microscopy (LM) or electron-dense markers to be observed by electron microscopy (EM). Correlative light and electron microscopy (CLEM) combine the strengths of both techniques and contribute to a precise localisation of the nanocarriers in the cell. Ideally, the CLEM preparation features a fluorophore with a stable inherent fluorescence suitable for cLSM which, in combination, has a contrasting component suitable for TEM. For instance, this can be achieved with inorganic, fluorescent nanoparticles. Current markers to track nanocarriers like quantum dots cannot be visualised readily because they are difficult to be distinguished from cellular components, due to their small size

(~5 nm) and spherical shape.^[169, 170] This means additional elemental analysis (e.g. EDX or ESI) confirms the identity of the quantum dots to ultimately locate the nanocarrier.^[171-173]

Here we developed a fluorescent system by using large (20-50 nm), rectangular nanoplatelets (NPLs) as markers for polymeric NCs in LM and EM. We encapsulated these NPLs into biocompatible NCs, a type of drug delivery vehicle, by a polyaddition at the droplet interface in inverse miniemulsion. The key to success of the NPL markers hinged on the protective coating on the NPLs.^[174] This coating makes NPLs both easy to disperse in aqueous medium and protects the NPLs' surface from major damage during the encapsulation process, thus leading to high fluorescence after encapsulation. We used NCs made of bovine serum albumin (BSA), crosslinked at the interface with toluene diisocyanate (TDI), forming a dense polymeric shell.^[33, 166] The NPLs were added to the aqueous dispersed phase during the miniemulsion process, leading to the encapsulation of the NPLs into the NCs.

To follow the intracellular pathway, RAW264.7 macrophages were incubated with these NCs followed by different techniques like flow cytometry, cLSM, and electron microscopy. By employing a combination of incubation and ripening time, the NCs were localised inside cells revealing different terminal destinations along the endolysosomal pathway involving early and late endosomes and endolysosomes.

Results and discussions

We used the miniemulsion method to synthesise protein NCs made of BSA,^[33] loaded with NPLs. We accomplished the loading of the NPLs into biocompatible NCs by adding water-dispersible NPLs to the aqueous phase of a miniemulsion. The number of NPLs per nanodroplet of the miniemulsion with the precursor for the subsequent NC is assumed to follow a Poisson distribution. Hence, we employed an excess of NPLs per expected NC to achieve a labelling of all capsules with at least one NPL. In addition, we synthesised a 1:1 ratio (NPLs : NCs) and NCs without NPLs to uncover any changes of the capsule properties due to excess NPLs.

After the NPLs have been evenly dispersed in the aqueous phase, BSA was added followed by emulsification in cyclohexane in presence of the surfactant poly-((ethylene-co-butylene)-b-(ethylene oxide) (P(E/B)-b-EO)).^[175] The final step to obtain the BSA NCs is the addition of a

crosslinker toluene diisocyanate (TDI), which reacts in a polyaddition reaction at the droplet interface and leads to a shell made of crosslinked BSA on the water-cyclohexane interphase.

However, in order to use these NCs for biomedical applications, they need to be transferred to an aqueous phase (Figure 2.3.1 a) by replacing the cyclohexane with water. This is achieved by redispersing the NCs in aqueous SDS solution followed by evaporation of the cyclohexane.

We then analysed the size distribution and hydrodynamic radii. Three different NPL:NC ratios and one NC sample without NPLs were synthesised and the size distribution was measured in cyclohexane as well as in aqueous phase after the transfer of the NCs from the organic to the water phase. Furthermore, we analysed the morphologies of the obtained BSA NCs in cyclohexane (Figure 2.3.1 c) and in water (Figure 2.3.1 d) by cryo-TEM. To check the suitability for cLEM measurements, we studied the photoluminescence of the BSA NCs with different NPLs loadings in cyclohexane (Figure 2.3.1 e) and after redispersion to water (Figure 2.3.1 f).

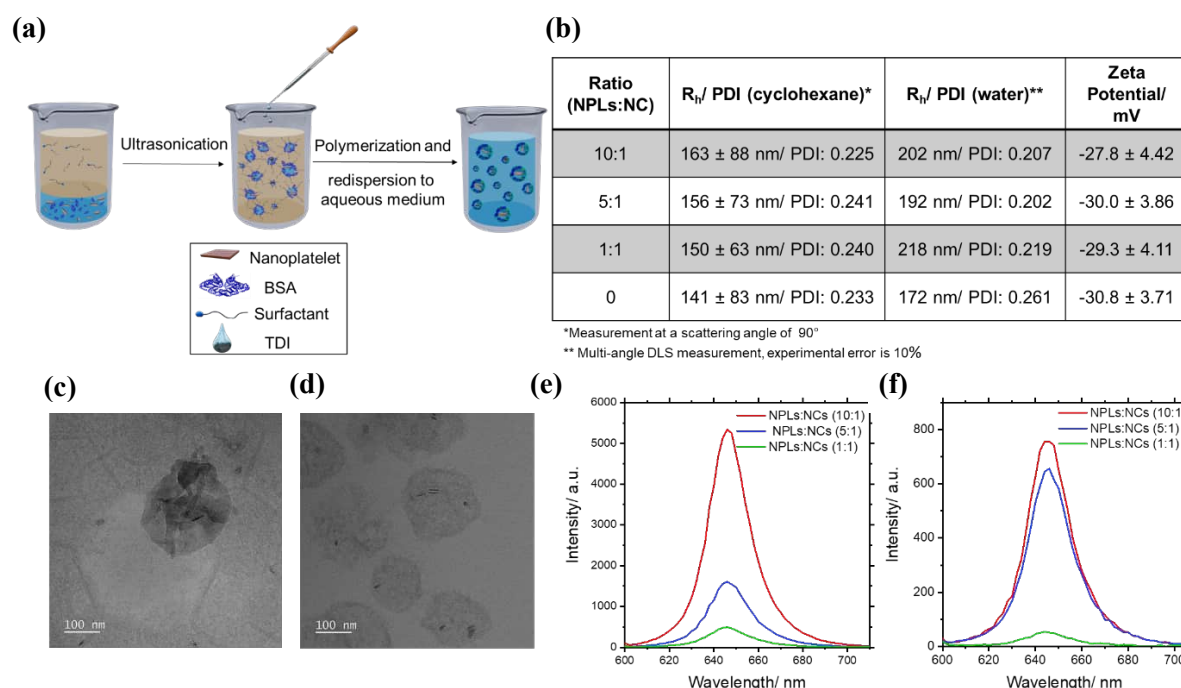


Figure 2.3.1 Characterization of BSA nanocapsules (NCs) loaded with different amounts of water-dispersible nanoplatelets (NPLs). **a.** Synthesis scheme for the inverse miniemulsion. **b.** Table with physicochemical properties of BSA NCs containing different NPLs ratios. **c.** Cryo-TEM image of a BSA NCs loaded with NPLs (5:1 ratio) in cyclohexane and **d** in water. **e.** Fluorescence intensity measurements of BSA NCs encapsulating different NPLs ratios in cyclohexane and **f** after redispersion in water. Synthesis and fluorescence intensity measurement were performed by Maire-Luise Frey.

The average hydrodynamic radius (R_h) of the capsules with the different NPL loadings in cyclohexane is 153 ± 9 nm (Figure 2.3.1 b), where the NCs without NPLs have the smallest R_h (141 ± 83 nm), while NCs with the 1:10 ratio of NPLs revealed the largest capsule R_h (163 ± 88 nm). These results point out, that BSA NC formation is not significantly influenced by the presence of NPLs. After transfer to the water phase we observed a moderate increase of the capsule radii ranging from 172 nm (without NPLs) to 218 nm (at a NC:NPL ratio of 1:1). The light scattering results clearly show the similarity of the NCs at the different NPL loadings with regard to size distribution. Zeta potentials were negative for all NCs (Figure 2.3.1 b).

Cryo-TEM images confirmed the spherical core-shell morphology of the capsules in both phases (Figure 2.3.1 c-d), revealing contrast-rich NPLs encapsulated inside the NCs. Imaging in water phase showed contrast-poor objects indicating the gel-like appearance of the BSA NCs in water (Figure 2.3.1 d). Cryo-TEM confirmed that by encapsulating a 5:1 ratio of NPLs into NCs, every NC contains at least one NPL.

We analysed the fluorescence intensity of the BSA NCs in cyclohexane (Figure 2.3.1 e) and in water (Figure 2.3.1 f), revealing the fluorescence emission maximum at 646 nm in both cases. As expected, the measured fluorescence intensity increases with increasing NPL concentration. After transfer to water, the capsules were again subjected to fluorescence intensity measurements, demonstrating similar fluorescence intensities for the 10:1 and the 5:1 ratio and a low fluorescence intensity for the 1:1 ratio. These observations corroborate, that excess NPLs, which were not encapsulated, were removed during the water transfer process. In addition, we confirmed successful loading of the NPLs to the NCs by fluorescence quenching of fluorescein isothiocyanate (FITC) attached to the capsule surface.^[176] The fluorescence quenching of the FITC increases with the number of encapsulated NPLs, which suggests Förster resonance energy transfer (FRET) to the NPLs. Previous studies of FRET with NPLs^[177, 178] determined Förster radii of just a few nm, indicating close proximity of the NPLs to the FITC attached to the thin capsule shell. This indicates, that the NPLs stay close to the capsule walls, rather than freely disperse outside or inside the capsule, where fluorescence quenching via FRET from the FITC to the NPLs would be less likely. In addition, we did not observe NPLs in the supernatant of aqueous capsule dispersions, but the NPLs were always associated within the BSA NCs. Based on these findings, we continued with cell experiments using BSA NCs prepared at a 5:1 ratio.

In order to study the uptake behaviour of the BSA NCs, RAW264.7 macrophages were exposed to BSA NCs for 1 h (Figure 2.3.2). We analysed time-dependent cell uptake by confocal laser scanning microscopy (cLSM). Cells were treated with BSA NCs (75 $\mu\text{g}/\text{mL}$, + FBS) and identified by means of their fluorescence emission. We visualised lysosomal cell compartments using LysoTracker™ Green (Figure 2.3.2 a) and correlated the measured fluorescence intensities to the BSA NCs signal (Figure 2.3.2 b-c). The LysoTracker™ Green DND-26 marker stains acidic compartments, thus marking endolysosomal membranes.

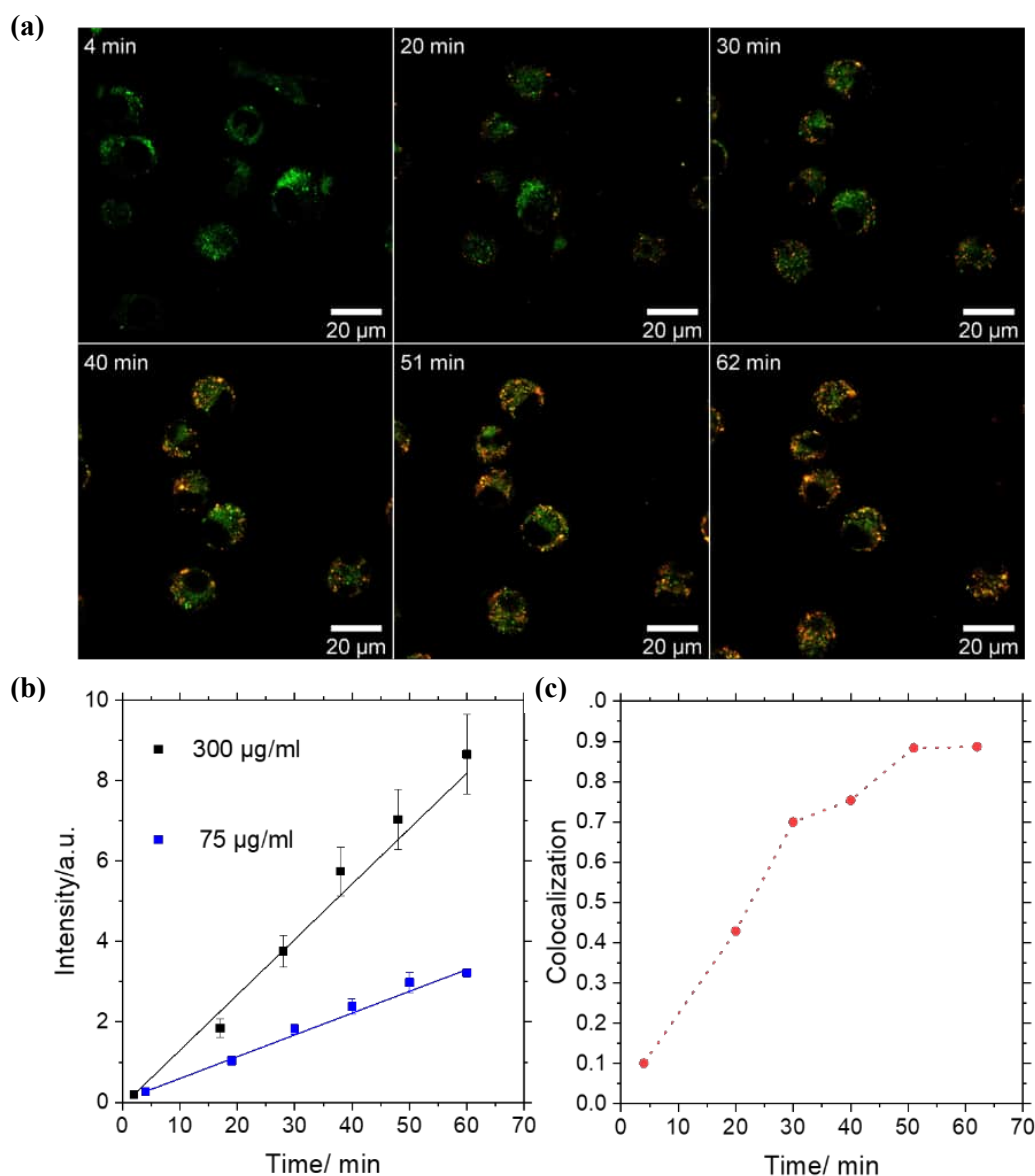


Figure 2.3.2 Cell uptake experiments of NPL loaded NCs (5:1) into RAW264.7 macrophages.

a. Live cell imaging by confocal laser scanning microscopy (cLSM) of macrophages stained with LysoTracker™ Green after the uptake of NCs (NPL displayed in red) at a concentration of 75 µg/mL. **b.** Time-dependent increase of detected fluorescence intensity of NPLs encapsulated in BSA NCs in RAW264.7 macrophages. **c.** Time-dependent correlation of overlapping fluorescence signals obtained from the cLSM data **a** of the cell uptake of BSA NCs into macrophages determined by Manders (M2) coefficient. The M2 coefficient shows the fraction of NPLs that colocalised with endosomes/lysosomes. It ranges between 0 and 1.

We observed a low amount of intracellular NPLs after 4 min of incubation time, with almost a linear increase in uptake during the next 62 min for high (300 $\mu\text{g/mL}$) and low (75 $\mu\text{g/mL}$) NC loadings (Figure 2.3.2 a-b). The NCs were transported during that time from the membrane into the cell where they gradually colocalise with endosomes/lysosomes marked by LysoTracker™ Green.

Shortly after the uptake, there is almost no colocalisation of the NPLs with LysoTracker since they were not yet transferred to the acidic compartments like late endosomes/lysosomes. Within the first 30 min, the fraction of NPLs that are found in late endosomes/lysosomes linearly increases. Despite linear uptake of NPLs with time over 60 min, we stopped live cell imaging to avoid phototoxicity having an impact on the uptake process. The M2 colocalisation coefficient levels off after about 50 min (Figure 2.3.1 c). Considering a continuous uptake of NCs, this levelling off can be interpreted as a reduction of endosome maturation to lysosomes or may indicate endosomal escape as NCs were continuously taken up (Figure 2.3.1 b). Moreover, TEM images are used to corroborate this hypothesis.

To analyse NCs trafficking inside the cell, we incubated RAW264.7 macrophages with BSA NCs loaded with water-dispersible NPLs (5:1) at a concentration of 300 $\mu\text{g/mL}$. We exposed the macrophages to the NCs for 2 h, to ensure sufficient and continuous uptake, washed them to stop the uptake. Subsequently, they were allowed to ripe for another 24 h to allow processing of the NCs inside the cells (ripening time).

We performed CLEM on 100 nm sections to precisely localise intracellular BSA NCs in high resolution after incubation of BSA NCs with RAW264.7 macrophages. The precise high resolution identification of the BSA NCs via the TEM localisation of the NPLs (Figure 2.3.3) showed that cell integrity was well maintained and the fluorescence from NPLs was clearly detected in cLSM even after the harsh electron microscopy preparation with OsO₄, UA and embedding in an epichlorohydrin derived epoxy resin (EPON) (Figure 2.3.4).

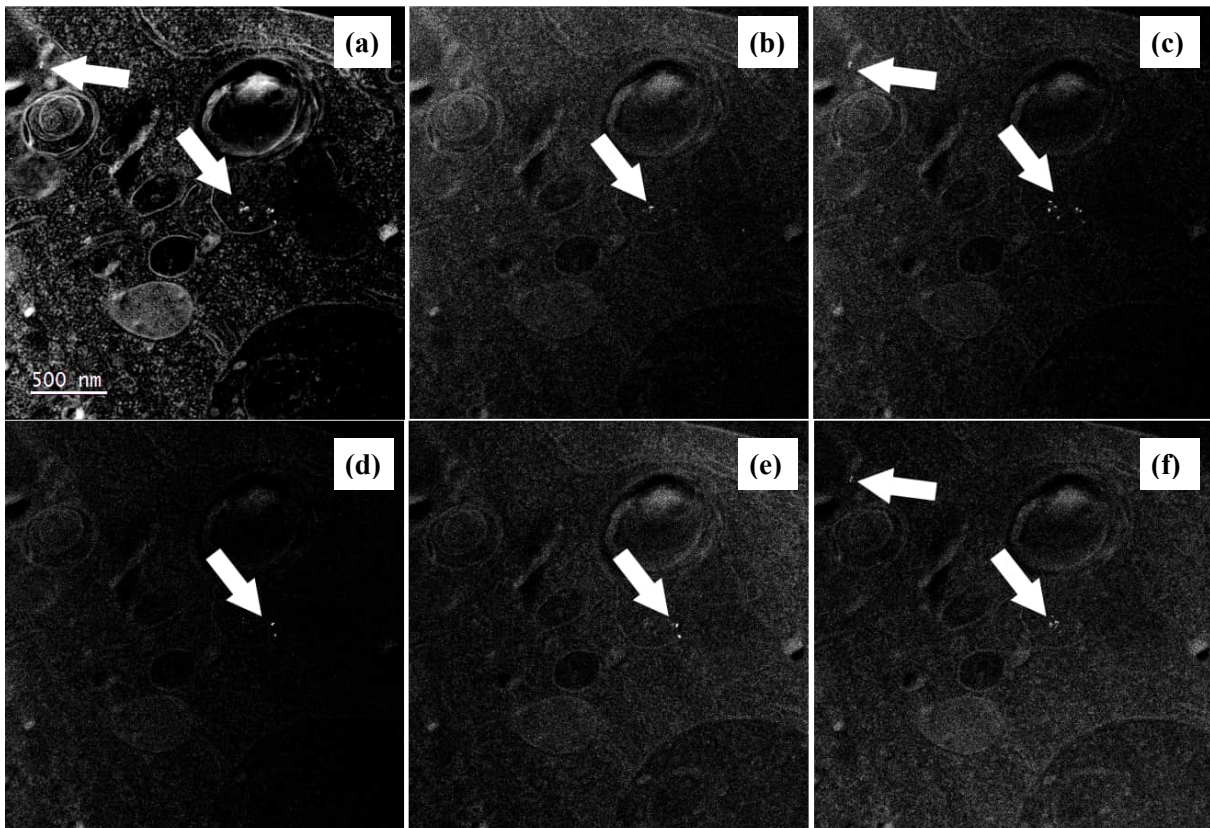


Figure 2.3.3 Finding the NPLs using TEM darkfield methods. The azimuth angle of the beam tilt is changed in steps of 30° resulting in different NPLs lighting up, some of them marked by white arrows (Figures **b-f**, with azimuth beam tilt angles of 0°, 30°, 60°, 90° and 120°, respectively. The 150° dark field micrograph is not displayed. The addition of all the individual dark field micrographs yields the localisation of most of the NPLs in the field of view **a**.

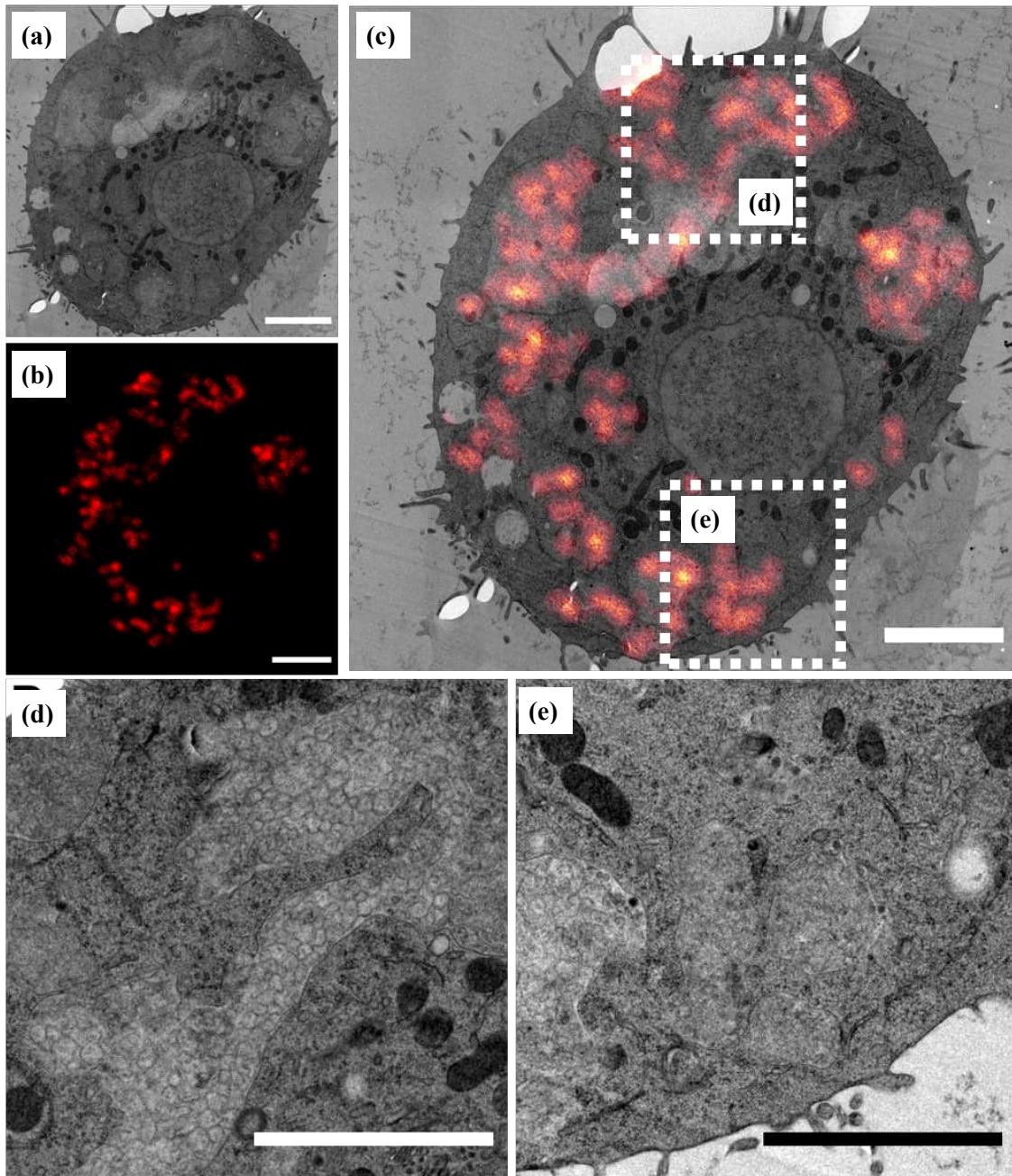


Figure 2.3.4 CLEM micrograph of BSA NCs containing NPLs (5:1) in RAW264.7 macrophages after 2 h uptake + 24 h ripening (300 μg/mL). **a.** Electron microscopy micrograph of one macrophage with internalised BSA NCs; **b.** Fluorescence microscopy micrograph of the same macrophage in **a.** **c.** CLEM overlay of **a** and **b.** **d.** and **e.** Zoomed in area of **c** showing BSA NCs in an enlarged vesicle and a late endosome. Scale bars: 2 μm.

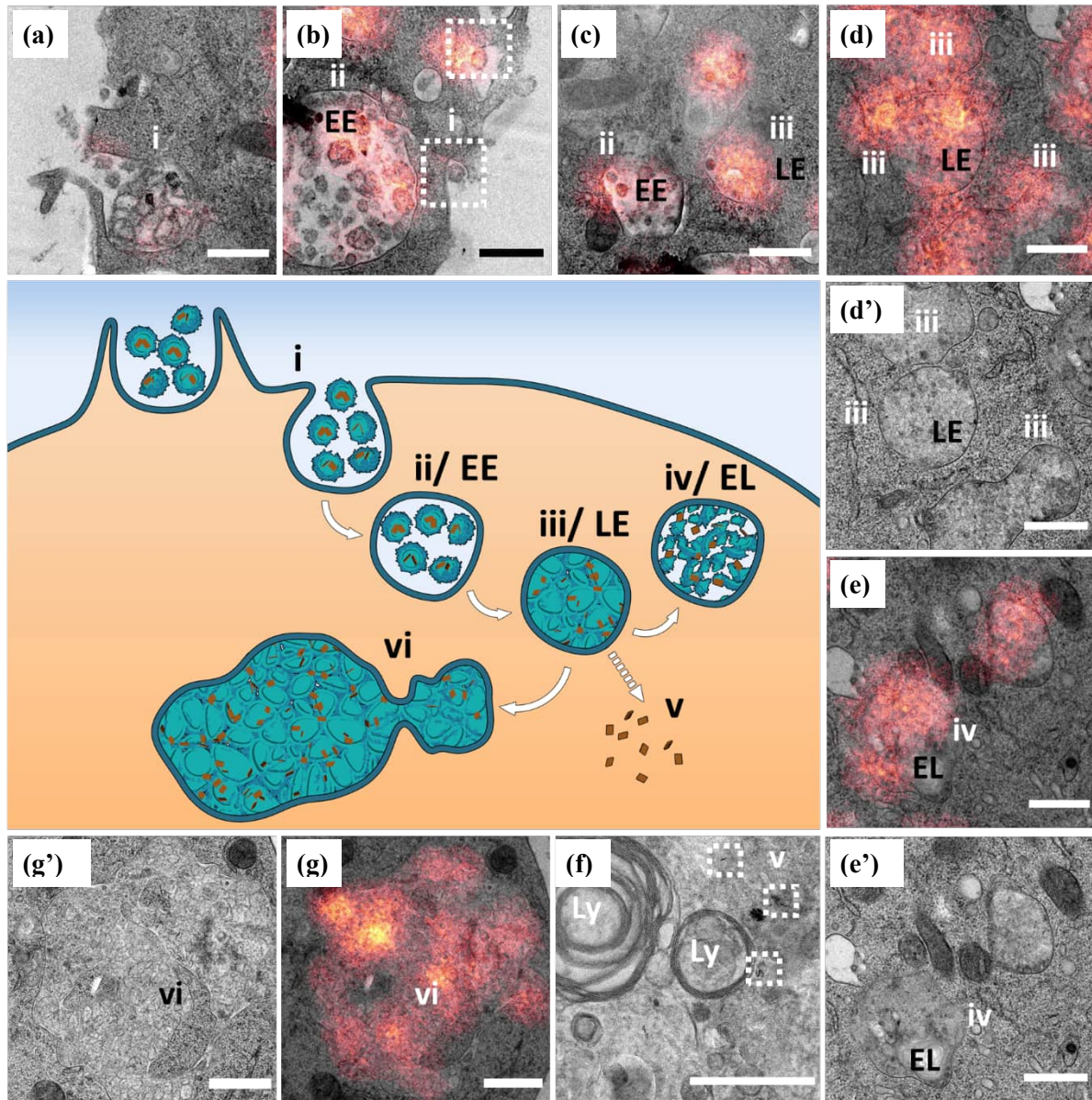


Figure 2.3.5 Intracellular fate of BSA NCs by TEM micrographs. **a.** Uptake event (i) of BSA NCs in a cell captured after 2 h incubation. **b.** Uptake event (i) and early endosome (ii/EE) of BSA NCs captured after 2 h incubation. **c.** Early endocytosis of BSA NCs (ii) and a late endosome (iii/LE) with BSA NCs after 2 h incubation + 24 h ripening. **d.** Late endosomes (LE) with BSA NCs visible after 2 h incubation + 24 h ripening. **e.** Degradation of BSA NCs in an endolysosome (iv/EL) after 2 h incubation + 24 h ripening. **f.** Escaped NPLs (v) captured after 24 h ripening. Ly: lysosome **g.** Enlarged endosome with BSA NCs at high concentration (300 $\mu\text{g}/\text{mL}$) after 2 h incubation + 24 h ripening **d'**, **e'** and **g'** correspond to the same respective EM images without fluorescence correlation. Scale bars: 500 nm.

We analysed the uptake of the nanocapsules into a macrophage in detail by TEM (Figure 2.3.4 a) and fluorescence microscopy (Figure 2.3.4 b). Superimposing the EM (a) with the fluorescence microscopy micrograph (b) yields the CLEM micrograph (Figure 2.3.4 c). The bright fluorescence from the NPLs helps to unambiguously facilitate the localisation of BSA NCs in the cell. The NCs are distributed over the whole cell except for the nucleus. We clearly localised different parts of the macrophage exhibiting accumulations of BSA NCs (d and e) showing a high fluorescence intensity. Here, the electron micrographs reveal irregular shaped vesicles which are packed with BSA NCs (Figure 2.3.4 d) as well as late endosomes, in which the structural identity of the NCs is no longer clearly recognisable (Figure 2.3.4 e). These findings indicate, that the NCs are processed by the cell in different manners: On the one hand there was a high accumulation of NCs in irregularly shaped, large vesicles (d) and on the other hand a degradation of the NCs (e). We captured the different processing mechanisms by varying the ripening time of the BSA NCs inside the macrophages at 2 h uptake + 0 h ripening time and 2 h uptake + 24 h ripening time. Based on our findings, we can reconstruct the processing pathway and therefore follow the track of the BSA NCs inside the cells (Figure 2.3.5).

Within the first 2 h of incubation, we observe the uptake of BSA NCs into RAW264.7 (Figure 2.3.5 a (i) and Figure 2.3.6). During this incubation phase, all events which take place during the first 120 min interval of uptake can be observed. During the incubation time we can also observe early endosomes (EE) with NCs (Figure 2.3.5 b (ii) and Figure 2.3.7). These findings are consistent with the cLSM images revealing that within one hour a colocalisation of NPLs with endolysosomal compartments occurred (Figure 2.3.2 e). To enable further processing of the NCs in the cells, we performed a ripening phase to complete the observation of the NCs' processing. During the 24 h ripening phase, we found BSA NCs in EE and also in densely packed late endosomes (LE) (Figure 2.3.5 c (ii), (iii) and Figure 2.3.8). The integrity of the BSA NCs was maintained at the early stage of endocytosis, while they started to lose their integrity since the acidic environment in endolysosomal compartments enables the conditional degradation of the NCs (Figure 2.3.5 d (iii) Figure 2.3.9 a').^[179] Some LE were found fusing with lysosomes forming endolysosomes (EL) (Figure 2.3.5 e (iv) and Figure 2.3.10) where the shape integrity of the NCs was not observed anymore. The missing integrity is particularly visible in images Figure 2.3.5 d', 2.3.4 e'. The respective fluorescence overlays (Figure 2.3.5 d-e) confirm that the endosomes contained capsules with NPLs as the endosomes appear highly fluorescent. These results indicate that the shell of the BSA NCs was impaired within 24 h by enzymatic and acidic conditions in endolysosomal compartments, which are normally revealing a dark contrast, like lysosomes, in TEM micrographs.^[180] These findings are supported by previously reported observations of fully degradable protein-NCs enabling cargo release upon enzymatic cleavage leading to CD86 upregulation of bone-marrow derived dendritic cells.^[181] Only at high concentrations (300 µg/mL) we found enlarged endosomes filled with NCs (Figure 2.3.5 g/g'(vi) and Figure 2.3.11) revealing the capsule integrity (Figure 2.3.9 b'). We conclude from these findings, that at high capsule loadings, endosomal compartments fuse to enlarged endosomes with a big storage capacity of the NCs. The maintained capsule integrity may be explained with the pH value in the large endosomal vesicles. There, the pH is not sufficient to degrade the capsules and NCs are hindered from moving further along the pH gradient with increasing acidity. This observation indicates a kind of blockade of the degradation pathway.

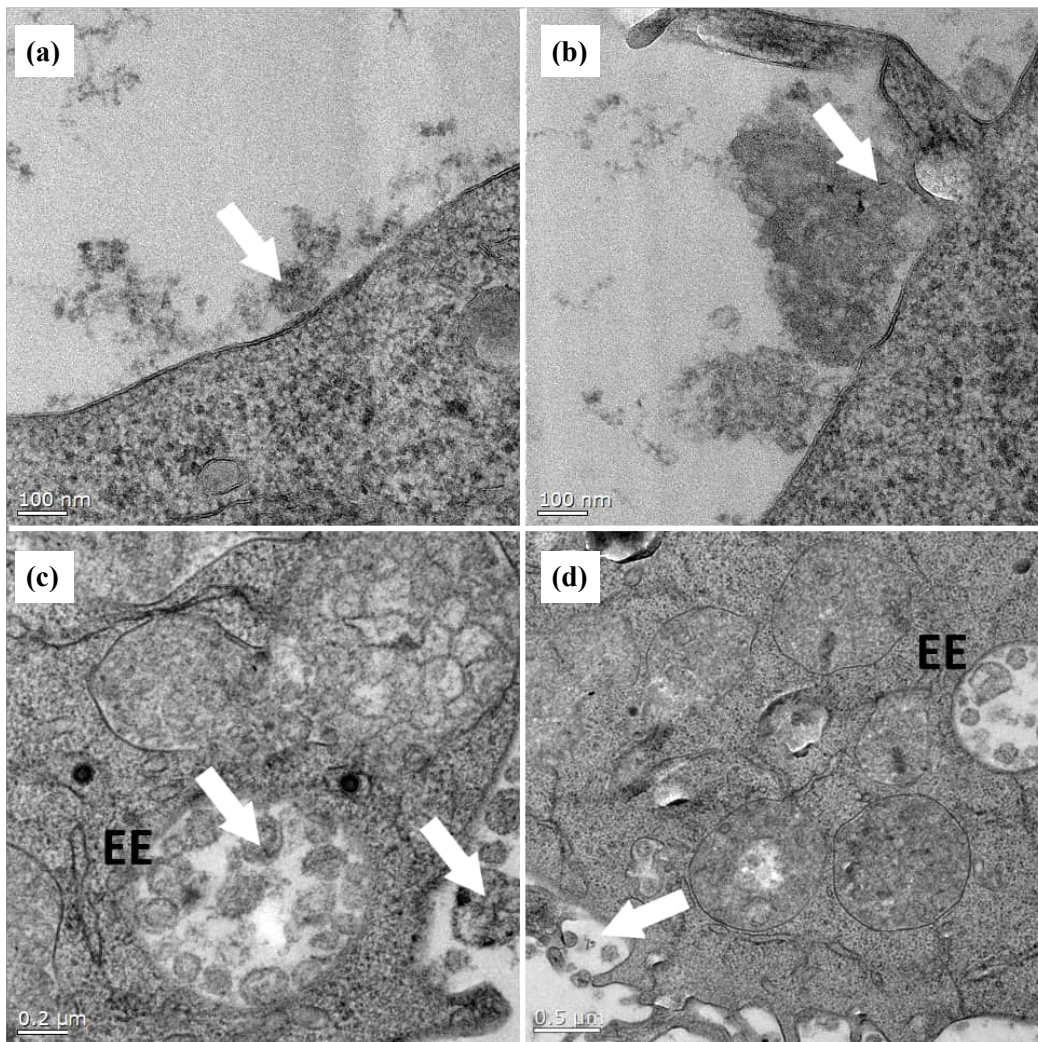


Figure 2.3.6 TEM micrographs illustrating the uptake process (event i in Figure 2.3.5). **a** and **b** show the cell after 10 min incubation with 75 $\mu\text{g}/\text{mL}$ NC concentration. **c** and **d** are snapshots after 2 h incubation at 300 $\mu\text{g}/\text{mL}$ BSA NC concentration. The arrows indicate some of the NPs in the micrograph, showing the location of the BSA NCs.

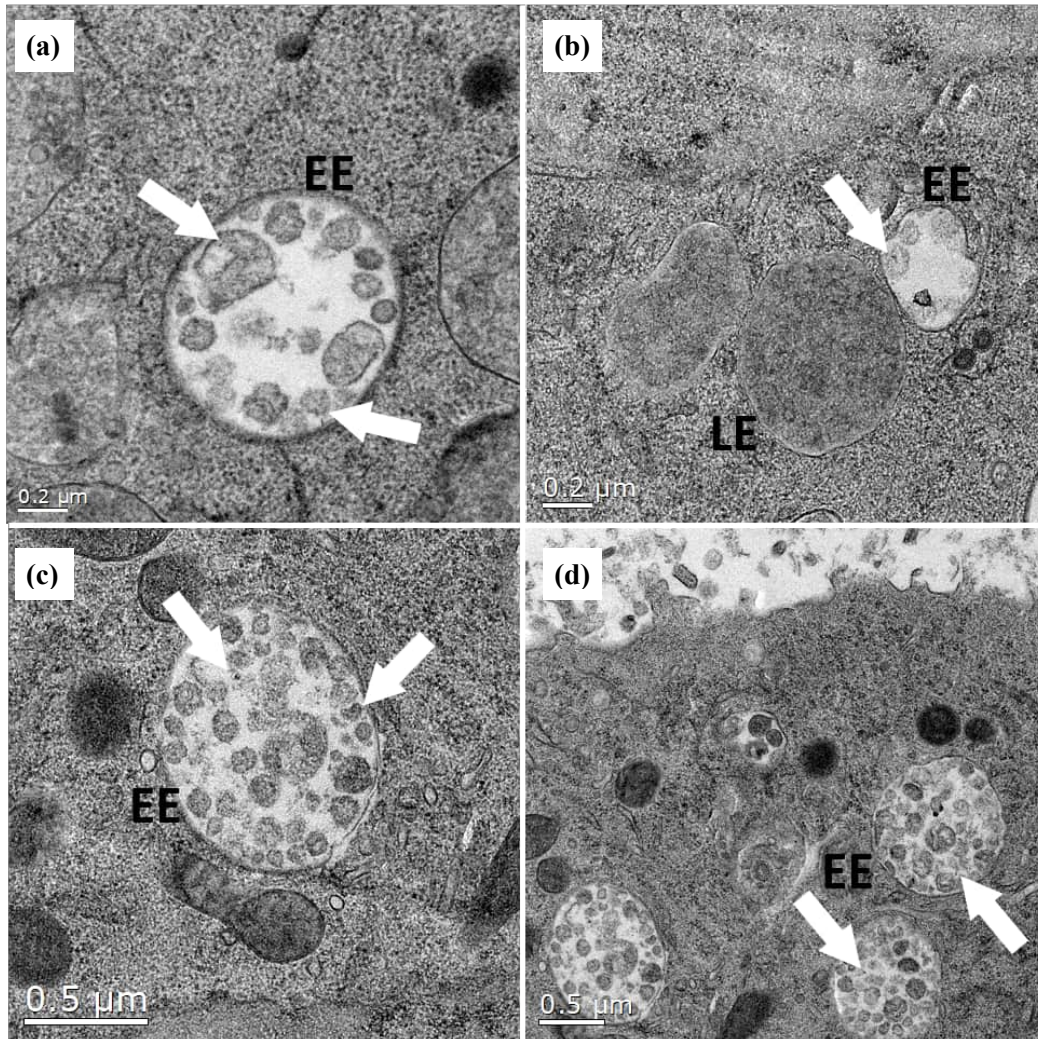


Figure 2.3.7 TEM micrographs showing examples of early endosomes (EE, event ii in Figure 2.3.5). **a** and **b** show the cell after 2 h incubation at 300 μg/mL NC concentration. **c** and **d** are snapshots after 2 h incubation at 75 μg/mL BSA NC concentration. The arrows indicate some of the NPs in the micrographs, showing the location of the BSA NCs.

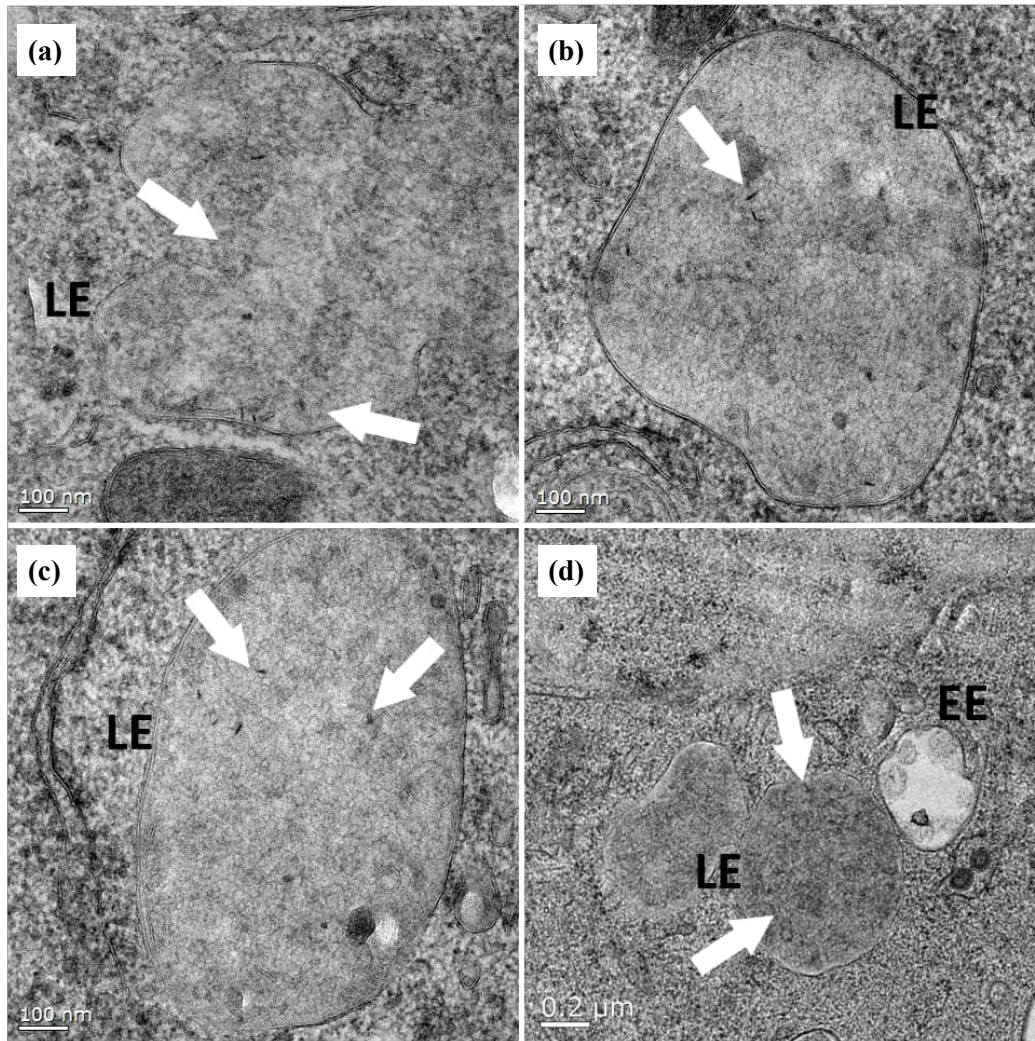


Figure 2.3.8 TEM micrographs showing examples of LE endosomes (LE, event iii in Figure 2.3.5). **a** and **d** show the cell after 2 h incubation at 75 µg/mL NC concentration. **b** and **c** are snapshots after 2 h incubation at 75 µg/mL BSA NC concentration followed by 24 h ripening. The arrows indicate some of the NPs in the micrographs, showing the location of the BSA NCs.

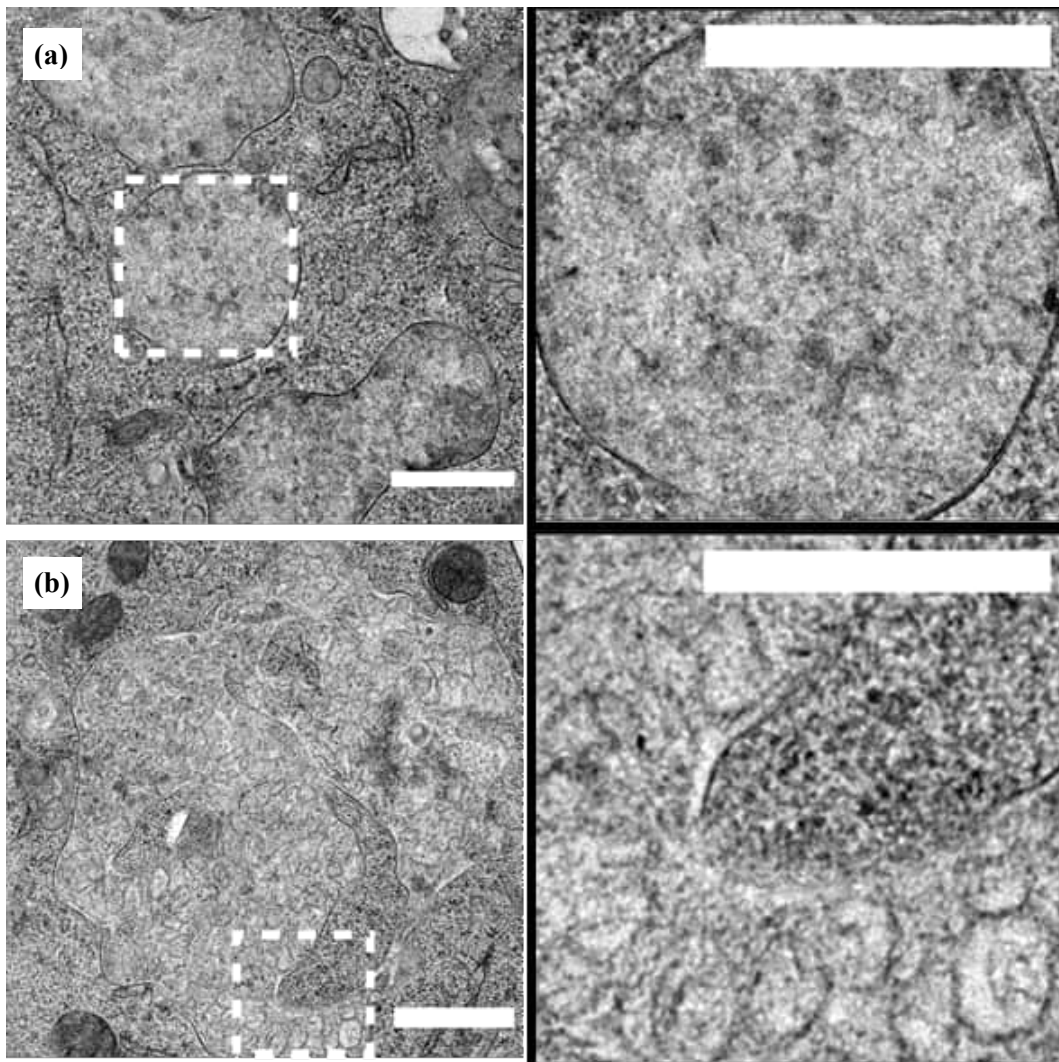


Figure 2.3.9 Zoom-in image to show the integrity of the BSA NCs. **a.** Corresponding image of Figure d'. **b.** Corresponding image of Figure 2.3.5 g'. Scale bars: 500 nm.

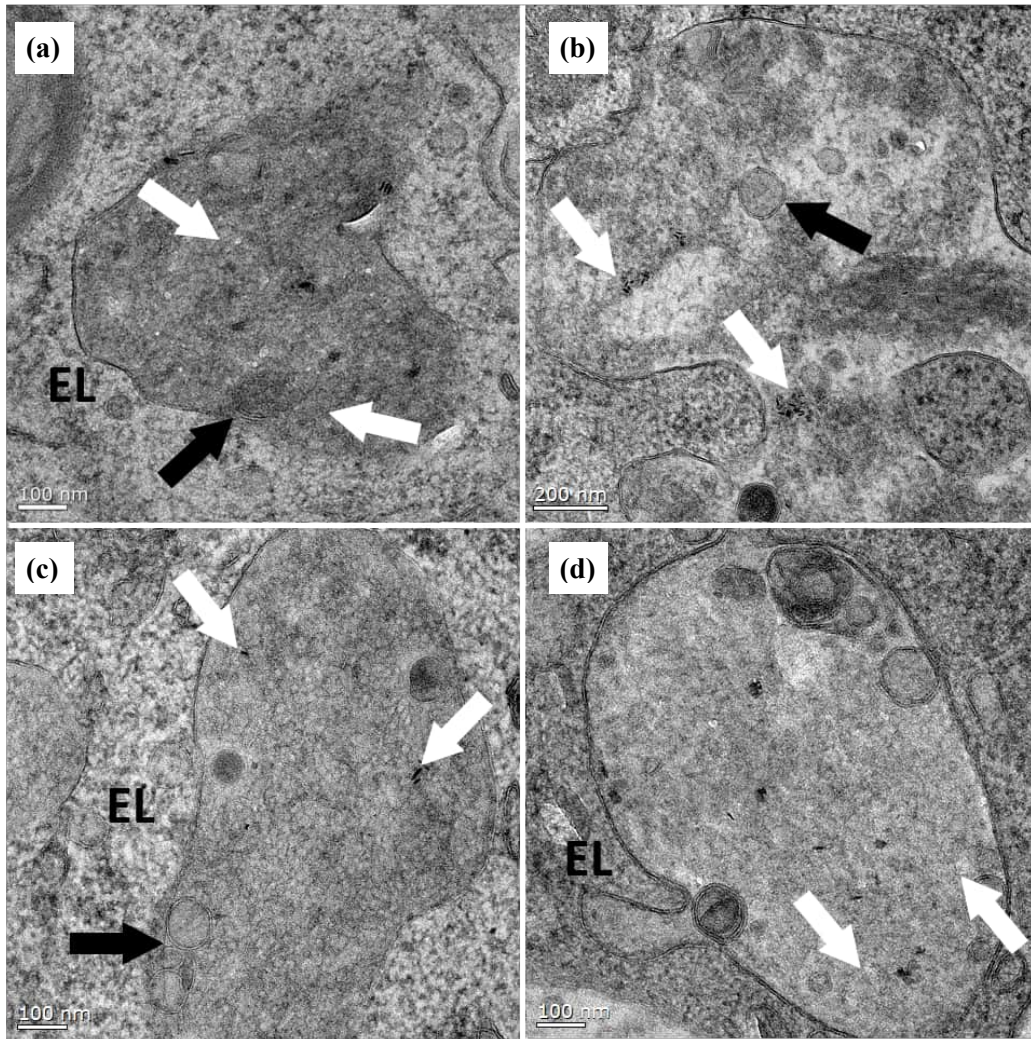


Figure 2.3.10 TEM micrographs showing examples of endolysosome (EL, event iv in Figure 2.3.5). **a.** shows the cell after 2 h incubation at 300 µg/mL NC concentration. **b.** same as A but with additional 22 h ripening time. **c.** was prepared at a concentration of 75 µg/mL with 2 h incubation and 24 h additional ripening. **d.** same as C but at 300 µg/mL NC concentration. The white arrows indicate some of the NPs in the micrographs, showing the location of the BSA NCs. Black arrows indicate membrane structures within the EL.

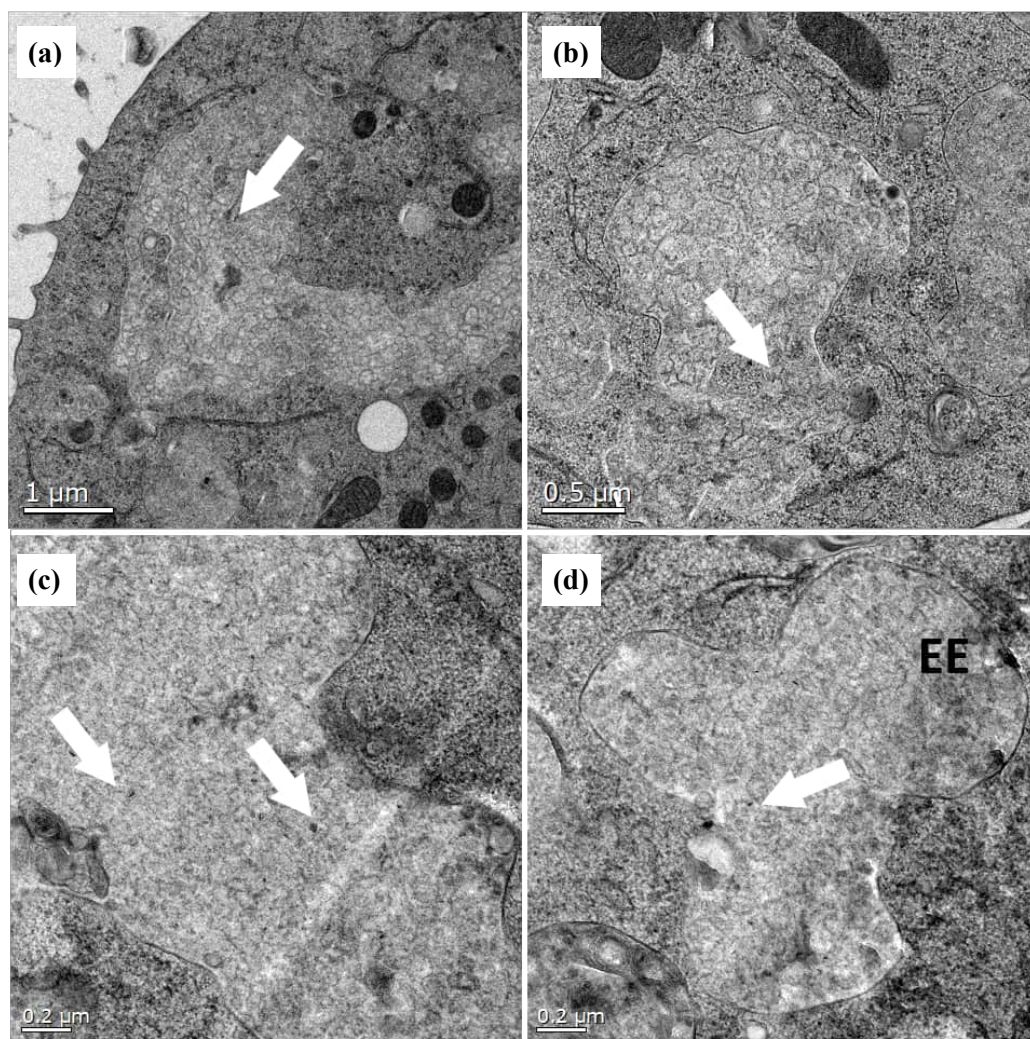


Figure 2.3.11 TEM micrographs illustrating the enlarged endosome (event vi in Figure 4). **a** and **b** show the cell after 2 h incubation with 300 µg/mL NC concentration, followed by 22 h ripening. **c** and **d** are snapshots after 2 h incubation at 300 µg/mL BSA NC concentration and 24 h ripening time. The arrows indicate some of the NPs in the micrograph, showing the location of the BSA NCs.

In some cases, we observed NPLs in the cytosol (Figure 2.3.5 f (v)). Since no freely diffusing NPLs were found neither in TEM images nor in the performed FRET experiments, this finding is concluded to be an endosomal escape. This result is supported by the observation that the shell of the NCs degraded during endolysosomal processing and therefore releasing NPLs upon ripening.

Conclusions

We demonstrated that NPL containing NCs were detected and unambiguously localised in different endolysosomal compartments by CLEM. The encapsulation of the NPLs into biocompatible NCs was accomplished without disturbing the NC formation and damaging the NPLs' properties, obtaining a stable dispersion with high fluorescence intensity. We were able to adjust different NPL concentrations inside the NCs and obtained reproducible size distributions. The bright fluorescent signal in the cLSM examinations indicated that the NCs were taken up and incorporated into the macrophages used for the uptake experiments. From the CLEM data we could identify the different cell compartments containing the NCs. In this way, we could not only determine the timing of endolysosomal colocalisation, but also trace the NCs in each compartment. We show that the NCs are processed at three different locations upon the endolysosomal pathway: The NC shell was impaired in late endosomes, indicating degradation, the NCs were stored in large endosomes at high capsule concentrations revealing an intact shell, and we observed an endolysosomal escape which is crucial for the successful delivery of a potential drug encapsulated inside the BSA NCs. The findings are very important for future research on cell uptake mechanisms and may reveal the metabolic pathway of an encapsulated drug.

2.4. Correlative microscopy to visualise polymeric nanoparticles in cells

Localising intracellular polymeric nanoparticles (NPs) is of great importance to understand the fate of nanomedicine and the most powerful way to visualise intracellular NPs is by using electron microscopy (EM). However, it is commonly agreed that the organic dyes which are used to label NPs lose their fluorescence after harsh EM preparation, impeding powerful applications such as correlative light and electron microscopy (CLEM). Here I demonstrate a straightforward CLEM approach to image the fluorescence from the organic dyes and meanwhile maintaining excellent subcellular structures without omitting OsO₄ and UA.

Visualisation plays a predominant role in monitoring intracellular activities. In particular, in the field of drug delivery, characterisation of nanoparticles relies massively on microscopic imaging. However, unlike inorganic NPs (e.g. gold particles, quantum dots), polymeric NPs are usually round-shaped, non-fluorescent and low electron dense material with sizes up to 150~200 nm,^[1] meaning that visualising them in cellular environment can be very challenging.

Generally, conventional fluorescence light microscopy (FLM) is used to gain the insight of NPs in cellular processes. In order to facilitate the imaging process, NPs as well as necessary cellular compartments need to be labelled with organic dyes to give off fluorescence. Accordingly, localisation of different fluorescence signals instantly provides relevant information making FLM a relatively straightforward imaging method. However, despite the direct and easy imaging process offered by conventional FLM, resolution is nevertheless restricted to ≈ 200 nm.^[42] Another drawback is that the unlabelled cellular environment always remains unseen, which hinders further investigation of other valuable NPs-cell interactions. Last but not least, depending on the labelling efficiency, small amounts of free dye could remain after the synthesis of NPs and the fluorescence signal from the free dye can be easily misinterpreted as labelled NPs because the resolution in conventional FLM is not enough to distinguish free dyes from labelled NPs. Although thanks to the recently developed super-resolution (SR) techniques, resolution in FLM is greatly improved and even realising single-particle tracking,^[128, 129] application of SR to more general samples still remains a challenging task. To overcome the resolution inadequacy of FLM, electron microscopy (EM) with a much higher resolution is the method of choice. On one hand, due to the equal staining of all subcellular surroundings and the use of electrons as illumination source, EM provides

unmatched details and resolution compared to FLM. On the other hand, EM only provides static and monochromatic images, which inhibits the chances to study real-time interactions and to use fluorescence as markers. Without the help of fluorescent labels, it is even harder to distinguish other round structures (e.g. caveolae, exosomes) from NPs in cells. However, despite obvious limitations, visualisation of polymeric NPs in cells is still mainly relying on EM up to date.^[45, 46]

The ideal way to precisely image NPs in cells is to combine two microscopic techniques. Correlative light and electron microscopy (CLEM) incorporates the strength of FLM and EM, which subsequently provides precise localisation of fluorescent NPs on a highly resolved EM image, which is not executable in only one microscopic technique. Ideally, the most precise way to perform CLEM is by acquiring fluorescence and EM image on the same section.^[56, 121] However, the challenge to perform a same-section CLEM approach on fluorescent NPs is to retain the fluorescence after the harsh EM sample preparation while preserving the fine ultrastructure of the cell. In the field of CLEM, there is a general assumption that fluorescence does not survive with the presence of OsO₄ and EPON embedding. Because OsO₄ is a strong oxidiser which holds responsibility for fluorescence quenching in fluorophores and fluorescence proteins (FPs) ^[182] while EPON is a highly cross-linked resin that requires polymerisation at high temperature which tends to destroy fluorophores ^[182] in spite of the better cellular preservation.^[183] Most studies focus on FPs for CLEM, but synthetic fluorophores offer wider spectrum in favour of FLM and versatility in labelling especially for NPs in cellular environment.

In this current study, we introduce straightforward on-section CLEM approaches to image intracellular polymeric NPs. It is the first time to report visualisation of polymeric NPs in cells by high precision CLEM. Fluorescence from NPs is successfully retained after EM sample preparation and cellular structures are perfectly preserved with reasonable amount of OsO₄ and UA staining and finally embedded in EPON resin.

Results and discussions

In order to have an initial understanding of how much EM preparation procedure affect the fluorescence signal of organic dyes, we performed a simple cLSM imaging for several cellular staining dyes after being treated with 1 % OsO₄ and 4 % UA and EPON resin because these are the concentrations we use for staining after room temperature fixation (method for in-dish CLEM preparation, chapter 2.2). We concentrate on the observation of how OsO₄ and EPON influence the fluorescence quantum yield, since they are supposed to be the key factors for fluorescence fading. As shown in Figure 2.4.1, after treatment of OsO₄, most of the signal is still linked to the target compartment, but the dye also starts to diffuse throughout the cell and into nucleus. After embedment in EPON, Phalloidin (actin staining), Mitotraker Red (MTR, mitochondria), and CellMask DeepRed (CMDR, cell membrane) lose their affinity with specific cellular compartments, Sytox Green (nucleus) still is found inside the cell nucleus. We also found that UA contributes around 2 to 16 fold less to fluorescence fading than OsO₄ (Table 2), except for Sytox Green. In contrast to the other dyes tested, Sytox Green is more sensitive to the presence of UA. It can only be speculated, that the localisation in the cell nucleus protects the Sytox Green from the agitation of the OsO₄.

Despite the results from live imaging, the measurements were carried out only 15 min after incubation of OsO₄ which is a significantly less amount of time compared to freeze substitution (up to several days). Therefore, a longer incubation time with OsO₄ might lead to a higher level of fluorescence quenching. Needless to say that polymerised EPON resin would most probably quench the fluorescence even more because of its highly crosslinked nature. However, this simple cLSM imaging measurement provides an initial overview of how OsO₄ and EPON can influence the fluorescence during the preparation process.

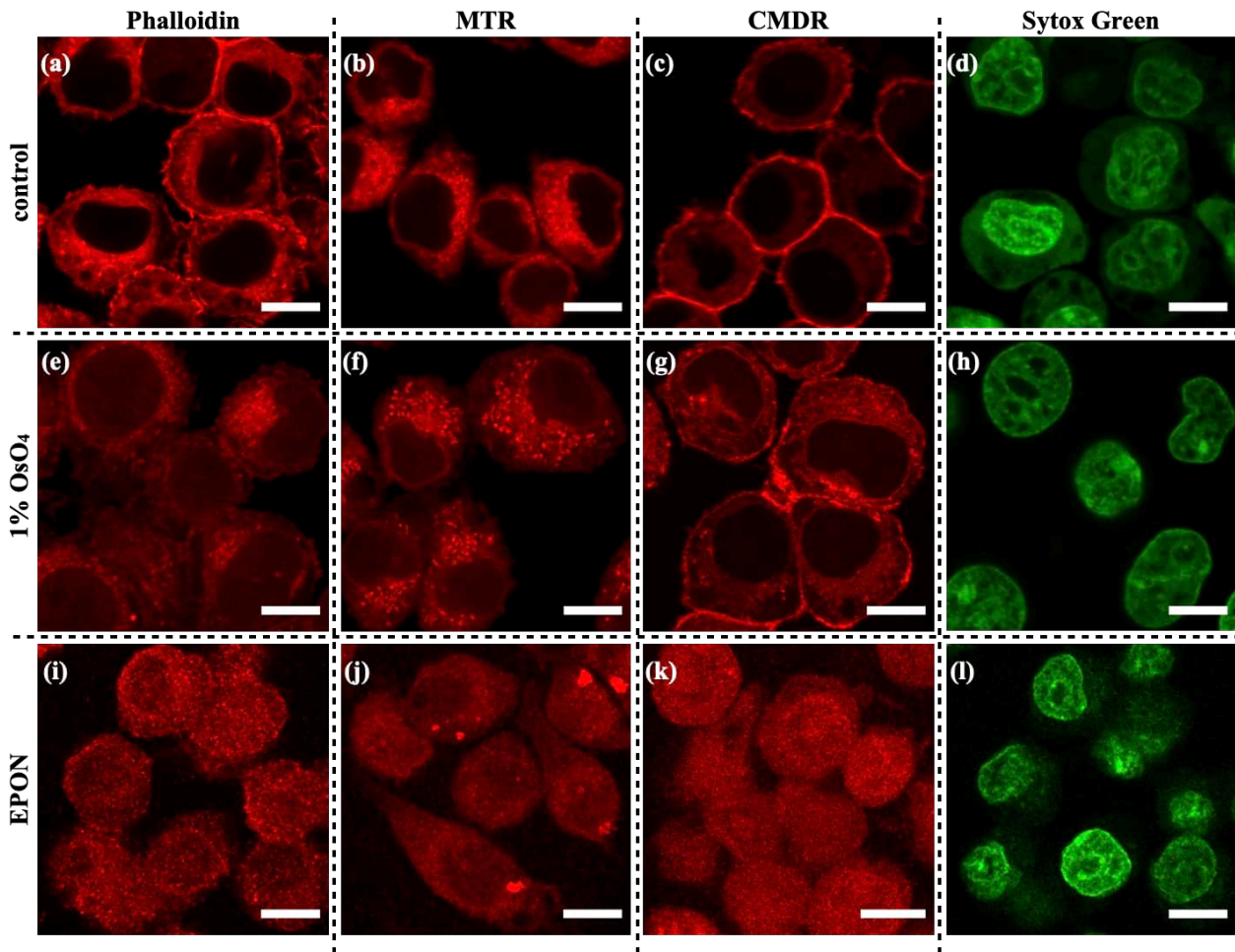


Figure 2.4.1 Different dyes under 1 % OsO₄ treatment and embedment in EPON. **a,e,i.** Phalloidin stained actin filaments in RAW264.7 macrophages in control group, then after 1 % OsO₄ for 15 min, and finally embedded in EPON. **b,f,j.** Mitotracker Red stained mitochondria in RAW264.7 macrophages undergoing the same treatments as previous. **c,g,k.** Cellmask DeepRed stained plasma membrane in RAW264.7 macrophages. **d,h,l.** Sytox Green stained cellular nucleus in RAW264.7 macrophages. Scale bars: 10 μ m.

Table 2. Loss of fluorescence intensity from different dyes under OsO₄ and UA treatment.

	Phalloidin	MTR	CMDR	Sytox Green
Intensity decrease after 1% OsO ₄ by factor	33	43	14	~4
Intensity decrease after 4% UA by factor	2	3	5,5	~10
Intensity decrease in total by factor	66	129	77	~40

To initially test NPs for CLEM visualisation, we co-incubated PS NPs with HeLa cells. After co-incubation, NPs were washed and replaced with new cell medium. Cells were then chemically fixed and stained with 1 % OsO₄ and 4 % UA. After gradient dehydration in ethanol, cells were embedded in EPON and cured in the oven as previously described in the “in-dish” CLEM method. [121] After being sectioned and imaged, fluorescence from PSNP (labelled with BODIPY dye) was successfully retained on the section after OsO₄ and UA staining and after EPON embedding (Figure 2.4.2 a). However, the drawback of this method is that cellular structures are sometimes not perfectly preserved by chemical fixation. As shown in Figure 2.4.2 c-d, the cell nucleus was preserved after the fixation, but other membrane-based organelles were not. Moreover, PS NPs could not be easily distinguished without the help of the fluorescence.

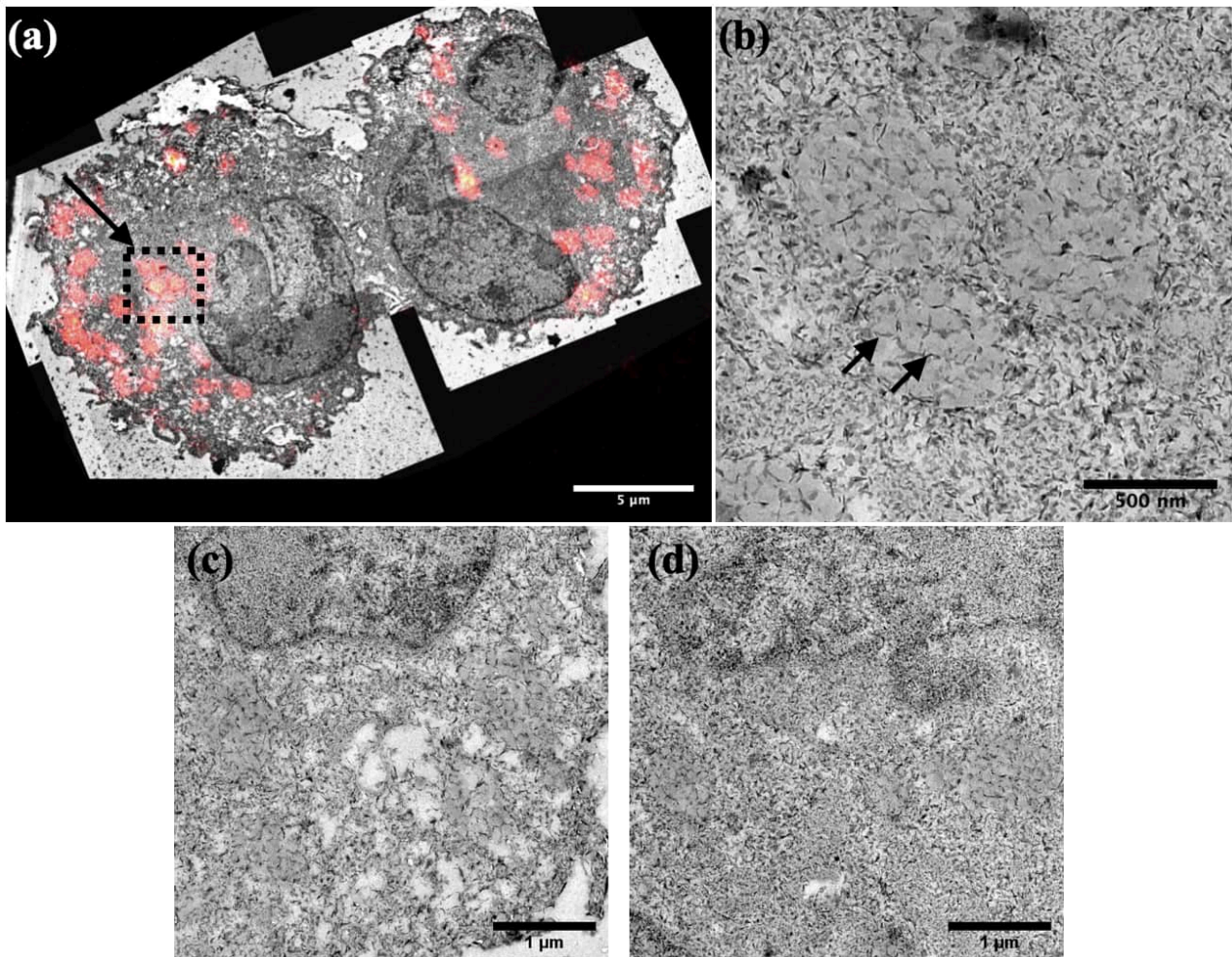


Figure 2.4.2 In-dish CLEM of PS NPs in HeLa cells. **a.** CLEM overview of two HeLa cells with PS NPs prepared by chemical fixation using EPON embedding and OsO₄ staining. Red: fluorescence signal of the PS NPs due to the labeling with BODIPY. **b.** Zoom-in image of the area marked by the black square in **a** showing the PS NPs. **c.** and **d.** Bad preservation of the cellular structures. PS NPs are indicated with arrows.

To optimise and achieve a better cellular structure preservation in EM, we replaced the initial fixation by high pressure freezing (HPF). Firstly, macrophages were cultivated and co-incubated with NPs on sapphire discs for high pressure freezing and transferred in liquid nitrogen (Figure 2.4.3). Since fluorescence from BODIPY were already successfully retained after 1 % OsO₄ and EPON embedding, standard freeze substitution (FS) cocktail containing 0.2 % OsO₄ and 5 % water [184] was used for a better cellular structure preservation using a longer incubation time. After being embedded in EPON and cured at 60 °C, the cells in the resin block were initially checked by cLSM

to ensure that the fluorescence is retained. Resin blocks were then trimmed and later sectioned into ultrathin sections (around 100 nm) for further cLSM and EM imaging (Figure 2.4.3).

In order to achieve the best imaging condition for both microscopes, we examined two substrates for section transfer suitable for different EM approaches (Figure 2.4.3). For the TEM approach, sections were transferred onto carbon-coated copper finder grids and inspected by LM and EM subsequently. BODIPY-labelled PS NPs and Cy5-labelled hydroxyethyl starch nanocapsules (HES NCs) were successfully localised by CLEM with the TEM approach (Figure 2.4.4). For the SEM approach, sections are transferred onto ITO coated glass coverslips. Sections on the coverslip were first imaged by cLSM with recording some landmark positions and were then transferred to the SEM for imaging the same regions of interest (ROI). Since SEM enables a larger field of view, multiple sections can be transferred onto one coverslip. Both, PS NPs and HES NCs were precisely visualised by CLEM with SEM approach using this method (Figure 2.4.5).

Both approaches, using SEM as well as TEM, can be used to precisely localise fluorescently labelled NPs/NCs using CLEM. The advantage of the TEM approach is its intrinsically higher resolution. However, the SEM approach provides adequate resolution for most membrane-bound organelles like mitochondria, Golgi apparatus (GA) and endoplasmic reticulum (ER) (Figure 2.4.5 e). Anyway, sub-nanometer resolution is usually not necessary for cellular EM imaging. Therefore, the resolution of TEM does not pose more advantages than SEM in this case. Moreover, the possible specimen size and the field of view in the SEM are much larger than for TEM, making the searching of the targeted cells from cLSM much easier and applicable.

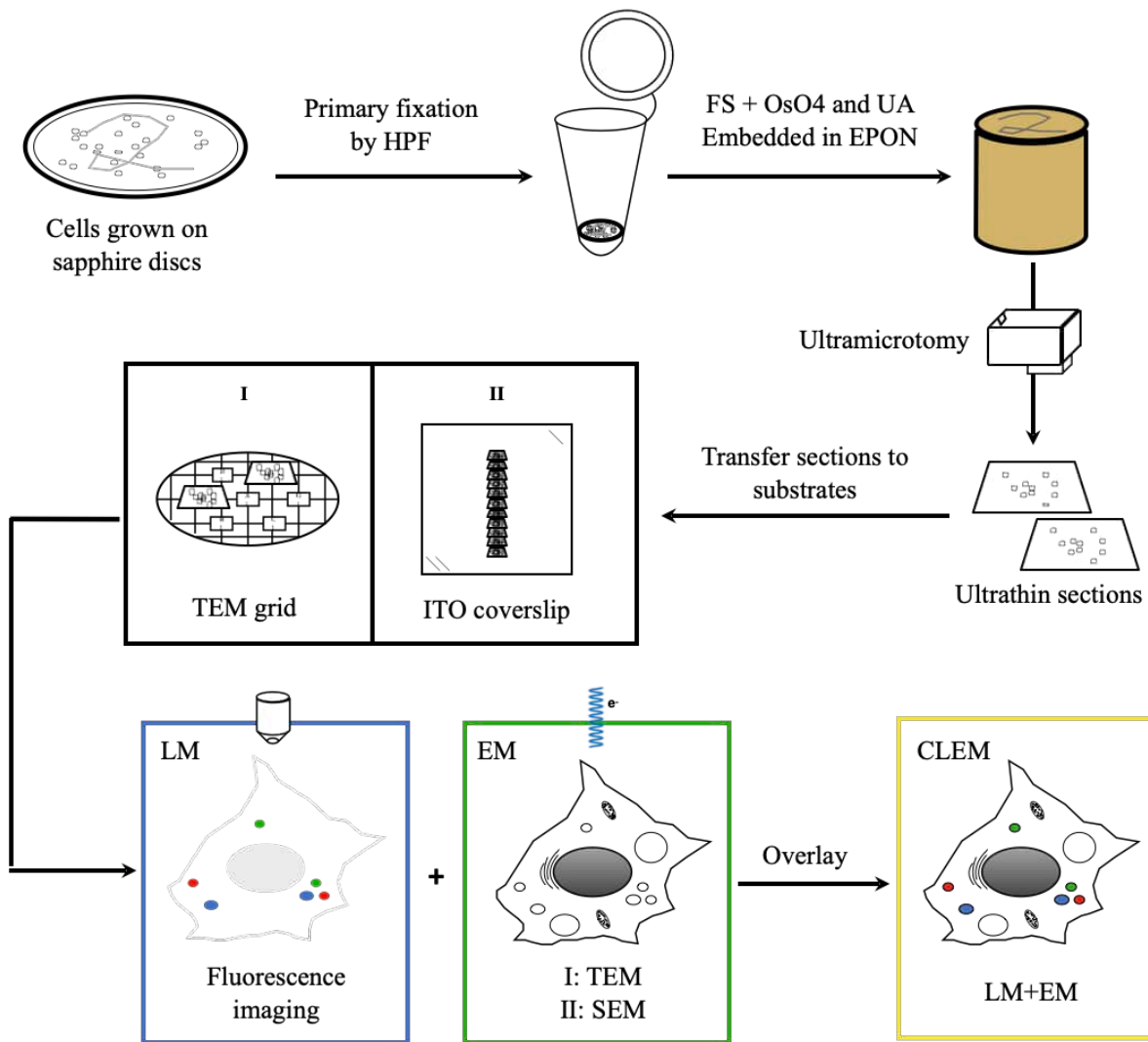


Figure 2.4.3 CLEM workflow using HPF preparation with OsO₄ and UA staining followed by embedding in EPON. Starting with the cells grown on a sapphire disc followed by HPF and FS, the cells are embedded in an epoxy resin, that is going to be sectioned using an ultramicrotome. After ultramicrotomy, the ultrathin sections were transferred to ITO coverslips for SEM inspection or to TEM grids for TEM inspection. Images from LM and EM were later overlaid manually to create the final CLEM image.

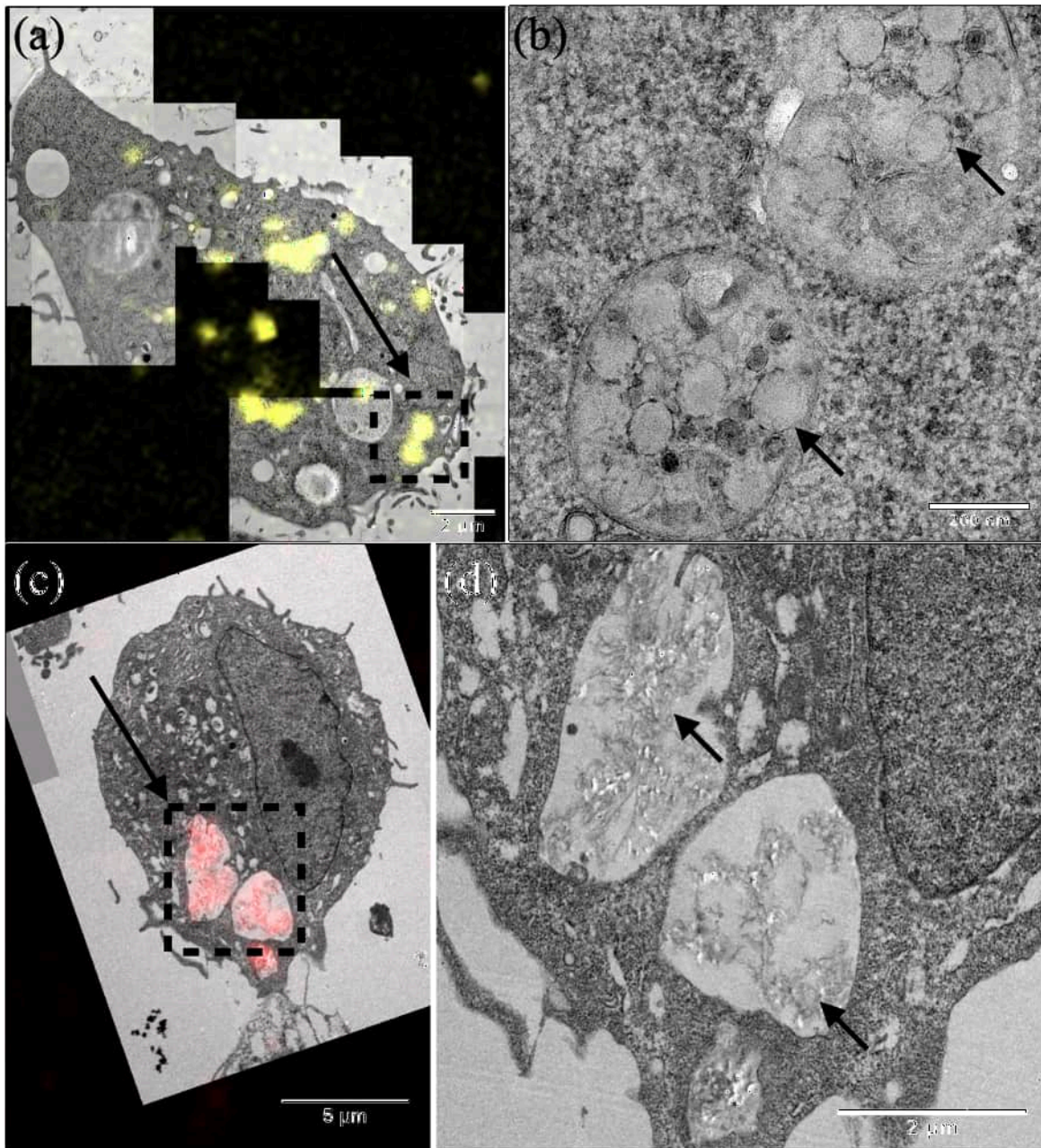


Figure 2.4.4 CLEM micrographs using the TEM approach visualizing different polymeric nanoparticles in RAW264.7 macrophages. **a,c.** CLEM overviews of macrophages containing PS NPs (yellow, a) and HES NCs (red, c). **b.** Zoom-in image of the marked area in (a) showing the PS NPs in endosomes. **d.** Zoom-in image of the marked area in (c) showing HES NCs in endosomes. NPs/NCs are indicated with arrows.

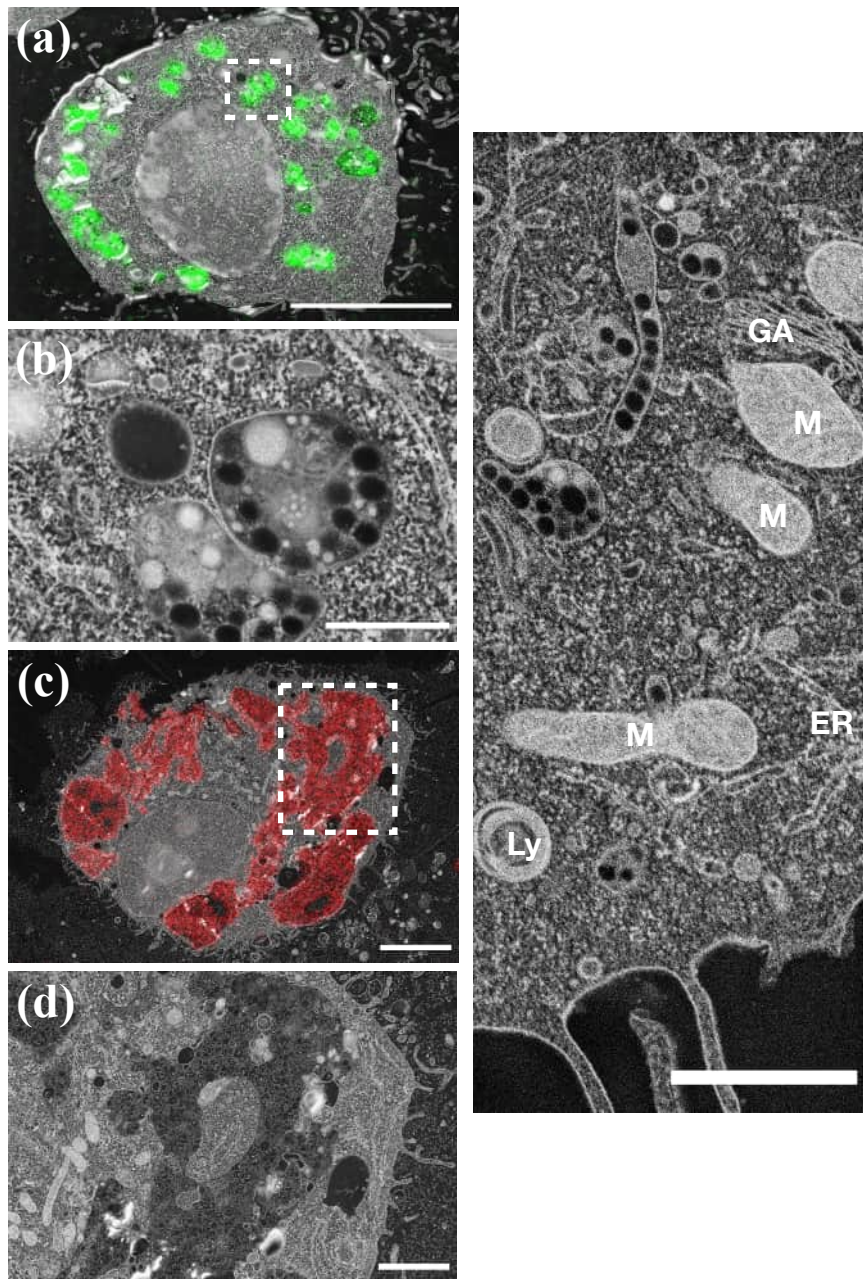


Figure 2.4.5 CLEM micrographs demonstrating the SEM approach to visualise different polymeric nanoparticles in RAW264.7 macrophages. **a,c.** CLEM overviews of macrophages containing PS NPs (green, a) and HES NCs (red, c). **b.** Zoom-in micrographs of the marked area in **a** showing the PS NPs in endosomes. **d.** Zoom-in micrograph of the marked area in (c) showing HES NCs in endosomes. **e.** SEM micrograph of cellular structures, Golgi apparatus (GA), mitochondria (M), lysosomes (Ly), endoplasmic reticulum (ER). Scale bars: a,c: 2 μm . b,d,e: 500 nm.

Visualisation using the TEM approach was performed on copper finder grids. EPON sections were first placed onto the finder grids and then imaged by cLSM accordingly. Finder grids were previously coated with a formvar film and a thin carbon layer for later EM investigation. Interestingly, carbon coated grids were sensitive against the excitation laser even at low power (around 7 %). In order to test the influence of carbon layer on fluorescent detection, on-section Sytox Green was used because it survives the EM preparation (Figure 2.4.6) and the relatively large area of nucleus staining enables a more pronounced observation. As shown in Figure 2.4.7 a-c, fluorescence in the EPON section can easily be bleached while being imaged (Figure 2.4.7 c). The fluorescence intensity of Sytox Green from the same sample was around three times higher on ITO-coated coverslip than on carbon-coated finder grids by using the same excitation intensity of 20 % (Figure 2.4.8). Therefore, imaging the fluorescence signal via the SEM approach is more efficient than with the TEM approach and hence less precaution is needed for the fluorescence fading.

Besides the differences for fluorescence imaging, sections on ITO-coated coverslips also provided clearer cell outline including the nucleus than the sections on the EM grids in the reflection channel of the cLSM (Figure 2.4.7 d, Figure 2.5.7 e). The clear nucleus structures help to facilitate the positioning and registration of the landmarks in SEM and ensures a precise overlay of LM and EM data.

We suspected that the fast bleaching on carbon-coated EM grids might be due to the light adsorption induced temperature raise of the carbon layer. The carbon layer efficiently adsorbs the laser photons and transfers their energy into heat. Because the EPON sections were placed directly on the carbon layer, the heat transferred from the energy of the laser beam was directly transported from the carbon layer to the sections, and eventually induces the bleaching of the fluorescence. On the other hand, the ITO thin layer is transparent and hence very resistant against light induced temperature rise,^[185] the laser-induced heat is less and it can easily be transported within the ITO layer and eventually prevents the rapid bleaching of fluorescence. Moreover, the heat stability of ITO-coated coverslips also enabled the use of higher laser power which provided stronger emission fluorescence intensity. The clearer nucleus structures obtained by sections on ITO-coated coverslip might due to close adherence of the sections to the glass substrates, the flatness of the sections ensured the stable focal length and eventually guaranteed sharper images.

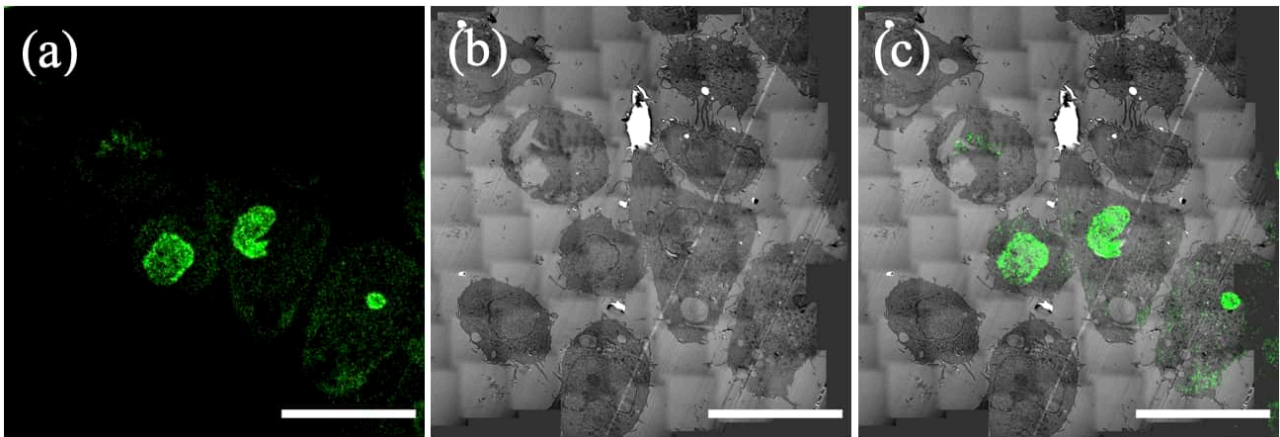


Figure 2.4.6 Sytox Green in EPON section. (a). Fluorescence image of on-section Sytox Green. **b.** EM image of same area in **a.** **c.** Overlaid CLEM image of **a** and **b.** Scale bars: 20 μm .

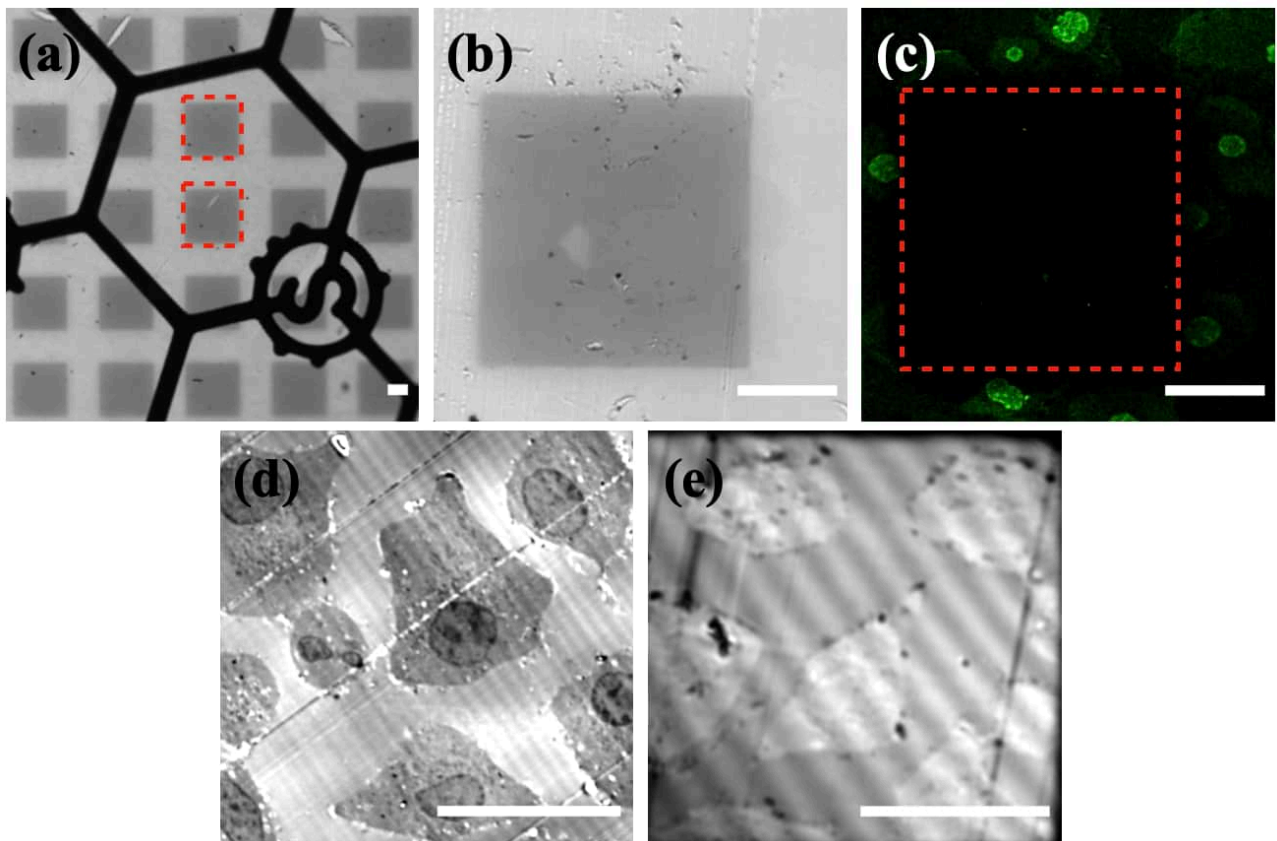


Figure 2.4.7 Fluorescence imaging conditions on carbon coated TEM grids and ITO coated coverslips. **a.** Demonstration of carbon coated EPON section on a TEM copper finder grid in confocal LM, carbon coated areas are highlighted by red boxes. **b.** zoomed-in image to the carbon coated area. **(c)** fluorescence channel of Sytox Green on the same area as in **b**, carbon coated area is highlighted by a red box. Due to the carbon coating, the fluorescence signal is gone whereas in the uncovered areas, outside the red box, there still is a clear fluorescence signal of the Sytox Green. **d.** Reflection channel in confocal LM of an EPON section on ITO coated coverslip. Cellular outline and nucleus can be clearly identified. **e.** Reflection channel in confocal LM of an EPON section on

a carbon coated TEM grid. Here, do to the mechanical unstable support, the focus length is hardly to be kept constant and hence the image is blurred. Scale bars: 20 μm .

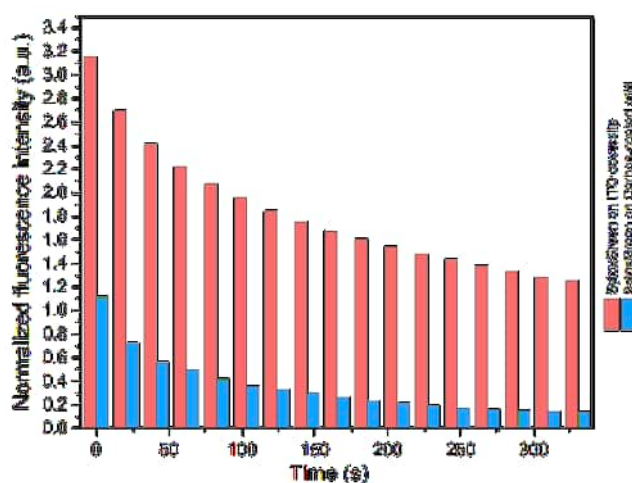


Figure 2.4.8 Comparison of normalised fluorescence intensity of Sytox Green on ITO coverslips and on carbon coated TEM grids.

To achieve a successful imaging by CLEM, the fluorescence images are of great importance. For the fluorescence imaging in our CLEM routine, an avalanche photodiode (APD) was used instead of photomultiplier tubes (PMTs) in the Leica SP5 cLSM. APDs are photodetectors which provides very low noise ratio ^[186] and are sensitive down to single-photon level by amplifying the received photon into many electrical charges.^[187] Moreover, during fluorescence detection by APD, an addition dichroic beam splitter (DBS) is applied in front of the detector to surpass most scattered light in order to emphasise the desired fluorescence signal. Scattered light generated at the air interface of the EPON section can create a strong image background. Applying the APD with DBS can efficiently filter out the reflected and scattered light compared to the prism-based PMT detection because the prisms are still able to create scattered light at the interface of the glass and air and eventually projected onto the detector.

For SEM imaging, the backscattered electron (BSE) detector was mainly used to visualise the cellular structures on the sections. The information of the cells is contained in the staining only and hence a signal providing a high electron density contrast is best to image the ultrathin sections. The intensity of the BSE electrons is proportional to the square of the atomic number of the specimen and hence provide an excellent contrast for heavy metal stained soft material. The backscattered electrons (BSE) provide a deeper penetration depth and their intensity scales only with the atomic number of the specimen.^[188, 189] Therefore, information within the EPON section can be revealed clearer with BSE detector than with a secondary electron (SE) detector.^[190]

Conclusions

In this study, we demonstrated precise on-section CLEM methods to visualise intracellular polymeric NPs for the first time. With two different EM approaches, NPs were precisely localised in cells. The SEM approach provided more convenience and flexibilities in sample positioning and fluorescence imaging. Despite the minor drawbacks during fluorescence imaging, TEM approach still remains to be a faithful routine for high resolution CLEM. The establishment of precise CLEM for intracellular polymeric NPs not only enables the study within nanometer resolution but also increases the precision to investigate subcellular interactions. Meanwhile, although our study only focused on room temperature CLEM, with the rapidly developed cryo-EM technique, much faithful information can be unraveled in hydrated state. Within cryo-condition, even NPs with extremely soft shells can be revealed. We strongly believe that with the application of CLEM technique more valuable intracellular fate of different NPs can be revealed and the study of nanomedicine can be greatly facilitated.

2.5 In-cell separation of the protein corona from nanoparticles and snapshots of how it evolves intracellularly

This section is based on a manuscript under preparation.

This section used the optimised CLEM workflow described in the previous section to visualise organic dye labelled protein corona and polymeric NPs in cells. It also explores the use of CLEM to understand the intracellular fate of the protein corona and how they evolve after being internalised in cells.

Potential title: In-cell separation of the protein corona from nanoparticles and snapshots of how it evolves intracellularly

Author list: Shen Han, Richard da Costa Marques, Johanna Simon, Anke Kaltbeitzel, Volker Mailänder, Ingo Lieberwirth and Katharina Landfester

I performed the CLEM experiments, volume CLEM experiments, image processing including alignment and reconstruction and manuscript writing. Johanna Simon performed the labelling of the protein corona with Cy5, cellular uptake experiments, flow cytometry, SDS PAGE and LC-MS experiments. Richard da Costa Marques analysed, drawn and integrated the data from flow cytometry, SDS PAGE and LC-MS experiments and manuscript writing. Anke Kaltbeitzel analysed the fluorescence colocalisation. Ingo Lieberwirth, Volker Mailänder and Katharina Landfester supervised and wrote the manuscript.

For any medical application of nanoparticles (NPs), we have to consider that they are subjects of complex and diverse interactions with cells. Among these interactions, many NPs are taken up and internalised by cells.^[45] However, before they are able to interact with cells in a biological environment, many NPs interact with proteins and other biomolecules once they are introduced into a biological environment.^[125] A coat of biomolecules adsorbs instantaneously on most NPs due to their high surface free energy, termed biomolecular corona or protein corona.^[191] Indeed, the protein corona alters the chemical identity of NPs and changes it to a biological identity that can impact blood circulation,^[192] cellular uptake,^[193, 194] and cytotoxicity.^[195] Recently, the work on NPs has expanded from its interaction with biological fluids to its impact on cellular uptake and finally to their intracellular effect^[196, 197], trafficking^[198], and fate.^[199]

However, it remains unclear how cellular processes alter the protein corona and how long it persists on the surface of the NPs within the cell. Previous studies have highlighted the dynamic nature of the protein corona and the continuous exchange of the adsorbed proteins after the transition of the NPs to different protein-containing media. These studies demonstrate the exchange of proteins in both, single protein solutions^[200] and complex protein mixtures.^[201] The protein exchange of the protein corona occurs also within the confined subcellular environment after internalisation of the NPs with a distinct protein corona composition.^[197] A previous study has approached the intracellular destiny of the protein corona by confocal laser scanning microscopy (cLSM) showing the internalisation of the NP together with the PC in A549 cells, followed by subsequent lysosomal degradation.^[199] These studies rely on staining distinct subcellular compartments in separate staining procedures. By combining fluorescence staining techniques with the highest achievable resolution in electron microscopy, termed correlative light and electron microscopy (CLEM), we provide unbiased information about the subcellular fate of NPs and the protein corona.

Here, we demonstrate the co-internalisation and the subsequent in-cell separation of the protein corona from the NP in murine macrophages by combining cLSM with electron microscopy (EM). To realise a trackable protein corona, we fluorescently labelled murine plasma proteins and formed a fluorescent protein corona on NPs. For the first time, we performed single-cell volume CLEM to visualise the protein corona and the NPs within the cell with high resolution and faithfully reveal their subcellular location and fate by fluorescence.

After co-internalisation of the fluorescently labelled NPs and the protein corona, we observe a distinct decrease of both fluorescence signals over time and a local separation of the NP from the PC signal in cLSM. We further visualise the separation of NPs and protein corona after 24 h in CLEM snapshots and by volume CLEM analysis we witness a clear distribution of separated protein corona and NPs. Ultimately, the NPs and protein corona are enriched in morphologically different compartments, namely recycling endosomes (REs) and multivesicular bodies (MVBs), followed by possible exocytosis of the separated NPs and protein corona.

Results and discussions

In order to form the protein corona and study its fate after cellular internalisation, we synthesised carboxyl-functionalised polystyrene nanoparticles (PS NPs). The synthesised PS NPs were stabilised with Lutensol AT50. Their average diameter is at 116 nm with a zeta potential of -7.21 mV. We labelled the murine plasma proteins with Cy5 by NHS-chemistry and formed the protein corona on the NPs with both, unlabelled and labelled proteins (Figure. 2.5.1).

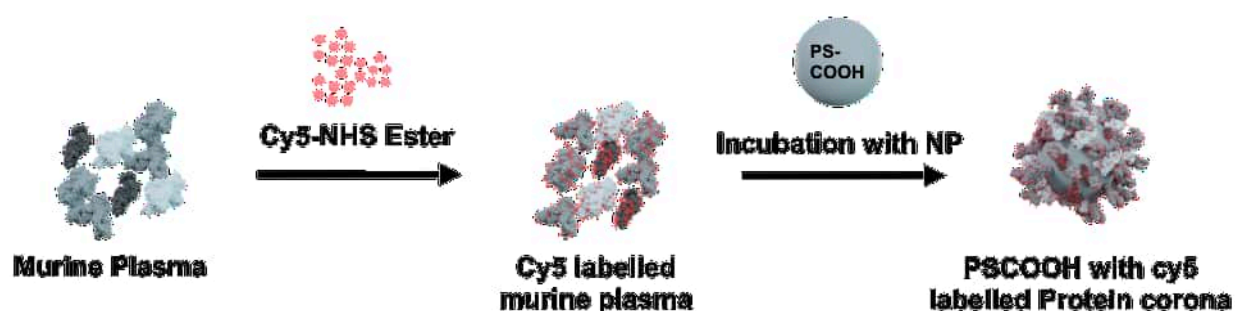


Figure 2.5.1 Scheme of murine serum Cy5 labelling and protein corona formation on PSCOOH nanoparticles.

Subsequently, we characterised the composition of the unlabelled and labelled plasma and protein corona to show possible differences after fluorescent labelling. Unlabelled and labelled samples, respectively, showed minor differences in band pattern on the SDS-PAGE (Figure 2.5.2 a). To further detail the protein composition, we employed quantitative LC-MS measurements. Overall, the protein composition remained similar after the Cy5-labelling. Noticeable changes in the protein composition of the murine plasma were an ~ 1.2 fold increase of serum albumin, a ~ 6 fold decrease of immunoglobulin kappa, and a ~ 1.5 fold decrease of serotransferrin after labelling. In the case of the protein corona samples, we measured a ~ 1.8 fold enrichment of apolipoprotein A1 and a ~ 1.8 fold enrichment of beta-2 glycoprotein 1 was observed but generally complement C1q subunits were decreased 2.7 fold to 3.6 fold, respectively (Figure 2.5.2 b). Nevertheless, the differences in protein composition before and after labelling for the plasma and protein corona were considered minor. We, therefore, assumed that the labelling would not alter the outcome of a fluorescently labelled protein corona compared to an untreated protein corona.

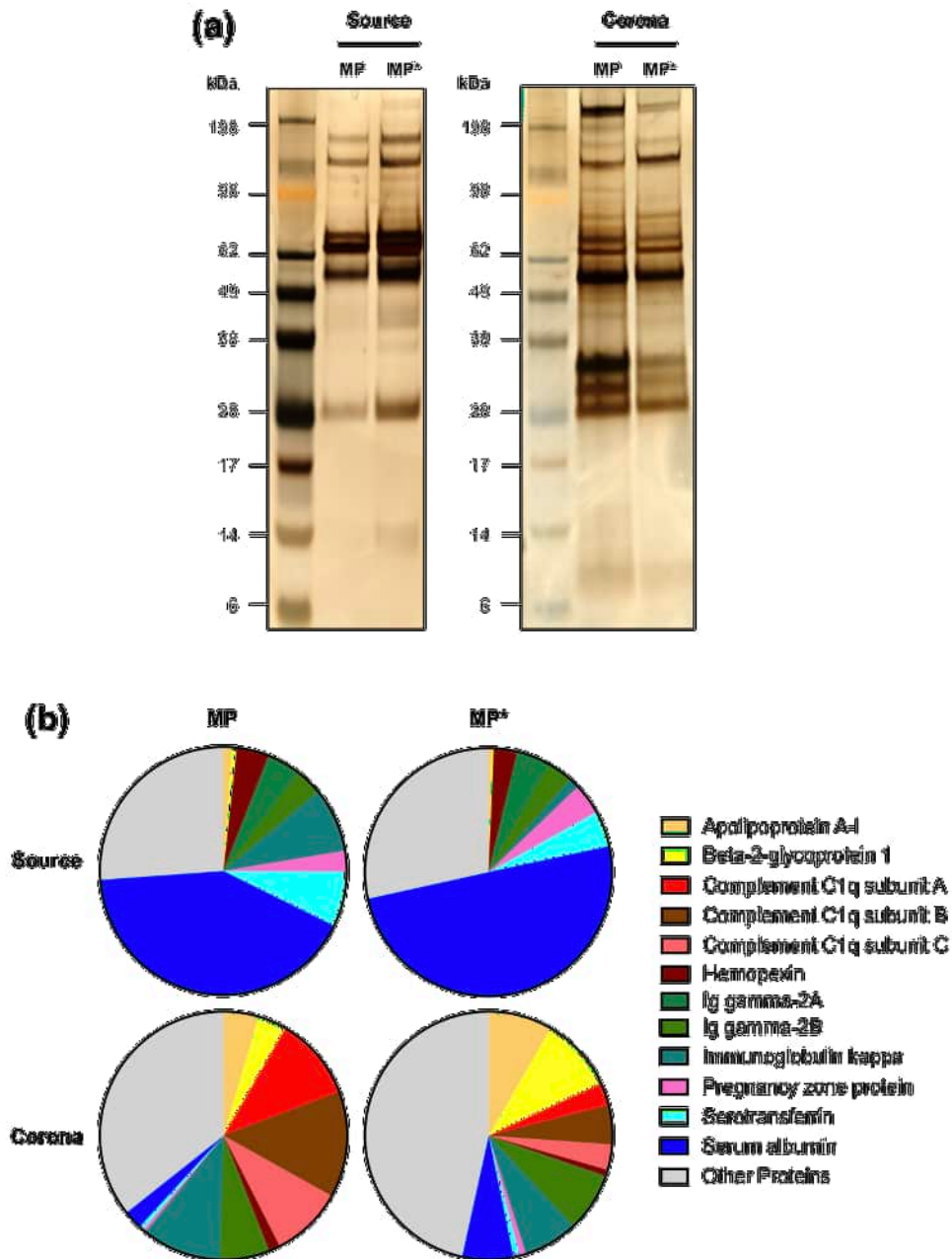


Figure 2.5.2 SDS-PAGE and LC-MS analysis of unlabelled and Cy5-labelled plasma serum and protein corona. **a.** Unlabelled murine plasma (MP) and Cy5-labelled murine plasma (MP*) and respective protein corona samples were analysed by SDS-PAGE and silver staining. Corona proteins were obtained after incubation of carboxyl-functionalised PS NPs in plasma, washing, and desorption with 2 % of SDS. **b.** Quantitative LC-MS proteomic analysis. The pie charts displays the proteins with at least 4 % presence in the proteome. Values are represented as the percentage based on all identified proteins. SDS-PAGE and LC-MS were performed by Dr. Johanna Simon.

Next, we employed flow cytometry to understand the uptake of both, PS NPs and the protein corona. Murine macrophages RAW264.7 were incubated with untreated PS NPs, PS NPs with an unlabelled protein corona, and PS NPs with a Cy5-labelled protein corona (Fig. 2.5.3). After an incubation of 2 h with the nanoparticles, almost 100 % of the cells were BODIPY positive, indicating the uptake of the PS NPs by most cells. Untreated PS NPs and PS NPs with an unlabelled corona did not evoke positive signals for Cy5. However, almost all measured cells were Cy5 positive, if the cells were incubated with PS NPs with a Cy5-labelled protein corona. Therefore, our findings prove a co-internalisation of the PS NPs and the associated protein corona.

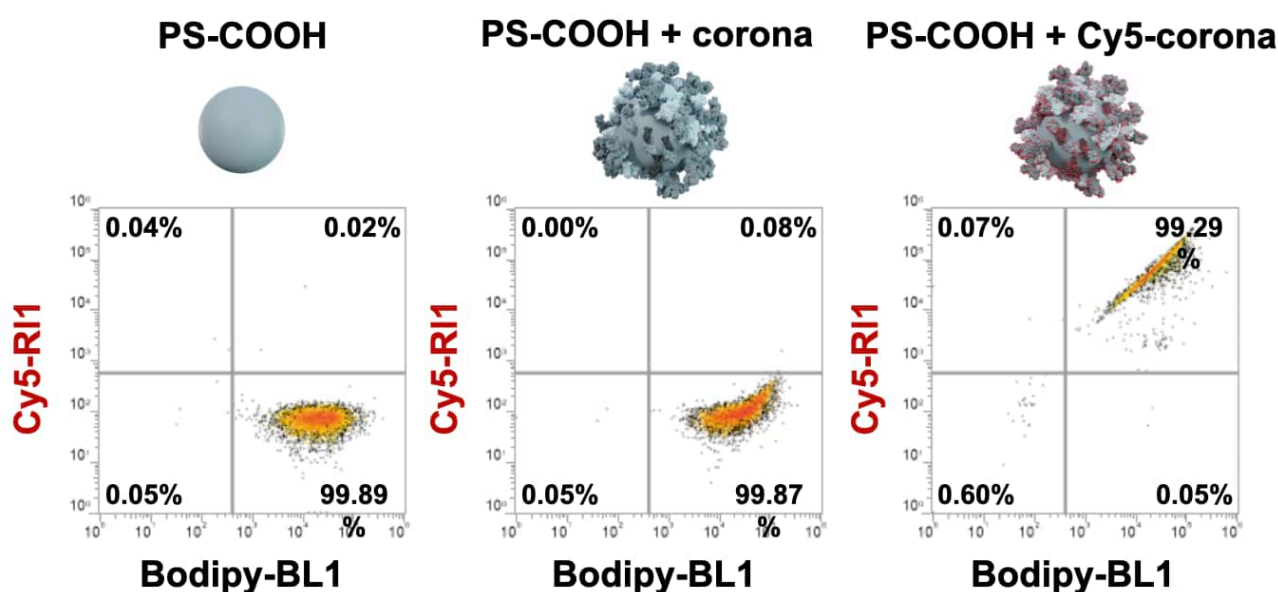


Figure 2.5.3 Flow cytometry of the cellular uptake of protein corona coated PS NPs. Flow cytometry was performed to measure BODIPY (PS NPs) fluorescence and Cy5 (labelled corona proteins) fluorescence. Values are shown as the percentage of measured events in regard to the fluorescence. Flow cytometry was performed by Dr. Johanna Simon.

In order to study the intracellular behaviour of the protein corona, volume CLEM in RAW264.7 macrophage was performed with a Cy5-labelled protein corona on BODIPY-labelled PS NPs. After 24 h of co-incubation of protein corona coated PS NPs with macrophages, samples were immediately vitrified by high pressure freezing (HPF) to preserve the native structures. After undergoing the preparation steps of freeze substitution and EPON embedding, samples were finally sectioned and investigated in cLSM (Figure 2.5.4) and SEM sequentially to get. In total 15 EPON sections (100 nm each) were imaged in both microscopic modalities and the images from both microscopes were superimposed as previously described (Figure. 2.5.5).^[121] CLEM images of each section were aligned in the correct order and eventually segmented for the reconstruction model with a volume of 1.5 μm (Figure. 2.5.6 f). Each object of interest was segmented in a different colour for better distinction. Totally, 1446 BODIPY-labelled PS NPs were segmented in green (Figure. 2.5.6 a) and they were found within 172 endocytotic vesicles (Figure. 2.5.6 c). Furthermore, 20 endocytotic vesicles containing separated Cy5-labelled protein corona (Figure. 2.5.6 b) were segmented within the PS-vesicles complex (Figure 2.5.7 a), and 271 objects of protein corona (Figure. 2.5.6 d) were segmented according to CLEM images. In addition, 12 mitochondria (Figure. 2.5.6 e) were found within the vesicle complex. Vesicles containing the separated protein corona and vesicles containing PS NPs were closely located together with mitochondria (Figure 2.5.7 b).

Volume CLEM extends two dimension CLEM images to a more comprehensive three dimensional volume, it is mostly used to capture rare pathology events in thick tissues.^[202] Since 2D images are sometimes not representative enough to closure the exact morphology of some cellular structures, 3D volume helps to describe a thorough readout of the same region of interest. For example, in our case, a 2D EM image cannot guarantee an intracellular vesicle to be a MVB or a RE because it is just a readout of an ultrathin 100 nm section. Therefore, a superposition of continuous sections from different z-axis creates a more faithful model in 3D, and eventually enables the study of the distribution of protein corona and NPs in different endosomes.

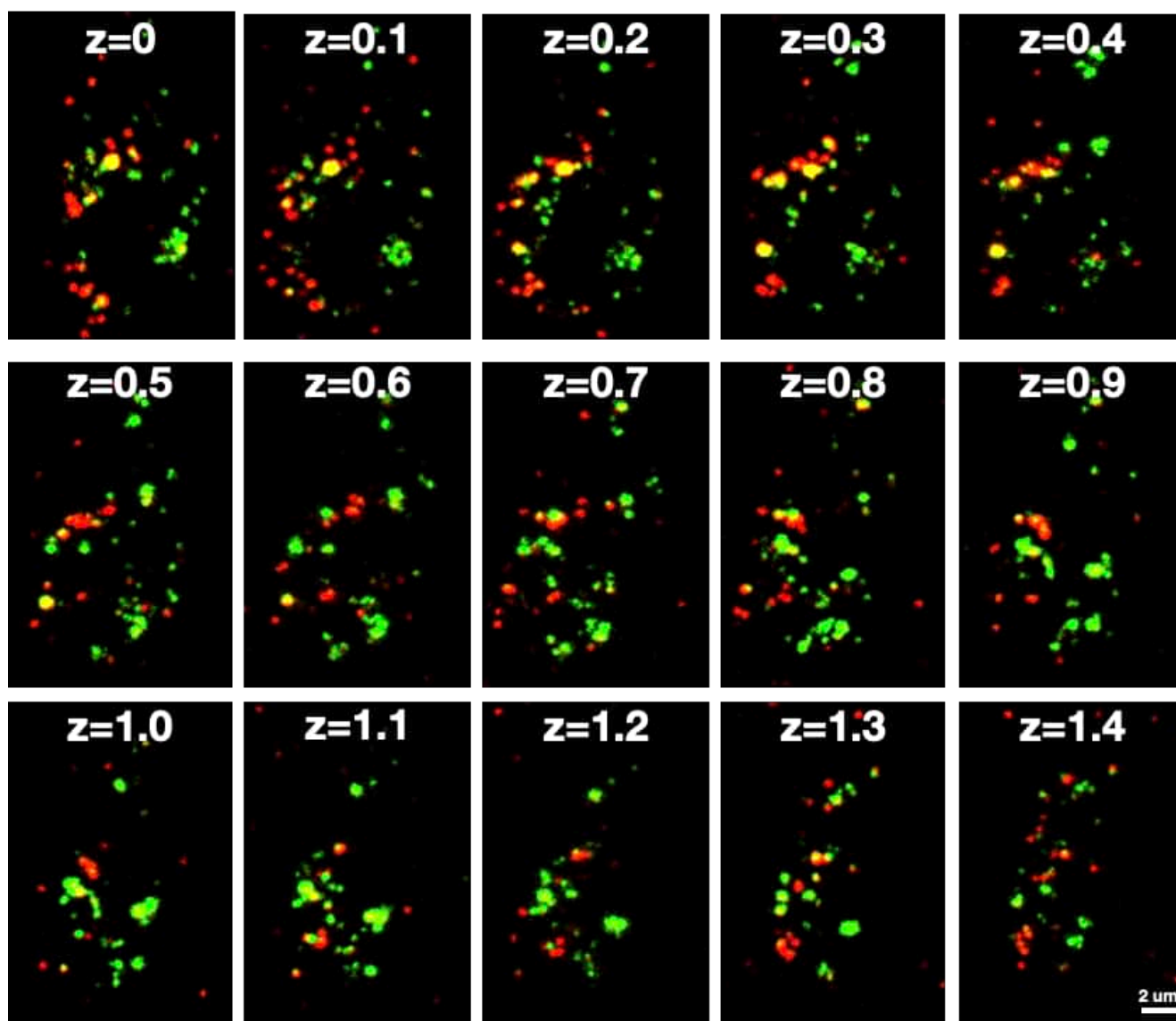


Figure 2.5.4 Fluorescence micrographs of the same cell in EPON sections. Fifteen 100 nm EPON sections were imaged in cLSM sequentially. Red represents Cy5-labelled protein corona, green represents BODIPY-labelled PS NP, colocalisation of both is presented in yellow. Z represents the relative depth of each section in μm .

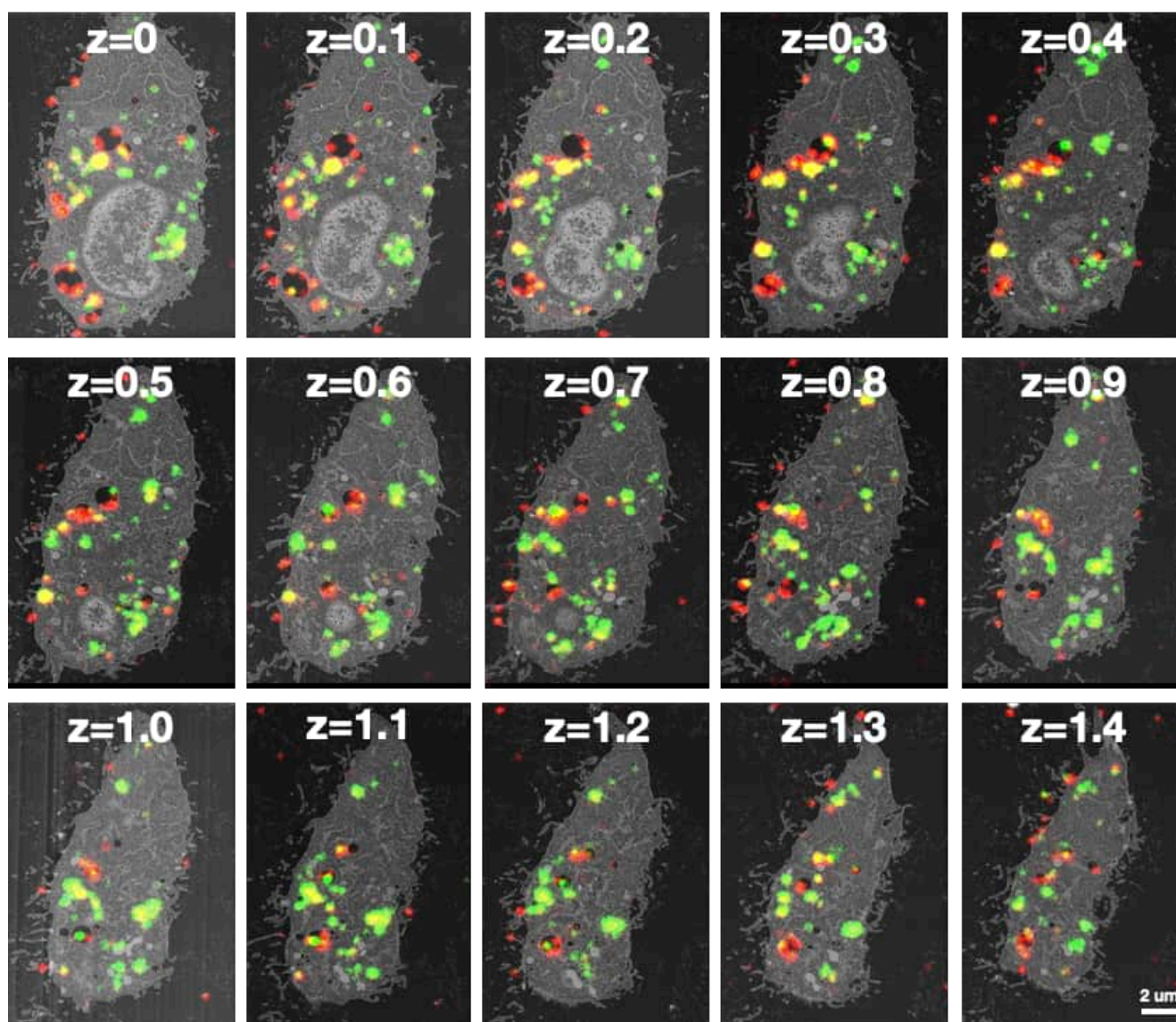


Figure 2.5.5 CLEM micrographs of the same cell in EPON sections. Fifteen CLEM images of 100 nm EPON sections of the same cell were overlaid from cLSM and SEM images respectively. Red represents Cy5-labelled protein corona, green represents BODIPY-labelled PS NP, colocalisation of both is presented in yellow. Z represents the relative depth of each section in µm.

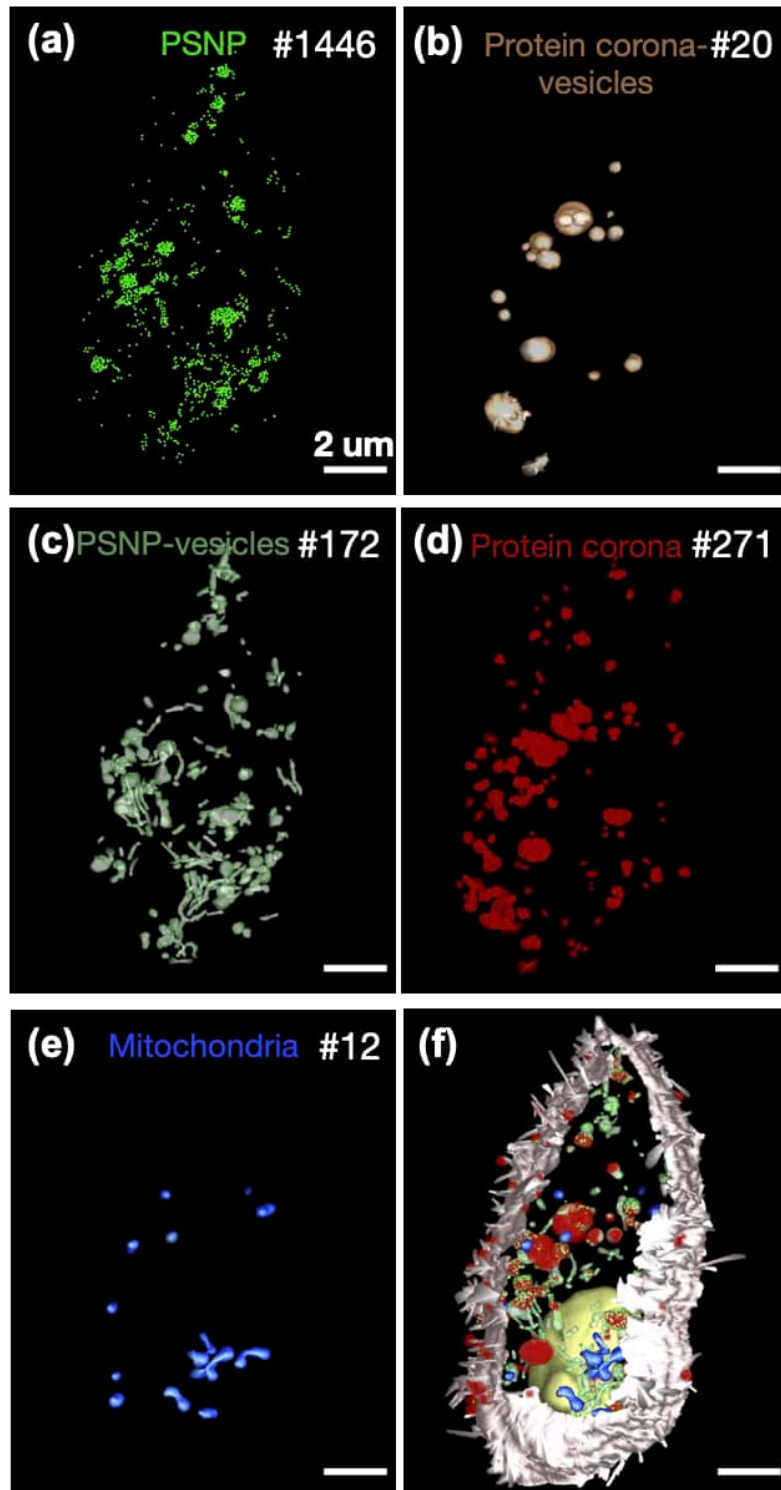


Figure 2.5.6 Segmented model of the one cell from volume CLEM. Segmented model of individual or combined objects with the number of segmented objects (upper right). **a.** Polystyrene nanoparticles. **b.** Vesicles contain protein corona. **c.** Vesicles contain polystyrene nanoparticles. **d.** Protein corona. **e.** Mitochondria. **f.** Segmented model of the whole cell with cell membrane (light pink) and nuclei (yellow). Scale bars: 2 μm

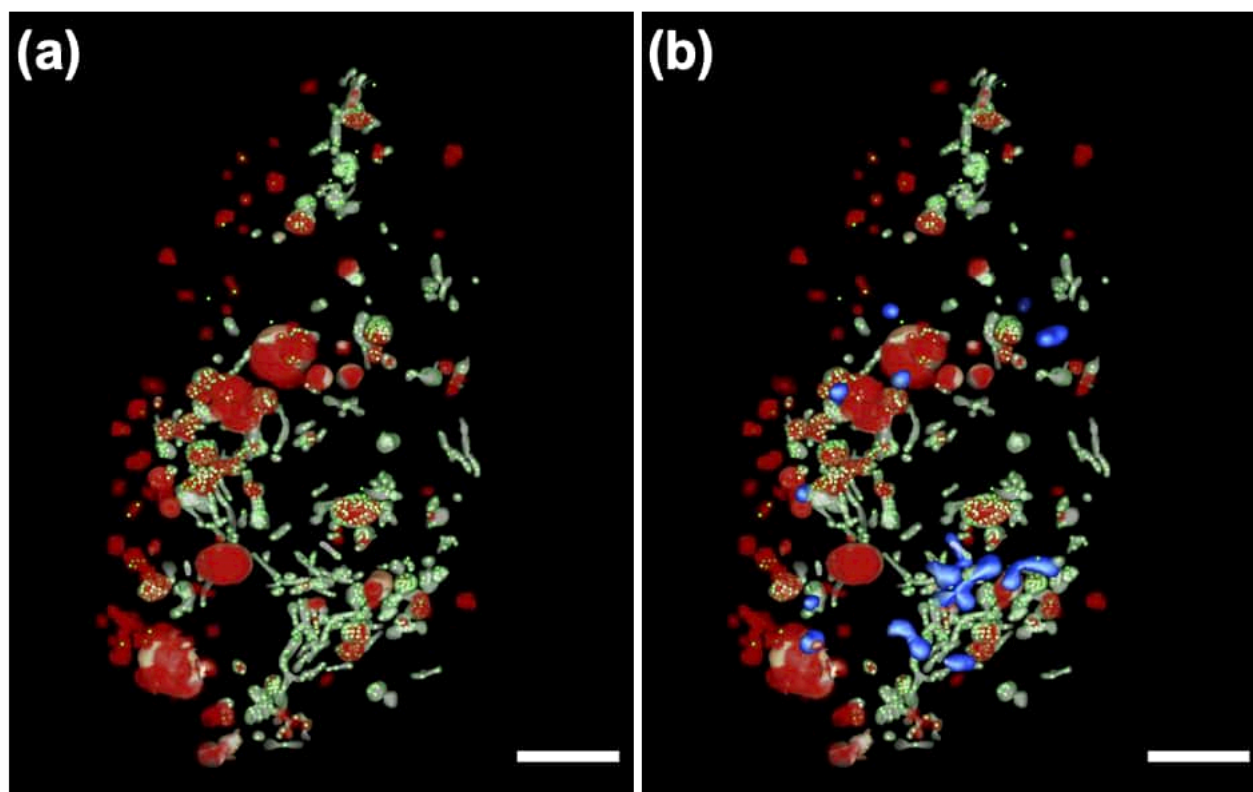


Figure 2.5.7 Segmented model of the one cell from volume CLEM. a. Combined segmented objects of protein corona, polystyrene nanoparticles, vesicles contain polystyrene nanoparticles, vesicles contain protein corona. **b.** Segmented objects in **a** with mitochondria. Scale bars: 2 μm

We conducted additional flow cytometry analysis at different time points to investigate the fate of the internalised PS NPs and protein corona. For this, we retrieved the NPs-containing supernatant on RAW264.7 macrophages after an incubation time of 2 h and evaluated the BODIPY and Cy5 signal by flow cytometry after different additional incubation times. This procedure was performed for untreated PS NPs, PS NPs with an unlabelled protein corona, and PS NPs with a Cy5-labelled protein corona. Similar to the uptake analysis after 2 h, almost all measured cells were positive for BODIPY at every time point. If the cells were incubated with PS NPs with a Cy5-labelled protein corona we also that almost all measured cells were positive for Cy5 at every time point. Additionally, we evaluated the median fluorescence intensity (MFI) to understand the intensity of the signal after different incubation times and link this intensity to the fate of the NPs and the protein corona. Overall, the MFI for BODIPY decreased over time, indicating a lowering amount of PS NPs in the cells with time. This decrease of PS NPs with time was observed for all three conditions of PS NPs (Figure 2.5.8 a). The MFI for Cy5 showed a similar decrease over time for cells that were incubated with PS NPs with a Cy5-labelled protein corona (Figure 2.5.8 a). To

compare the decrease of the BODIPY and Cy5 signal in the case of the uptake of PS NPs with a Cy5-labelled protein corona, we calculated a percentual MFI. This percentual MFI is based on the normalisation of the MFI value compared to the highest MFI value (the MFI value of 2 h). Interestingly, we observed that the MFI of Cy5 decreased faster than the MFI of BODIPY (Figure 2.5.8 a). Accordingly, we assume that the protein corona remains less persistently in the cell than PS NPs due to destined degradation or possible exocytosis which will be discussed later.

To support the flow cytometry findings, cLSM was employed to study the colocalisation of the BODIPY and Cy5 signal on embedded sections. An imageJ macro was used to evaluate the colocalised signals. The intensities of the colocalised signals were subsequently compared with the total signal intensities and a percentual fraction of colocalised signal intensity was calculated. We observed a decrease in colocalisation over the same time frame as in the flow cytometric experiment (Figure 2.5.8 b). Therefore, we draw the conclusion that the fluorescently labelled protein corona must be separated from the PS NP after the uptake. This separation is a process that takes several hours.

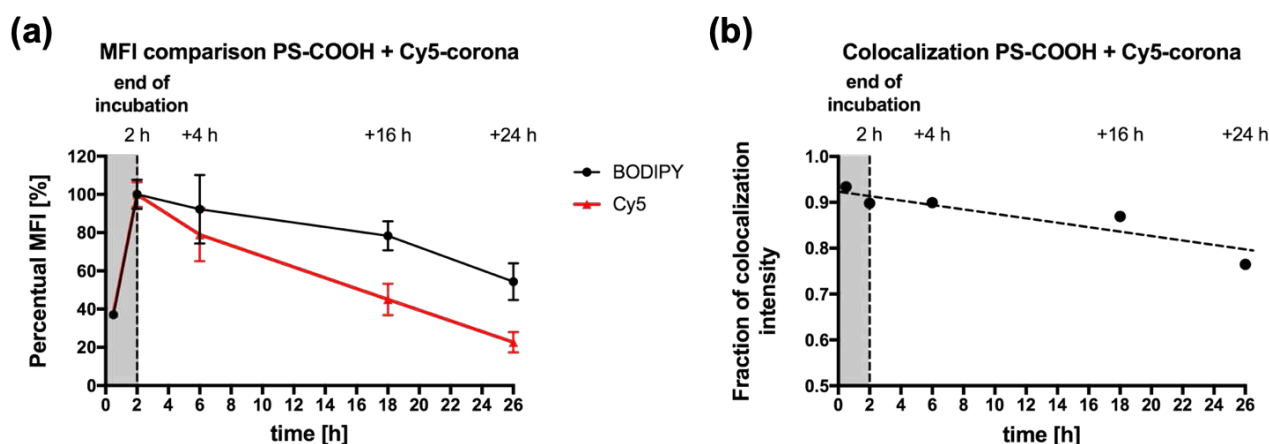


Figure 2.5.8 Flow cytometry and cLSM colocalisation analysis reveal a slow separation of NP and protein corona after cell uptake. The percentual MFI was plotted for the BODIPY and the Cy5 fluorescence in the case of the uptake of NPs with a Cy5-labelled corona. **a.** The percentual MFI value was calculated for each time point, comparing it to the highest MFI value measured (here: 2 h; data is shown as mean \pm SD, $n = 3$). **d.** The colocalisation in cLSM pictures of BODIPY and Cy5 was analysed for the uptake of NPs with a Cy5-labelled corona. **b.** The colocalisation analysis was conducted by using an in-house ImageJ plugin, calculating the fraction of connected or colocalised signal intensities compared to the total intensities. As a guide to the eye, a dotted line was inserted into the graph, visualising the decreasing trend of the colocalisation ($n = 1$).

The intracellular fate of the protein corona and PS NPs was further revealed by serial CLEM images. The protein corona (Cy5, red) and PS NPs (BODIPY, green) was mostly localised in round endosomes (Figure 2.5.10 b, b'), whereas the separated protein corona signal was exclusively found in multivesicular bodies (MVBs) (Figure 2.5.8, Figure 2.5.9 a-b). At the same time, we also localised elongated tubular vesicles around MVBs containing only PS NPs. These tubular vesicles can be morphologically identified as recycling endosomes (REs) (Figure 2.5.10 e, e'). Upon the observation that the protein corona and PS NPs were distributed separately in morphologically different endosomes, we further identified the separation event (Figure 2.5.10 c, c') by investigating the CLEM images where two signals were closely connected but not overlapped. Depending on the EM micrograph (Figure 2.5.10 c'), the endosome containing protein corona exhibited a ruffling toward the endosome containing PS NPs (Figure 2.5.10 c', white arrow), indicating a possible dynamic exchange of two endosomes. Meanwhile, the endosome that contained only the protein corona (Figure 2.5.10 c) was found developed into an MVB in later sections (Figure 2.5.9 a), this finding confirms the earlier observation of separated protein corona. Additionally, we observed exocytosis of separated PS NPs (Figure 2.5.10 f, f'), implying that PS NPs could be exocytosed by REs after being separated from the protein corona. To further demonstrate the separation event and the distribution of separated protein corona in MVBs, serial CLEM images of areas in Figure 2.5.10 c and Figure 2.5.10 d were shown in detail accordingly (Figure 2.5.9 a, Figure 2.5.9 b). The segmented models (Figure 2.5.9 a', a'', a''') of Figure 2.5.9 a showed the close spacial relationship between an endosome containing separated PS NPs (green) and an MVB containing the separated protein corona (red). An endosome with protein corona coated PS NPs and tubular REs with separated PS NPs were located next to the MVB indicating the separation might be an ongoing process. The segmented model (Figure 2.5.9 b', b'', b''') of Figure 2.5.9 b revealed dimensionally that several REs containing separated were located close to the MVB containing separated protein corona. The spacial information from both models further hinted that the separation and distribution of protein corona and PS NPs were closely related to the functions of different endosomes.

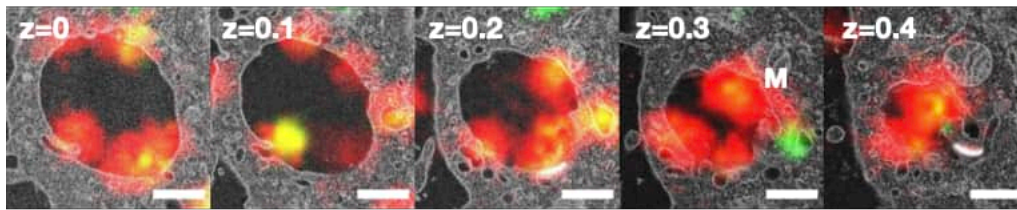
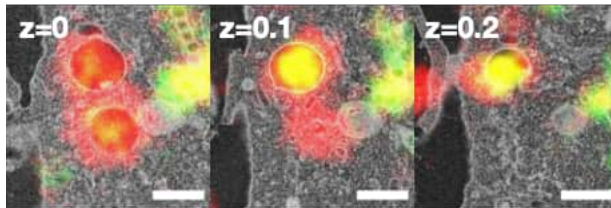
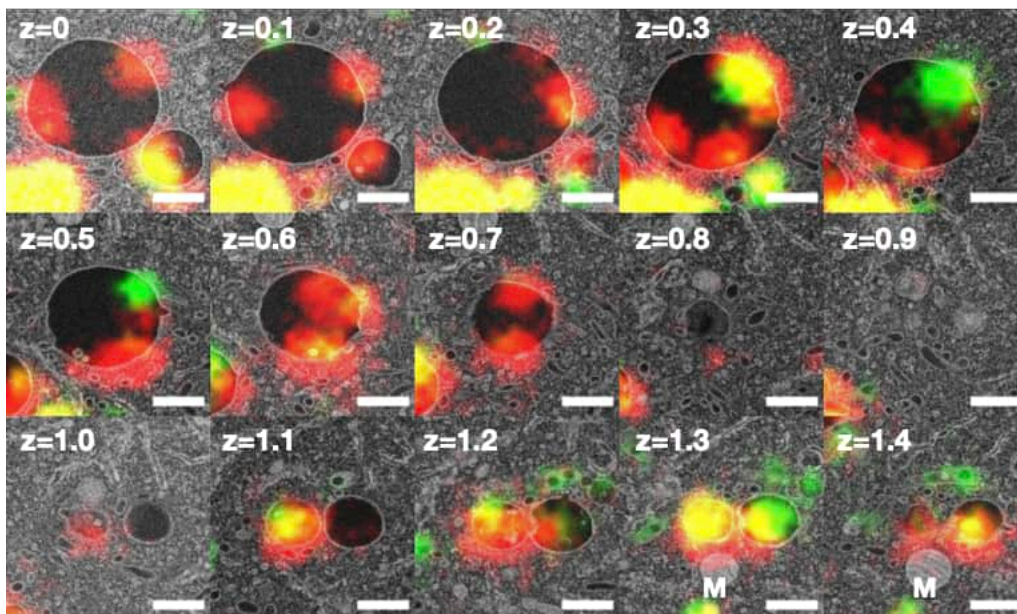
Vesicle 1**Vesicle 2****Vesicle 3**

Figure 2.5.8 Endocytotic vesicles containing Cy5-protein corona signal. relative depth of each section in μm . Red represents Cy5-labelled protein corona, green represents BODIPY-labelled PSNP, yellow represents the overlay of protein corona and PSNP. Scale bars: 500 nm

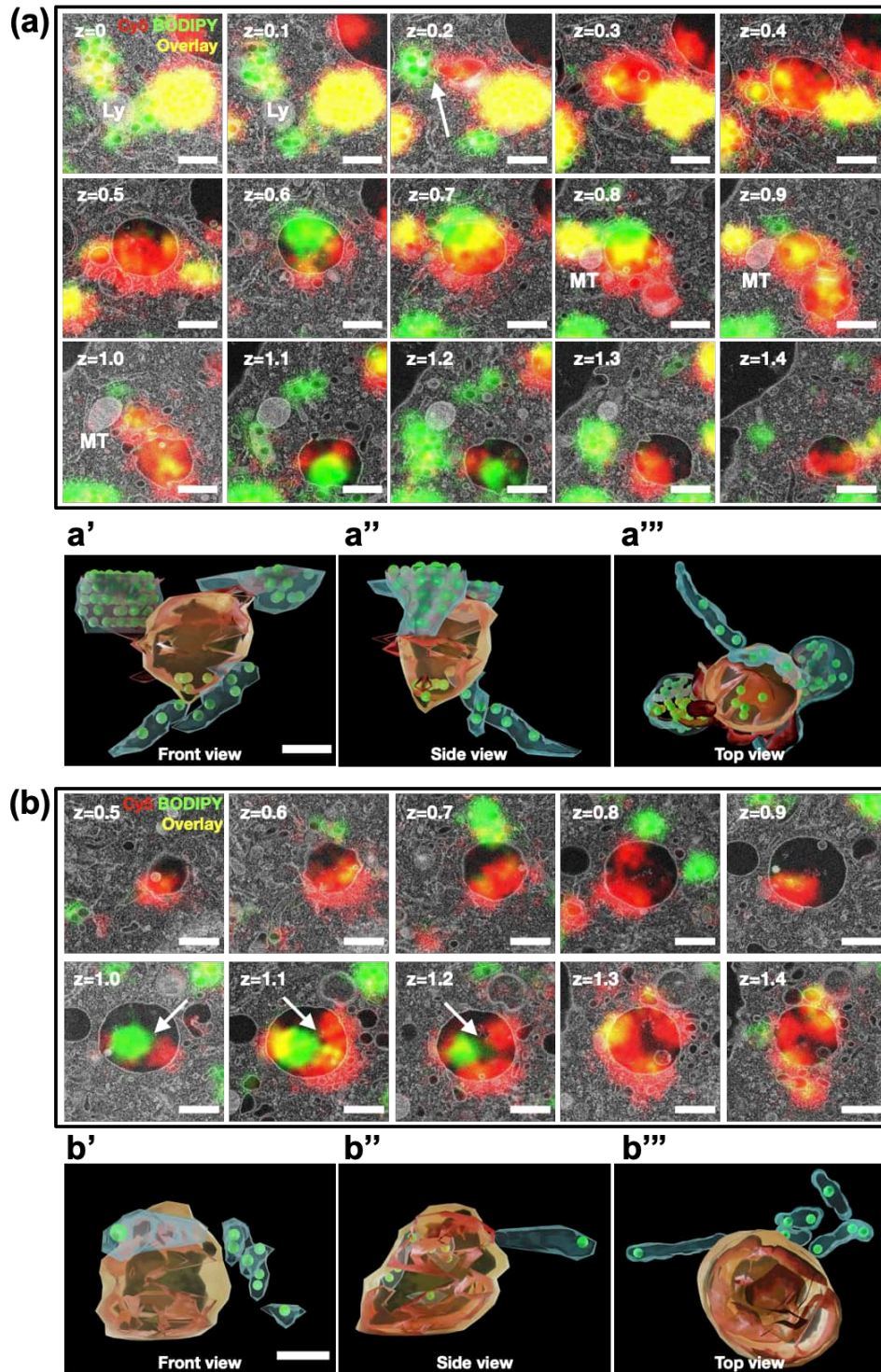


Figure 2.5.9 Segmented model of two MVBs contains separated protein corona. **a.** Volume CLEM of the separation of protein corona and PS NPs in endosomes, separation of protein corona and NPs is indicated by an arrow. Ly: lysosome; MT: mitochondria. **a'**. Front view of the segmented model in g. **a''**. Side view of the segmented model in g. **a'''**. Top view of the segmented model in g. **b.** Volume CLEM of an MVB with separated protein corona and PS NPs. **b'**. Front view of segmented model in h. **b''**. Side view of segmented model in h. **b'''**. Top view of segmented model in h. Scale bars: 500 nm.

According to our CLEM results, the protein corona-coated NPs were mainly located in crowded round-shaped endosomes, whereas the separated protein corona was exclusively located in MVBs, and the separated NPs were found in tubular REs. Because our flow cytometry results showed the successful co-internalisation of the protein corona and NPs, we assume that the endosomes with the protein corona-coated NPs were primary or early endosomes (EEs). At the same time, it is known that EEs are crucial for sorting functions [203-205] and are able to generate tubular REs for further transportation or recycling.[204, 206] Therefore we consider that the sorting of the protein corona and NPs happens at the site of early endosomes when REs containing NPs begin to form while the protein corona begins to separate from NPs. Furthermore, we observed the separated protein corona only in large MVBs containing intraluminal vesicles.[207, 208] These MVBs mature from EEs [207] and more specifically from the main bodies of the EEs after the formation of REs.[203, 205] We hypothesise that during the maturation of the EEs after internalisation, NPs start to separate from the protein corona and are gradually transported into REs. As the maturation of the EEs into MVBs completes, most NPs are then transported into REs leaving behind the protein corona within the matured MVBs (Figure 2.5.8). This hypothesis correlates with the endosome maturation during the endocytic pathway and is supported by our CLEM results. Exocytosed NPs within a vesicle were also observed at the same condition, and this phenomenon has been reported in different cell lines. [209, 210] We speculate that the exocytosis might happen via the recycling of REs to the plasma membrane after protein corona separation. On the other hand, depending on the MVB maturation, the separated protein corona in the MVBs might eventually accumulate in lysosomes [208] or exocytose via exosomes [211]. Degradation of the protein corona in lysosomes is predictable and was previously observed.[199] Nevertheless, we have captured the Cy5 signals around the plasma membrane, either colocalising with some membranous vesicles or on the membrane ruffling (Figure 2.5.11). These Cy5 signals outside of the cell might be the evidence of the exocytosed protein corona from MVBs and suggest an alternative destiny of the separated protein corona.

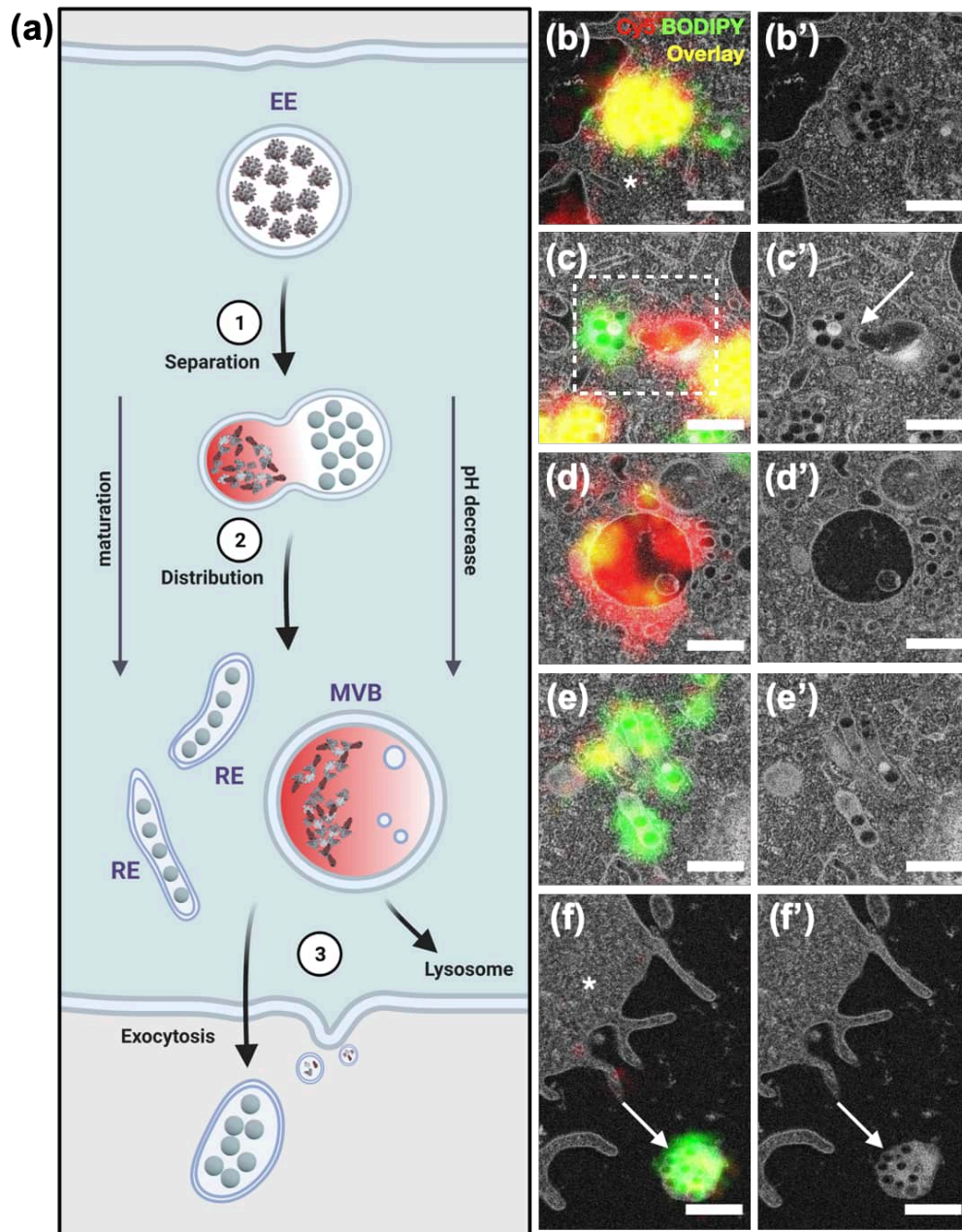


Figure 2.5.10 Intracellular fate of protein corona and NPs illustrated by CLEM and EM micrographs. **a.** Scheme of intracellular separation of protein corona and NPs and exocytosis of NPs. **b,b'**. Protein corona coated PS NPs in an endosome after internalization. Intracellular space is indicated with a star symbol. **c,c'**. Separation of protein corona and PS NPs. Separation event is highlighted with a dotted square and an arrow. **d,d'**. Distribution of separated protein corona in an MVB. **e,e'**. Distribution of separated PS NPs in tubular recycling endosomes. **f,f'**. Exocytosis of separated PS NPs. Exocytosis of naked PS NPs is indicated by an arrow and intracellular space is indicated with a star symbol.

The reason behind the separation of the protein corona and NPs might be related to the changing acidification within different endosomes. The pH value in different endosomes decreases along the endocytic pathway during the endosomal maturation.^[203, 212] It is well understood that the composition and stability of the protein corona is strongly affected by the environmental pH *in vitro*.^[213, 214] We suggest, that due to the decreased pH from EEs to MVBs, the proteins on the protein corona might lose their affinity to the surface of the NPs because the evolution of protein corona is dynamic under a fickle environment.^[79, 215] Additionally, the acidification might cause conformation changes of the adsorbed proteins ^[213, 216] which can consequently influence and alter protein-protein and most protein-NP interactions of the protein corona.

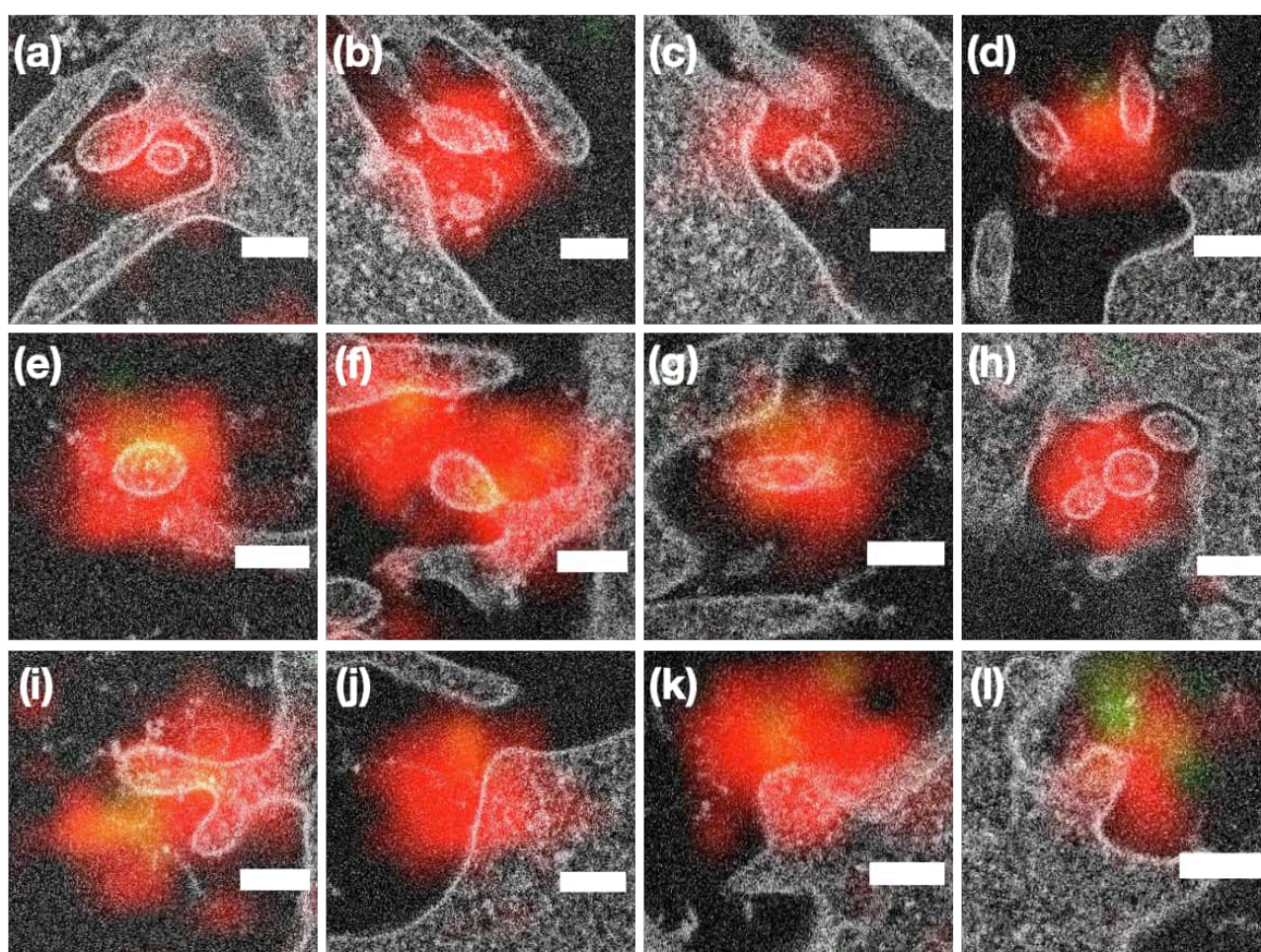


Figure 2.5.11 CLEM micrographs of extracellular Cy5-labelled protein corona close to plasma membrane. **a-h.** Cy5 signal located within extracellular vesicles. **i-l.** Cy5 signal located close to membrane ruffling. Scale bars: 200 nm.

Furthermore, the protein corona-coated NPs transit through dynamic biological environments, leading to encounters with new, intracellular proteins which were not present in the plasma. Previous research has highlighted the dynamic behaviour of the protein corona after transitioning through different biological fluids.^[197, 200, 201] Some of the intracellular proteins might exhibit a higher affinity towards the NPs surface and, therefore, adsorb on the NPs surface intracellularly and replace the previous proteins, leading to a newly formed protein corona. This enrichment of intracellular proteins might contribute to the separation of the fluorescently labelled plasma proteins from the corona.

Conclusions

We have reconstructed the uptake, intracellular tracking, and the possible fates of an extracellularly formed protein corona on NPs. By utilising fluorescent proteins to generate a protein corona, we demonstrated a co-internalisation of the NPs and the protein corona. Furthermore, we took advantages of volume CLEM to faithfully identified intracellular protein corona and PS NPs and to reveal their distinct distributions in three dimension. For the first time, by referring to correlative imaging snapshots with quantifying measurements of the separating protein corona and PS NPs, we could draw sufficient conclusions to explain a possible intracellular evolution of the protein corona once it is internalised. With our findings, we want to contribute to a deeper understanding of adsorbed proteins on nanoscale surfaces in intracellular environments. Here, we see the necessity to further expand our understanding of the internalisation of the protein corona and its intracellular fate. We believe that this knowledge will improve, not only the future design of nanoscale drug delivery systems but elucidate the possible pitfalls or chances of the internalised protein corona to induce targeted effects upon cellular uptake.

3. Experimental methods

In this chapter, the general protocols and examination methods, which are applied in this thesis, are described. Details regarding further methods, that were performed by my collaboration partners in the context of joint publications, can be found in the respective publications..

3.1 General protocols for the preparation of cells for EM and CLEM

3.1.1 Cell culture for adherent cells

Usually, HeLa cells or RAW264.7 macrophages were cultured in Dulbecco's modified eagle medium (DMEM; Invitrogen, Germany) supplement with 10 % fetal bovine serum (FBS; Sigma Aldrich, Germany), 1 % glutamine (Gibco, USA) , and 1 % penicillin/streptomycin (Gibco, USA) in a 95 % humidified incubator at 37 °C and 5 % CO₂ (C200, Labotect, Germany).

Disassociation of adherent cells were performed by co-incubation with 0.25 % trypsin (Gibco, USA) for 3 min. Treated cell media were collected in a 15 mL Falcon tube and centrifuged at 300 g for 5 min. The cell pellet was then resuspended in DMEM complete medium and diluted to the desired concentration for further applications. Cell viability was determined by trypan blue exclusion method performed with TC10™ automated cell counter (Bio-Rad, USA).

3.1.2 Cellular uptake experiments and high pressure freezing (HPF)

In order to perform HPF of cellular samples, adherent cells have to be seeded onto specially made substrates, called sapphire disks. Sapphire disks (3 mm; M. Wohlwend GmbH) were pre-coated with a 10-nm-thick carbon layer using an EM MED020 instrument (Figure 3.1) (Leica, Germany). The coated sapphire disks were dried and sterilised in an oven at 120 °C overnight before use. Adherent cells were seeded onto sapphire disks in a 24-well plates at a concentration of 50,000 cells/mL overnight for cell attachment. Chosen NPs were co-incubated with seeded cells with desired duration in a humidified incubator at 37 °C and 5% CO₂. After the incubation, each sapphire disk was collected from the 24-well plates and slightly immersed into 1-hexadecene before placing them between two aluminium plates (3 mm, Plano). This “sandwich’ structure was placed into a

specimen holder for high pressure freezing in a Wohlwend HPF Compact 01 high pressure freezer operating at a pressure of 2,100 bar. The specimen holder was withdrawn from the freezer and immersed into liquid nitrogen to release the sample. The frozen sample was then labelled and stored in a container filled with liquid nitrogen.

3.1.3 Freeze substitution and embedding in resin

Subsequently, freeze substitution of the sample was carried out in a 0.5 mL Eppendorf tube using an AFS2 automated freeze substitution device (Leica, Germany). Each tube contained 1 mL of freeze substitution solution, consisting of 0.2 wt/vol % OsO₄, 0.1 wt/vol% UA, and 5 % distilled water in acetone. The tubes were initially kept at -90 °C and slowly warmed up to 0 °C in 24 h. After keeping at room temperature for 1 h, the substitution solution was removed and the samples were washed 3 times with acetone. Each sample was infiltrated in an ascending epoxy resin series (30 %, 50 %, and 75 % in acetone) for 1 h before finally infiltration in 100 % epoxy resin overnight. Finally, each sample was transferred into a new Eppendorf tube containing freshly prepared pure epoxy resin following the final polymerisation at 60 °C for 24 h.

3.1.4 Ultramicrotomy and imaging

After polymerisation, sample blocks were kept at room temperature until they were sectioned. The sample blocks were trimmed and sectioned to 100 nm sections using a 35° diamond knife (Diatome) or an ultra 45° Jumbo diamond knife (Diatome) in an EM UC6 ultramicrotome (Leica, Germany). The sections were then carefully placed onto 300-mesh copper grid for standard bright-field TEM imaging, finder grids for correlative light and electron microscopy (CLEM) or transmission electron microscopy (TEM) imaging, or Indium-Tin-Oxide (ITO)-coated coverslip (SPI supplies, USA) for CLEM and scanning electron microscopy (SEM) imaging. Electron energy loss spectroscopy (EELS), and energy dispersive X-ray spectroscopy (EDX) analysis were performed in a Tecnai F20 200 kV TEM (FEI, USA). Bright-field TEM micrographs were obtained with a Gatan US1000 2k CCD camera. EDX images were collected with an EDAX detector.

3.1.5 Confocal laser scanning microscopy (cLSM)

Conventional fluorescence microscopes such as wide-field fluorescence microscope are using a beam of laser or light to illuminate the full volume of a sample, which inevitably causes blurriness and misalignment of the images and the molecule of interest.^[217] In contrast, a cLSM only images and focuses on a single focal plane of the sample and the focused laser beam is scanning point by point on the focal plane to generate an image. Therefore, images generated by cLSM are more site-specific than conventional fluorescence microscopes. A 3D imaging can be achieved by moving the focal plane through the sample to generate a stack of images. Another advantage of a cLSM is the pinhole setup before the detector. Any fluorescence which is not coming from the focal plane is blocked by the pinhole in order to create sharper images.^[218] Finally, the emission light will be detected by a photon-multiplier (PMT) which converts the photons into multiplied photoelectrons.
[218]

3.1.6 Transmission electron microscopy (TEM) and Scanning electron microscopy (SEM)

TEM is powerful method to visualise an object of interest with nanometer and it was first invented by Max Knoll and Ernst Ruska in 1931. It is widely applied for characterisation and visualisation in biological science^[219] by emitting a beam of electron through a thin layer of sample and forming the images by detecting the projection of transmitted electrons. The unique imaging feature by using electrons as the illumination source enables TEM to provide unmatched resolution compared to light microscopy. However, the architecture of a TEM is somehow adopted from an optical microscope, a condenser lens to focus and parallel the electron beam, an objective lens for imaging, and a projector lens for the enlargement of the image. An intermediate lens is extra for the change of magnification and imaging mode in a TEM.^[220] And the operation in TEM is completely under high vacuum in order to prevent electrical discharge and contamination from electron scattering.

SEM is another type of electron microscope which characterises the sample by scanning a beam of focused electrons onto the surface. Unlike TEM, SEM generates the surface information of the sample by detecting the elastic or inelastic scattered electrons. It is useful for determine the surface topography or chemical constitution of a sample.^[221] There are generally two types detectors for SEM, one is a secondary electron (SE) detector, the other one is a backscattered electron (BSE)

detector. A SE detector detects the electrons generated from the surface of the sample and used to characterise the surface topography of the sample. Whereas, a BSE detector detects the inelastic scattered electrons which are reflected from the deeper area of the samples. Operation in SEM is also performed under high vacuum environment.

In this thesis, TEM and SEM were used to image biological samples which were fixed and embedded in resin. Ultrathin sections (100 nm) were prepared by ultramicrotome and place onto TEM grids or ITO-coated coverslips for TEM or SEM inspections.

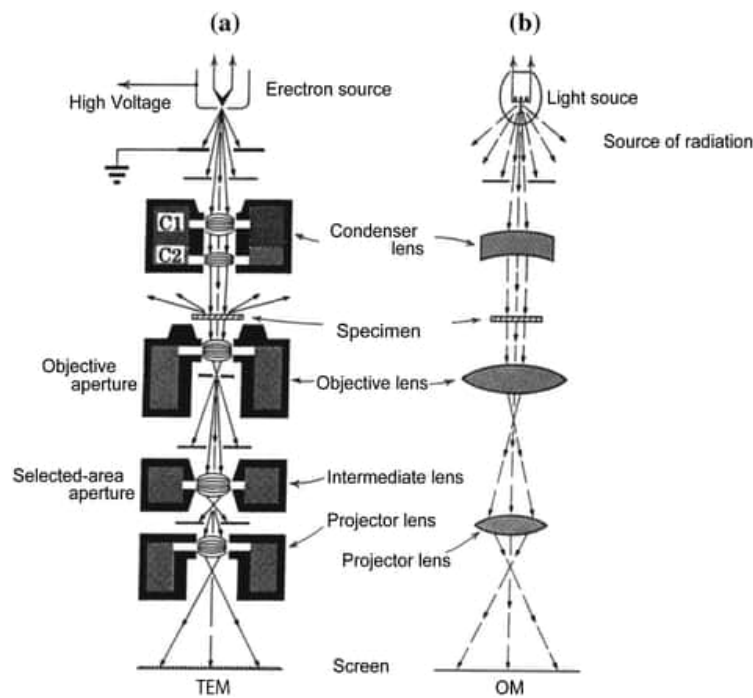


Figure 3.1 Comparison of a transmission electron microscope (TEM) and an optical microscope. Reprinted with permission from ref [219]. Copyrights © Springer Japan KK 2017

3.1.7 Electron energy loss spectroscopy (EELS)

EELS is a spectroscopy technique which is used to determine the elemental composition of a sample. It measures the losses of energy from the inelastic scattered electrons which are coming out of the sample. The energy intensity from the inelastically scattered electron is represented by a function of electron kinetic energy detected by an element spectrometer.^[222] The EELS spectrum of the examined region is demonstrated by low-loss region and high-loss region, which represent respectively the atomic composition of the outmost and the inner atom shell of the element. Since

EELS is rather sensitive to the loss of energy by the incident beam, therefore it can also be used to identify the oxidative stages of some metallic elements.^[223]

3.2 Correlating TEM and EDX to localise intracellular SiO₂ NCs

This part of protocol corresponds to chapter 2.1

Protocols of other measurements in the papers can be found in the original publication: *Part. Part. Syst. Charact.* 2020, 37, 1900484 and *Nanoscale*, 2020, 12, 2626-2637.

3.2.1 Energy-dispersive X-ray spectroscopy (EDX)

EDX was performed on FEI Tecnai F20 TEM with an EDX spectrometer. A beam of electron was focused onto the sample in order to excite the electrons within the inner shell. A replacement of electrons from the outer shell to inner shell of the sample may happen during this process and generate an energy difference via the form of x-ray radiation. Since every element has its unique atomic arrangement, the energy difference represents the unique characteristic of each element, and the energy-dispersive spectrometer within TEM is then able to measure the radiated energy differences in order to identify different elements.

3.3 CLEM for intracellular NDs

This part of protocol corresponds to chapter 2.2

Characterisation of coated fNDs, fluorescence measurement, dynamic light scattering (DLS) and zeta-potential were performed by collaborator Dr. Marco Raabe, corresponding protocols of these measurements can be found in the original publication: *Nano Lett.* 2019, 19, 3, 2178–2185.

3.3.1 Material

Fluorescent nanodiamonds (fND) were bought from FND Biotech (Taiwan).

3.3.2 Preparation of in-dish CLEM specimens for cLSM and TEM

In-dish CLEM was defined as the detection of fluorescence signals prior to EM preparation. HeLa cells were incubated with fNDs (75 µg/mL) at 37 °C (5 % CO₂) for 4 h and then fixed in 4 % formaldehyde (Carl Roth, Germany) for 10 min in MatTek gridded glass bottom dishes (Ashland, USA). Nucleus counterstaining with Hoechst 33342 dye in DMEM (1:1000) was performed after the paraformaldehyde (PFA) fixation for 5 min. Three times of washing in PBS were performed after nucleus staining. Prepared samples were investigated on Leica SP8 AOBS system attached to a Leica DM I6000 inverted microscope with a 63X 1.4 NA oil immersion objective. The Hoechst 33342 dye and fNDs were excited with 50 mW diode laser at 405 nm and 20 mW solid state yellow laser at 561 nm. Fluorescence signals were collected at 461 nm for Hoechst and 660-700 nm for fNDs. Stack images of ROIs with the step of ~0.2 µm were recorded. The position of the cell of interest was simultaneously recorded.

After fluorescent imaging, samples were subjected to a postfixation in 4 % glutaraldehyde in phosphate buffer (pH = 7). Staining with OsO₄ and UA were performed sequentially, each step followed by three times washing in phosphate buffer. Samples were then subjected to dehydration through ethanol in ddH₂O with the gradient of 70 %, 80 %, 90 %, 100 % for 10 min each and subsequently embedded in EPON. Polymerised blocks were trimmed to the ROIs recorded by cLSM, and cut into 300 nm thick sections using a 45° diamond knife (Diatome, Switzerland) in EM UC6 ultramicrotome (Leica, Germany). Sections were then collected onto formvar coated slot copper grid (Plano, Germany) and air dried overnight for TEM imaging and tomography. Region of interests (ROIs) were retraced in TEM and tomography was performed with a single-axis tilt series from -65.5° to +67° using tilt increments of 1.5° above +/- 45° and 2.5° between -45° and +45°. Totally 65 images were collected using a CCD Camera. TEM imaging and tomography were performed with a Tecnai G20 - FEI 200 kV Twin Lens with Lab6 filament and FEI Eagle 4k x 4k CCD camera and with a Tecnai F20 – FEI 200 kV with FEG and Gatan US1000 CCD camera.

3.3.3 Preparation of in-resin CLEM specimens for cLSM and TEM

In-resin CLEM requires samples to be vitrified and embedded into resin prior LM and EM acquisition. HeLa cells were incubated with fNDs (75 µg/mL) for 4 h at 37 °C (5 % CO₂). After the

cell uptake experiment, cells in the petri dish were harvested and transferred into 2 mL Eppendorf tubes. After centrifugation at 1,000 g for 5 min, 1 μ L of thick cell suspension were collected and loaded into a 100 μ m deep membrane carrier (Leica, Germany) and vitrified in Leica EM PACT2 (Leica, Germany). Frozen membrane carriers were then transferred into flow through containers with freeze substitution cocktail (0.1 % UA, 0.01 % tannic acid, 5 % water in acetone). Freeze substitution was done in an AFS2 automated freeze substitution device (Leica, Germany) equipped with an attachment for automated exchange of reagent (Freeze substitution processor, FSP, Leica, Germany). Samples were kept at -90 °C for 5 h and gradually warmed up to -45 °C at the rate of 5 °C/h. After being held at -45 °C for 2 h, samples were washed twice in acetone for 30 min each. Samples were then infiltrated in 25 %, 50 %, 75 % of Lowicryl HM20 resin in acetone for 2.5 h each and finally infiltrated in 100 % resin overnight. Resin was exchanged for twice with the duration of 3 h each after the overnight infiltration. Polymerisation of resin was carried out under UV light for 43 h, with the first 19 h being held at 45 °C, followed by warming up to 0 °C within 12 h, and finally being kept at 0 °C for another 12 h.

After polymerisation, resin blocks were removed from the containers. The carriers were detached from the resin blocks by using liquid nitrogen and the warmed up specimen carrier detaching tool (Leica, Germany). The blocks were then trimmed to desired sizes and sectioned to 120 nm thick sections using a 45° diamond knife (Diatome, Switzerland) in EM UC6 ultramicrotome (Leica, Germany). Sections were collected onto carbon coated formvar films on F1 copper finder grids (Agar Scientific). After being air dried, grids were stained with Hoechst 33342 dye in ddH₂O (1:1000) for 5 min, and washed three times in ddH₂O for 1 min each. Each stained grid was then mounted between a coverslip and a glass slide in 15 μ L of 50 % glycerol in ddH₂O. Mounted grids were then imaged by Leica DMI4000 B inverted epifluorescence microscope with 20X 0.75 NA dry lens for fluorescence detection. After imaging, the grids were carefully retrieved using a sharp razor blade and washed in H₂O. The grids were then post-stained with UA and lead citrate before TEM imaging.

3.3.4 Image alignment and analysis

For tomogram alignment and reconstruction, IMOD software (version 4.9.7) was used. Acquired images from the tilt series were initially aligned and stacked in the software. The stacked file was then computationally reconstructed using a weighted back-projection algorithm. For CLEM image

registration, images from light and electron microscopy were manually tracked and aligned using eC-CLEM plugin in Icy.^[224]

3.3.6 Image registration for CLEM in icy eC-CLEM

In order to successfully align images from EM and cLSM, images from both microscopies should be in the same bit type (e.g. 8-bit and 8-bit RGB). Adjusting bit type can be done by imageJ. Afterwards, open icy and apply plugin eC-CLEM. Drag the EM and cLSM images into the operation dock and specify the type of images by using the option button in the operation dock and selection “2D but let me update myself”. Following the instructions on the screen, select at least 3 corresponding points of the same area in both images to increase the accuracy of alignment. Once the point selection is done, press “update information” and the stop button to create an aligned CLEM image. Redo or delete any points that are not perfectly colocalised to create the best outcome.

3.3.5 Transmission electron microscopy (TEM)

TEM examination was performed on a Tecnai F20 transmission electron microscope operated at an acceleration voltage of 200 kV. The instrument was equipped with a scanning unit for scanning TEM (STEM) and a Tridiem 863 (Gatan) post column electron energy loss spectrometer capable of both, electron energy loss spectroscopy (EELS) and image filtering (EFTEM). Conventional image acquisition was done with a Gatan US 1000 CCD Camera at on-axis position. In post-filter position another Gatan US1000 CCD camera was used for EFTEM and EELS. For bright field imaging and for the acquisition of tomogram tilt series an objective aperture with diameter of 20 μm was used. The same aperture was used for dark field imaging; the beam tilt was adjusted to a value around 2×6.1 mrad, which is the angle of the diamond (111) diffraction for 200 kV electrons. Under these conditions, only electrons that have been diffracted (or inelastically scattered) exactly to the hole of the objective aperture contribute to the image formation. With this imaging mode it is possible, to identify and highlight crystalline areas in the specimen.

STEM was done using a fishione high-angle annual dark-field (HAADF) detector and if not otherwise stated, the camera length was adjusted to 520 mm. At this camera length the diamond

(111) diffraction angle falls into the acceptance angle of the HAADF detector and hence the crystalline areas yield bright contrast.

EFTEM was done using an energy selecting slit width of 10 eV, if not otherwise stated.

3.4 CLEM for intracellular polymeric NPs

This part of protocol corresponds to chapter 2.4.

3.4.1 Cell culture and co-incubation with NPs

RAW264.7 macrophages were seeded in a 24-well plate pre-placed with carbon coated sapphire discs (d:3mm) with a density of 50,000 cells/mL. Macrophages were then cultured in Dulbecco's modified eagle medium (DMEM; Invitrogen, Germany) supplement with 10 % fetal bovine serum (FBS; Sigma Aldrich, Germany), 1 % glutamine, and 1 % penicillin/streptomycin (Invitrogen, Germany) in a humidified incubator at 37 °C and 5 % CO₂. After cell seeding, 24-well plate was placed into the incubator for overnight. Nanoparticles/nanocapsules solution in medium with desired concentration (PS NP-Qdots: 75 µg/mL, nanocapsules: 150 µg/mL, PSNP-PC: 150 µg/mL) were co-incubated with cells for 2 h and then washed away with culture medium.

3.4.2 Sample preparation for correlative light and electron microscopy (CLEM)

After co-incubation, sapphire discs were placed between two aluminium plates to create a 'sandwich' and afterwards were mounted into a holder (Engineering Office, M. Wohlwend) and immediately fixated in a Wohlwend HPF Compact 01 high-pressure freezer (Engineering Office, M. Wohlwend) with a pressure of 2,100 bar. The frozen samples were then stored in liquid nitrogen.

Frozen sapphire discs were carefully removed from the aluminium 'sandwich' and transferred into 1 mL pre-cooled freeze substitution medium (0.2 % (w/v) OsO₄, 0.1 % (w/v) UA, 5 % (v/v) distilled water in acetone) and kept in a freeze substitution unit (AFS2, Leica, Germany). Samples were then slowly warmed up to 0 °C over a period of 20 h in the unit. After being warmed up, the freeze-substituted samples were brought to room temperature, then the substitution medium was removed and the discs were washed 3 times with acetone at half an hour intervals. Then the discs

were infiltrated sequentially in gradient epoxy resin-acetone mixture (1:1, 1:2 and 2:1) for 1 h. Samples were then infiltrated in 100 % epoxy resin overnight. Finally, each sample was transferred into a new Eppendorf tube containing fresh epoxy resin for polymerisation at 60 °C for 24 h.

Following polymerisation, sapphire discs were detached using liquid nitrogen. Resin blocks with the cells imprinted on were trimmed and sectioned into 100 nm sections by a 45° diamond knife (Diatome) in EM UC6 ultramicrotome (Leica, Germany).

3.4.3 For CLEM by TEM inspection

sections were carefully collected on H6 copper finder grids and coated with carbon. Grids were placed onto a coverslip and mounted onto a coverslip holder to be imaged by Leica SP5 cLSM fitted with a 20X dry lens (NA 0.40) or a 64X oil-immersion lens (NA 1.4) and an avalanche photodiode detector (APD). After imaging in cLSM, grids were transferred in a FEI Tecnai F20 transmission electron microscope operated at an acceleration voltage of 200 kV. Micrographs were taken on a Gatan US1000 2k slow scan CCD camera. Image registration and alignment of light and electron microscopy images were accomplished in Icy with eC-CLEM plugin.

3.4.4 For CLEM by SEM inspection

Sections were collected onto ITO-coated coverslip (SPI supplies, USA). Coverslips were then imaged in cLSM with a 20X dry lens (NA 0.40) a 64X oil-immersion lens (NA 1.4) with an avalanche photodiode detector (APD) and later on mounted onto a clap holder to be imaged in HITACHI SU8000 with 2.5 V accelerating voltage and images were acquired with a HA-BSE detector. Image registration and alignment of light and electron microscopy images were done in Icy as previously described.

3.5 CLEM for intracellular protein corona

This part of protocol corresponds to chapter 2.5

3.5.1 Synthesis of carboxy-functionalised PS NPs

Nanoparticles were synthesised by Katja Klein. A macroemulsion was prepared with a continuous phase containing 600 mg Lutensol AT50 (BASF, Germany) solution in 24 mL Milli-Pore water as surfactant and a dispersed phase containing 5.88 g distilled styrene, 251 mg hexadecane (Acros Thermo Fisher, Germany) as hydrophobe, 153 mg distilled acrylic acid for the introduction of carboxy-functionalities, 6.1 mg BODIPY methacrylate as fluorescent dye and 100 mg 2,2'azobis(2methylbutyronitrile) V59 (Wako, Germany) as oilsoluble azo initiator.

The dispersed phase was mechanically stirred. The continuous phase was slowly added to the dispersed phase to achieve homogenization. The macroemulsion was stirred for 1 h at the highest speed. The macroemulsion was then ultrasonicated with a Branson Sonifier (1/2" tip) for 2 min at 450 W 90 % amplitude under icecooling to obtain a miniemulsion. The miniemulsion was transferred into a 50 mL flask and heated to 72 °C in an oil bath under stirring. The polymerisation was performed for 11 h. Subsequently, the dispersion was centrifuged for 1.5 h at 13,000 rpm, 5 times for purification. The supernatant was removed after each centrifugation and the pellet redispersed in Milli-pore water.

3.5.2 RAW264.7 cell culture

The murine macrophage cell line RAW264.7 was cultivated with Dulbecco's Modified Eagle Medium, supplemented with 10 % FBS, 100 U/mL penicillin, and 100 mg/mL streptomycin (all Gibco/Thermo Fisher, Germany). The cells were cultured in an incubator (CO₂ Incubator C200, Labotect, Germany) at 37 °C, 5 % CO₂, and 95 % relative humidity. For subculturing and harvesting, RAW264.7 cells were briefly washed with PBS prior to adding 0.25 % Trypsin-EDTA (Gibco/Thermo Fisher, Germany) for detachment. Cells were collected after incubation for 5 min at 37 °C, 5 % CO₂, and 95 % relative humidity. The same volume of cell culture medium was added and the cells were sedimented by a centrifugation step of 300 g for 5 min. The supernatant was removed. The cell viability and count were measured by an automated cell counter (TC10, Bio-Rad, Germany). The cells were diluted in cell culture medium for the next passage or experiment.

3.5.3 Sample preparation for CLEM

RAW264.7 macrophages were seeded onto 3 mm sapphire disks (M. Wohlwend GmbH). Sapphire disks were pre-coated with a 10-nm-thick carbon layer using an EM MED020 instrument (Leica). The coated sapphire disks were dried and sterilised in an oven at 120 °C overnight before use. Macrophages were seeded onto sapphire disks in 12-well plates overnight for cell attachment. PSCOOH nanoparticles were co-incubated with macrophages in a humidified incubator at 37 °C and 5 % CO₂. After the incubation, each sapphire disk was collected from the 12-well plates and slightly immersed into 1-hexadecene before placing them between two aluminium plates (3 mm, Plano). The aluminium ‘sandwich’ structure was placed into a specimen holder for high pressure freezing in a Wohlwend HPF Compact 01 high pressure freezer with a pressure of 2,100 bar for 2-3 s. The specimen holder was withdrawn from the freezer and immersed into liquid nitrogen to release the sample. The frozen sample was then labelled and stored in a container filled with liquid nitrogen.

Frozen sapphire discs were carefully removed from the aluminium ‘sandwich’ and transferred into 1 mL pre-cooled freeze substitution medium (0.2 % (w/v) OsO₄, 0.1 % (w/v) UA, 5 % (v/v) distilled water in acetone) and kept in a freeze substitution unit (AFS2, Leica). Samples were then slowly warmed up to 0 °C over a period of 20 h in the unit. After being warmed up, the freeze-substituted samples were brought to room temperature, then the substitution medium was removed and the discs were washed 3 times with acetone at half an hour intervals. Then the discs were infiltrated sequentially in gradient epoxy resin-acetone mixture (1;1, 1:2 and 2:1) for 1 h. Samples were then infiltrated in 100 % epoxy resin overnight. Finally, each sample was transferred into a new Eppendorf tube containing fresh epoxy resin for polymerisation at 60 °C for 24 h.

3.5.4 Serial sectioning and CLEM imaging

After polymerisation, sapphire discs were detached using liquid nitrogen. Afterwards, resin blocks were trimmed for later serial sectioning. Trimmed resin blocks were sectioned by an ultra 45° Jumbo diamond knife (Diatome) with a home-made water draining setup. An ITO coated coverslip (SPI) was placed and fixed at the other end of the diamond knife. Diluted glue was placed on either top or bottom side of the trimmed resin block to make sure the sections stay attached in the correct order while sectioning. Section band was carefully moved to coverslip with an eyelash brush until

one end of the band touched the coverslip. Afterwards, water level was carefully lowered with the draining setup until the whole section band slowly attached to the coverslip. Coverslip was then placed on a preheated hotplate to dry completely. Dried coverslip was then imaged in cLSM (SP5, Leica) with a 20X 0.75 NA dry objective for overviews or 63X 1.4 NA oil immersion objective to capture images of selected areas. The same coverslip was later mounted onto a clap holder to be imaged in HITACHI SU8000 with 2.5 V landing voltage 15 mA and a HA-BSE detector. Image registration and alignment of light and electron microscopy images were accomplished in TrackEM in imageJ and icy with eC-CLEM plugin.

3.5.5 Fluorescence colocalisation measurement

To identify protein that has been released from the compartment enclosing the nanoparticles, we developed a macro that measures colocalisation of red and green channels in ImageJ. The ism file of the used ImageJ macro can be found in the SI. After thresholding, a rectangular box is defined around the nanoparticle objects and the protein objects using the ParticleAnalyzer plugin. A protein object is counted as “connected” to a nanoparticle, if its box overlaps or touches a box in the nanoparticle channel.

4. Summary and outlook

Advances in microscopy introduce a new perspective to understand the process of life. The developments in microscopic imaging also connect different fields in science such as structural biology and molecular biology to work more sufficiently together towards solving tough questions. The gap between rapid development of engineered polymeric NPs and relatively small amount of proven applications pinpoints the restrained understanding about the intracellular behaviour of the NPs. This knowledge is urgently needed to optimise the blueprint of smarter nanomedicine for efficient drug delivery.

Chapter 2 addressed the utilisation of correlative imaging techniques to study intracellular NPs and the exploration of new CLEM routine to answer the ultimate question for NPs uptake which is the intracellular fate of protein corona. Accelerated by the extensive sample preparations and informative multi-module analysis of correlative microscopy, the comprehensive study of polymeric NPs transits from in vitro to dynamic cellular milieu. The exploitation of correlative microscopy is instrumental to understand not only the distribution but also the dynamic evolvement of the internalised NPs. The aim of this chapter is to apply and develop suitable imaging methods to comprehend the change of polymeric NPs during cellular processes such as internalisation, cytosol trafficking and lysosomal degradation. Since the content of each section in **Chapter 2** has been summarised in the abstract at the beginning of this chapter, this summary and outlook focus on concluding and extracting the biological information from the imaging findings in each section. **Section 2.4** mainly described the development of an optimised on-section CLEM workflow. This optimised workflow includes OsO₄ staining and EPON embedding for better cellular structure preservation. Fluorescence from the organic dyes Cy5 and BODIPY survived the EM preparation and NPs/NCs were precisely localised in the cells. This workflow was further employed to study intracellular protein corona in **Section 2.5**.

The first step of the intracellular journey for NPs is initiated by internalisation. **Section 2.1-2.3** captured the internalisation events of NPs with the help of different microscopic techniques. **Section 2.1** applied EDX and TEM to localise Fe₃O₄ NPs encapsulated SiO₂ NCs at the site of uptake cellular membrane in HeLa cells (Figure 4.1 a). **Section 2.2** took advantages of ETTEM to precisely capture a single fND during the uptake procedure in HeLa cells (Figure 4.1 b). **Section 2.3** performed CLEM to identify NPLs encapsulated BSA NCs during the engulfment in RAW264.7 macrophages (Figure 4.1 c). The sizes of the NPs/NCs in **Section 2.1** and **Section 2.3** were around 100 nm, and the diameter of fNDs in **Section 2.2** was around 35 nm. The uptake mechanism of NPs is influenced by various factors such as sizes, shapes and surface charges.^[1, 167] Depending on our results, the uptake of SiNCs and BSA NCs were driven by invagination formed by cellular membrane, which is likely to be pinocytosis.^[225] The single particle uptake of fND showed a flask-shaped membrane structure which mostly resembled the caveolae-mediated endocytosis.^[167] All of these NPs/NCs were actively internalised by endocytosis, the exact mediated mechanisms of each NPs/NCs still need to be confirmed with further experiments.

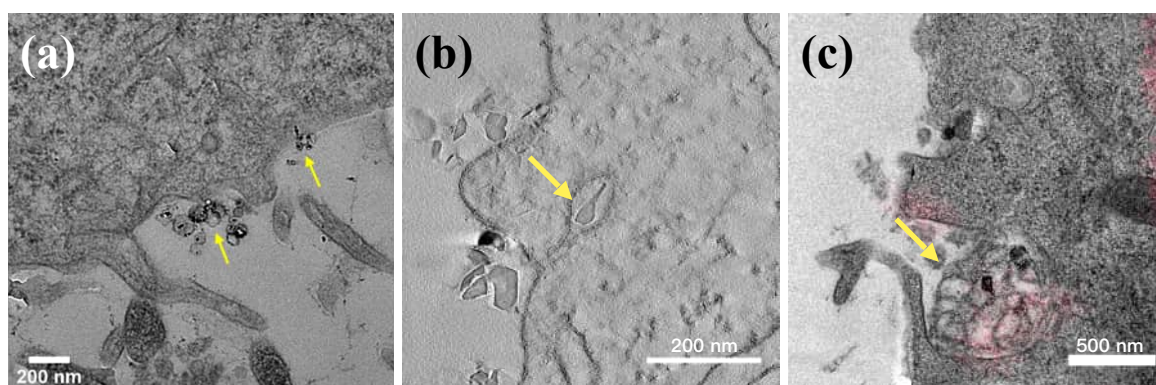


Figure 4.1 Uptake events of different NPs/NCs. a. Pinocytosis of Fe₃O₄ NPs encapsulated SiNCs. **b.** Caveolae-mediated endocytosis of single fNDs. **c.** Pinocytosis of NPLs encapsulated BSA NCs. NPs and NCs are indicated with yellow arrows.

The cellular distribution of NPs after internalisation explains a lot about the biocompatibility and degradability of the NPs. **Section 2.1-2.3** and **Section 2.5** demonstrated the distribution of different NPs/NCs in cells by means of various imaging techniques. With the help of element mapping, **Section 2.1** showed SiNCs and encapsulated Fe₃O₄ NPs in an endolysosome already after 2 h and the electron dense Fe₃O₄ NPs facilitated the locating of SiNCs (Figure 4.2 a). **Section 2.2** and **Section 2.3** demonstrated the applications of in-dish and on-section CLEM to localise fNDs (after 4 h) and BSA NCs (after 2 h) in MVBs and late endosomes (Figure 4.2 b, Figure 4.2 c). **Section 2.5** described an unexpected distribution of protein corona and PS NPs at the time point of 24 h. After the intracellular separation of the protein corona and PS NPs, the separated protein corona were found exclusively in MVBs and the separated PS NPs were mostly found in tubular-like REs (Figure 4.2 d-e). Despite different uptake machineries, the NPs/NCs used the endocytic pathway in cells and ended up in late endosomes or MVBs.

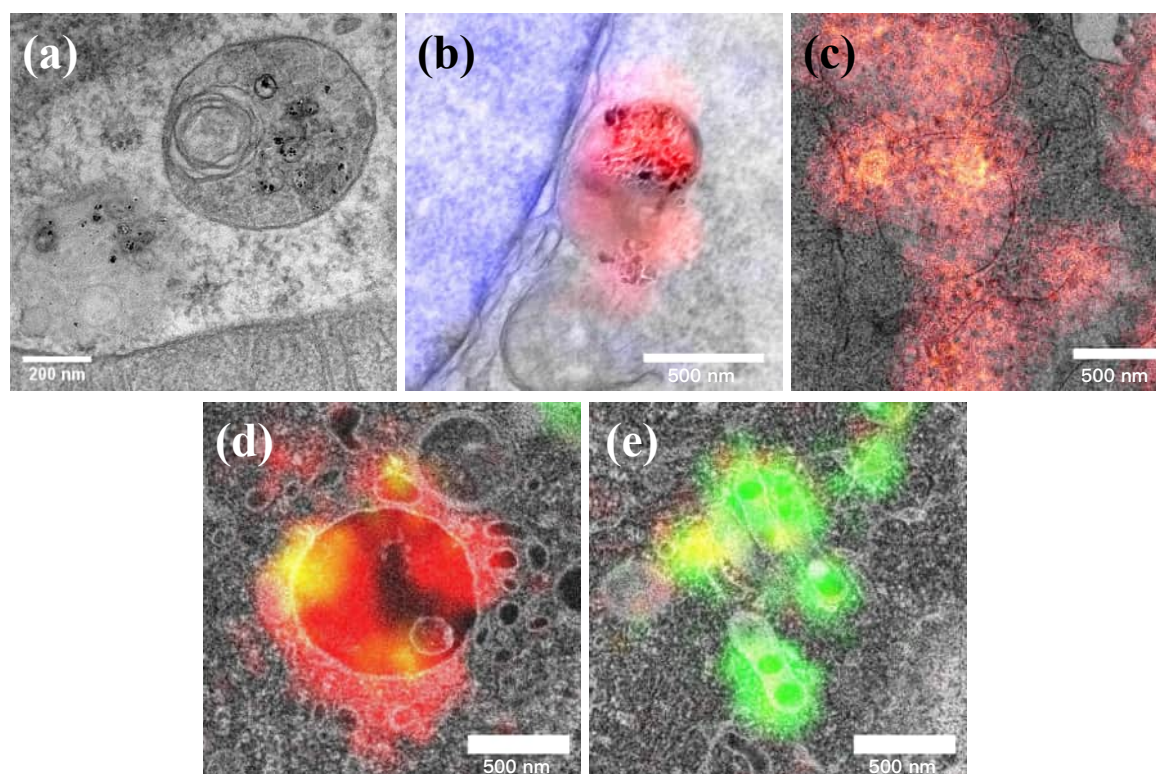


Figure 4.2 Intracellular distribution of different NPs/NCs. **a.** Distribution of Fe₃O₄ NPs encapsulated SiNCs in an endolysosome. **b.** fNDs located in a MVB by CLEM. **c.** NPLs encapsulated BSA NCs located in late endosomes by CLEM. **d.** Distribution of Cy5-labelled protein corona in a MVB. **e.** Distribution of BODIPY-labelled PS NPs in REs.

Degradation is the important final step for NPs in cells. **Section 2.1** and **Section 2.3** showed the degradation of NCs and **Section 2.5** discussed the possible intracellular degradation or exocytosis of protein corona and NPs. The SiNCs in **Section 2.1** and BSA NCs in **Section 2.3** were both designed as potential drug carriers. Degradation of SiNCs were confirmed by EDX of locally separated Si and Fe signal in late endosomes (Figure 4.3 a). The degradation of BSA NCs was confirmed by the lost of capsule's integrity at the site where the fluorescence of NPLs was located in late endosomes and endolysosomes (Figure 4.3 b-c). In **Section 2.5**, PS NPs were used as a model system to study the intracellular pathway of protein corona. Since PS NPs were not degradable for cells,^[45] they were transported into REs after separating from protein corona. Protein corona remained into the matured MVBs and would be degraded by lysosome or secreted via exosomes.

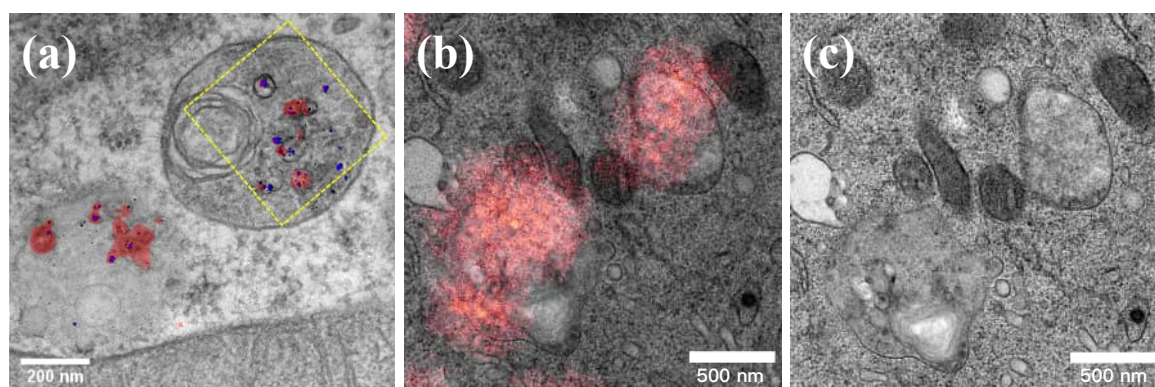


Figure 4.3 Intracellular degradation of NPs. **a.** Degradation of SiNCs in an endolysosome confirmed by EDX, red represents Si signal, blue represents Fe signal. SiNCs and Fe_3O_4 NPs in the endolysosome are highlighted with a yellow dotted square. **b.** BSA PCs located in an end-lysosome and a late endosome by CLEM. **c.** EM micrograph of the CLEM image in **b.**

The cellular procedures for engineered NPs are influenced by many factors such as particle size, shape, and cell types.^[1, 45, 119, 167] The most underlying barrier for the use of engineered NPs is the encounter of the dynamic environment. When studying NPs *in vitro*, there are always limited factors which can be controlled, for example the particles can only be studied with one cell type at a time but not within a multi-cellular environment. That is why an *in vivo* study is always necessary for an in-depth opinion. Once the NPs come in contact with an individual cell, their functional groups will eventually interact with the plasma membrane. However, the distribution of a certain receptor on the membrane highly differs among the cell population and the receptor distribution within one cell is also highly dynamic.^[226] It means that the effective interactions between NPs and cells also depend on the incubation time and the location where the interactions happen. **Section 2.1** and

Section 2.3 didn't describe a specific modification of SiNCs and BSA NCs for targeting functions, this is the reason why we observed the internalisation primarily by pinocytosis. The comparably small fNDs in **Section 2.2** were coated with PEGylated cationic HSA to enhance the interaction with plasma membrane, and that could be the reason why we could identify a single particle uptake. The NPs/NCs all followed the endocytic pathway in the cells and were found in late endosomes or MVBs with an observed degradation for SiNCs and BSA NCs. It is worth mentioning that it is the first time to observe the degradation of NPs in cells by high resolution TEM and CLEM. **Section 2.5** was a further application of the workflow described in **Section 2.4** to finally visualise intracellular fate of protein corona. The separation of protein corona and NPs was purposed for the first time and the exclusive distribution of separated protein corona in MVBs gave a hint on its final fate.

The leverage of different imaging techniques discussed in this thesis have shown immense capacity to study different kinds of engineered NPs in cells. The results of this thesis not only aimed to explore the possibility to develop novel imaging workflow like CLEM, but also unravel the intracellular behaviour of different NPs. By adding an extra layer of information produced by fluorescence or element mapping, more details of hidden interactions between NPs and cells are lit up. The future applications of such advanced microscopic techniques are expected to resolve much softer nanocarriers in cells since the ideal material to form NPs has to be more and more biodegradable and biocompatible, and this kind of material is usually difficult to be seen by conventional imaging.

Literatures

1. Mitchell, M.J., Billingsley, M.M., Haley, R.M., Wechsler, M.E., Peppas, N.A., and Langer, R., *Engineering precision nanoparticles for drug delivery*. Nat Rev Drug Discov, 2021. **20**(2): p. 101-124.
2. Faraji, A.H. and Wipf, P., Nanoparticles in cellular drug delivery. Bioorg Med Chem, 2009. **17**(8): p. 2950-62.
3. Fokkema, J., Fermie, J., Liv, N., van den Heuvel, D.J., Konings, T.O.M., Blab, G.A., Meijerink, A., Klumperman, J., and Gerritsen, H.C., *Fluorescently Labelled Silica Coated Gold Nanoparticles as Fiducial Markers for Correlative Light and Electron Microscopy*. Scientific Reports, 2018. **8**.
4. Calzoni, E., Cesaretti, A., Polchi, A., Di Michele, A., Tancini, B., and Emiliani, C., Biocompatible Polymer Nanoparticles for Drug Delivery Applications in Cancer and Neurodegenerative Disorder Therapies. J Funct Biomater, 2019. **10**(1).
5. Voura, E.B., Jaiswal, J.K., Mattoussi, H., and Simon, S.M., Tracking metastatic tumor cell extravasation with quantum dot nanocrystals and fluorescence emission-scanning microscopy. Nature Medicine, 2004. **10**(9): p. 993-998.
6. Landfester, K., Miniemulsion polymerization and the structure of polymer and hybrid nanoparticles. Angew Chem Int Ed Engl, 2009. **48**(25): p. 4488-507.
7. Wagner, A.M., Gran, M.P., and Peppas, N.A., Designing the new generation of intelligent biocompatible carriers for protein and peptide delivery. Acta Pharmaceutica Sinica B, 2018. **8**(2): p. 147-164.
8. Cheng, Q., Wei, T., Farbiak, L., Johnson, L.T., Dilliard, S.A., and Siegwart, D.J., Selective organ targeting (SORT) nanoparticles for tissue-specific mRNA delivery and CRISPR-Cas gene editing. Nature Nanotechnology, 2020. **15**(4): p. 313-+.
9. Duncan, R., The dawning era of polymer therapeutics. Nature Reviews Drug Discovery, 2003. **2**(5): p. 347-360.
10. Valcourt, D.M., Dang, M.N., Scully, M.A., and Day, E.S., Nanoparticle-Mediated Co-Delivery of Notch-1 Antibodies and ABT-737 as a Potent Treatment Strategy for Triple-Negative Breast Cancer. ACS Nano, 2020. **14**(3): p. 3378-3388.
11. Harris, J.M. and Chess, R.B., Effect of pegylation on pharmaceuticals. Nature Reviews Drug Discovery, 2003. **2**(3): p. 214-221.
12. Ferrari, M., Cancer nanotechnology: opportunities and challenges. Nat Rev Cancer, 2005. **5**(3): p. 161-71.
13. Fenton, O.S., Olafson, K.N., Pillai, P.S., Mitchell, M.J., and Langer, R., *Advances in Biomaterials for Drug Delivery*. Advanced Materials, 2018. **30**(29).
14. Anselmo, A.C. and Mitragotri, S., *Nanoparticles in the clinic: An update*. Bioengineering & Translational Medicine, 2019. **4**(3).
15. Fonseca-Santos, B., Gremiao, M.P.D., and Chorilli, M., Nanotechnology-based drug delivery systems for the treatment of Alzheimer's disease. International Journal of Nanomedicine, 2015. **10**.
16. Sercombe, L., Veerati, T., Moheimani, F., Wu, S.Y., Sood, A.K., and Hua, S., *Advances and Challenges of Liposome Assisted Drug Delivery*. Frontiers in Pharmacology, 2015. **6**.
17. Schoenmaker, L., Witzigmann, D., Kulkarni, J.A., Verbeke, R., Kersten, G., Jiskoot, W., and Crommelin, D.J.A., *mRNA-lipid nanoparticle COVID-19 vaccines: Structure and stability*. Int J Pharm, 2021. **601**: p. 120586.
18. Wang, X., Safety and Efficacy of the BNT162b2 mRNA Covid-19 Vaccine. N Engl J Med, 2021. **384**(16): p. 1577-1578.
19. Hafez, I.M., Maurer, N., and Cullis, P.R., On the mechanism whereby cationic lipids promote intracellular delivery of polynucleic acids. Gene Therapy, 2001. **8**(15): p. 1188-1196.

20. Reichmuth, A.M., Oberli, M.A., Jaklenec, A., Langer, R., and Blankschtein, D., *mRNA vaccine delivery using lipid nanoparticles*. *Therapeutic Delivery*, 2016. **7**(5): p. 319-334.
21. Caldorera-Moore, M., Ramirez, J.E.V., and Peppas, N.A., Transport and delivery of interferon-through epithelial tight junctions via pH-responsive poly(methacrylic acid-grafted-ethylene glycol) nanoparticles. *Journal of Drug Targeting*, 2019. **27**(5-6): p. 582-589.
22. Liu, X.Y., Li, C., Lv, J., Huang, F., An, Y.L., Shi, L.Q., and Ma, R.J., Glucose and H₂O₂ Dual-Responsive Polymeric Micelles for the Self-Regulated Release of Insulin. *ACS Applied Bio Materials*, 2020. **3**(3): p. 1598-1606.
23. Zhang, L.B., Beatty, A., Lu, L., Abdalrahman, A., Makris, T.M., Wang, G.R., and Wang, Q., Microfluidic-assisted polymer-protein assembly to fabricate homogeneous functionalnanoparticles. *Materials Science & Engineering C-Materials for Biological Applications*, 2020. **111**.
24. Strand, M.S., Krasnick, B.A., Pan, H., Zhang, X., Bi, Y., Brooks, C., Wetzel, C., Sankpal, N., Fleming, T., Goedegebuure, S.P., DeNardo, D.G., Gillanders, W.E., Hawkins, W.G., Wickline, S.A., and Fields, R.C., *Precision delivery of RAS-inhibiting siRNA to KRAS driven cancer via peptide-based nanoparticles*. *Oncotarget*, 2019. **10**(46): p. 4761-4775.
25. Patra, J.K., Das, G., Fraceto, L.F., Campos, E.V.R., Rodriguez-Torres, M.D.P., Acosta-Torres, L.S., Diaz-Torres, L.A., Grillo, R., Swamy, M.K., Sharma, S., Habtemariam, S., and Shin, H.S., *Nano based drug delivery systems: recent developments and future prospects*. *J Nanobiotechnology*, 2018. **16**(1): p. 71.
26. Baier, G., Baumann, D., Siebert, J.M., Musyanovych, A., Mailander, V., and Landfester, K., Suppressing unspecific cell uptake for targeted delivery using hydroxyethyl starch nanocapsules. *Biomacromolecules*, 2012. **13**(9): p. 2704-15.
27. He, X.X., Wang, K.M., Tan, W.H., Liu, B., Lin, X., He, C.M., Li, D., Huang, S.S., and Li, J., *Bioconjugated nanoparticles for DNA protection from cleavage*. *Journal of the American Chemical Society*, 2003. **125**(24): p. 7168-7169.
28. Jiang, S., Prozeller, D., Pereira, J., Simon, J., Han, S., Wirsching, S., Fichter, M., Mottola, M., Lieberwirth, I., Morsbach, S., Mailander, V., Gehring, S., Crespy, D., and Landfester, K., *Controlling protein interactions in blood for effective liver immunosuppressive therapy by silica nanocapsules*. *Nanoscale*, 2020. **12**(4): p. 2626-2637.
29. Kaczmarek, J.C., Kauffman, K.J., Fenton, O.S., Sadder, K., Patel, A.K., Heartlein, M.W., DeRosa, F., and Anderson, D.G., Optimization of a Degradable Polymer-Lipid Nanoparticle for Potent Systemic Delivery of mRNA to the Lung Endothelium and Immune Cells. *Nano Letters*, 2018. **18**(10): p. 6449-6454.
30. Chen, G.J., Abdeen, A.A., Wang, Y.Y., Shahi, P.K., Robertson, S., Xie, R.S., Suzuki, M., Pattnaik, B.R., Saha, K., and Gong, S.Q., *A biodegradable nanocapsule delivers a Cas9 ribonucleoprotein complex for in vivo genome editing*. *Nature Nanotechnology*, 2019. **14**(10): p. 974-+.
31. He, Q.J., Shi, J.L., Zhu, M., Chen, Y., and Chen, F., The three-stage in vitro degradation behavior of mesoporous silica in simulated body fluid. *Microporous and Mesoporous Materials*, 2010. **131**(1-3): p. 314-320.
32. Hirsch, L.R., Stafford, R.J., Bankson, J.A., Sershen, S.R., Rivera, B., Price, R.E., Hazle, J.D., Halas, N.J., and West, J.L., *Nanoshell-mediated near-infrared thermal therapy of tumors under magnetic resonance guidance*. *Proceedings of the National Academy of Sciences of the United States of America*, 2003. **100**(23): p. 13549-13554.
33. Piradashvili, K., Fichter, M., Mohr, K., Gehring, S., Wurm, F.R., and Landfester, K., *Biodegradable protein nanocontainers*. *Biomacromolecules*, 2015. **16**(3): p. 815-21.
34. Frey, M.L., Simon, J., Bruckner, M., Mailander, V., Morsbach, S., and Landfester, K., Bio-orthogonal triazolinedione (TAD) crosslinked protein nanocapsules affect protein adsorption and cell interaction. *Polymer Chemistry*, 2020. **11**(23): p. 3821-3830.

35. Sedighi, M., Sieber, S., Rahimi, F., Shahbazi, M.A., Rezayan, A.H., Huwyler, J., and Witzigmann, D., Rapid optimization of liposome characteristics using a combined microfluidics and design-of-experiment approach. *Drug Delivery and Translational Research*, 2019. **9**(1): p. 404-413.
36. Li, M.Y., Jiang, S., Simon, J., Passlick, D., Frey, M.L., Wagner, M., Mailander, V., Crespy, D., and Landfester, K., Brush Conformation of Polyethylene Glycol Determines the Stealth Effect of Nanocarriers in the Low Protein Adsorption Regime. *Nano Letters*, 2021. **21**(4): p. 1591-1598.
37. Palanikumar, L., Al-Hosani, S., Kalmouni, M., Nguyen, V.P., Ali, L., Pasricha, R., Barrera, F.N., and Magzoub, M., *pH-responsive high stability polymeric nanoparticles for targeted delivery of anticancer therapeutics*. *Communications Biology*, 2020. **3**(1).
38. Wang, X.Y., Ishida, T., and Kiwada, H., Anti-PEG IgM elicited by injection of liposomes is involved in the enhanced blood clearance of a subsequent dose of PEGylated liposomes. *Journal of Controlled Release*, 2007. **119**(2): p. 236-244.
39. Yang, Q., Jacobs, T.M., McCallen, J.D., Moore, D.T., Huckaby, J.T., Edelstein, J.N., and Lai, S.K., Analysis of Pre-existing IgG and IgM Antibodies against Polyethylene Glycol (PEG) in the General Population. *Analytical Chemistry*, 2016. **88**(23): p. 11804-11812.
40. Blanco, E., Shen, H., and Ferrari, M., Principles of nanoparticle design for overcoming biological barriers to drug delivery. *Nature Biotechnology*, 2015. **33**(9): p. 941-951.
41. Tantra, R. and Knight, A., Cellular uptake and intracellular fate of engineered nanoparticles: A review on the application of imaging techniques. *Nanotoxicology*, 2011. **5**(3): p. 381-392.
42. Schermelleh, L., Heintzmann, R., and Leonhardt, H., *A guide to super-resolution fluorescence microscopy*. *J Cell Biol*, 2010. **190**(2): p. 165-75.
43. Reisch, A., Didier, P., Richert, L., Oncul, S., Arntz, Y., Mely, Y., and Klymchenko, A.S., *Collective fluorescence switching of counterion-assembled dyes in polymer nanoparticles*. *Nat Commun*, 2014. **5**: p. 4089.
44. Flannigan, D.J. and Zewail, A.H., 4D electron microscopy: principles and applications. *Acc Chem Res*, 2012. **45**(10): p. 1828-39.
45. Reifarh, M., Hoepfner, S., and Schubert, U.S., Uptake and Intracellular Fate of Engineered Nanoparticles in Mammalian Cells: Capabilities and Limitations of Transmission Electron Microscopy-Polymer-Based Nanoparticles. *Adv Mater*, 2018. **30**(9).
46. Reifarh, M., Schubert, U.S., and Hoepfner, S., Considerations for the Uptake Characteristic of Inorganic Nanoparticles into Mammalian Cells-Insights Gained by TEM Investigations. *Advanced Biosystems*, 2018. **2**(8).
47. Abdallah, M.A., Sharkey, M., Berresheim, H., and Harrad, S., Hexabromocyclododecane in polystyrene packaging: A downside of recycling? *Chemosphere*, 2018. **199**: p. 612-616.
48. Jickells, S.M., Gancedo, P., Nerin, C., Castle, L., and Gilbert, J., Migration of styrene monomer from thermoset polyester cookware into foods during high temperature applications. *Food Addit Contam*, 1993. **10**(5): p. 567-73.
49. Bojic, S., Falco, M.M., Stojkovic, P., Ljubic, B., Gazdic Jankovic, M., Armstrong, L., Markovic, N., Dopazo, J., Lako, M., Bauer, R., and Stojkovic, M., *Platform to study intracellular polystyrene nanoplastic pollution and clinical outcomes*. *Stem Cells*, 2020. **38**(10): p. 1321-1325.
50. Kelly, P.M., Aberg, C., Polo, E., O'Connell, A., Cookman, J., Fallon, J., Krpetic, Z., and Dawson, K.A., *Mapping protein binding sites on the biomolecular corona of nanoparticles*. *Nat Nanotechnol*, 2015. **10**(5): p. 472-9.
51. Tonigold, M., Simon, J., Estupinan, D., Kokkinopoulou, M., Reinholz, J., Kintzel, U., Kaltbeitzel, A., Renz, P., Domogalla, M.P., Steinbrink, K., Lieberwirth, I., Crespy, D., Landfester, K., and Mailander, V., *Pre-adsorption of antibodies enables targeting of nanocarriers despite a biomolecular corona*. *Nat Nanotechnol*, 2018. **13**(9): p. 862-869.

52. Firdessa, R., Oelschlaeger, T.A., and Moll, H., Identification of multiple cellular uptake pathways of polystyrene nanoparticles and factors affecting the uptake: relevance for drug delivery systems. *Eur J Cell Biol*, 2014. **93**(8-9): p. 323-37.
53. Musyanovych, A., Dausend, J., Dass, M., Walther, P., Mailander, V., and Landfester, K., Criteria impacting the cellular uptake of nanoparticles: a study emphasizing polymer type and surfactant effects. *Acta Biomater*, 2011. **7**(12): p. 4160-8.
54. Lerch, S., Ritz, S., Bley, K., Messerschmidt, C., Weiss, C.K., Musyanovych, A., Landfester, K., and Mailander, V., *Nanoprobng the acidification process during intracellular uptake and trafficking*. *Nanomedicine*, 2015. **11**(6): p. 1585-96.
55. Yan, M., Du, J., Gu, Z., Liang, M., Hu, Y., Zhang, W., Priceman, S., Wu, L., Zhou, Z.H., Liu, Z., Segura, T., Tang, Y., and Lu, Y., *A novel intracellular protein delivery platform based on single-protein nanocapsules*. *Nat Nanotechnol*, 2010. **5**(1): p. 48-53.
56. de Boer, P., Hoogenboom, J.P., and Giepmans, B.N., Correlated light and electron microscopy: ultrastructure lights up! *Nat Methods*, 2015. **12**(6): p. 503-13.
57. Nune, S.K., Gunda, P., Thallapally, P.K., Lin, Y.Y., Forrest, M.L., and Berkland, C.J., *Nanoparticles for biomedical imaging*. *Expert Opin Drug Deliv*, 2009. **6**(11): p. 1175-94.
58. Day, E.S., Bickford, L.R., Slater, J.H., Riggall, N.S., Drezek, R.A., and West, J.L., Antibody-conjugated gold-gold sulfide nanoparticles as multifunctional agents for imaging and therapy of breast cancer. *International Journal of Nanomedicine*, 2010. **5**: p. 445-454.
59. Reifarth, M., Preussger, E., Schubert, U.S., Heintzmann, R., and Hoepfner, S., Metal-Polymer Hybrid Nanoparticles for Correlative High-Resolution Light and Electron Microscopy. *Particle & Particle Systems Characterization*, 2017. **34**(10).
60. Fortin, M.A., Simao, T., and Laprise-Pelletier, M., *Gold Nanoparticles for Imaging and Cancer Therapy*. *Nanooncology: Engineering Nanomaterials for Cancer Therapy and Diagnosis*, 2018: p. 1-50.
61. Robinson, J.M., Takizawa, T., and Vandre, D.D., Applications of gold cluster compounds in immunocytochemistry and correlative microscopy: comparison with colloidal gold. *J Microsc*, 2000. **199**(Pt 3): p. 163-79.
62. Takizawa, T., Powell, R.D., Hainfeld, J.F., and Robinson, J.M., *FluoroNanogold: an important probe for correlative microscopy*. *J Chem Biol*, 2015. **8**(4): p. 129-42.
63. Bose, K., Koch, M., Cavelius, C., Kiemer, A.K., and Kraegeloh, A., A Correlative Analysis of Gold Nanoparticles Internalized by A549 Cells. *Particle & Particle Systems Characterization*, 2014. **31**(4): p. 439-448.
64. Mutavdzic, D., Xu, J., Thakur, G., Triulzi, R., Kasas, S., Jeremic, M., Leblanc, R., and Radotic, K., *Determination of the size of quantum dots by fluorescence spectroscopy*. *Analyst*, 2011. **136**(11): p. 2391-6.
65. He, H., Lin, Y., Tian, Z.Q., Zhu, D.L., Zhang, Z.L., and Pang, D.W., Ultrasmall Pb:Ag₂S Quantum Dots with Uniform Particle Size and Bright Tunable Fluorescence in the NIR-II Window. *Small*, 2018. **14**(11): p. e1703296.
66. Saha, D. and Negi, D.P.S., Particle size enlargement and 6-fold fluorescence enhancement of colloidal CdS quantum dots induced by selenious acid. *Spectrochim Acta A Mol Biomol Spectrosc*, 2020. **225**: p. 117486.
67. Chan, W.C. and Nie, S., Quantum dot bioconjugates for ultrasensitive nonisotopic detection. *Science*, 1998. **281**(5385): p. 2016-8.
68. Dukes, M.J., Peckys, D.B., and de Jonge, N., Correlative fluorescence microscopy and scanning transmission electron microscopy of quantum-dot-labeled proteins in whole cells in liquid. *ACS Nano*, 2010. **4**(7): p. 4110-6.
69. Giepmans, B.N., Deerinck, T.J., Smarr, B.L., Jones, Y.Z., and Ellisman, M.H., Correlated light and electron microscopic imaging of multiple endogenous proteins using Quantum dots. *Nat Methods*, 2005. **2**(10): p. 743-9.

70. Butterworth, K.T., Coulter, J.A., Jain, S., Forker, J., McMahon, S.J., Schettino, G., Prise, K.M., Currell, F.J., and Hirst, D.G., *Evaluation of cytotoxicity and radiation enhancement using 1.9 nm gold particles: potential application for cancer therapy*. *Nanotechnology*, 2010. **21**(29): p. 295101.
71. Das, B., Girigoswami, A., Pal, P., and Dhara, S., Manganese oxide-carbon quantum dots nano-composites for fluorescence/magnetic resonance (T1) dual mode bioimaging, long term cell tracking, and ROS scavenging. *Mater Sci Eng C Mater Biol Appl*, 2019. **102**: p. 427-436.
72. Desai, M.L., Deshmukh, B., Lenka, N., Haran, V., Jha, S., Basu, H., Singhal, R.K., Sharma, P.K., Kailasa, S.K., and Kim, K.H., Influence of doping ion, capping agent and pH on the fluorescence properties of zinc sulfide quantum dots: Sensing of Cu(2+) and Hg(2+) ions and their biocompatibility with cancer and fungal cells. *Spectrochim Acta A Mol Biomol Spectrosc*, 2019. **210**: p. 212-221.
73. Hollander, H., The section embedding (SE) technique. A new method for the combined light microscopic and electron microscopic examination of central nervous tissue. *Brain Res*, 1970. **20**(1): p. 39-47.
74. Ando, T., Bhamidimarri, S.P., Brending, N., Colin-York, H., Collinson, L., De Jonge, N., de Pablo, P.J., Debroye, E., Eggeling, C., Franck, C., Fritzsche, M., Gerritsen, H., Giepmans, B.N.G., Grunewald, K., Hofkens, J., Hoogenboom, J.P., Janssen, K.P.F., Kaufman, R., Klumpermann, J., Kurniawan, N., Kusch, J., Liv, N., Parekh, V., Peckys, D.B., Rehfeldt, F., Reutens, D.C., Roeffaers, M.B.J., Salditt, T., Schaap, I.A.T., Schwarz, U.S., Verkade, P., Vogel, M.W., Wagner, R., Winterhalter, M., Yuan, H., and Zifarelli, G., *The 2018 correlative microscopy techniques roadmap*. *J Phys D Appl Phys*, 2018. **51**(44): p. 443001.
75. Zila, V., Margiotta, E., Turonova, B., Muller, T.G., Zimmerli, C.E., Mattei, S., Allegretti, M., Borner, K., Rada, J., Muller, B., Lusic, M., Krausslich, H.G., and Beck, M., *Cone-shaped HIV-1 capsids are transported through intact nuclear pores*. *Cell*, 2021. **184**(4): p. 1032-+.
76. Fermie, J., Liv, N., ten Brink, C., van Donselaar, E.G., Muller, W.H., Schieber, N.L., Schwab, Y., Gerritsen, H.C., and Klumperman, J., *Single organelle dynamics linked to 3D structure by correlative live-cell imaging and 3D electron microscopy*. *Traffic*, 2018. **19**(5): p. 354-369.
77. Scotuzzi, M., Kuipers, J., Wensveen, D.I., de Boer, P., Hagen, K.W., Hoogenboom, J.P., and Giepmans, B.N.G., *Multi-color electron microscopy by element-guided identification of cells, organelles and molecules*. *Scientific Reports*, 2017. **7**.
78. Arroyo-Camejo, S., Adam, M.P., Besbes, M., Hugonin, J.P., Jacques, V., Greffet, J.J., Roch, J.F., Hell, S.W., and Treussart, F., *Stimulated emission depletion microscopy resolves individual nitrogen vacancy centers in diamond nanocrystals*. *ACS Nano*, 2013. **7**(12): p. 10912-9.
79. Hadjidemetriou, M. and Kostarelos, K., NANOMEDICINE Evolution of the nanoparticle corona. *Nature Nanotechnology*, 2017. **12**(4): p. 288-290.
80. Jiang, S., Mottola, M., Han, S., Thiramanas, R., Graf, R., Lieberwirth, I., Mailaender, V., Crespy, D., and Landfester, K., *Versatile Preparation of Silica Nanocapsules for Biomedical Applications*. *Particle & Particle Systems Characterization*, 2020. **37**(4).
81. Heidel, J.D. and Davis, M.E., Clinical developments in nanotechnology for cancer therapy. *Pharm Res*, 2011. **28**(2): p. 187-99.
82. Lammers, T., Kiessling, F., Hennink, W.E., and Storm, G., Drug targeting to tumors: principles, pitfalls and (pre-) clinical progress. *J Control Release*, 2012. **161**(2): p. 175-87.
83. Wang, A.Z., Langer, R., and Farokhzad, O.C., *Nanoparticle delivery of cancer drugs*. *Annu Rev Med*, 2012. **63**: p. 185-98.
84. Kannan, R.M., Nance, E., Kannan, S., and Tomalia, D.A., Emerging concepts in dendrimer-based nanomedicine: from design principles to clinical applications. *J Intern Med*, 2014. **276**(6): p. 579-617.
85. Kim, J., Piao, Y., and Hyeon, T., Multifunctional nanostructured materials for multimodal imaging, and simultaneous imaging and therapy. *Chem Soc Rev*, 2009. **38**(2): p. 372-90.
86. Janib, S.M., Moses, A.S., and MacKay, J.A., Imaging and drug delivery using theranostic nanoparticles. *Advanced Drug Delivery Reviews*, 2010. **62**(11): p. 1052-1063.

87. Xie, J., Lee, S., and Chen, X., Nanoparticle-based theranostic agents. *Adv Drug Deliv Rev*, 2010. **62**(11): p. 1064-79.
88. Chen, X., Gambhir, S.S., and Cheon, J., *Theranostic nanomedicine*. *Acc Chem Res*, 2011. **44**(10): p. 841.
89. Yoo, D., Lee, J.H., Shin, T.H., and Cheon, J., *Theranostic magnetic nanoparticles*. *Acc Chem Res*, 2011. **44**(10): p. 863-74.
90. Li, Z., Barnes, J.C., Bosoy, A., Stoddart, J.F., and Zink, J.I., *Mesoporous silica nanoparticles in biomedical applications*. *Chem Soc Rev*, 2012. **41**(7): p. 2590-605.
91. Tang, F., Li, L., and Chen, D., Mesoporous silica nanoparticles: synthesis, biocompatibility and drug delivery. *Adv Mater*, 2012. **24**(12): p. 1504-34.
92. Yang, P., Gai, S., and Lin, J., Functionalized mesoporous silica materials for controlled drug delivery. *Chem Soc Rev*, 2012. **41**(9): p. 3679-98.
93. Maity, A. and Polshettiwar, V., Dendritic Fibrous Nanosilica for Catalysis, Energy Harvesting, Carbon Dioxide Mitigation, Drug Delivery, and Sensing. *ChemSusChem*, 2017. **10**(20): p. 3866-3913.
94. Wibowo, D., Hui, Y., Middelberg, A.P., and Zhao, C.X., *Interfacial engineering for silica nanocapsules*. *Adv Colloid Interface Sci*, 2016. **236**: p. 83-100.
95. Wang, D., Xu, Z., Chen, Z., Liu, X., Hou, C., Zhang, X., and Zhang, H., Fabrication of single-hole glutathione-responsive degradable hollow silica nanoparticles for drug delivery. *ACS Appl Mater Interfaces*, 2014. **6**(15): p. 12600-8.
96. Zhou, M., Du, X., Li, W., Li, X., Huang, H., Liao, Q., Shi, B., Zhang, X., and Zhang, M., One-pot synthesis of redox-triggered biodegradable hybrid nanocapsules with a disulfide-bridged silsesquioxane framework for promising drug delivery. *J Mater Chem B*, 2017. **5**(23): p. 4455-4469.
97. Huang, P., Chen, Y., Lin, H., Yu, L.D., Zhang, L.L., Wang, L.Y., Zhu, Y.F., and Shi, J.L., Molecularly organic/inorganic hybrid hollow mesoporous organosilica nanocapsules with tumor-specific biodegradability and enhanced chemotherapeutic functionality. *Biomaterials*, 2017. **125**: p. 23-37.
98. Ow, H., Larson, D.R., Srivastava, M., Baird, B.A., Webb, W.W., and Wiesner, U., *Bright and stable core-shell fluorescent silica nanoparticles*. *Nano Lett*, 2005. **5**(1): p. 113-7.
99. Burns, A., Ow, H., and Wiesner, U., Fluorescent core-shell silica nanoparticles: towards "Lab on a Particle" architectures for nanobiotechnology. *Chemical Society Reviews*, 2006. **35**(11): p. 1028-1042.
100. Chang, F.P., Chen, Y.P., and Mou, C.Y., Intracellular implantation of enzymes in hollow silica nanospheres for protein therapy: cascade system of superoxide dismutase and catalase. *Small*, 2014. **10**(22): p. 4785-95.
101. Chang, F.P., Hung, Y., Chang, J.H., Lin, C.H., and Mou, C.Y., Enzyme encapsulated hollow silica nanospheres for intracellular biocatalysis. *ACS Appl Mater Interfaces*, 2014. **6**(9): p. 6883-90.
102. Jiang, S., Landfester, K., and Crespy, D., Control of the release of functional payloads from redox-responsive nanocapsules. *Rsc Advances*, 2016. **6**(106): p. 104330-104337.
103. Jiang, S., Lv, L., Li, Q., Wang, J., Landfester, K., and Crespy, D., *Tailoring nanoarchitectonics to control the release profile of payloads*. *Nanoscale*, 2016. **8**(22): p. 11511-7.
104. Fickert, J., Rupper, P., Graf, R., Landfester, K., and Crespy, D., Design and characterization of functionalized silica nanocontainers for self-healing materials. *Journal of Materials Chemistry*, 2012. **22**(5): p. 2286-2291.
105. Qian, K., Shi, T.Y., He, S., Luo, L.X., Liu, X.L., and Cao, Y.S., Release kinetics of tebuconazole from porous hollow silica nanospheres prepared by miniemulsion method. *Microporous and Mesoporous Materials*, 2013. **169**: p. 1-6.
106. Wibowo, D., Zhao, C.X., and Middelberg, A.P.J., Emulsion-templated silica nanocapsules formed using bio-inspired silicification. *Chemical Communications*, 2014. **50**(77): p. 11325-11328.
107. Hayashi, K., Nakamura, M., and Ishimura, K., In situ synthesis and photoresponsive rupture of organosilica nanocapsules. *Chemical Communications*, 2011. **47**(5): p. 1518-1520.

108. Jiang, S., Ma, B.C., Reinholz, J., Li, Q.F., Wang, J.W., Zhang, K.A.I., Landfester, K., and Crespy, D., *Efficient Nanofibrous Membranes for Antibacterial Wound Dressing and UV Protection*. *ACS Applied Materials & Interfaces*, 2016. **8**(44): p. 29915-29922.
109. Sun, L., Zang, Y., Sun, M.D., Wang, H.G., Zhu, X.J., Xu, S.F., Yang, Q.B., Li, Y.X., and Shan, Y.M., *Synthesis of magnetic and fluorescent multifunctional hollow silica nanocomposites for live cell imaging*. *Journal of Colloid and Interface Science*, 2010. **350**(1): p. 90-98.
110. Ma, M., Yan, F., Yao, M.H., Wei, Z.J., Zhou, D.L., Yao, H.L., Zheng, H.R., Chen, H.R., and Shi, J.L., *Template-Free Synthesis of Hollow/Porous Organosilica-Fe₃O₄ Hybrid Nanocapsules toward Magnetic Resonance Imaging-Guided High-Intensity Focused Ultrasound Therapy*. *ACS Applied Materials & Interfaces*, 2016. **8**(44): p. 29986-29996.
111. Chen, H.M., He, J.H., Tang, H.M., and Yan, C.X., *Porous silica nanocapsules and nanospheres: Dynamic self-assembly synthesis and application in controlled release*. *Chemistry of Materials*, 2008. **20**(18): p. 5894-5900.
112. Latham, P.W., *Therapeutic peptides revisited*. *Nature Biotechnology*, 1999. **17**(8): p. 755-757.
113. Wibowo, D., Zhao, C.X., and Middelberg, A.P.J., *Interfacial Biomimetic Synthesis of Silica Nanocapsules Using a Recombinant Catalytic Modular Protein*. *Langmuir*, 2015. **31**(6): p. 1999-2007.
114. Jakhmola, A., Vecchione, R., Guarnieri, D., Belli, V., Calabria, D., and Netti, P.A., *Bioinspired Oil Core/Silica Shell Nanocarriers with Tunable and Multimodal Functionalities*. *Advanced Healthcare Materials*, 2015. **4**(17): p. 2688-2698.
115. Erni, P., Dardelle, G., Sillick, M., Wong, K., Beaussoubre, P., and Fieber, W., *Turning Coacervates into Biohybrid Glass: Core/Shell Capsules Formed by Silica Precipitation in Protein/Polysaccharide Scaffolds*. *Angewandte Chemie-International Edition*, 2013. **52**(39): p. 10334-10338.
116. Hans, M.L. and Lowman, A.M., *Biodegradable nanoparticles for drug delivery and targeting*. *Current Opinion in Solid State & Materials Science*, 2002. **6**(4): p. 319-327.
117. Lim, Y.T., Kim, J.K., Noh, Y.W., Cho, M.Y., and Chung, B.H., *Multifunctional silica nanocapsule with a single surface hole*. *Small*, 2009. **5**(3): p. 324-8.
118. Xuan, M., Shao, J., Dai, L., He, Q., and Li, J., *Macrophage Cell Membrane Camouflaged Mesoporous Silica Nanocapsules for In Vivo Cancer Therapy*. *Adv Healthc Mater*, 2015. **4**(11): p. 1645-52.
119. Behzadi, S., Serpooshan, V., Tao, W., Hamaly, M.A., Alkawareek, M.Y., Dreaden, E.C., Brown, D., Alkilany, A.M., Farokhzad, O.C., and Mahmoudi, M., *Cellular uptake of nanoparticles: journey inside the cell*. *Chemical Society Reviews*, 2017. **46**(14): p. 4218-4244.
120. Cauda, V., Schlossbauer, A., and Bein, T., *Bio-degradation study of colloidal mesoporous silica nanoparticles: Effect of surface functionalization with organo-silanes and poly(ethylene glycol)*. *Microporous and Mesoporous Materials*, 2010. **132**(1-2): p. 60-71.
121. Han, S., Raabe, M., Hodgson, L., Mantell, J., Verkade, P., Lasser, T., Landfester, K., Weil, T., and Lieberwirth, I., *High-Contrast Imaging of Nanodiamonds in Cells by Energy Filtered and Correlative Light-Electron Microscopy: Toward a Quantitative Nanoparticle-Cell Analysis*. *Nano Lett*, 2019. **19**(3): p. 2178-2185.
122. Pelaz, B., Alexiou, C., Alvarez-Puebla, R.A., Alves, F., Andrews, A.M., Ashraf, S., Balogh, L.P., Ballerini, L., Bestetti, A., Brendel, C., Bosi, S., Carril, M., Chan, W.C., Chen, C., Chen, X., Chen, X., Cheng, Z., Cui, D., Du, J., Dullin, C., Escudero, A., Feliu, N., Gao, M., George, M., Gogotsi, Y., Grunweller, A., Gu, Z., Halas, N.J., Hampp, N., Hartmann, R.K., Hersam, M.C., Hunziker, P., Jian, J., Jiang, X., Jungebluth, P., Kadhiresan, P., Kataoka, K., Khademhosseini, A., Kopecek, J., Kotov, N.A., Krug, H.F., Lee, D.S., Lehr, C.M., Leong, K.W., Liang, X.J., Ling Lim, M., Liz-Marzan, L.M., Ma, X., Macchiarelli, P., Meng, H., Mohwald, H., Mulvaney, P., Nel, A.E., Nie, S., Nordlander, P., Okano, T., Oliveira, J., Park, T.H., Penner, R.M., Prato, M., Puntès, V., Rotello, V.M., Samarakoon, A., Schaak, R.E., Shen, Y., Sjoqvist, S., Skirtach, A.G., Soliman, M.G., Stevens, M.M., Sung, H.W., Tang, B.Z., Tietze, R., Udugama, B.N., VanEpps, J.S.,

- Weil, T., Weiss, P.S., Willner, I., Wu, Y., Yang, L., Yue, Z., Zhang, Q., Zhang, Q., Zhang, X.E., Zhao, Y., Zhou, X., and Parak, W.J., *Diverse Applications of Nanomedicine*. ACS Nano, 2017. **11**(3): p. 2313-2381.
123. Velasco-Aguirre, C., Morales, F., Gallardo-Toledo, E., Guerrero, S., Giralt, E., Araya, E., and Kogan, M.J., *Peptides and proteins used to enhance gold nanoparticle delivery to the brain: preclinical approaches*. Int J Nanomedicine, 2015. **10**: p. 4919-36.
124. Mailander, V. and Landfester, K., Interaction of nanoparticles with cells. Biomacromolecules, 2009. **10**(9): p. 2379-400.
125. Ritz, S., Schottler, S., Kotman, N., Baier, G., Musyanovych, A., Kuharev, J., Landfester, K., Schild, H., Jahn, O., Tenzer, S., and Mailander, V., *Protein corona of nanoparticles: distinct proteins regulate the cellular uptake*. Biomacromolecules, 2015. **16**(4): p. 1311-21.
126. Kokkinopoulou, M., Simon, J., Landfester, K., Mailander, V., and Lieberwirth, I., Visualization of the protein corona: towards a biomolecular understanding of nanoparticle-cell-interactions. Nanoscale, 2017. **9**(25): p. 8858-8870.
127. Salvati, A., Pitek, A.S., Monopoli, M.P., Prapainop, K., Bombelli, F.B., Hristov, D.R., Kelly, P.M., Aberg, C., Mahon, E., and Dawson, K.A., *Transferrin-functionalized nanoparticles lose their targeting capabilities when a biomolecule corona adsorbs on the surface*. Nat Nanotechnol, 2013. **8**(2): p. 137-43.
128. Vandenberg, W., Leutenegger, M., Lasser, T., Hofkens, J., and Dedecker, P., *Diffraction-unlimited imaging: from pretty pictures to hard numbers*. Cell Tissue Res, 2015. **360**(1): p. 151-78.
129. Sahl, S.J., Hell, S.W., and Jakobs, S., *Fluorescence nanoscopy in cell biology*. Nat Rev Mol Cell Biol, 2017. **18**(11): p. 685-701.
130. Tzeng, Y.K., Faklaris, O., Chang, B.M., Kuo, Y., Hsu, J.H., and Chang, H.C., Superresolution imaging of albumin-conjugated fluorescent nanodiamonds in cells by stimulated emission depletion. Angew Chem Int Ed Engl, 2011. **50**(10): p. 2262-5.
131. Mari, M., Geerts, W.J., and Reggiori, F., Immuno- and correlative light microscopy-electron tomography methods for 3D protein localization in yeast. Traffic, 2014. **15**(10): p. 1164-78.
132. Mateos, J.M., Barmettler, G., Doehner, J., Ojeda Naharros, I., Guhl, B., Neuhaus, S.C.F., Kaech, A., Bachmann-Gagescu, R., and Ziegler, U., *Correlative Super-resolution and Electron Microscopy to Resolve Protein Localization in Zebrafish Retina*. J Vis Exp, 2017(129).
133. Hodgson, L., Tavaré, J., and Verkade, P., Development of a quantitative Correlative Light Electron Microscopy technique to study GLUT4 trafficking. Protoplasma, 2014. **251**(2): p. 403-16.
134. van Weering, J.R., Brown, E., Sharp, T.H., Mantell, J., Cullen, P.J., and Verkade, P., *Intracellular membrane traffic at high resolution*. Methods Cell Biol, 2010. **96**: p. 619-48.
135. Olmos, Y., Hodgson, L., Mantell, J., Verkade, P., and Carlton, J.G., *ESCRT-III controls nuclear envelope reformation*. Nature, 2015. **522**(7555): p. 236-9.
136. Bianco, S., Grigolini, P., and Paradisi, P., Fluorescence intermittency in blinking quantum dots: renewal or slow modulation? J Chem Phys, 2005. **123**(17): p. 174704.
137. Derfus, A.M., Chan, W.C.W., and Bhatia, S.N., Probing the Cytotoxicity Of Semiconductor Quantum Dots. Nano Lett, 2004. **4**(1): p. 11-18.
138. Butterworth, K.T., Coulter, J.A., Jain, S., Forker, J., McMahon, S.J., Schettino, G., Prise, K.M., Currell, F.J., and Hirst, D.G., *Evaluation of cytotoxicity and radiation enhancement using 1.9 nm gold particles: potential application for cancer therapy*. Nanotechnology, 2010. **21**(29).
139. Chipaux, M., van der Laan, K.J., Hemelaar, S.R., Hasani, M., Zheng, T.T., and Schirhagl, R., *Nanodiamonds and Their Applications in Cells*. Small, 2018. **14**(24).
140. Fu, C.C., Lee, H.Y., Chen, K., Lim, T.S., Wu, H.Y., Lin, P.K., Wei, P.K., Tsao, P.H., Chang, H.C., and Fann, W., *Characterization and application of single fluorescent nanodiamonds as cellular biomarkers*. Proceedings of the National Academy of Sciences of the United States of America, 2007. **104**(3): p. 727-732.

141. Mohan, N., Tzeng, Y.K., Yang, L., Chen, Y.Y., Hui, Y.Y., Fang, C.Y., and Chang, H.C., Sub-20-nm Fluorescent Nanodiamonds as Photostable Biolabels and Fluorescence Resonance Energy Transfer Donors. *Advanced Materials*, 2010. **22**(7): p. 843-+.
142. Prabhakar, N., Nareoja, T., von Haartman, E., Karaman, D.S., Jiang, H., Koho, S., Dolenko, T.A., Hanninen, P.E., Vlasov, D.I., Ralchenko, V.G., Hosomi, S., Vlasov, II, Sahlgren, C., and Rosenholm, J.M., *Core-shell designs of photoluminescent nanodiamonds with porous silica coatings for bioimaging and drug delivery II: application*. *Nanoscale*, 2013. **5**(9): p. 3713-22.
143. Wu, Y., Jelezko, F., Plenio, M.B., and Weil, T., *Diamond Quantum Devices in Biology*. *Angew Chem Int Ed Engl*, 2016. **55**(23): p. 6586-98.
144. Hsiao, W.W., Hui, Y.Y., Tsai, P.C., and Chang, H.C., Fluorescent Nanodiamond: A Versatile Tool for Long-Term Cell Tracking, Super-Resolution Imaging, and Nanoscale Temperature Sensing. *Acc Chem Res*, 2016. **49**(3): p. 400-7.
145. Glenn, D.R., Lee, K., Park, H., Weissleder, R., Yacoby, A., Lukin, M.D., Lee, H., Walsworth, R.L., and Connolly, C.B., *Single-cell magnetic imaging using a quantum diamond microscope*. *Nature Methods*, 2015. **12**(8): p. 736-U161.
146. Tsai, P.C., Chen, O.Y., Tzeng, Y.K., Hui, Y.Y., Guo, J.Y., Wu, C.C., Chang, M.S., and Chang, H.C., *Gold/diamond nanohybrids for quantum sensing applications*. *Epj Quantum Technology*, 2015. **2**.
147. Simpson, D.A., Morrisroe, E., McCoe, J.M., Lombard, A.H., Mendis, D.C., Treussart, F., Hall, L.T., Petrou, S., and Hollenberg, L.C.L., *Non-Neurotoxic Nanodiamond Probes for Intraneuronal Temperature Mapping*. *Acs Nano*, 2017. **11**(12): p. 12077-12086.
148. Sekiguchi, T., Sotoma, S., and Harada, Y., Fluorescent nanodiamonds as a robust temperature sensor inside a single cell. *Biophysics and Physicobiology*, 2018. **15**: p. 229-234.
149. Dolde, F., Fedder, H., Doherty, M.W., Nobauer, T., Rempp, F., Balasubramanian, G., Wolf, T., Reinhard, F., Hollenberg, L.C.L., Jelezko, F., and Wrachtrup, J., *Electric-field sensing using single diamond spins*. *Nature Physics*, 2011. **7**(6): p. 459-463.
150. Chang, Y.R., Lee, H.Y., Chen, K., Chang, C.C., Tsai, D.S., Fu, C.C., Lim, T.S., Tzeng, Y.K., Fang, C.Y., Han, C.C., Chang, H.C., and Fann, W., *Mass production and dynamic imaging of fluorescent nanodiamonds*. *Nature Nanotechnology*, 2008. **3**(5): p. 284-288.
151. Liu, W.L., Yu, F.L., Yang, J.B., Xiang, B., Xiao, P., and Wang, L., 3D Single-Molecule Imaging of Transmembrane Signaling by Targeting Nanodiamonds. *Advanced Functional Materials*, 2016. **26**(3): p. 365-375.
152. Hui, Y.Y., Hsiao, W.W.W., Haziza, S., Simonneau, M., Treussart, F., and Chang, H.C., *Single particle tracking of fluorescent nanodiamonds in cells and organisms*. *Current Opinion in Solid State & Materials Science*, 2017. **21**(1): p. 35-42.
153. Liu, W.N., Naydenov, B., Chakraborty, S., Wuensch, B., Hubner, K., Ritz, S., Colfen, H., Barth, H., Koynov, K., Qi, H.Y., Leiter, R., Reuter, R., Wrachtrup, J., Boldt, F., Scheuer, J., Kaiser, U., Sison, M., Lasser, T., Tinnefeld, P., Jelezko, F., Walther, P., Wu, Y.Z., and Weil, T., *Fluorescent Nanodiamond-Gold Hybrid Particles for Multimodal Optical and Electron Microscopy Cellular Imaging*. *Nano Letters*, 2016. **16**(10): p. 6236-6244.
154. Prabhakar, N., Peurla, M., Koho, S., Deguchi, T., Nareoja, T., Chang, H.C., Rosenholm, J.M., and Hanninen, P.E., *STED-TEM Correlative Microscopy Leveraging Nanodiamonds as Intracellular Dual-Contrast Markers*. *Small*, 2018. **14**(5).
155. Hemelaar, S.R., de Boer, P., Chipaux, M., Zuidema, W., Hamoh, T., Martinez, F.P., Nagl, A., Hoogenboom, J.P., Giepmans, B.N.G., and Schirhagl, R., *Nanodiamonds as multi-purpose labels for microscopy*. *Scientific Reports*, 2017. **7**.
156. Hsieh, F.J., Chen, Y.W., Huang, Y.K., Lee, H.M., Lin, C.H., and Chang, H.C., Correlative Light-Electron Microscopy of Lipid-Encapsulated Fluorescent Nanodiamonds for Nanometric Localization of Cell Surface Antigens. *Analytical Chemistry*, 2018. **90**(3): p. 1566-1571.

157. Wu, Y.Z., Ermakova, A., Liu, W.N., Pramanik, G., Vu, T.M., Kurz, A., McGuinness, L., Naydenov, B., Hafner, S., Reuter, R., Wrachtrup, J., Isoya, J., Fortsch, C., Barth, H., Simmet, T., Jelezko, F., and Weil, T., *Programmable Biopolymers for Advancing Biomedical Applications of Fluorescent Nanodiamonds*. *Advanced Functional Materials*, 2015. **25**(42): p. 6576-6585.
158. Zhang, T., Neumann, A., Lindlau, J., Wu, Y.Z., Pramanik, G., Naydenov, B., Jelezko, F., Schuder, F., Huber, S., Huber, M., Stehr, F., Hogege, A., Weil, T., and Liedl, T., *DNA-Based Self-Assembly of Fluorescent Nanodiamonds*. *Journal of the American Chemical Society*, 2015. **137**(31): p. 9776-9779.
159. Chu, Z.Q., Zhang, S.L., Zhang, B.K., Zhang, C.Y., Fang, C.Y., Rehor, I., Cigler, P., Chang, H.C., Lin, G., Liu, R.B., and Li, Q., *Unambiguous observation of shape effects on cellular fate of nanoparticles*. *Scientific Reports*, 2014. **4**.
160. Nisman, R., Dellaire, G., Ren, Y., Li, R., and Bazett-Jones, D.P., Application of quantum dots as probes for correlative fluorescence, conventional, and energy-filtered transmission electron microscopy. *Journal of Histochemistry & Cytochemistry*, 2004. **52**(1): p. 13-18.
161. Dunin-Borkowski, R.E., The development of Fresnel contrast analysis, and the interpretation of mean inner potential profiles at interfaces. *Ultramicroscopy*, 2000. **83**(3-4): p. 193-216.
162. Chakraborty, S., Agrawalla, B.K., Stumper, A., Veg, N.M., Fischer, S., Reichardt, C., Kogler, M., Dietzek, B., Feuring-Buske, M., Buske, C., Rau, S., and Weil, T., *Mitochondria Targeted Protein-Ruthenium Photosensitizer for Efficient Photodynamic Applications*. *Journal of the American Chemical Society*, 2017. **139**(6): p. 2512-2519.
163. Ventola, C.L., *Progress in Nanomedicine: Approved and Investigational Nanodrugs*. P T, 2017. **42**(12): p. 742-755.
164. Uchida, T. and Taneichi, M., Clinical application of surface-linked liposomal antigens. *Mini Rev Med Chem*, 2008. **8**(2): p. 184-92.
165. Landfester, K., Musyanovych, A., and Mailander, V., From Polymeric Particles to Multifunctional Nanocapsules for Biomedical Applications Using the Miniemulsion Process. *Journal of Polymer Science Part a-Polymer Chemistry*, 2010. **48**(3): p. 493-515.
166. Landfester, K. and Mailander, V., Nanocapsules with specific targeting and release properties using miniemulsion polymerization. *Expert Opin Drug Deliv*, 2013. **10**(5): p. 593-609.
167. Foroozandeh, P. and Aziz, A.A., Insight into Cellular Uptake and Intracellular Trafficking of Nanoparticles. *Nanoscale Research Letters*, 2018. **13**.
168. Reinholz, J., Landfester, K., and Mailander, V., *The challenges of oral drug delivery via nanocarriers*. *Drug Delivery*, 2018. **25**(1): p. 1694-1705.
169. Dubertret, B., Skourides, P., Norris, D.J., Noireaux, V., Brivanlou, A.H., and Libchaber, A., *In vivo imaging of quantum dots encapsulated in phospholipid micelles*. *Science*, 2002. **298**(5599): p. 1759-1762.
170. Seleci, M., Seleci, D.A., Scheper, T., and Stahl, F., Theranostic Liposome-Nanoparticle Hybrids for Drug Delivery and Bioimaging. *International Journal of Molecular Sciences*, 2017. **18**(7).
171. Mi, C.C., Wang, Y.Y., Zhang, J.P., Huang, H.Q., Xu, L.R., Wang, S., Fang, X.X., Fang, J., Mao, C.B., and Xu, S.K., *Biosynthesis and characterization of CdS quantum dots in genetically engineered Escherichia coli*. *Journal of Biotechnology*, 2011. **153**(3-4): p. 125-132.
172. Clift, M.J.D. and Stone, V., Quantum Dots: An Insight and Perspective of Their Biological Interaction and How This Relates to Their Relevance for Clinical Use. *Theranostics*, 2012. **2**(7): p. 668-680.
173. Kumar, K.V.P., Ghosh, O.S.N., Balakrishnan, G., Thirugnanasambantham, P., Raghavand, S.K., and Viswanath, A.K., Green synthesis of zinc oxysulfide quantum dots using aegle marmelos fruit extract and their cytotoxicity in HeLa cells. *Rsc Advances*, 2015. **5**(22): p. 16815-16820.
174. Halim, H., Simon, J., Lieberwirth, I., Mailander, V., Kovnov, K., and Riedinger, A., Water-dispersed semiconductor nanoplatelets with high fluorescence brightness, chemical and colloidal stability. *Journal of Materials Chemistry B*, 2020. **8**(1): p. 146-154.

175. Schlaad, H., Krasia, T., and Patrickios, C.S., Controlled synthesis of coordination block copolymers with beta-dicarbonyl ligating segments. *Macromolecules*, 2001. **34**(22): p. 7585-7588.
176. Xu, H.L., Shen, L., Xu, L., and Yang, Y.Q., Controlled delivery of hollow corn protein nanoparticles via non-toxic crosslinking: in vivo and drug loading study. *Biomedical Microdevices*, 2015. **17**(1).
177. Erdem, O., Gungor, K., Guzelurk, B., Tanriover, I., Sak, M., Olutas, M., Dede, D., Kelestemur, Y., and Demir, H.V., *Orientation-Controlled Nonradiative Energy Transfer to Colloidal Nanoplatelets: Engineering Dipole Orientation Factor*. *Nano Letters*, 2019. **19**(7): p. 4297-4305.
178. Halim, H., Trieb, D., Huber, N., Martinez-Negro, M., Meyer, L.A., Basche, T., Morsbach, S., Zhang, K.A.I., and Riedinger, A., *Lateral Size Dependence in FRET between Semiconductor Nanoplatelets and Conjugated Fluorophores*. *Journal of Physical Chemistry C*, 2020. **124**(45): p. 25028-25037.
179. Bright, N.A., Davis, L.J., and Luzio, J.P., Endolysosomes Are the Principal Intracellular Sites of Acid Hydrolase Activity. *Current Biology*, 2016. **26**(17): p. 2233-2245.
180. Aston, D., Capel, R.A., Ford, K.L., Christian, H.C., Mirams, G.R., Rog-Zielinska, E.A., Kohl, P., Galione, A., Burton, R.A.B., and Terrar, D.A., *High resolution structural evidence suggests the Sarcoplasmic Reticulum forms microdomains with Acidic Stores (lysosomes) in the heart*. *Scientific Reports*, 2017. **7**.
181. Piradashvili, K., Simon, J., Passlick, D., Hohner, J.R., Mailander, V., Wurm, F.R., and Landfester, K., Fully degradable protein nanocarriers by orthogonal photoclick tetrazole-ene chemistry for the encapsulation and release. *Nanoscale Horizons*, 2017. **2**(5): p. 297-302.
182. Watanabe, S., Punge, A., Hollopeter, G., Willig, K.I., Hobson, R.J., Davis, M.W., Hell, S.W., and Jorgensen, E.M., *Protein localization in electron micrographs using fluorescence nanoscopy*. *Nature Methods*, 2011. **8**(1): p. 80-U117.
183. Kim, D., Deerinck, T.J., Sigal, Y.M., Babcock, H.P., Ellisman, M.H., and Zhuang, X., *Correlative stochastic optical reconstruction microscopy and electron microscopy*. *PLoS One*, 2015. **10**(4): p. e0124581.
184. Walther, P. and Ziegler, A., Freeze substitution of high-pressure frozen samples: the visibility of biological membranes is improved when the substitution medium contains water. *Journal of Microscopy*, 2002. **208**: p. 3-10.
185. Gregory, O.J., Luo, Q., and Crisman, E.E., High temperature stability of indium tin oxide thin films. *Thin Solid Films*, 2002. **406**(1-2): p. 286-293.
186. Ma, F., Wang, S., and Campbell, J.C., Shot noise suppression in avalanche photodiodes. *Phys Rev Lett*, 2005. **95**(17): p. 176604.
187. Yanikgonul, S., Leong, V., Ong, J.R., Hu, T., Siew, S.Y., Png, C.E., and Krivitsky, L., *Integrated avalanche photodetectors for visible light*. *Nat Commun*, 2021. **12**(1): p. 1834.
188. Lloyd, G.E., Atomic-Number and Crystallographic Contrast Images with the Sem - a Review of Backscattered Electron Techniques. *Mineralogical Magazine*, 1987. **51**(359): p. 3-19.
189. Pinos, J., Mikmekova, S., and Frank, L., About the information depth of backscattered electron imaging. *Journal of Microscopy*, 2017. **266**(3): p. 335-342.
190. Howie, A., Recent developments in secondary electron imaging. *Journal of Microscopy-Oxford*, 1995. **180**: p. 192-203.
191. Cedervall, T., Lynch, I., Lindman, S., Berggard, T., Thulin, E., Nilsson, H., Dawson, K.A., and Linse, S., Understanding the nanoparticle-protein corona using methods to quantify exchange rates and affinities of proteins for nanoparticles. *Proc Natl Acad Sci U S A*, 2007. **104**(7): p. 2050-5.
192. Schottler, S., Becker, G., Winzen, S., Steinbach, T., Mohr, K., Landfester, K., Mailander, V., and Wurm, F.R., Protein adsorption is required for stealth effect of poly(ethylene glycol)- and poly(phosphoester)-coated nanocarriers. *Nature Nanotechnology*, 2016. **11**(4): p. 372-377.
193. Mirshafiee, V., Kim, R., Park, S., Mahmoudi, M., and Kraft, M.L., Impact of protein pre-coating on the protein corona composition and nanoparticle cellular uptake. *Biomaterials*, 2016. **75**: p. 295-304.

194. Francia, V., Yang, K., Deville, S., Reker-Smit, C., Nelissen, I., and Salvati, A., *Corona Composition Can Affect the Mechanisms Cells Use to Internalize Nanoparticles*. ACS Nano, 2019. **13**(10): p. 11107-11121.
195. Lee, Y.K., Choi, E.J., Webster, T.J., Kim, S.H., and Khang, D., Effect of the protein corona on nanoparticles for modulating cytotoxicity and immunotoxicity. Int J Nanomedicine, 2015. **10**: p. 97-113.
196. Zhang, X., Liu, Y., Gopalakrishnan, S., Castellanos-Garcia, L., Li, G., Malassine, M., Uddin, I., Huang, R., Luther, D.C., Vachet, R.W., and Rotello, V.M., *Intracellular Activation of Bioorthogonal Nanozymes through Endosomal Proteolysis of the Protein Corona*. ACS Nano, 2020. **14**(4): p. 4767-4773.
197. Wang, C., Chen, B., He, M., and Hu, B., Composition of Intracellular Protein Corona around Nanoparticles during Internalization. ACS Nano, 2021. **15**(2): p. 3108-3122.
198. Qin, M., Zhang, J., Li, M., Yang, D., Liu, D., Song, S., Fu, J., Zhang, H., Dai, W., Wang, X., Wang, Y., He, B., and Zhang, Q., *Proteomic analysis of intracellular protein corona of nanoparticles elucidates nano-trafficking network and nano-bio interactions*. Theranostics, 2020. **10**(3): p. 1213-1229.
199. Bertoli, F., Garry, D., Monopoli, M.P., Salvati, A., and Dawson, K.A., The Intracellular Destiny of the Protein Corona: A Study on its Cellular Internalization and Evolution. ACS Nano, 2016. **10**(11): p. 10471-10479.
200. Vilanova, O., Mittag, J.J., Kelly, P.M., Milani, S., Dawson, K.A., Radler, J.O., and Franzese, G., *Understanding the Kinetics of Protein-Nanoparticle Corona Formation*. ACS Nano, 2016. **10**(12): p. 10842-10850.
201. Lundqvist, M., Stigler, J., Cedervall, T., Berggard, T., Flanagan, M.B., Lynch, I., Elia, G., and Dawson, K., *The evolution of the protein corona around nanoparticles: a test study*. ACS Nano, 2011. **5**(9): p. 7503-9.
202. Hegermann, J., Wrede, C., Fassbender, S., Schliep, R., Ochs, M., Knudsen, L., and Muhlfield, C., *Volume-CLEM: a method for correlative light and electron microscopy in three dimensions*. Am J Physiol Lung Cell Mol Physiol, 2019. **317**(6): p. L778-L784.
203. Maxfield, F.R. and McGraw, T.E., *Endocytic recycling*. Nat Rev Mol Cell Biol, 2004. **5**(2): p. 121-32.
204. Cullen, P.J., Endosomal sorting and signalling: an emerging role for sorting nexins. Nature Reviews Molecular Cell Biology, 2008. **9**(7): p. 574-582.
205. Grant, B.D. and Donaldson, J.G., Pathways and mechanisms of endocytic recycling. Nat Rev Mol Cell Biol, 2009. **10**(9): p. 597-608.
206. Tooze, J. and Hollinshead, M., In Att20 and Hela-Cells Brefeldin-a Induces the Fusion of Tubular Endosomes and Changes Their Distribution and Some of Their Endocytic Properties. Journal of Cell Biology, 1992. **118**(4): p. 813-830.
207. Gruenberg, J. and Stenmark, H., *The biogenesis of multivesicular endosomes*. Nature Reviews Molecular Cell Biology, 2004. **5**(4): p. 317-323.
208. Fader, C.M. and Colombo, M.I., Autophagy and multivesicular bodies: two closely related partners. Cell Death and Differentiation, 2009. **16**(1): p. 70-78.
209. Ekkapongpisit, M., Giovia, A., Nicotra, G., Ozzano, M., Caputo, G., and Isidoro, C., Labeling and exocytosis of secretory compartments in RBL mastocytes by polystyrene and mesoporous silica nanoparticles. International Journal of Nanomedicine, 2012. **7**: p. 1829-1840.
210. Fiorentino, I., Gualtieri, R., Barbato, V., Mollo, V., Braun, S., Angrisani, A., Turano, M., Furia, M., Netti, P.A., Guarnieri, D., Fusco, S., and Talevi, R., *Energy independent uptake and release of polystyrene nanoparticles in primary mammalian cell cultures*. Exp Cell Res, 2015. **330**(2): p. 240-247.
211. Thery, C., Zitvogel, L., and Amigorena, S., *Exosomes: composition, biogenesis and function*. Nat Rev Immunol, 2002. **2**(8): p. 569-79.
212. Hu, Y.B., Dammer, E.B., Ren, R.J., and Wang, G., The endosomal-lysosomal system: from acidification and cargo sorting to neurodegeneration. Transl Neurodegener, 2015. **4**: p. 18.

213. Raoufi, M., Hajipour, M.J., Kamali Shahri, S.M., Schoen, I., Linn, U., and Mahmoudi, M., *Probing fibronectin conformation on a protein corona layer around nanoparticles*. *Nanoscale*, 2018. **10**(3): p. 1228-1233.
214. Kihara, S., van der Heijden, N.J., Seal, C.K., Mata, J.P., Whitten, A.E., Koper, I., and McGillivray, D.J., *Soft and Hard Interactions between Polystyrene Nanoplastics and Human Serum Albumin Protein Corona*. *Bioconjugate Chemistry*, 2019. **30**(4): p. 1067-1076.
215. Mohammad-Beigi, H., Hayashi, Y., Zeuthen, C.M., Eskandari, H., Scavenius, C., Juul-Madsen, K., Vorup-Jensen, T., Enghild, J.J., and Sutherland, D.S., *Mapping and identification of soft corona proteins at nanoparticles and their impact on cellular association*. *Nature Communications*, 2020. **11**(1).
216. Vila-Vicosa, D., Campos, S.R., Baptista, A.M., and Machuqueiro, M., *Reversibility of prion misfolding: insights from constant-pH molecular dynamics simulations*. *J Phys Chem B*, 2012. **116**(30): p. 8812-21.
217. Jonkman, J. and Brown, C.M., *Any Way You Slice It-A Comparison of Confocal Microscopy Techniques*. *J Biomol Tech*, 2015. **26**(2): p. 54-65.
218. Jonkman, J., Brown, C.M., and Cole, R.W., *Quantitative confocal microscopy: beyond a pretty picture*. *Methods Cell Biol*, 2014. **123**: p. 113-34.
219. Baumeister, W., Grimm, R., and Walz, J., *Electron tomography of molecules and cells*. *Trends Cell Biol*, 1999. **9**(2): p. 81-5.
220. Tanaka, N., *Structure and Imaging of a Transmission Electron Microscope (TEM)*. *Electron Nano-Imaging: Basics of Imaging and Diffraction for Tem and Stem*, 2017: p. 17-28.
221. Carrassi, A. and Abati, S., [Introduction to scanning electron microscopy]. *Mondo Odontostomatol*, 1987. **29**(2): p. 29-36.
222. Grogger, W., Hofer, F., Kothleitner, G., and Schaffer, B., *An Introduction to High-resolution EELS in Transmission Electron Microscopy*. *Topics in Catalysis*, 2008. **50**(1-4): p. 200-207.
223. Riedl, T., Gemming, T., Gruner, W., Acker, J., and Wetzig, K., *Determination of manganese valency in La_{1-x}Sr_xMnO₃ using ELNES in the (S)TEM*. *Micron*, 2007. **38**(3): p. 224-230.
224. Paul-Gilloteaux, P., Heiligenstein, X., Belle, M., Domart, M.C., Larijani, B., Collinson, L., Raposo, G., and Salamero, J., *eC-CLEM: flexible multidimensional registration software for correlative microscopies*. *Nat Methods*, 2017. **14**(2): p. 102-103.
225. Zhao, F., Zhao, Y., Liu, Y., Chang, X.L., Chen, C.Y., and Zhao, Y.L., *Cellular Uptake, Intracellular Trafficking, and Cytotoxicity of Nanomaterials*. *Small*, 2011. **7**(10): p. 1322-1337.
226. van Deventer, S., Arp, A.B., and van Spriel, A.B., *Dynamic Plasma Membrane Organization: A Complex Symphony*. *Trends in Cell Biology*, 2021. **31**(2): p. 119-129.

Publication list

[1] Machtakova, M., **Han, S.**, Yangazoglu, Y., Lieberwirth, I., Thérien-Aubin, H., Landfester, K. Self-sustaining enzyme nanocapsules perform on-site chemical reactions. *Nanoscale*, **2021**, 13, 4051-4059.

[2] Pieszka, M., **Han, S.**, Volkmann, C., Graf, R., Lieberwirth, I., Landfester, K., Y. W. Ng, D., Weil, T., Controlled supramolecular assembly inside living cells by sequential multistaged chemical reactions. *J. Am. Chem. Soc.* **2020**, 142, 37, 15780–15789

[3] Jiang, S., Prozeller, D., Pereira, J., Simon, J., **Han, S.**, Wirsching, S., Fichter, M., Mottola, M., Lieberwirth, I., Morsbach, S., Mailänder, V., Gehring, S., Crespy, D., Landfester, K. Controlling protein interactions in blood for effective liver immunosuppressive therapy by silica nanocapsules. *Nanoscale*, **2020**, 12, 2626.

[4] Jiang, S., Mottola, M., **Han, S.**, Thiramanas, R., Graf, R., Lieberwirth, I., Mailänder, V., Crespy, D., Landfester, K. Versatile preparation of silica nanocapsules for biomedical applications. *Part. Part. Syst. Charact.* **2020**, 37, 1900484.

[5] **Han, S.**, Raabe, M., Hodgson, L., Mantell, J., Verkade, P., Lasser, T., Landfester, K., Weil, T., Lieberwirth, I., High-contrast imaging of nanodiamonds in cells by energy filtered and correlative light-electron microscopy: toward a quantitative nanoparticle-cell analysis. *Nano Lett.* **2019**, 19, 3, 2178–2185.

During master thesis:

[6] **Han, S.**, Kollmer, M., Markx, D., Claus, S., Walther, P., Fändrich, M., Amyloid plaque structure and cell surface interactions of β -amyloid fibrils revealed by electron tomography. *Sci. Rep.* **2017**, 7, 43577.

Curriculum Vitae



Shen Han

PHD CANDIDATE

Nationality: China

Date of birth: 20.09.1990

Address: Adam-karrillon-str. 1, 55118, Mainz, Germany

Employment History

Ph.D student, Max-Planck-Institute for Polymer Research, Mainz

DECEMBER 2016 — APRIL 2021

SFB1066 Nanodimensional polymer therapeutics for tumor therapy , Mainz

DECEMBER 2016 — APRIL 2021

Collaborators: JGU, BioNTech, LMU, etc.

Section Q: characterization of intracellular polymeric nanoparticles for drug delivery

Education

B.Sc in Biotechnology, Shenzhen University, Shenzhen, China

SEPTEMBER 2009 — JULY 2013

M.Sc in Biology, University of Ulm, Ulm, Germany

OCTOBER 2013 — JUNE 2016

Doctor of Philosophy, Max-Planck-Institute for Polymer Research, Mainz, Germany

DECEMBER 2016 — JUNE 2021

Conferences and Awards

2019 Microscopy & Microanalysis, Portland, OR, USA

AUGUST 2019

2019 Microscopy & Microanalysis Student Scholar Award, Portland, OR, USA

AUGUST 2019

EMBO Workshop: In situ Structural Biology: From Cryo-EM to Integrative Modelling

JANUARY 2021 — JANUARY 2021

Research Experience

Doctoral thesis project “ Correlative microscopy to study nanoparticle-cell interactions ”, Mainz, Germany

DECEMBER 2016 — APRIL 2021

Max-Planck-Institute for Polymer Research, AK Landfester, Prof. Dr. Katharina Landfester

Visiting Student project "Correlative Light and Electron Microscopy for Biological Samples", Bristol, United Kingdom

OCTOBER 2017 — NOVEMBER 2017

University of Bristol, School of Biochemistry, Wolfson Bioimaging Facility, Prof. Dr. Paul Verkade

Master thesis project "Electron Tomography of A-beta amyloid plaques from cell culture", Ulm, Germany

OCTOBER 2015 — JUNE 2016

University of Ulm, Institute of Protein Biochemistry, Prof. Dr. Marcus Fändrich

University of Ulm, Zentrale Einrichtung Elektronenmikroskopie, Prof. Dr. Paul Walther